

Sascha Weiß

Contributions to On Board Navigation on 1U CubeSats



Sascha Weiß

Contributions to On-Board Navigation on 1U CubeSats

The scientific series *Institute of Aeronautics and Astronautics:
Scientific Series* of the Technische Universität Berlin is edited by:
Prof. Dr.-Ing. Dieter Peitsch,
Prof. Dr.-Ing. Andreas Bardenhagen,
Prof. Dr.-Ing. Klaus Briß,
Prof. Dr.-Ing. Robert Luckner,
Prof. Dr.-Ing. Julien Weiss

Sascha Weiß

Contributions to On-Board Navigation on 1U CubeSats

Bibliographic information published by the Deutsche Nationalbibliothek

The Deutsche Nationalbibliothek lists this publication in the Deutschen Nationalbibliografie; detailed bibliographic data are available on the Internet at <http://dnb.dnb.de>.

Universitätsverlag der TU Berlin, 2022

<http://verlag.tu-berlin.de>

Fasanenstr. 88, 10623 Berlin
Tel.: +49 (0)30 314 76131 / Fax: -76133
E-Mail: publikationen@ub.tu-berlin.de

Zugl.: Berlin, Techn. Univ., Diss., 2021
Gutachter: Prof. Dr.-Ing. Klaus Briß
Gutachter: Prof. Dr.-Ing. Sabine Klinkner
Die Arbeit wurde am 8. Juni 2021 an der Fakultät V unter
Vorsitz von Prof. Dr.-Ing. Andreas Bardenhagen erfolgreich verteidigt.

This work – except for quotes, figures and where otherwise noted –
is licensed under the Creative Commons Licence CC BY 4.0
<http://creativecommons.org/licenses/by/4.0/>

Cover image: Palm Islands of Dubai, recorded by BEESAT-9 on 2020-02-15 | CC-BY 4.0

Print: Pro BUSINESS
Layout: Sebastian Grau, Karsten Gordon
Typesetting: Sascha Weiß

ISBN 978-3-7983-3232-4 (print)
ISBN 978-3-7983-3233-1 (online)

ISSN 2512-5141 (print)
ISSN 2512-515X (online)

Published online on the institutional Repository
of the Technische Universität Berlin
DOI 10.14279/depositonce-12416
<http://dx.doi.org/10.14279/depositonce-12416>

Contents

- 1 Introduction 1**
 - 1.1 The Rise of CubeSats 1
 - 1.1.1 CubeSat Standard and its Benefits 4
 - 1.1.2 Application Fields for Nano- and Picosatellites 5
 - 1.2 The BEESAT Line 7
 - 1.2.1 Precise Position and Orbit Determination on BEESAT-4 . 10
 - 1.2.2 Precise Position and Orbit Determination on BEESAT-9 . 11
 - 1.3 Thesis Outline 12

- 2 Position Determination and On-Board Navigation on Satellites 15**
 - 2.1 Significance of GNSS Receivers on Board of Satellites 15
 - 2.1.1 Position Determination 16
 - 2.1.2 Orbit Determination and Propagation 18
 - 2.1.3 Time Synchronization 19
 - 2.1.4 Constellations, Swarms and Formation Flight 20
 - 2.2 Selected Missions of CubeSats with GNSS Receivers 21
 - 2.2.1 CanX-1 22
 - 2.2.2 Compass-1 23
 - 2.2.3 AeroCube-4 24
 - 2.2.4 BEESAT-10-13 27
 - 2.3 Developments of 1U CubeSat Compatible GNSS Receivers 28
 - 2.3.1 Orion 29
 - 2.3.2 Phoenix 29
 - 2.3.3 SSTL 30
 - 2.3.4 CubeSat GPS Receiver 31
 - 2.3.5 GPS-601 31
 - 2.3.6 NOVATEL OEM4-G2L 31
 - 2.3.7 NanoSense GPS Kit 32
 - 2.3.8 GPSRM 1 32
 - 2.3.9 NEO-M8 32
 - 2.3.10 GNSS200 33

2.3.11	Warpspace	33
2.3.12	Venus828/838	34
2.3.13	Summary of Introduced Modules	34
3	Challenges of On-Board Navigation on 1U CubeSats	35
3.1	A Hypothetical 1U CubeSat	36
3.2	Subsystems of 1U CubeSats	36
3.3	Effects of a GNSS Receiver on the Satellite Bus	38
3.3.1	Electrical Power System	39
3.3.2	Communication System	40
3.3.3	Attitude Determination and Control System	41
3.4	Conclusions of Challenges for 1U CubeSats Regarding On-Board Navigation	42
4	System Concept	45
4.1	BEESAT Satellite Bus	45
4.1.1	Development of BEESAT-1	46
4.1.2	Summary of the System Concept of BEESAT-1	57
4.1.3	Adaptations to BEESAT-2	58
4.1.4	Summary of the Modifications of BEESAT-2	61
4.1.5	Adaptations to BEESAT-4	61
4.1.6	Summary of the Modifications to BEESAT-4	65
4.1.7	Adaptations to BEESAT-9	65
4.2	Summary of the Modifications to BEESAT-9	67
4.3	Ground Station	68
4.3.1	Ground Operations Software	68
4.3.2	Tools for Navigation Data Processing	69
4.4	Conclusions of the System Concept of the BEESAT line	72
5	Verification and Launch Campaign	77
5.1	Verification Campaign of BEESAT-4	77
5.1.1	Manufacturing and Integration	79
5.1.2	Ground Testing of ADCS	80
5.1.3	Ground Tests of GPS	82
5.1.4	Calibration Campaign	87
5.1.5	Environmental Test Campaign	91
5.1.6	Check Out and Launch	96
5.2	Conclusions from Verification Campaign of BEESAT-4	96

- 5.3 Verification Campaign of BEESAT-9 97
 - 5.3.1 Manufacturing and Integration 98
 - 5.3.2 Ground Testing of ADCS 98
 - 5.3.3 Ground Tests of GNSS 99
 - 5.3.4 Calibration Campaign 101
 - 5.3.5 Environmental Test Campaign 104
 - 5.3.6 Check Out and Launch 105
- 5.4 Conclusions from Verification Campaign of BEESAT-9 106

- 6 Mission Operations of BEESAT-4 and BEESAT-9 107**
 - 6.1 On-Orbit Experiments of BEESAT-4 107
 - 6.1.1 LEOP and Commissioning 108
 - 6.1.2 Orbit Experiments with the Attitude Determination and Control System on BEESAT-4 109
 - 6.1.3 GPS Operations 116
 - 6.1.4 Inter Satellite Link 121
 - 6.1.5 Conclusions from On-Orbit Experiments of BEESAT-4 . . 124
 - 6.2 On-Orbit Experiments of BEESAT-9 126
 - 6.2.1 LEOP and Commissioning 126
 - 6.2.2 Orbit Experiments with the Attitude Determination and Control System on BEESAT-9 128
 - 6.2.3 GNSS Operations 131
 - 6.2.4 Conclusions from On-Orbit Experiments of BEESAT-9 . . 134

- 7 Analysis of Navigation Experiments 137**
 - 7.1 Object Identification during LEOP 137
 - 7.1.1 Method for Orbit Identification of BEESAT-9 138
 - 7.1.2 Results of Orbit Identification of BEESAT-9 139
 - 7.2 Comparison of SGP4 Ephemerides to GNSS Based Positions . . . 140
 - 7.2.1 Method for Processing TLE Sets for Comparison 141
 - 7.2.2 Results of Comparison between TLE and GNSS Data Sets 143
 - 7.2.3 Summary of the Comparison of TLE and GNSS Based Ephemerides 152
 - 7.3 GNSS Signal Strength at the GNSS200 153
 - 7.3.1 Method for the Analysis of the Signal Strength 153
 - 7.3.2 Results from the Analysis of GNSS Signal Strength 156
 - 7.3.3 Summary of Signal Strength Analysis of GNSS Satellites . 159

7.4	Orbit Determination and Propagation of Ephemerides	159
7.4.1	Method of Orbit Determination for Ephemerides	160
7.4.2	Results from Orbit Determination	163
7.4.3	Summary of Orbit Determination and Propagation	166
7.5	Conclusion of Navigation Experiments	167
8	Summary, Conclusion and Outlook	169
8.1	Summary	169
8.2	Conclusion	173
8.3	Outlook for Future Missions	176
	Bibliography	179
A	Basic Navigation Data of BEESAT-4 from [31]	195
B	Basic Navigation Data of BEESAT-9 (Binary Protocol)	197
C	NMEA Messages of BEESAT-9 from [206]	199
C.1	GPGSV and BDGSV	199
C.2	GNRMC	200
D	Pictures of BEESAT-4	201
E	Pictures of BEESAT-9	205
F	Plots from Orbit Determination and Propagation	209

List of Figures

1.1	Nanosatellite launches by type from 1999 to 2023	2
1.2	Nanosatellite launches by organization from 1999 to 2023	3
1.3	The BEESAT line	10
2.1	Flight model of AeroCube-4	25
2.2	GPS fixes of AeroCube-4B and Aerocube 4C	26
2.3	The in-track, cross-track, and radial differences between the AC4-B GPS fixes and SGP-4 propagated TLEs	27
2.4	Flight model of the Phoenix GPS receiver for BEESAT-4	30
2.5	Flight model of GNSS200 for BEESAT-9 [53]	33
4.1	Evolution of the payloads on BEESAT	46
4.2	System overview of the subsystems of BEESAT-1	47
4.3	Schematic configuration of the communication system	49
4.4	Overview of the ADCS	50
4.5	Attitude sensors of BEESAT-1	50
4.6	Solar panel with dark rectangular magnetic coil	52
4.7	Reaction wheel system with Wheel Drive Electronic (WDE)	53
4.8	Modes of the ADCS	56
4.9	EGSE and camera board of BEESAT-1	57
4.10	Payload Data Handling of BEESAT-2 with camera modul	60
4.11	PDH with GPS receiver and camera	63
4.12	PDH of BEESAT-9	66
4.13	3D visualization tool of the Telemetry Analyzer	69
4.14	Radiation pattern of GNSS antenna of BEESAT-9	71
5.1	Integration process of BEESAT-4	80
5.2	Lock status in relation to signal strengths of the Phoenix receiver	84
5.3	Setup for the calibration of sun sensors on BEESAT-4	88
5.4	Temperature dependency of the offset of gyroscope MAX21000	90
5.5	BEESAT-4 on the shaker in an SPL	94
5.6	BEESAT-4 in a thermal vacuum chamber	95

5.7	Adapter for the GNSS200	100
5.8	Sun sensors of BEESAT-9 before and after calibration	102
6.1	Difference of angles between inertial and body-fixed frames	111
6.2	Comparison of field of view of the camera	112
6.3	Angular rates during Blind Damping Mode	113
6.4	Control error angle and angular rates of BEESAT-4 during zenith pointing	114
6.5	Elevation of GPS satellites over the antenna of BEESAT-4	119
6.6	Distance between BEESAT-4 and BIROS	121
6.7	Approximation of BEESAT-4 to BIROS	124
6.8	Error angle during experiment	129
6.9	Comparison of angular rate between the sensors	130
7.1	Flowchart of object identification of BEESAT-9	138
7.2	Object identification on 2019-07-07, GNSS compared to TLEs	139
7.3	Object identification on 2019-07-17, GNSS compared to TLEs	140
7.4	Flowchart of calculation of distances between GNSS and TLE ephemerides	142
7.5	Calculation of limit for a TLE update	144
7.6	In-track difference development of the “best” TLE	146
7.7	In-track amplitude change after two months of the “best” TLE	146
7.8	Cross-track (left) and radial (right) difference development over two months	147
7.9	Maximum in-track difference after two months for all TLEs	148
7.10	Development of the B^* value during the mission	149
7.11	Correlation between in-track difference and B^*	149
7.12	Differences from GNSS to SGP4 for all three directions for the “worst” TLE	150
7.13	Differences from GNSS to SGP4 for all three directions for the “worst” TLE with a modified B^* value	151
7.14	In-track difference for best, worst, mean and median TLE	152
7.15	Flowchart of the calculation of signal strengths over elevation	154
7.16	Accumulated signal strengths of GNSS satellites during the mission	157
7.17	Carrier Signal-to-Noise Ratio of tracked GNSS satellites depending on elevation	158
7.18	Carrier signal-to-Noise Ratio over elevation and azimuth	158
7.19	Flowchart of orbit determination and propagation	161

7.20	Comparison of residuals for different estimation times	163
7.21	In-track, cross-track and radial difference 24h after last GNSS data input	164
D.1	Dubai palm tree, used for Attitude Determination and Control System (ADCS) experiment	201
D.2	Salt desert Salar de Uyuni in Bolivia, commanded via BIROS . . .	202
D.3	Hurricane Irma on top of the Caribbean Sea, September 2017	203
E.1	Palm tree in Dubai for ADCS experiment	205
E.2	Bahamas on 2020-03-26	206
E.3	Chile on 2020-05-04	207
E.4	Moon over South America on 2020-04-01	208
F.1	Residuals for a three day GNSS data set from 2020-02-28	209
F.2	Residuals for a two day GNSS data set from 2020-02-29	210
F.3	Residuals for a one day GNSS data set from 2020-03-01	210
F.4	Residuals for a one orbit GNSS data set from 2020-03-01	211
F.5	Residuals for a one day GNSS data set from 2020-03-03	211
F.6	Residuals for a one orbit GNSS data set from 2020-03-03	212
F.7	Residuals for a one day GNSS data set from 2020-03-10	212
F.8	Residuals for a one orbit GNSS data set from 2020-03-10	213
F.9	Orbit propagation of two weeks from 2020-02-28, based on three days of GNSS data	213
F.10	Orbit propagation of two weeks from 2020-02-28, zoomed in . . .	214
F.11	Orbit propagation of two weeks from 2020-02-29, based on two days of GNSS data	214
F.12	Orbit propagation of two weeks from 2020-02-29, zoomed in . . .	215
F.13	Orbit propagation of two weeks from 2020-03-01, based on three orbits of GNSS data	215
F.14	Orbit propagation of two weeks from 2020-03-01, zoomed in . . .	216
F.15	Orbit propagation of two weeks from 2020-03-01, based on one orbit of GNSS data	216
F.16	Orbit propagation of two weeks from 2020-03-01, zoomed in . . .	217
F.17	Orbit propagation of two weeks from 2020-03-03, based on 20h of GNSS data	217
F.18	Orbit propagation of two weeks from 2020-03-03, zoomed in . . .	218

F.19 Orbit propagation of two weeks from 2020-03-03, based on one orbit of GNSS data	218
F.20 Orbit propagation of two weeks from 2020-03-03, zoomed in . . .	219
F.21 Orbit propagation of two weeks from 2020-03-10, based on 10h of GNSS data	219
F.22 Orbit propagation of two weeks from 2020-03-10, zoomed in . . .	220
F.23 Orbit propagation of two weeks from 2020-03-10, based on one orbit of GNSS data	220
F.24 Orbit propagation of two weeks from 2020-03-10, zoomed in . . .	221

List of Tables

- 2.1 GNSS receivers for 1U CubeSats 17
- 2.2 Milestones in navigation on picosatellites 22
- 2.3 Position error of AeroCube-4 relative to the GPS-based ephemerides at T_0 (adapted from [87]) 28

- 4.1 Overview of modifications on the BEESAT satellites 72

- 5.1 Qualification matrix of subsystems, components and applications of BEESAT-4 78
- 5.2 Test parameters for Phoenix 82
- 5.3 Test results for Phoenix 87
- 5.4 Calibration parameters of attitude sensors on BEESAT-4 87
- 5.5 Calibration parameters of magnetic field sensors on BEESAT-4 91
- 5.6 Test results for GNSS200 101
- 5.7 Calibration parameters of attitude sensors on BEESAT-9 101
- 5.8 Calibration parameters of magnetic field sensors on BEESAT-9 104

- 6.1 Events during LEOP of BEESAT-4 109
- 6.2 Results of on-orbit experiments with Phoenix 120
- 6.3 Overview of all operations of N-Link and ISL 123
- 6.4 Operational statistics of BEESAT-4 including software uploads (SW-UL) 125
- 6.5 Events during LEOP of BEESAT-9 127
- 6.6 Error angle of the control algorithm with old and new gyroscopes 128
- 6.7 All GNSS experiments of BEESAT-9 and the TTFF statistics 133
- 6.8 Operational statistics of BEESAT-9 including software uploads (SW-UL) 135

- 7.1 Statistics of the limit crossing by day 145
- 7.2 Results of the comparison after two months for selected TLE 151
- 7.3 Assorted array of NMEA data in reference to elevation and range of GNSS satellites 156

7.4	Used data sets for orbit determination and propagation	162
7.5	Residuals and orbit propagation results for the eight data sets after 1/3/7/14 days	165
A.1	F40 - Cartesian navigation data from WinMon protocol	195
A.2	F48 - Cartesian navigation data from WinMon protocol	196
B.1	Basic navigation data from GNSS200 on BEESAT-9	197
C.1	NMEA message for GNSS satellites in view	199
C.2	NMEA message for time, date, position, course and speed data . .	200

Glossary

Astro- und Feinwerktechnik GmbH

Berlin based manufacturer of satellite components and provider of environmental test facilities. 45, 93, 95, 105

Astrocast

Company from Switzerland providing IoT applications with their nanosatellite constellation. 3

BIROS

Bi-spectral InfraRed Optical System, microsatellite for fire detection using an infrared camera system. Deployer for BEESAT-4 was integrated and a formation was flown including ISL experiments. 9

D-Orbit

Italian launch provider. Deployment is executed from a satellite carrier, which allows for orbit adaptations. 4

EXOLAUNCH

Berlin based company, arranging rideshare launches with all leading launch providers worldwide. Offered free launch opportunity for BEESAT-9. 4, 9, 101, 105

Fleet Space Technologies

Company from Australia providing IoT applications with a Tyvak built nanosatellite constellation. 4

Fraction of day

Fraction of Day for Julian Date of Universal Time. 142

GCRF

Earth centered reference frame used for the navigation of satellites. 161

Helmholtz Cage

A Helmholtz cage consists of two identical magnetic coils for each axis and is used as a ADCS testbed to simulate the magnetic field of the Earth. 103

International Earth Rotation and Reference Systems Service

Organization to maintain global time and reference frame standards by updating the Earth observation parameters. 143

ISIS

Innovative Solutions In Space, a company providing launches, CubeSat platforms and products and entire satellite missions. 4

ITRF

The International Terrestrial Reference Frame, an Earth centered Earth fixed coordinate system similar to the WGS84. 161

JSpOC

The Joint Space Operations Center estimates the TLEs of the satellites on a daily basis. 13, 16, 70, 138–140, 167

Julian Centuries of TT

Julian Centuries of Terrestrial Time. 142, 143

Julian Date of UT1

Julian Date of Universal Time. 142, 143

Length of Day

Excess length of day used for the conversion of TEME to ECEF. 142, 143

LVLH

Coordinate system aligned to the orbit of the satellite, with the x-axis pointing in flight direction and the z-axis pointing nadir.. 70, 143

MATLAB

Math Laboratory: Software for simulations. 70, 81, 141, 159

MJD

Modified Julian Date, days since 1858-11-17 00:00:00. 142

NanoFF

Nanosatellite mission for formation flight and Earth observation. 5, 6, 160, 176, 177

N-Link

UHF transceivers on BIROS for the Inter Satellite Link to BEESAT-4. xiii, 9, 64, 108, 121–123

Planet

US-American company for Earth Observation, operating the Flock constellations. 3, 5, 20, 169

Precession

Orientation change of the rotation axes of a rotating body. xxx

Spaceflight

US based company, organizing launch services with several launch providers worldwide. 4

Spire Global

US-base company operating an constellation of nanosatellites, providing weather, maritime and aviation data information. 3, 20, 169

STK

Tool for orbital simulations of satellites. 70, 153, 154, 157

TAI-UTC

Difference between International Atomic Time and Universal Time Coordinated in seconds. 143

Taoglas

Company providing GNSS antennas. 98

TEME

The True Equator and Mean Equinox (TEME) coordinate system has its origin at the geometrical center of the Earth. The x-axis points towards the mean equinox and the z-axis is the instantaneous rotational axis of the Earth. 143

TOD

The True Equator and Mean Equinox (TEME) coordinate system has its origin at the geometrical center of the Earth. The x-axis points towards the mean equinox and the z-axis is the instantaneous rotational axis of the Earth. 161

TRACE

Orbit determination and propagation tool developed by the Aerospace Corporation, used for the AeroCube-4 mission . 26

TU Berlin

Technische Universität Berlin. xxiv, 1, 6–8, 11–13, 27, 65, 72, 79, 81, 92, 104, 116, 121, 122, 127, 139, 169, 176

UT1-UTC

Difference between Universal Time and Universal Time Coordinated in seconds. 143

Acronyms

1-PPS	1-Pulse Per Second. 19, 39
ADC	Analog-to-Digital Converter. 46, 51
ADCS	Attitude Determination and Control System. xi, xvi, 7, 12, 13, 24, 28, 32, 37, 39, 41, 42, 46, 49, 53–55, 58, 60–62, 64, 65, 68, 70, 72, 77, 81, 82, 87, 91, 97–99, 106, 107, 109, 112, 113, 115, 116, 118, 124, 126–132, 134, 140, 144, 145, 153, 170–174, 176, 201, 205
ADS	Automatic Dependant Surveillance. 6
ANDESITE	Ad-Hoc Network Demonstration for Extended Satellite-Based Inquiry and Other Team Endeavors. 22
AOCS	Attitude and Orbit Control System. 16, 38, 176
APID	Application Identifier. 197
ASCII	American Standard Code for Information Interchange. 86, 132, 154
AVANTI	Autonomous Vision Approach Navigation and Target Identification. 9, 11, 38, 40, 96, 108, 121, 124
BDGSV	Beidou Satellites in View. 132, 154, 199
BEESAT	Berlin Experimental and Educational Satellite. ix, xiii, xxvii, 5, 7–13, 15, 20–22, 24, 28, 30, 33, 35–43, 45, 47–49, 51–59, 61, 62, 64–73, 77–83, 85, 87–89, 93–99, 101–109, 111–131, 134, 135, 137–143, 145, 146, 152–157, 159–161, 166, 167, 169, 171–177, 195, 197
BIROS	Bi-spectral InfraRed Optical System. xv, 8, 9, 11, 38, 64, 91, 96, 107, 108, 121–124, 172, 177, 195
CAN	Controller Area Network. 46–48, 59, 61, 66, 133

CanX	Canadian Advanced Nanospace eXperiment. 21, 22, 31
CCSDS	Consultative Committee for Space Data Systems. 73
CDS	CubeSat Design Specification. 1, 4, 7, 169
CMOS	Complementary Metal-Oxide-Semiconductor. 23
COCOM	Coordinating Committee for Multilateral Export Controls. 17, 29, 32, 34, 38
COM	Communications System. 7, 12, 37, 46, 58, 62, 67, 160, 170, 173
COTS	Commercial Off-The-Shelf. 23, 29, 74
DLR	Deutsches Zentrum für Luft- und Raumfahrt. 5, 11, 23, 79, 96, 126
DOP	Dilution of Precision. 160, 170
ECEF	Earth Centered Earth Fixed. 138, 141
ECI	Earth Centered Inertial. 54
ECSS	European Cooperation for Space Standardization. 92
EGSE	Electrical Ground Support Equipment. 57
EPS	Electrical Power System. 7, 9, 12, 20, 37, 39, 40, 42, 46, 47, 62, 65, 160, 170, 173
EQM	Engineering Qualification Model. 9, 65, 83, 87, 97–99, 106
ESA	European Space Agency. 21
ETH	Eidgenössische Technische Hochschule. 32
FEES	Flexible Experimental Embedded Satellite. 20–22
FFT	Full Functional Test. 93, 96, 105, 106, 108
FIFO	First In - First Out. 67
FM	Flight model. 33, 77, 81, 83, 93, 101
FOV	Field of View. 67, 88, 117

GCRF	Geocentric Celestial Reference Frame. xvi, 161
GDOP	Geometrical Dilution of Precision. 160
GLONASS	GLObal NAvigation Satellite System. 30, 33
GMSK	Gaussian Minimum Shift Keying. 48
GNRMC	Global Navigation Recommended Minimum Specific Global Navigation Satellite System (GNSS) Data. 132, 154, 199
GNSS	Global Navigation Satellite System. xxi, xxvii, 3, 6, 9, 11–13, 15, 16, 18–21, 27–43, 45, 47, 65–68, 70, 71, 77, 82, 85, 97, 99, 101, 103–106, 126, 127, 131–134, 137–145, 147, 151, 153–157, 159–162, 166, 167, 169–176
GPSV	Global Positioning System (GPS) Satellites in View. 132, 154, 199
GPS	Global Positioning System. xxi, 8, 10, 15, 16, 19, 21–26, 28–30, 32, 33, 38, 61–64, 77, 78, 80, 82–86, 91–93, 96–100, 104, 108, 115–120, 125, 132, 142, 154, 156, 170–172, 199
GSOC	German Space Operations Center. 8, 29, 63, 82, 83, 85, 86, 97, 122
HAUSAT	Hankuk Aviation University SATellite. 21
HISPICO	Highly Integrated S-Band transmitter for Picosatellites. 8
IAA	International Academy of Astronautics. 108
IC	Integrated Circuit. 2, 92
IGRF	International Geomagnetic Reference Field. 24, 54, 90, 109–111
IoT	Internet of Things. 4–6
ISL	Inter Satellite Link. xiii, 9, 12, 13, 61, 64, 108, 121–124, 172, 174, 176, 177
ITRF	International Terrestrial Reference Frame. xvi, 161
JPL	NASA's Jet Propulsion Laboratory. 19
JSpOC	Joint Space Operations Center. xvi, 13, 16, 70, 138–140, 167

LEO	Low Earth Orbit. 6, 15, 19, 20, 39
LEOP	Launch and Early Orbit Phase. 9, 107, 108, 126, 127, 137, 167, 171, 172, 175
LNA	Low Noise Amplifier. 13, 63, 70, 84, 104, 120, 125, 137, 153, 159, 167, 172, 174
LVLH	Local Vertical Local Horizontal. xvii, xxix, 70, 143
M2M	Machine to Machine. 6
MarCO	Mars Cube One. 6
MAST	Multi-Application Survivable Tether. 30
MEMS	Micro-Electro-Mechanical System. 42, 62, 101, 115, 117, 171, 174
MOVE	Munich Orbital Verification Experiment. 36
NanoFEEP	Nano Field Effect Electric Propulsion. 37
NanoFF	Nanosatellites in Formation Flight. 10, 170
NASA	National Aeronautics and Space Administration. xxi, 6, 19
NMEA	National Marine Electronics Association. 67, 132, 153, 154, 159, 167, 195, 199
NOP	No Operation Command. 122, 123
NSP	Nanosatellite Protocol. 17
OBC	On-Board Computer. 7, 20, 37, 51, 53, 57–62, 65–67, 72, 77, 79, 80, 96, 98, 106, 119, 132–134, 197
ONS	On-Board Navigation System. 38
PCSat	Prototype Communication Satellite. 29
PCU	Power Control Unit. 7, 39, 47, 48, 52, 58, 60, 62, 65, 67, 79, 80, 98

PDH	Payload Data Handling. 8, 9, 58, 59, 61–63, 65–67, 72, 77, 79, 80, 86, 91, 92, 96–100, 106, 116, 117, 119, 120, 122, 129, 132–134, 171, 175
PDOP	Position Dilution of Precision. 160
pFDA	pico Fluid Dynamic Actuator. 36, 65–67, 72, 97, 98, 105, 106, 127, 131, 171
PiNaSys	Further Development and Verification of Miniaturized Components for Distributed Pico- and Nanosatellite Systems. 9, 36
PPOD	Precise Position and Orbit Determination. 8–13, 42, 45, 65, 77, 107, 124, 126, 132, 134, 137, 153, 160, 169, 170, 176
PPU	Payload Processing Unit. 122
PSD	Position Sensitive Device. 51, 62, 78, 88
PSLV	Polar Satellite Launch Vehicle. 23
QUEST	QUaternion ESTimation. 24, 49, 50, 55, 60, 103, 109, 110, 114
RAM	Random Access Memory. 7, 92, 133
RBF	Remove Before Flight. 57
RF	Radio Frequency. 85
RODOS	Realtime Onboard Dependable Operating System. 64
RTC	Real Time Clock. 19, 20
RTK	Real Time Kinematics. 34
SALSAT	Spectrum AnaLysis SATellite. 6
SAR	Synthetic Aperture Radar. 6, 19, 21, 31, 170
SDR	Software Defined Radio. 24
SFL	Space Flight Laboratory. 22, 23, 31, 38
SGP4	Simplified General Perturbations 4. 11, 13, 16, 25, 26, 70, 132, 137, 138, 140, 143, 148, 164, 172, 173, 176, 183

S-NET	S-Band Network for Cooperative Nanosatellites. 42
SNR	Signal-to-Noise Ratio. 8, 13, 48
SPL	Single Picosatellite Launcher. 8, 91, 93, 96, 108
SSO	Sun Synchronous Orbit. 27, 85, 86, 92, 97
SSTL	Surrey Satellite Technology Limited. 30
STK	Systems Tool Kit. xviii, 70, 119, 153–155, 157
TanDEM-X	TerraSAR-X-Add-on for Digital Elevation Measurements. 21
TC	Telecommand. 67
TCS	Thermal Control System. 37, 94
TDOP	Time Dilution of Precision. 160
TID	Total Ionizing Dose. 92, 153
TLE	Two Line Elements. xvi, xxix, 13, 16, 25, 26, 54, 69, 70, 83, 86, 110, 116, 132, 137–148, 150–153, 160, 161, 164, 166, 167, 172, 173, 175, 176
TM	Telemetry. 67, 68
TNC	Terminal Node Controller. 48, 49, 60, 65, 79, 80
TTF	Time-To-First-Fix. 11, 16, 28, 31, 33, 36–38, 41, 83, 85, 86, 100, 106, 121, 126, 133, 170, 175
TUBIN	TU Berlin Infrared Nanosatellite. 6
TUBSAT	TU Berlin Satellite. 1, 7
UART	Universal Asynchronous Receiver Transmitter. 18, 57, 66, 67, 72, 83, 86, 92
UHF	Ultra High Frequency. 6, 8, 9, 23, 40, 41, 48, 79, 80, 86, 108, 121, 122, 170, 172, 175
UTC	Universal Time Coordinated. xxix, 54, 86, 119, 140, 142, 162, 200
UTIAS	University of Toronto Institute for Aerospace Studies. 23

UWE	University Würzburg Experimental Satellite. 5, 30, 37
VC	Virtual Channel. 73
VHF	Very High Frequency. 6, 40, 41, 170
WDE	Wheel Drive Electronic. ix, 52, 53, 58, 62, 79, 98
WGS84	World Geodetic System 1984. 161, 162

Symbols

A	Apogee of the satellite. 145
α_{err}	Error angle of Attitude Control. 115, 129–131, 144, 145, 172
B^*	Aerodynamic drag term from TLEs. x , 138, 141, 144, 145, 148–153, 167, 172, 175
C	Carrier power of GPS signal. 24, 70, 82–87, 100, 101, 117, 118, 120, 125, 132, 137, 153, 154, 156–159, 167, 173, 175, 176, 199
c	Speed of light. 155
c_{dpm}	Proportional factor of the quaternion feedback controller for the Damping Mode. 117
C	Gain matrix for quaternion feedback controller. 56
c_{slm}	Proportional factor of the quaternion feedback controller for the Slew Mode. 115
D	Distance between GNSS satellites and BEESAT-9. 155
f	Frequency of GNSS signals. 155
FSPL	Free space path loss for an isotropic antenna. 155
g_{rms}	Total root mean square load over the frequency spectrum. 93
I_{sat}	Moment of inertia of the satellite. 115, 117
i_{slm}	Integration factor of the quaternion feedback controller for the Slew Mode. 115

J	Loss function from Wahba. 55
K	Gain matrix for quaternion feedback controller. 56
k_{slm}	Proportional factor of the quaternion feedback controller for the Slew Mode. 115
L	Angular momentum of the reaction wheels. 52, 59
\vec{m}_{mag}	Magnetic dipole momentum of the coils. 52
N_0	Noise power density. 24, 70, 82–87, 100, 101, 117, 118, 120, 125, 132, 137, 153, 154, 156–159, 167, 173, 175, 176, 199
N	Noise Power Level at a bandwidth of 1 Hz. 84
$\vec{\omega}$	Angular rate of the satellite. 50, 52, 56, 112, 113, 115, 117, 130, 133, 154
P	Perigee of the satellite. 145
P_r	Power density at the receiving antenna. 155
P_t	Power density at the transmitting antenna. 155
\vec{q}_e	Error quaternion, representing the difference between current and desired attitude. 50, 56, 115
\vec{q}	Current attitude representation of the satellite. 50, 154
\vec{q}_{des}	Desired attitude of the satellite. 50, 81, 114
\vec{r}_{SGP4}^{ECEF}	Position of the satellite calculated with the orbit model SGP4, based on TLEs in an ECEF reference frame. 138, 142, 143
\vec{r}_{gnss}^{ECEF}	Position of the satellite from the GNSS receiver. 138, 141, 142, 161
\vec{r}_{hill}	Position vector in Hill reference frame, from GNSS to TLE based position. 142

\vec{r}_{prop}^{ECEF}	Position of the satellite from the orbit propagation. 161
\vec{r}_{res}^{LVLH}	Residuals from the orbit determination in a LVLH reference frame. 161
\vec{r}_{sat}^{ECEF}	Position vector of the satellite in Earth fixed frame. 50
\vec{r}_{sat}^{ECI}	Position vector of the satellite in inertial frame. 50
\vec{r}_{SGP4}^{TEME}	Position of the satellite calculated with the orbit model SGP4, based on TLEs in a TEME reference frame. 142, 143
$T_{bf \leftarrow i}$	Transformation matrix from inertial to body-fixed reference frame. 54
t_{est}	Estimation time for orbit determination. 161
Θ_{bf}	Angle between sun and magnetic field vector in body-fixed reference frame. 110
Θ_i	Angle between sun and magnetic field vector in inertial reference frame. 110
t_{gnss}^{utc}	Time from GNSS200 converted to UTC. 138, 142, 161
τ	Torque of the reaction wheels. 52
t_{prop}	Propagation time for orbit propagation. 161
t_{since}	Time since epoch of Two Line Elementss (TLEs) in minutes. 142
t_{utc}	Satellite time in Universal Time Coordinated (UTC). 50, 138, 142, 154
\vec{u}	Actuating variable for reaction wheels. 50, 56
\vec{u}_{dpm}	Actuating variable for reaction wheels from the Damping Mode. 117
\vec{u}_{slm}	Actuating variable for reaction wheels from the Slew Mode. 115
\vec{v}_{SGP4}^{ECEF}	Velocity of the satellite calculated with the orbit model SGP4, based on TLEs in an ECEF reference frame. 138
\vec{v}_{BF}	Vector in body-fixed reference frame. 54
\vec{v}_{gnss}^{ECEF}	Velocity of the satellite from the GNSS receiver. 138, 161

\vec{v}_{hill}	Velocity vector in Hill reference frame, from GNSS to TLE based position. 142
\vec{v}_I	Vector in inertial reference frame. 54
\vec{v}_{mag}^{BF}	Magnetic field vector in body-fixed reference frame. 50, 110
\vec{v}_{mag}^{ECI}	Magnetic field vector in inertial reference frame. 50, 110
\vec{v}_{prop}^{ECEP}	Velocity of the satellite from the orbit propagation. 161
\vec{v}_{sun}^{BF}	Sun vector in body-fixed reference frame. 50, 110
\vec{v}_{sun}^{ECI}	Sun vector in inertial reference frame. 50, 110
w_k	Weight factors for different input vectors of QUEST. 50
x_{pole}	Polar motion coefficient x to compensate the Precession of the Earth. 142, 143
y_{pole}	Polar motion coefficient y to compensate the Precession of the Earth. 142, 143

1 Introduction

In 1957, the era of artificial objects orbiting planet Earth was initiated by the Soviet Union with the launch of Sputnik-1. Since then, several thousand satellites have followed its path, to explore the universe, to send humans into space and to help research in many different scientific fields. In the early years, most of the satellites were technology demonstration missions with low masses [1], which would be considered nanosatellites nowadays. Following the suggestion of Brieß [2], in this thesis they are classified at a launch mass of 4–20 kg. Further development of launch vehicles and higher demands of satellite payloads led to bigger satellites, which stopped the launch of nanosatellites until 1996. The TU Berlin was actually one of the first, after three decades, to launch a nanosatellite. In 1998 the communication satellites TU Berlin Satellite (TUBSAT)-N/N1 [3] were brought into space.

A milestone was set in 1999 with the introduction of the CubeSat Design Specification (CDS) by Cal Poly and the Stanford University [4]. This led to a whole new level of standardization and provided an access to space for many new participants, in particular universities, space agencies and the private sector.

1.1 The Rise of CubeSats

Making it more applicable for new participants, the CDS set requirements for CubeSats regarding their mechanical properties and dimensions. One unit (1U) was defined to be a satellite with a mass of less than 1.33 kg and dimensions of 10 cm × 10 cm × 10 cm. Furthermore, electrical restrictions were pointed out, e.g. during launch it has to be switched off. Besides other requirements regarding the mechanisms, materials and operations, suggestions were made for the environmental test campaign to ensure the safety of all spacecrafts during a launch.

After the specification was introduced, it took a couple of years until the first CubeSats were ready for launch and brought into space in 2003. The early years

saw a high number of 1U CubeSats, which were mainly developed by universities. In Figure 1.1 the number of CubeSats launched each year (along with their sizes) are displayed. Starting in 2013, 3U CubeSats became the preferred form factor and will continue to play a major role within CubeSat launches according to Williams, Doncaster and Shulman [5], as predicted in 2018. This is accompanied by an increasing market for 6U CubeSats, which satisfy the demand for higher payload volume and a more powerful satellite bus, as reported by DelPozzo and Williams in 2020 [6]. Many launchers integrate a 12U standard deployer, which is capable of launching CubeSats from 1U to 12U. The deployer features four slots for 3U CubeSats in the standard configuration, thus a form factor of 3U is highly beneficial for this setup and ensures high utilized capacities. Small adaptations ensure the same efficiency for 6U and 12U CubeSats.

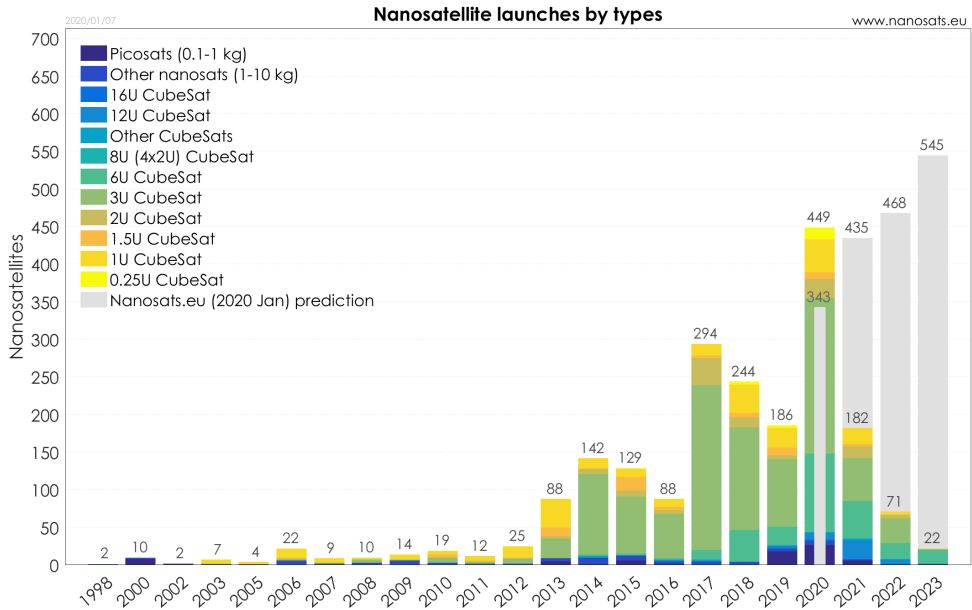


Figure 1.1: Nanosatellite launches by type from 1999 to 2023 [7]

The tremendous increase in CubeSat launches was driven by the miniaturization of electronics in sensor technology as well as in almost all Integrated Circuits (ICs). Furthermore, many small companies developed components, subsystems and devices, qualified those for space and partially implemented standardized interfaces, simplifying the development of spacecrafts for new participants. From

2013, the commercialization of the CubeSat market was initiated with the launch of Dove-1 for commercial constellations. Figure 1.2 indicates that the majority of the launched CubeSats was developed by companies.

Two of those, Planet and Spire Global, both requiring large constellations for their business model, are responsible for most of these launches. Until April 2020, Planet launched more than 400 satellites to daily monitor the entire Earth with a ground pixel size of 3–5 m [8]. For its global data analysis of weather, aviation, maritime and Earth, Spire Global launched 85 satellites until December 2019 [9].

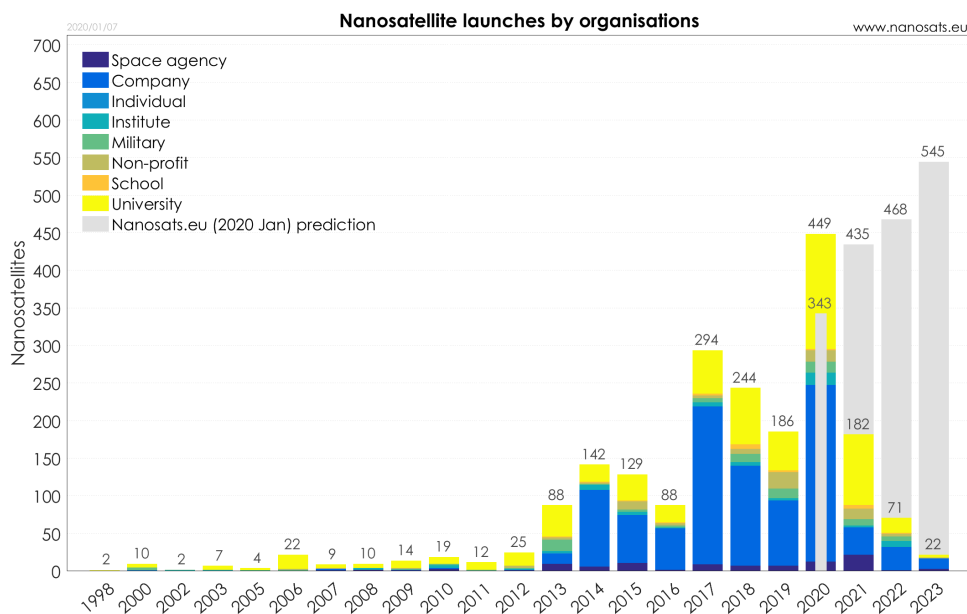


Figure 1.2: Nanosatellite launches by organization from 1999 to 2023 [7]

In 2019, Planet and Spire Global entered a new phase, bringing the sector growth to an end with a decrease of 25 % of CubeSat launches compared to 2018. New operators would have to step in to maintain a certain growth in the market [6]. Several constellations, especially in the communications segment, were announced and some technology demonstration missions were launched.

Astrocast is one of the upcoming companies, which already launched two 3U CubeSats (including the GNSS receiver u-blox NEO-M8, see Table 2.1) and has

announced another 20 satellites to be launched in 2020. The full constellation and their services, mainly Internet of Things (IoT), will be ready in 2023 [10].

The Australian based company Fleet Space Technologies likewise focuses in connecting IoT devices all around the globe with their 3U CubeSats. They launched two of their satellites in 2018. After a funding in 2019, they announced a mass production of satellites by Tyvak Australia to build their constellation [11].

Many more constellations were announced over the last years, most of them serving the IoT market [5, 6]. During the years 2017–2019, missions were launched by Sky and Space, ZeroG Lab, Kepler Communications, Lacuna Space amongst others, with all of them accomplishing technology demonstration (see [12]).

Another development of the recent years was the growing number of launch vehicles dedicated to small satellites, e.g. Electron, Kuaizhou 1A or Astra [6]. Despite their successful launches, more than 75 % of the nano- and microsattellites used a rideshare into their orbit in 2019 [6]. Given the estimated prices of a minimum of \$12 000/kg (see [6]), the percentage might increase, once all these launchers are fully available. Due to the given standards and the deriving benefits from those standards, the rise of CubeSats will continue [6].

1.1.1 CubeSat Standard and its Benefits

With the introduction of the CDS [4], several barriers to develop, manufacture and launch a satellite were removed. A launch of a satellite was a complicated issue and mainly executed by national space agencies and governments [13]. Given the cost of a dedicated launch, it was not affordable for smaller institutions or universities. Along with the standardization, many start ups (e.g. EXOLAUNCH, ISIS, Spaceflight, D-Orbit) were founded in the last 20 years, creating an interface between the launch providers and the satellite developers. This not only eased the access, but also came along with guidelines [14] regarding the required environmental tests, security levels on the launch sites and brought more launch providers into the ride-share market. For the launch provider, the safety of the primary payload has the highest priority. With the development of qualified deployment containers for CubeSats, safety could be guaranteed and the capabilities of the launch vehicles are now used more efficiently.

A special role was taken by 1U CubeSats, after the specification was published. From the first 60 CubeSats launched from 2003 until 2010, a total of 50 complied

to the 1U CubeSat specifications [7]. There were several reasons why especially 1U CubeSats were playing a major role in the beginning. Most missions were funded by universities or national space agencies (DLR funded UWE-1, COMPASS-1 and BEESAT-1 in this period), thus the budget was limited. A bigger form factor increases the cost of many parts of a mission, launch, manufacturing, development of bigger subsystems and payloads and subsequently higher personnel expenses. Furthermore, no components, nor subsystems were available by that time [15]. This forced the universities to develop most subsystems from scratch or search the market for commercial hardware, that components or subsystems could be based on. Additionally, most of the missions were used for amateur radio applications, technology demonstration of satellite bus components and only some of them included small payloads, e.g. a camera.

Starting with the development of components and subsystems, many spin-off companies were founded, complementing those that were individually founded (see [16] for a complete list of nanosatellite and CubeSat companies). Starting with 1U CubeSats, a huge market for sensors, subsystems and entire satellite buses has developed in the last 20 years. The advance in consumer electronics, regarding the miniaturization pushed this development, which led to a big variety of CubeSat compatible and space qualified components. With many suppliers supporting the standardized interface PC/104, several electronic boards from different companies can be easily stacked together.

The availability of entire satellite buses as well as subsystems and components opened the field to many more institutions, which is highly beneficial for the advance of science and technology. Recent developments showed scientific missions, where the satellite operator develops the payload with a defined interface and the satellite bus is bought from one of the CubeSat shops. This leads to an ever increasing role of CubeSats to complement bigger satellites, replace them in several fields and open new application fields, e.g. for world wide communication networks, IoT or Earth observation.

1.1.2 Application Fields for Nano- and Picosatellites

The last sections mentioned many applications that are already in space and will be in the near future. They are widespread over many scientific fields. Earth observation with a panchromatic camera in the visible wavelength range, as is done by Planet [8], or with a hyperspectral camera system as planned with the NanoFF

mission by TU Berlin [17], are complementing bigger satellites. Additionally, detectors for other wavelengths, e.g. radar or infrared, for fire detection, are implemented on smaller satellites as well. A 3U CubeSat constellation to detect bushfires in Australia was proposed by the university UNSW Australia [18]. TU Berlin Infrared Nanosatellite (TUBIN), another satellite from the TU Berlin will be launched in 2020, to detect and monitor fires all around the globe. Weather observations and Synthetic Aperture Radar (SAR) are further fields that will be occupied by nanosatellites. The listing of all the constellations in the NewSpace index [12] suggests that also Machine to Machine (M2M), IoT, internet from satellites and the monitoring of airplanes via Automatic Dependant Surveillance (ADS)-B will be done with CubeSats. A study by Lal et al [19] supports the scenarios of big constellations of nanosatellites and foresees a near-parity between big satellites and their smaller counterparts for remote sensing in general.

Within all these mostly commercially driven constellations and missions, niches for university missions for different purposes are still available. Two important questions were raised by Swartwout and Jayne in 2017 [20], whether university missions matter and if they are worth the effort. Scientific results from the successful missions led by academic institutions clearly affirm both questions and further developments are relevant and justified.

Satellite missions developed and operated by universities will always keep the educational purpose with students being involved in the projects worldwide. All the categories of university class spacecraft invented by Swartwout and Jayne [20] would fit this criteria, either being flagship universities with high reliability and significance at the state of the art, independent universities with their own string of successful missions or hobbyists with a high failure and low launch rate.

TU Berlin was considered a flagship university, with missions for technology demonstration for components of all subsystems and newly developed payloads. One of these components, a GNSS receiver, is considered a key feature for some of the future missions visioned by the Chair of Space Technology at TU Berlin. Especially the formation flight mission NanoFF relies on a sophisticated navigation concept based on a GNSS receiver to accomplish its mission objectives.

Further satellite missions for fire detection (TUBIN [21]) and analysis of usage of frequency bands in VHF, UHF and S-Band (SALSAT [22]) are ready to be launched in 2020. Flying nanosatellites to the Moon or Mars, like Mars Cube One (MarCO), a 6U CubeSat by National Aeronautics and Space Administration (NASA) [23] could be complementary options to Low Earth Orbit (LEO) missions.

Becoming one of these sophisticated flagship universities took the TU Berlin several years, starting with the development of TUBSAT-A. A new line followed the introduction of the CDS, starting with BEESAT-1, a miniaturized 1U CubeSat with mostly single-fault tolerance.

1.2 The BEESAT Line

In July 2004 the project Microwheels was kicked off at the TU Berlin. Its objective was the development of reaction wheels for picosatellites. The follow-up project Microwheels II, better known as Berlin Experimental and Educational Satellite (BEESAT)-1, started at the Chair of Space Technology in March 2005 to verify this development in space. It was the initialization of the BEESAT satellites [24, 25].

The idea was to build a mostly single-fault tolerant satellite bus compliant to the CubeSat Design Specification to achieve the main objective, but at that point in time CubeSat components or even subsystems were rarely available [15]. For this reason the focus was set on in-house developments of key subsystems, such as the Communications System (COM), the On-Board Computer (OBC), the ADCS, the structure and the Power Control Unit (PCU). The subsystems, components and sensors were qualified for their usage in space with functional, radiation, vibration and thermal-vacuum tests (see Section 4.1.1) [15].

After qualifying this highly redundant satellite, it was launched from India in September 2009. For more than three years it worked nominally and the mission objectives were fulfilled. Since 2013 its telemetry is not transferred to the ground station correctly, the cause being a failure of the Random Access Memory (RAM) on the OBCs or a software problem. Nevertheless, it was commanded for its 10th anniversary in 2019 and is still replying, meaning that the Electrical Power System (EPS), the COM and the OBC apart from the RAM are still functional during eclipse and sun phase.

With BEESAT-1 the technological basis was given for a subsequent mission to further enhance technology and implement a more advanced payload into the satellite. In April 2010 the project Microwheels III was launched with the primary mission objective to verify an innovative attitude control system for three-axis stabilization of the picosatellite BEESAT-2 [26, 27]. During the development of the satellite bus, several adaptations were applied to hard- and software, making it

capable of implementing a complex Payload Data Handling (PDH) and a camera (Section 4.1.3). Furthermore, several tools on the ground were adapted to process the data appropriately. The groundstation was also prepared for multi satellite operation, to handle BEESAT-1/2/3 simultaneously [28].

The new hardware was qualified, and after the following test campaign BEESAT-2 was launched in April 2013 together with BEESAT-3. It is still fully operational (on 2020-07-15), although some degradation can be seen, especially in the batteries. Throughout its mission operations it has seen several software updates, took many pictures of the Earth and fulfilled its mission objectives.

For the sake of completeness, BEESAT-3 is introduced here, even though it was built using a different approach and will not be mentioned further within this thesis. It is a satellite developed by students within lectures at the Chair of Space Technology. Besides education, the primary mission objective was the technology demonstration of the Highly Integrated S-Band transmitter for Picosatellites (HISPICO) using a passive attitude control. Some space proven components of the precursor missions were used, e.g. microcontrollers, the Ultra High Frequency (UHF) transceiver, charge regulators and batteries. Nevertheless, the subsystems were built independently and all the software was written from scratch [29]. After its launch in April 2013, no signals were received, but the team members and employees of the Chair kept trying to receive a beacon or data signals. After the reception of weak signals in January 2018, the breakthrough came with the construction of a new antenna at the TU Berlin ground station which increased the Signal-to-Noise Ratio (SNR) and allowed to decode telemetry. Since then, the missions objectives were achieved and the HISPICO transmitter was verified. BEESAT-3 is still operational (on 2020-07-15) and is commanded occasionally [30].

Given the status of GPS receivers in 2012, a three-axis stabilized satellite was seen as a requirement to acquire navigation solutions (see Section 3.3.3 and Table 2.1). Thus, the BEESAT-4 mission was proposed, based on the primary mission objective of BEESAT-2. Together with the on-orbit verification of Phoenix, a GPS receiver developed by the German Space Operations Center (GSOC) [31], on a 1U CubeSat, the implementation of a Precise Position and Orbit Determination (PPOD) package was the primary mission objective [32]. Furthermore, the mission proposal intended a deployment of the satellite from a Single Picosatellite Launcher (SPL) integrated into the microsatellite Bi-spectral InfraRed Optical System (BIROS) [33]. Providing navigation data to BIROS was another objective of BEESAT-4 to support the

experiment Autonomous Vision Approach Navigation and Target Identification (AVANTI) [34]. Both satellites can communicate, using a UHF Inter Satellite Link to exchange data (see Section 3.3 and Section 6.1.4). Each of the satellites was equipped with a similar transceiver module, which was called N-Link on BIROS.

The integration of the Phoenix receiver entailed several modifications to the satellite bus, leading to a new development of three electronic boards, the EPS, the PDH and one solar panel (see Section 4.1.5) [35, 36, 37].

Launching the satellite from India in June 2016 was not immediately followed by the Launch and Early Orbit Phase (LEOP) and commissioning, due to the cooperative mission with BIROS. Finally, in September 2016 the commissioning of BIROS was completed and BEESAT-4 was deployed. Since then it is operated on a daily basis and is still fully operational (on 2020-07-15). All the experiments conducted are described in Chapter 6.

Within the Further Development and Verification of Miniaturized Components for Distributed Pico- and Nanosatellite Systems (PiNaSys) project a new approach was taken. A quarter unit CubeSat was the output of an iteration process, where miniaturization was taken to a new level. Called BEESAT-5-8, the four satellites stacked together, equal the form factor of a 1U CubeSat. They are fully redundant and nearly single-fault tolerant. Their primary mission objective is the technology demonstration of a newly designed UHF communication system and an experimental GNSS receiver, flown together with a reference GNSS receiver from u-blox (see Table 2.1). The satellites are planned to be launched in Q3 2020, while their identical flight spare models BEESAT-10–13 were already launched in July 2019 [38].

A free launch opportunity, provided by EXOLAUNCH, gave the Chair of Space Technology at TU Berlin the chance to qualify further technology within the picosatellite BEESAT-9. Being the Engineering Qualification Model (EQM) of BEESAT-4 it was modified to integrate new technologies (see Section 4.1.7). The primary objective remained the same, the implementation of a PPOD package [39]. For this purpose a different receiver was integrated, the GNSS200 from Hyperion Technologies (see Table 2.1).

BEESAT-9 was launched from Vostochny, Russia in July 2019. After the LEOP and commissioning it is operated on a daily basis from several ground stations conducting experiments, especially with the GNSS receiver. In Chapter 6 a detailed

description of the executed experiments can be found. It is still fully operational (on 2020-07-15) and further experiments will be commanded.

Launched together with BEESAT-9 from the same deployer, the picosatellites BEESAT-10–13 are in orbit since July 2019. Being the flight spares of BEESAT-5–8, they are identical and have the same mission objectives.

The most recent CubeSat mission of the Chair of Space Technology is Nanosatellites in Formation Flight (NanoFF). The space segment will consist of two 2U CubeSats (BEESAT-14/15) demonstrating formation flight capabilities. The flight models will integrate newly developed and already space proven technologies from the BEESAT line. The benefits for NanoFF and other future missions from the research of this thesis will be outlined in Section 8.3.

The NanoFF satellites are planned to be launched in 2022, merging all the space proven technologies, the experiences in operation and the knowledge gained from its predecessors. One of the key technologies for formation flight is the on-orbit navigation, based on the PPOD package implemented on BEESAT-4 and BEESAT-9. In Figure 1.3 all the BEESAT satellites are displayed.



Figure 1.3: The BEESAT line (image credits: TU Berlin)

1.2.1 Precise Position and Orbit Determination on BEESAT-4

The primary mission objective of BEESAT-4 is the implementation of a PPOD package. The foundation for obtaining the required data is to integrate the GPS

receiver Phoenix from Deutsches Zentrum für Luft- und Raumfahrt (DLR). It is space proven and was used in several missions. Among those were three CubeSat missions, but none acquired a navigation solution (see Section 2.3.2). Proving the feasibility on a 1U CubeSat was the first step.

Further analysis of the possibilities revealed duty cycle limitations due to inherently smaller power and data downlink capabilities (see Section 3.2). Based on this information, a strategy was worked out. The position and timing information gathered from Phoenix was seen as payload data and is not meant to be used as an input for subsystems of the satellite bus. The acquired navigation data should be sent to the ground station for comparison with the Simplified General Perturbations 4 (SGP4) orbit model and to BIROS to support the AVANTI experiment. Based on the navigation data, an orbit determination tool is used on the ground and the quality of the determination is then compared to newly acquired position data of BEESAT-4 [40].

1.2.2 Precise Position and Orbit Determination on BEESAT-9

Since BEESAT-9 is part of the BEESAT-4 mission, the mission objectives have not changed officially. Nevertheless, from 2013 to 2018 technology has evolved. Therefore, several new components were integrated into BEESAT-9 (see Section 4.1.7). Regarding the PPOD package, a different GNSS receiver, the GNSS200 developed by Hyperion Technologies, was used, which is more suitable for a 1U CubeSat than the Phoenix (see Chapter 3). Changing the receiver had several reasons. The specifications of the GNSS200 regarding Time-To-First-Fix (TTFF), energy consumption and its dimensions are favorable for 1U CubeSats compared to Phoenix (see Table 2.1). Furthermore, the on-orbit experiments with Phoenix were limited and the performance was not satisfactory (see Section 6.1.3). Additionally, a GNSS receiver will be used in future missions of the TU Berlin and the Phoenix receiver is not built anymore with remaining units based on technology from 1998. Including a state of the art GNSS receiver therefore fits well into the strategic concept of the Chair of Space Technology.

Nevertheless, the baseline remained the same (see Section 1.2.1). The GNSS receiver is treated as a payload for navigation experiments. Despite that, there are more options of data acquisition compared to BEESAT-4, as can be seen in the detailed experiment descriptions in Chapter 6.

1.3 Thesis Outline

The previous sections provided a brief introduction to the history and milestones of CubeSat projects. Furthermore, the benefits of the standardization were emphasized and several application fields for Pico- and Nanosatellites were highlighted. An overview of the BEESAT satellites including their mission objectives was given and the main objective of BEESAT-4 and BEESAT-9, the PPOD was described. In this context, this work presents the enhancement of an educational and experimental CubeSat bus at TU Berlin over several years with a focus on navigation matters. Several aspects that could be preconditions for navigation applications, such as attitude control and an Inter Satellite Link (ISL), were verified on orbit as well during the research. The structure of the research within this thesis is set in the following way.

In Chapter 2 the author emphasizes the significance of GNSS receivers on board of satellites. Benefits regarding accuracies of several parameters, e.g. time, position and orbit propagation are discussed. Furthermore, some applications are highlighted, with the focus on the possibilities of implementing them on CubeSats. Moreover, special attention is given to several picosatellite missions (CanX-1, Compass-1, AeroCube-4, BEESAT-10-13), that set some milestones regarding the integration of GNSS receivers. To complete this chapter, an overview of developments of GNSS receivers is given. The selection is limited to receivers that fit the 1U CubeSat form factor.

Resources on 1U CubeSats are limited. This affects all subsystems, making the implementation of an on-board navigation package quite challenging, especially compared to bigger satellites. Chapter 3 will address the challenges deduced from this task. At first a hypothetical 1U CubeSat is introduced, which could solve most issues, but is highly theoretical, followed by a description of impacts to each subsystem of the satellite bus, caused by the implementation of a PPOD package, using a GNSS receiver. The EPS, COM and the ADCS were dealt with in detail, since they are the most affected subsystems.

In Chapter 4 the system concept of BEESAT is introduced. It describes the development and manufacturing of BEESAT-1, followed by the modifications applied to BEESAT-2, BEESAT-4 and BEESAT-9. The last section is dedicated to the ground tools needed for satellite operations and data evaluation. It is divided into two parts, basic ground station software, required for telecommands and telemetry and special tools for GNSS data analysis.

Manufacturing the satellites and integrating the receivers was mainly done at the university. It was the basis for a thorough verification campaign. Chapter 5 provides all the details about the ground testing of the ADCS and the GNSS receivers of BEESAT-4 and BEESAT-9. Furthermore, the calibration of the sensors and its significance to the primary mission objective is described. Another section is dedicated to the environmental test campaign where radiation, vibration and thermal-vacuum tests were conducted to verify the design of the satellites. The chapter concludes with the check-out campaign at the launch site.

All the systems were tested in space and many experiments were executed on orbit. Both satellites had slightly different agendas and mission objectives, which is pointed out additionally to the GNSS experiments in Chapter 6. One of the experiments of BEESAT-4 was an Inter Satellite Link (ISL) as a unique feature, which is a requirement regarding formation flights. All the experiments are described by the author and the results are discussed.

In Chapter 7 the retrieved navigation data is used for several research questions. At first a brief description is given on how BEESAT-9 was identified amongst the other 25 satellites that were launched into the same orbit together. The GNSS based positions are then compared to the TLE based orbit model SGP4 to analyze the quality of the TLEs provided by JSpOC. Furthermore, the performance of the GNSS antenna and its Low Noise Amplifier (LNA) is analyzed using the SNR of each channel of the GNSS receiver and the attitude data of the satellite. As a part of the PPOD package the navigation data is used to determine the orbit and propagate future ephemerides. For a statement regarding the quality of the propagated ephemerides, they are compared to the navigation data obtained on orbit.

Ultimately, the work of this thesis is summarized and concluded in Chapter 8. Moreover, a recommendation for the usage of GNSS receivers is given together with an outlook to future work in the field of on-board navigation on 1U CubeSats.

The proposed solutions to integrate a GNSS receiver are narrowly tied to the design of BEESAT-4 and BEESAT-9. Nevertheless, the implementation is applicable to any other CubeSat fulfilling the minimum requirements. As a whole, this work provides the current state of PPOD research at TU Berlin. At the same time, it highlights several additional segments and elements of a space mission, which have to be taken into account for the implementation of on-board navigation on 1U CubeSats.

2 Position Determination and On-Board Navigation on Satellites

Position determination and on-board navigation on satellites using GNSS receivers has a long history, starting in 1982 with the first integration into a satellite (see Section 2.3 [41]). The significance of accurate timing, position and orbit knowledge for selected applications, formations and swarms of satellites and several scientific fields has grown since then.

In 2003, CanX-1 was the first CubeSat, that was equipped with a GPS receiver. Further satellites, with form factors of 1U or even smaller followed afterwards. Most of these satellites focused on position determination on board and orbit determination on the ground. For on-board navigation, both parts have to be done in space. Several milestones were set, regarding the dimensions and the outcome of these missions (see Table 2.2).

A few of these key missions and their results are described in detail, starting with the first picosatellite with an integrated GPS receiver (CanX-1, launched 2003) to the first German university satellite Compass-1, the AeroCube 4 to the recently launched BEESAT-10–13 [7].

The development of GNSS receivers during the last two decades has seen major improvements leading to around 15 available GNSS receivers in 2020, that could fit into a 1U CubeSat.

2.1 Significance of GNSS Receivers on Board of Satellites

Many applications require a precise position determination, highly accurate timing and on-board or ground-based orbit determination to produce relevant scientific data. Depending on the accuracy needs, the navigation tasks are either ground-based or on-board. All currently available GNSS receivers, usable on LEO CubeSats, provide at least a 10 m position and a 0.1 m/s velocity accuracy (see Table 2.1 and Section 2.3 for a description of all the receivers).

The navigation solution given by the GNSS receivers is based on single frequency measurements. For use in the Attitude and Orbit Control System (AOCS), this accuracy is considered to be sufficient [42]. Nevertheless, various applications need position accuracies at sub-decimeter level and velocity knowledge accuracy of less than 1 mm/s. This requires ground based calculations using dual-frequency carrier phase measurements next to auxiliary environmental information of the atmosphere and precise GPS ephemerides [42].

Satellites without an integrated GNSS receiver usually use an orbit model propagator such as SGP4 [56, p. 62] which is based on TLEs. They are either generated using GNSS data or estimated by JSpOC using radar data. The position error is immense compared to GNSS data. Especially the along-track direction produces errors of more than 1 000 m directly after the TLEs are estimated [57]. Other orbit models produce similar accuracies, thus are inadequate for precision based applications. It emphasizes the necessity of GNSS receivers on-board of satellites, with any GNSS based application starting with the acquisition of the position of the satellite.

2.1.1 Position Determination

Knowing the position of a spacecraft is a basic information which needs to be available on-board as well as on the ground. All spacecrafts are tracked with radar and orbit elements are usually provided daily by JSpOC. Thus, ground based orbit models are able to calculate the position at any given time. On board the spacecraft it is generally the same strategy, with a big difference regarding the availability of the newest TLE. The orbit elements have to be uploaded daily from a ground station to maintain an accuracy of around 1 km (see Section 7.2).

Compared to an orbit model, the position accuracy of a GNSS receiver is significantly better (see TLEs vs. GPS in Section 7.2). Furthermore, there is no update needed by the ground station. All GNSS receivers have a “cold start” option, which does not require any further input. The receiver is switched on and broadcasts its navigation data every second. The Time-To-First-Fix (TTFF), regarding the “cold start” option has improved over the years (see Table 2.1), whereas older receivers are usually operated with a priori information about the GNSS constellations (“warm start” option) to obtain a navigation fix. These can be stored on board, updated from the ground or automatically via GNSS satellites (see [31]). Regardless of the used option, the receiver outputs navigation data via

Table 2.1: GNSS receivers for 1U CubeSats

GNSS Receiver	Dimension [mm ³]	Mass [g]	Constellations	Power [mW]	TTF (cold/warm)	Channels	Interface	Protocol	Status	Heritage
GPS Orion [43]	95 x 50 x 10	50	GPS	2000	8 min/ 60 s	12	UART	NMEA WinMon	Expired	2001
Phoenix [44]	70 x 47 x 11	22	GPS	850	10 min/ 3 min	12	UART	NMEA WinMon	Request	2009
SGR-05U [45]	70 x 45 x 10	45	GPS	800		12	UART		Expiring	2007
SGR-Ligo [46]	92 x 87 x 12	90	GPS	1000		24+	UART I ² C, CAN		Active	2019
CubeSat GPS Receiver [47]	96 x 96 x 15	110	GPS	1000	15 min/ 3 min	12	UART	NSP	Active	2017
GPS-601 [48]	94 x 56 x 26	160	GPS, GLONASS GALILEO, Beidou	1400	90 s/ 45 s	120	UART	NMEA Binary	Active	
OEM4-G2L [49]	60 x 100 x 16	56	GPS	1600	50 s/ 40 s	24	UART, USB	NMEA Binary	Active	2008
NanoSense GPS Kit [50]	46 x 72 x 11	31	GPS	1320	39 s/ 20 s	555	UART CAN, USB	NMEA Binary	Active	2015
GPSRM 1 [51]	96 x 90 x 12.6	109	GPS	1300	50 s/ 40 s	24	UART, USB	NMEA	Active	2017
NEO-M8 [52]	12.2 x 16 x 2.4	1	GPS, GLONASS GALILEO, Beidou	180	26 s/ 3 s	72	UART	NMEA UBX	COCOM Limited	2019
GNSS200 [53]	20 x 15 x 3	3	GPS/Beidou	150	90 s/ 30 s	167	UART	NMEA Binary	Active	2018
Warpspace [54]	24.1 x 20.2 x 7.5	3	GPS, GLONASS	150	29 s/ -	167	UART	NMEA Binary	Active	May 2021
Venus838 [55]	7 x 7 x 1.4	1	GPS/Beidou	150	29 s/ 3 s	167	UART	NMEA Binary	Active	2018

a standard interface, e.g. UART, for processing and the provision to all relevant subsystems on board.

Regarding swarms, constellations and formations of satellites, the knowledge of the relative position between spacecrafts is required as well. It can be done with a sub-meter accuracy using the estimated navigation data (position and velocity vectors) or with pseudorange and carrier phase measurements (raw data from the GNSS receiver) to reach sub-decimeter accuracy. Both concepts are applicable to nanosatellites and the latter has been verified in the CanX-4/5-mission [58] and will be applied to NanoFF in the near future.

2.1.2 Orbit Determination and Propagation

Usually based on sets of position and velocity vectors, measured by a GNSS receiver, an orbit can be determined. A well known orbit is the foundation to propagate its future motion, thus estimating its ephemerides precisely. There are many influences on the satellite, such as atmospheric drag, gravity of Earth and other celestial objects, solar pressure and spacecraft thrusters [59]. There are random uncertainties regarding the observations by the GNSS receiver next to the external disturbances. Modeling all these forces is complex and leads to a set of nonlinear equations of motion. The accuracy of the determination and propagation depends on the available data and on the depth of the models. Given the uncertainties it is always an approximation, which is computationally demanding [60, 61], thus precise orbit determination to sub-decimeter level is done on the ground.

On the Ground

Precise orbit determination was used in several missions (TerraSAR-X, TOPEX-Poseidon, Jason-1 [62]). On these missions it was based on dual-frequency GNSS measurements (carrier phase and pseudorange) and the orbit had to be estimated on the ground. Given the complexity of the models, by the time the missions were planned, it was the only option and the experiments were developed accordingly. Accuracies of sub-decimeter level and sub mm/s velocity knowledge were achieved and are required for some applications (see [42]).

On Board

In contrast to relative position determination, highly accurate orbit determination and propagation required for applications like altimetry, gravimetry or SAR interferometry [42] is still experimental and not yet part of on-board navigation systems. Accuracy requirements for the applications are high and the inherent complexity of the necessary models demand new approaches and computational power. According to Hausschild et al. [63, 64] simulations for Swarm-C provide orbit determination with a sub-decimeter accuracy (8.5 cm 3D rms). It would fulfill the requirements for several Earth observation applications done on the above mentioned missions.

2.1.3 Time Synchronization

One of the biggest benefits of GNSS receivers is the accurate timing. All the GNSS constellations provide a time alongside the necessary data to determine the position. The atomic clocks on the GPS satellites keep their time within three nanoseconds [65]. Maintaining this accuracy requires a synchronization with a ground based atomic clock twice a day. For the GPS satellites it is located in the USA, has the size of a refrigerator and is not qualified to survive a launch into space or the space environment [66]. Satellites in LEO could theoretically integrate atomic clocks, but it is not feasible for several reasons. They are expensive, big and have a high mass, e.g. the Deep Space Atomic Clock developed by NASA's Jet Propulsion Laboratory (JPL) has a mass of 16 kg and dimensions of 29 cm x 27 cm x 23 cm [67]. Additionally, a ground based update would have to be done twice a day, requiring access to a precise atomic clock on the ground. For the given reasons GNSS receivers are used for accurate timing and synchronization.

The data signals from the GNSS constellations are provided at the exact same time to ensure precise position determination on the GNSS receivers. All the receivers used in spacecrafts have a 1-Pulse Per Second (1-PPS) signal. The common accuracy of this signal is usually given at less than 40 ns in 95 % of the time using GPS [68]. The subsystems of a satellite synchronize to this signal, ensuring that all operations are executed at a precise dedicated time.

Satellites without an integrated GNSS receiver need different approaches. One of the options is a Real Time Clock (RTC), usually accompanied with a backup battery. This ensures the satellite still provides a valid time after a power-off. The

RTC technology is based on a crystal oscillator, with an accuracy between 20 and 100 ppm. This adds up to an error of two to eight seconds per day. Another option is to connect a crystal oscillator directly to the OBC or the EPS and provide a time stamp to the other subsystems. In both cases the time drifts away. The drift can be compensated, but depending on the temperature it varies over time as well. Nevertheless, this always requires commands from the ground for correction.

The clocks in GNSS receivers are based on crystal oscillators as well. Within a few seconds the accuracy is acceptable, but these oscillators are affected by a drift, too. The clocks have to be reset constantly, using the data signals from at least four GNSS satellites to maintain the necessary accuracy. Given that LEO satellites move at a speed of 6–8 km/s an inaccuracy of up to several seconds is intolerable for most scientific, technology based or commercial applications.

2.1.4 Constellations, Swarms and Formation Flight

Recent years have seen many proposals for big constellations and swarms of satellites. Many nations (USA, Russia, China, India, European Union) have set up a GNSS constellation [69]. Obviously those require highly accurate atomic clocks on-board to provide data signals to LEO satellites.

Many LEO constellations are planned, some with bigger satellites (e.g. OneWeb, Starlink [70, 71]) and many with CubeSats (see Section 1.1.2). Moreover, some commercial constellations with 3U CubeSats were built already. The two biggest are operated by Spire Global and Planet, two companies focusing on Earth observation (see Section 1.1.2) [8, 9]. All these satellites have an integrated GNSS receiver for several reasons. One of those is timing accuracy (see Section 2.1.3). Another reason is the position determination, which is used for guidance and navigation of the spacecrafts, because satellites in swarms and constellations are usually controlled separately, maintaining an absolute position and orbit, while formations are usually based on relative positions [72]. Additionally, it is necessary for an accurate attitude determination.

For 1U CubeSats or even smaller satellites these reasons would apply as well. Some platforms like BEESAT-10–13 (0.25U) [38] or the Flexible Experimental Embedded Satellite (FEES) (0.33U)[73] are launched in batches to comply the 1U form factor and have an integrated GNSS receiver. Both could potentially form a swarm or constellation and address scientific purposes cooperatively. In 2019,

BEESAT-10–13 were launched for technology demonstration, the FEES satellites will follow in 2020 [73].

Formation flights usually have even higher accuracy requirements, since the topology of the formation is crucial for the mission objectives. Some of these formations work as a single, large, virtual instrument (JC2SAT [74], FAST [75]) [72]. Furthermore, the distance between satellites could be lower than 50 m, as shown in the CanX-4/CanX-5-mission [58].

In-track or along-track orbits are so called trailing formations where two or more satellites follow each other at a precisely maintained distance. This can produce 3D views of a target, document processes of natural disasters or other moving objects [72]. The most famous formations are the 'A-Train' [76], Landsat-7 and EO-1 [77] and Terra-SAR and TerraSAR-X-Add-on for Digital Elevation Measurements (TanDEM-X) [78]. Newer concepts such as swarm formations are tested by the European Space Agency (ESA) with the mission SWARM [79]. In this case, images of a target are provided from different angles while increasing the swath width and maintaining a high resolution.

All these mentioned missions are flagship missions of the respective space agency. Nevertheless, GNSS receivers were also flown on 1U CubeSats and experiments were conducted regarding on-board navigation.

2.2 Selected Missions of CubeSats with GNSS Receivers

A total of 1200 CubeSats have been launched since 2003 [7]. A fractional amount of those are 1U CubeSats with an integrated GNSS receiver. The launch of Canadian Advanced Nanospace eXperiment (CanX)-1 in 2003 brought the first 1U CubeSat with an integrated GPS receiver into space [80]. In fact, this was the first launch of CubeSats ever, with five 1U and one 3U CubeSat integrated on a Rokot-KS and launched from Plesetsk, Russia [81]. Many CubeSats have demonstrated the capabilities of position and orbit determination, but only a few were picosatellites. Table 2.2 summarizes the milestones chronologically. There were several other missions for technology demonstration of GNSS receivers on 1U CubeSats, but for the following reasons they will not be described in detail in this thesis. Hankuk Aviation University SATellite (HAUSAT)-1, a South Korean 1U CubeSat was launched together with ICECube 1/2 in 2006. Due to a launch failure they never made it into their dedicated orbit [82]. The first Chilean CubeSat

called Suchai was launched in 2017, but there are no published results regarding the GPS receiver yet. Launched in 2019 together with BEESAT-9, the satellite Lucky-7 from Czech Republic was put into space for a technology demonstration mission including position determination using a GPS receiver [83].

Two interesting missions, regarding the dimensions of the satellites, will be launched in 2020. One is called Ad-Hoc Network Demonstration for Extended Satellite-Based Inquiry and Other Team Endeavors (ANDESITE) [84]. It is a 6U CubeSat, that will deploy eight sensor nodes (17.5 cm x 10 cm x 1.75 cm and a mass of 380 g), all of them equipped with a SkyTraq Venus GPS receiver [85, 86]. The other mission is called FEES, a 0.3U CubeSat platform for on-orbit validation of various technologies being launched with Soyuz. After the technology demonstration it can be used as a testbed for electronic components [73]. For more information on all known CubeSat missions see [7].

Table 2.2: Milestones in navigation on picosatellites

Satellite	Size	Launch Date	Milestone	Results
CanX-1	1U	2003-06-30	First worldwide	No signal
Compass-1	1U	2008-04-28	First German	No navigation fix
AeroCube 4	1U	2012-09-13	First with orbit determination	Successful, see section 2.2.3, [87]
AeroCube 6A	0.5U	2014-06-19	Smaller than 1U	Successful, [88]
BEESAT-4	1U	2016-06-22	First TU Berlin	No navigation fix, see section 6.1.3
BEESAT-9	1U	2019-07-05	First TU Berlin successfull	Successful, see section 6.2.3
BEESAT-10–13	0.25U	2019-07-05	Smallest ever	No navigation fix

2.2.1 CanX-1

One of the first six CubeSats launched in June 2003 was CanX-1 [81]. It was a technology demonstration mission built by graduate students of the Space

Flight Laboratory (SFL) at the University of Toronto Institute for Aerospace Studies (UTIAS). The main new technologies were a Complementary Metal-Oxide-Semiconductor (CMOS) horizon sensor, a star tracker, active three-axis magnetic stabilization and a Commercial Off-The-Shelf (COTS) GPS receiver from CMC Electronics [89, 90]. The receiver was connected to two omnidirectional antennas and was supposed to deliver an accurate position of CanX-1. This would have been the first step towards orbit determination and possible future missions including formation flights of nanosatellites [89]. For the acquisition of GPS satellites a stabilized satellite was necessary in 2003, due to the fact that a navigation solution was delivered by receivers in approximately 10 min in space with a “cold start”. Therefore an active stabilization based on magnetic coils was implemented [89]. It was confirmed that the satellite was successfully deployed into its orbit, but no signal was received, neither by the ground station operators in Toronto, nor by the amateur radio community worldwide [89]. Thus the functionality of the GPS receiver could not be verified on CanX-1.

SFL caught up on the verification in 2008 with their next satellite CanX-2, a 3U CubeSat that took the navigation topic a step further with radio occultation, position and orbit determination based on a GPS receiver from NovAtel [91].

2.2.2 Compass-1

In September 2003, the University of Applied Sciences in Aachen finished a concept study for a picosatellite project called COMPASS-1 [92]. The mission objectives were adapted throughout the years, but finally fixed to remote sensing with a color camera, GPS receiver validation and further technology demonstration of a UHF communication downlink, active magnetic control and Lithium-Polymer batteries [93]. The flight model was launched from India with a Polar Satellite Launch Vehicle (PSLV) on 2008-04-28 and the satellite was operational until April 2012 [94, 95].

For position determination, the Phoenix receiver (see Section 2.3) of DLR was integrated. It was the first time it was used in an actual satellite mission, being flown in sounding rocket experiments before [96]. Referring to the flight results published by the COMPASS-1 team, it was operated several times. The initialization process was confirmed and the output was nominal. Nevertheless, the receiver did not manage to track a satellite. The problem was traced back to an improper integration of the patch antenna, which caused a limited field of view [94]. Furthermore,

COMPASS-1 was equipped with the F-19 active patch antenna [97, p. 43], with a ground plane of 3.6 cm^2 . This decreases the C/N_0 additionally, compared to the recommend antenna by DLR, which has a ground plane of 62 cm^2 . With its height of 1.5 cm and a power consumption of 1 W [98, 99], it is not feasible for a 1U CubeSat (see Chapter 3).

Moreover, the experience of flying the Phoenix receiver on BEESAT-4 shows that an active attitude control is essential for the acquisition of GPS satellites (see Section 6.1.3). The attitude determination on COMPASS-1 is based on the QUaternion ESTimation (QUEST) algorithm [100, 101, chapter 4.5.5]. COMPASS-1 used magnetic field sensors and sun sensors together with model based data as an input for QUEST. Apparently, there was a technical problem with the International Geomagnetic Reference Field (IGRF) model, making the magnetic field sensor useless and the entire attitude determination impossible. Furthermore, the ADCS never indicated a valid sun vector. Active attitude control requires the knowledge of a valid attitude, thus the controller never created a magnetic control torque [94].

2.2.3 AeroCube-4

The Aerospace Corporation launched three 1U CubeSats called AeroCube-4A/B/C on 2012-09-12. One of the main mission objectives was orbit control by changing the ballistic coefficient with deployable and retractable solar panels [102]. Figure 2.1 shows one of the flight models of AeroCube-4 with deployed solar panels.

All three satellites were equipped with a GPS receiver, which was developed and built in-house. It is a Software Defined Radio (SDR) receiver that was adopted for space applications [104]. It was used for position determination, highly accurate orbit determination and ultimately for the detection of changes in the ballistic coefficient [87].

The functionality of the GPS receiver was verified with a GPS simulator on the ground with a specific strategy for a tumbling spacecraft. All three AeroCubes-4 had a three-axis stabilized ADCS, but due to power budget limitations the spacecraft was left tumbling most of the time. The GPS operations were driven by two main limitations, data download capability and power budget. This lead to a query of three GPS fixes with a gap of a few seconds repeated nine times every ten minutes. It accumulates to a total of 27 fixes evenly spread over one orbit. In a typical

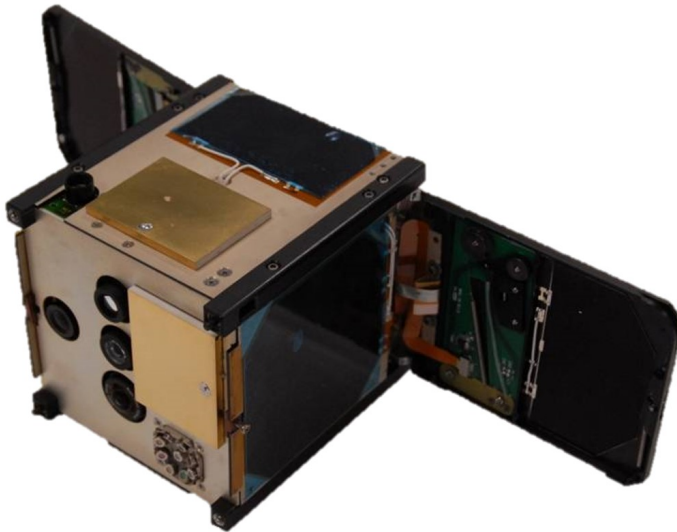


Figure 2.1: Flight model of AeroCube-4 [103] (*Courtesy of and reprinted by permission of The Aerospace Corporation.*)

scenario this was executed once a day [87]. In Figure 2.2 all the GPS fixes of AeroCube-4B and AeroCube-4C are displayed (the contact to AeroCube-4A was lost shortly after the solar panels were closed [104]).

Navigation solutions were returned on approximately 75 % of the days, leaving around 60 days without a GPS fix. There are no further explanations made for these gaps. Some of the possible reasons are tumbling satellites, i.e. GPS antenna pointing towards Earth or a high angular rate, resets of the satellite, deleting the time-tagged command lists, operational failures or low powered batteries that required breaks of GPS operations.

The datasets were stored on-board and transmitted to the ground station for further processing. One of the objectives was the comparison of navigation fixes and TLE based positions obtained from the SGP4 model. It was essential, since many daily operations for the AeroCube-4 used TLE, e.g. ground-station pointing. A three-day gap was the maximum estimation until new TLEs were available and could be uploaded to the satellites [87]. Figure 2.3 displays the results for in-track, cross-track and radial differences. The GPS fixes were received from AeroCube-4B and the TLE based ephemerides were acquired with the SGP4 orbit model propagator.

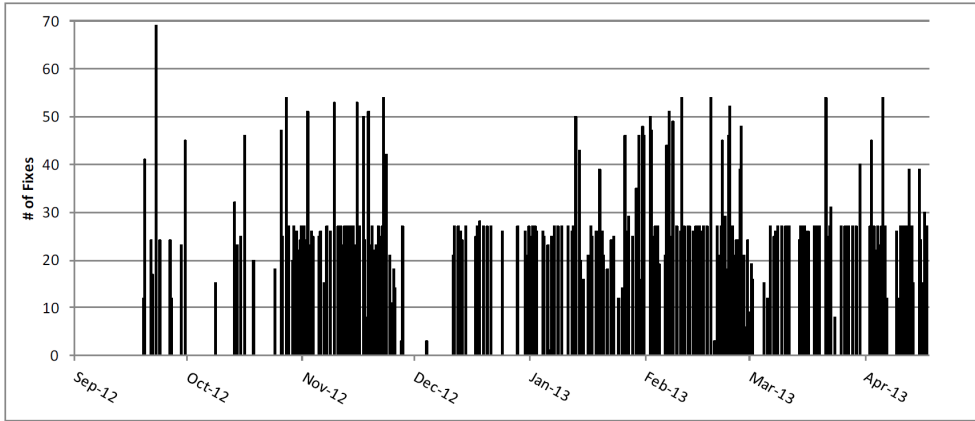


Figure 2.2: GPS fixes of AeroCube-4B and Aerocube 4C for the first eight months in orbit [87] (Courtesy of and reprinted by permission of The Aerospace Corporation.)

The in-track difference is the main concern for accurate ground-station pointing, increasing at a quadratic rate of 10–20 km daily. The limited gravity model of the SGP4 model, the inaccuracies of the TLEs and the variable drag profile, due to a tumbling satellite are the main contributions to the error [87]. Nevertheless, the error remains acceptable within a three-day range.

The last objective regarding navigations was the orbit determination based on the GPS measurements and the propagation of ephemerides in a time frame of 3 and 14 days. It was realized with the orbit determination tool TRACE. Table 2.3 shows the average position error relative to the GPS-based ephemerides. An error of less than 25 m at the starting point averages to an error of 54 km for GPS based propagation [87].

The AeroCube4 mission was a success regarding the navigation objectives. The GPS receiver was verified in space and it was shown that TLEs can be used for several days for common operations. Orbit determination with a maximum error of several meters requires data sets from three consecutive days, especially for in-track uncertainties. Starting from these errors a propagation of up to 14 days was made which leads to high errors of more than 50 km even for GPS based calculations. All the experiments show a much higher accuracy for GPS compared to TLE based calculations [87].

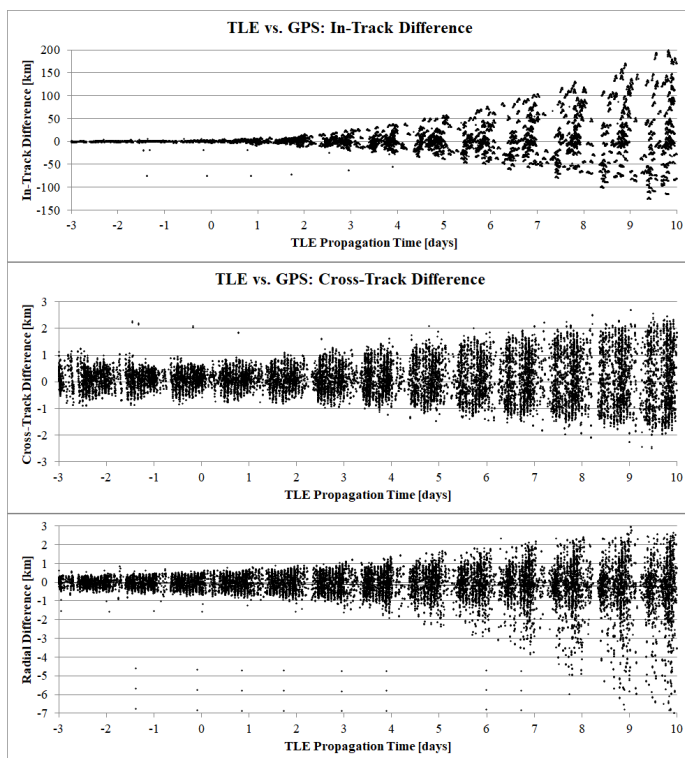


Figure 2.3: The in-track, cross-track, and radial differences between the AeroCube-4B GPS fixes and SGP-4 propagated TLE [87] (*Courtesy of and reprinted by permission of The Aerospace Corporation.*)

2.2.4 BEESAT-10-13

On 2020-07-05, four quarter unit CubeSats were launched from the cosmodrome Vostochny into their dedicated Sun Synchronous Orbit (SSO) at an altitude of 530 km. Together with the SpaceBEE satellites [105, 106] they are the only CubeSats launched with such a form factor. Four GNSS receivers on each satellite would have made them the smallest spacecraft capable of precise position determination. One of the mission objectives is the verification of a receiver that was developed at TU Berlin. For verification purposes a commercially available GNSS receiver was integrated as well (see Section 2.3.9). It is a module developed by the company u-blox and was modified to work in space.

Table 2.3: Position error of AeroCube-4 relative to the GPS-based ephemerides at T₀ (adapted from [87])

Ephemeris	Average Differences [km]		
	In-Track	Cross-Track	Radial
TLE @ T-14	135	3.5	3.2
GPS @ T-14	54	0.1	0.6
TLE @ T-3	11	1.9	1.3
GPS @ T-3	3	0.01	0.05
TLE @ T ₀	4	1.1	0.9

The GNSS receiver u-blox Neo-M8 is one of the newest on the market, leading to very fast TTFFs of less than 30 s. This has a huge impact on the requirements of the ADCS (see Section 3.3.3). Precise position determination does not depend on three-axis stabilization in case of BEESAT-10–13. It only requires a low angular rate to be able to acquire navigation satellites and track them. Magnetic coils in all three axes are capable of lowering the angular rate close to zero. Once a low angular rate is achieved the GNSS receiver will see the same navigation satellites for a sufficient time to get a fix.

The satellites are active and commanded several times a week. Due to software issues, the GNSS receivers were not switched on. In November 2020 another batch (BEESAT-5–8) will be launched with an updated software, making precise orbit determination possible.

2.3 Developments of 1U CubeSat Compatible GNSS Receivers

In 1982, the first civilian GPS receivers were integrated into Landsat 4/5 and flown in space [41]. At that time only six GPS satellites were launched [13], which implies it was long before the system became fully operational in 1993 [107]. Nevertheless, the breakthrough came with the discontinuation of selective availability in 2000, making high precision timing available to all users [108]. This led to a development of many GPS receivers on the ground and for space. This

section will describe some developments and gives an overview of all available CubeSat compatible GNSS receivers.

All but one receiver is generally available without Coordinating Committee for Multilateral Export Controls (COCOM) limitation. It restricts civil GNSS modules to a velocity of 1 000 kn (~1 900 km/h) and an altitude of 60 000 ft (~18 000 m). The restrictions were mainly applied to avoid the usage of regular GNSS receivers inside weapons [109].

2.3.1 Orion

The GSOC developed a GPS receiver for space applications based on a COTS solution called Orion by Mitel Semiconductor (introduced in 1997). High dynamics in space and sounding rockets required software modifications as well as hardware changes for the integration into existing satellite bus systems [110].

In February 2001, Kiruna served as the location for the first test flight on a rocket. It was successful and led to the first verification on a satellite in September 2001 on board of the Prototype Communication Satellite (PCSat). Table 2.1 summarizes the main characteristics of the GPS Orion receiver.

Theoretically it is small enough to fit into a 1U CubeSat, but especially the power consumption of 2 W would make a useful operation difficult. It was never used in a CubeSat mission, since its successor, Phoenix, was developed quite shortly after Orion and is less demanding.

2.3.2 Phoenix

The second GPS receiver developed at GSOC is called Phoenix. It is based on the Orion receiver, with an advanced chipset, which led to a tighter integration and especially to a lower power consumption [111]. The receiver is able to provide a navigation solution with an update rate of 5 Hz, whereas by default it is set to output the position and velocity data once per second with an accuracy of 0.1 ms and on the integer number of GPS seconds per week [31].

Additionally it is possible to receive the raw data measurements for higher precision in position and orbit determination. On several missions (TET-1, BIROS) it is used as a part of the on-board navigation system [112].



Figure 2.4: Flight model of the Phoenix GPS receiver for BEESAT-4

The Phoenix receiver was integrated into several CubeSats. The first mission was Multi-Application Survivable Tether (MAST), a 3U CubeSat, which was able to acquire an almanac from GPS satellites, but never locked onto a navigation solution [113]. The second mission was COMPASS-1, where no GPS signals were received at all (see Section 2.2.2). Another German 1U CubeSat mission, that flew the Phoenix receiver, was UWE-2. Unfortunately, after 12 days in orbit, no more signals were received from the satellite [114]. Thus, the Phoenix receiver was never used on UWE-2. The last CubeSat mission to integrate a Phoenix receiver was BEESAT-4 (see Section 4.1.5). In Table 2.1, important parameters of Phoenix are summarized. Figure 2.4 shows the flight model that was used in the BEESAT-4 mission.

2.3.3 SSTL

The British company Surrey Satellite Technology Limited (SSTL) sells several GNSS receivers. Two of those receivers physically fit into a 1U CubeSat. The SGR-05U was first flown in 2007 while the SGR-Ligo was verified in 2019 [115]. For future missions, SSTL will only provide the SGR-Ligo, while the SGR-05U is not produced anymore. Both receivers provide navigation data based on GPS L1 C/A Code, while the SGR-Ligo optionally can receive signals from the GLObal NAVigation Satellite System (GLONASS) and Galileo constellation as well. Carrier

phase and pseudorange measurements are not available, which makes potential orbit determination less accurate. One very interesting feature regarding the use on a 1U CubeSat is the low power mode on the SGR-Ligo. It uses 12 channels instead of 24, which lowers the power consumption to less than 0.4W. The main characteristics are summarized in Table 2.1.

2.3.4 CubeSat GPS Receiver

This receiver produced by the South African company NewSpace Systems is fully qualified for the loads during launch and the expected radiation for a lifetime of one year. Configured to fit into a stack of the standardized PC/104 connector, it is compatible with boards of other companies. It is a single frequency receiver, which does not provide carrier phase or pseudorange measurements. In Table 2.1 the specifications are summarized. Its power requirements of 1W are challenging for a 1U CubeSat for continuous operation.

2.3.5 GPS-601

SpaceQuest, a company based in Virginia, USA, developed the GPS-601 receiver. It is highly accurate with its 120 Channels and a fast TTFF. Furthermore, all global GNSS systems are trackable. It is fully space qualified and of the 42 delivered modules, a total of 18 were already launched [48]. The receiver is capable of raw measurement data output, to provide even higher accuracies for post processing. The main characteristics can be found in Table 2.1.

2.3.6 NOVATEL OEM4-G2L

NovAtel is a Canadian company specializing in GNSS receivers. They provided receivers to many satellite missions, e.g. to SFL for their CanX program. The OEM4-G2L is a high performance receiver, which could be used in 1U CubeSats. Given the dual frequency capability, it can be used for applications like altimetry, gravimetry or SAR interferometry, which require a sub-decimeter precision in orbit determination [42]. At the moment these applications require bigger satellites, but future missions might be implemented on CubeSats. The power consumption of 1.6W is another topic, that would need addressing for the implementation into

a 1U CubeSat (see Chapter 3) [49]. Table 2.1 provides an overview of the main parameters.

2.3.7 NanoSense GPS Kit

The Danish company Gomspace provides a GPS kit, which is based on the NovAtel OEM719 GPS module. It is recommended to use it on their NanoDock ADCS module, but can also be integrated separately [50]. It is a very powerful GNSS receiver, being able to receive signals from all GNSS constellations. Furthermore, dual-frequency use is supported as well as the output of carrier phase measurements [116]. The power consumption of 1.3W is demanding for a 1U CubeSat. All parameters are summarized in Table 2.1.

2.3.8 GPSRM 1

The GPSRM 1 module is sold by the company Pumpkin Space, which is located in San Francisco. The used chipset is the NovAtel OEM719 (see Section 2.3.7). All features given by the chip are available on this module. It is compatible with the CubeSat standard connector PC/104, providing the option of stacking several boards from different companies. The main characteristics are summarized in Table 2.1, where most of them are equal to the NanoSense GPS Kit.

2.3.9 NEO-M8

Founded in 1997, the Swiss company u-blox developed several series of GNSS receivers. Their products are sold with COCOM limits, making them useless for space applications. In a cooperation between the Eidgenössische Technische Hochschule (ETH) Zürich, Astrocaster and the TU Berlin, several modules without COCOM limits were provided. The NEO-M8 receiver works with all GNSS constellations, while its 72 channels can track three systems simultaneously. It receives the C/A code signals, providing a high accuracy. Nevertheless, it lacks the capability of carrier phase measurements as well as dual-frequency use [52]. Many applications could still be realized using a u-blox receiver. Given the main parameters (see Table 2.1), it is a great solution for a 1U CubeSat. Its availability depends on cooperations at the moment, but u-blox might sell a version without COCOM limits at one point.

2.3.10 GNSS200

The GNSS200 manufactured by the company Hyperion Technologies from the Netherlands is a multi-constellation receiver (GPS, Beidou). Its dimensions are actually smaller than the warpspace module (see Table 2.1). It has been flown on several missions including BEESAT-9 (see Section 4.1.7).

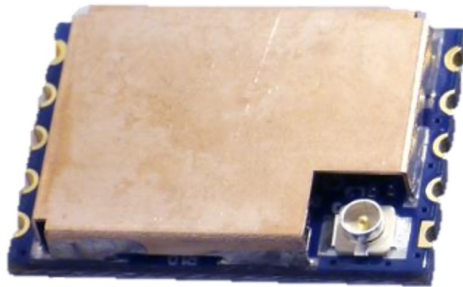


Figure 2.5: FM of GNSS200 for BEESAT-9 (image credit: Hyperion Technologies [53])

The module flying on BEESAT-9 has no raw data output capability, but the used GNSS chipset (Venus838) is theoretically capable of providing carrier phase and pseudorange measurements. Furthermore, dual-frequency reception is not possible. In general the GNSS200 is well suited for the implementation on 1U CubeSats, due to its low power consumption and TTFF [53].

2.3.11 Warpspace

Warpspace is a Japanese company specializing in CubeSat technology. One of their products is a GNSS receiver which is claimed to be the smallest module worldwide [117]. It provides navigation data based on C/A code from GPS and GLONASS. Raw or dual-frequency data is not available. Nevertheless, the main characteristics (see table Table 2.1) make it an excellent choice for 1U CubeSat, if the provided accuracy given by C/A code is feasible for the mission objectives. Several parameters (TTFF, U.FL connector, UART, supported GNSS, power consumption, sensitivity) lead to the conclusion that the used chip is provided by NavSpark (see Section 2.3.12) [54, 55].

2.3.12 Venus828/838

The SkyTraq GNSS modules are provided by the Taiwanese company NavSpark. Several modules are available, with different capabilities, regarding the constellations (GPS and Beidou or GPS and GLONASS), Real Time Kinematics (RTK) capability, the output of raw data and the dimensions of the chipset. It is available for universities and small companies working with small satellites. Furthermore, it is the smallest solution on the market without COCOM limits. Its integration into a CubeSat requires the development of electronic boards, where the module needs to be connected to the satellite bus. The low power consumption, dimension, prize and its availability (see Table 2.1) make it a feasible solution for 1U CubeSats [55].

2.3.13 Summary of Introduced Modules

Depending on the design of the CubeSat, the experience of the project team and the mission objectives, a selection from one of the introduced receivers can be made. Building a satellite with the standardized connector PC/104 would call for the GPSRM 1 or the CubeSat GPS Receiver, requiring little knowledge in developing electronic boards and being compatible to other self designed or bought electronic boards. On the other hand there are high-end modules with either dual-frequency output like the OEM4-G2L or with the capability of receiving all GNSS, like NanoSense GPS Kit and the GPS-601. All these modules, together with SGR-05U and SGR-Ligo come along with high power requirements and big dimensions.

The last four described modules require the development of an electronic board, thus experience in that field. Nevertheless, their dimensions and power requirements are fitting much better to 1U CubeSats, but still many challenges are to overcome and are discussed in the next chapter.

3 Challenges of On-Board Navigation on 1U CubeSats

Since their first integration into a satellite in 1982 (see Section 2.3 [41]), GNSS receivers are a common subsystem of microsattelites or bigger. These satellites constantly control their attitude, have high power capabilities and enough space to integrate the receiver as well as the antennas. Compared to the payloads, flown in satellites with a mass greater than 50 kg, the requirements of a GNSS receiver are small (see Table 2.1), in contrary to CubeSats, which have limits in all subsystems.

The main purpose for the integration of a GNSS receiver is the necessity of precise knowledge of time and position, which is already challenging for 1U CubeSats. Implementing an on-board navigation system with orbit propagation is more demanding in several ways (see Chapter 2). Furthermore, acquiring raw GNSS signals, like carrier phase and pseudorange data, especially in a dual-frequency mode for high accuracy orbit determination (see Section 2.1.2) is an even more complex task. The next sections are focusing on the main purpose of on-board navigation and its consequences for 1U CubeSats. The on-board orbit determination and raw data acquirement will just be described shortly, due to the fact that most applications that require these systems and data are based on payloads that do not fit into a 1U CubeSat.

All the challenges described in this chapter focus on the satellite itself. Especially universities, which are the major developers of 1U CubeSats, have to cope with further issues, which are usually minor problems for companies or institutions. Money shortages, fluctuation of personnel, need of in-house development of subsystems and ground station tools and the lack of test facilities are some of those. Addressing all these challenges would go far beyond the scope of this thesis, but should always be considered.

First of all, a hypothetical 1U CubeSat is described, including subsystems, that have been flown to date in 2020. It is mentioned, due to the improving availabilities of components and subsystems over time. Regardless, for BEESAT-4 and BEESAT-9 the preconditions were different and the challenges are addressed accordingly.

3.1 A Hypothetical 1U CubeSat

The integration of a GNSS receiver influences most subsystems (see Section 3.2). In Section 3.3 the subsystems are examined individually, while several impacts to others are mentioned. Being a complex system, changes to one part of the satellite have an effect to other subsystems. Therefore, the integration of a new component, in this case a GNSS receiver has to be considered altogether.

Putting all the challenges and requirements together and looking at the latest subsystem developments for 1U CubeSats it seems possible to build a picosatellite capable of continuous and reliable operation of a GNSS receiver.

The energy shortage could be solved with deployable solar panels, which were flown by Munich Orbital Verification Experiment (MOVE)-II [118]. In sun pointing mode it could produce around 23 W, compared to roughly 2.3 W on most 1U CubeSats (based on two solar cells per panel). Within the PiNaSys project an X-Band transmitter was developed. The data rate of up to 2 Mbit/s could solve the problem of limited downlink capability [38]. The attitude determination issues can be addressed with the fusion of several sensor arrays or with a small star tracker, e.g. pinasysSTAR [119] to obtain a valid attitude knowledge during eclipse. Controlling the attitude could be done with miniaturized reaction wheels (RW1, [120], Hyperion [121], CubeSpace [122]) or with the newly developed pico Fluid Dynamic Actuator (pFDA), flown on BEESAT-9 and TUPEX-7 [123]. Generally, recommendations for highly integrated picosatellites can be taken from Grau [124] to be able to allocate more space for a payload. The integration of a low power GNSS receiver with a small TTFF on one of the electronic boards is feasible, too.

The proposed satellite model would most likely be capable of a continuous operation of a GNSS receiver. So far, most of the needed components are not available as a product, thus this solution is only theoretical. For BEESAT-4 and BEESAT-9 many conditions were set already, hence the challenges were addressed based on the available system.

3.2 Subsystems of 1U CubeSats

A volume of one cubic decimeter is all the space available for the subsystems of a 1U CubeSat and to give the satellite a meaningful purpose, some space has to be reserved for a payload as well. Thus, the volume is very limited, especially

regarding the available space proven systems for CubeSats at the starting point of the development of BEESAT-1 in 2005. Satellite buses are usually divided into seven subsystems:

1. Structure & Mechanisms
2. Electrical Power System (EPS)
3. Communications System (COM)
4. On-Board Computer (OBC)
5. Attitude Determination and Control System (ADCS)
6. Thermal Control System (TCS)
7. Propulsion System

A primary structure to integrate all the subsystems and to protect the sensitive components from the loads of the rocket launch is essential. Furthermore, to operate the satellite, an EPS is required to gain, store and distribute energy around the satellite. A COM is needed for the downlink of the generated data, housekeepings and payload data,. The handling of commands, gathering data, mode control and further tasks make an OBC mandatory.

The other subsystems are optional, depending on the requirements. A Thermal Control System (TCS) is needed to some extent, but it can be done passively, with only some temperature sensors and an elaborated concept regarding the emission and generation of thermal energy. The ADCS is not necessary and many 1U CubeSats, do not have a three-axis stabilization. Most picosatellites still integrate several attitude sensors, e.g. gyroscopes, magnetic field and sun sensors. The last subsystem, the propulsion system was not a part of any 1U CubeSat since 2018, when NanoFEEP of TU Dresden was launched with UWE-4 [125].

For the integration of a GNSS receiver advanced satellite capabilities become obligatory. First of all, more space is needed for an additional subsystem and as listed in Table 2.1, most GNSS receivers have a high power consumption, but the available surface for solar cells, to generate energy, is limited. Furthermore, a high TTFF of the GNSS receiver requires a stabilized satellite, because the GNSS satellites have to maintain within the lobe of the antennas for several minutes. Recent developments of GNSS receivers have seen miniaturization

and improvements in power consumption and TTFF which could handle these restrictions [55, 117, 53].

From the limits of the satellite bus some operational constraints derive. For several reasons a GNSS receiver, including those with lower power consumptions, cannot be operated continuously. Considerations have to be made how to overcome these outages, if the mission objectives rely on precise timing and position knowledge.

Another constraint, which affected BEESAT-4 in 2012, is the availability of GNSS receivers. Unless an in-house developed GNSS receiver is available it was difficult to obtain receivers without COCOM limits, because they were basically only obtainable through cooperations with institutions or companies. For BEESAT-4 the AVANTI experiment on BIROS was the reason for the purchase of the Phoenix receiver. It was used within the On-Board Navigation System (ONS) of BIROS, thus the choice was mandatory. An example for collaborations with companies is seen between NovAtel and SFL in Canada, where NovAtel provided GPS receivers for SFLs CanX-satellites. In 2020, these restrictions only affect countries with export and import limitations.

3.3 Effects of a GNSS Receiver on the Satellite Bus

The integration of a GNSS receiver affects the satellite bus on several subsystems. As described before, most subsystems are limited due to the dimension of the satellite. Going through the list in Section 3.2 the structure needs to integrate the receiver as well as the related GNSS antenna. The placement of the antenna could furthermore have consequences on the amount of solar cells, that can be mounted to the panels. This directly has an impact on the electrical power system, which is a key subsystem regarding the operation of a GNSS receiver and is described in detail in Section 3.3.1.

Depending on the amount of additional data generated by the GNSS receiver and required on the ground for further processing, the communication system needs to be taken into account as well (see Section 3.3.2). For the on-board computer the consequences depend on the data processing concept. Being part of an on-board navigation system, there is usually a dedicated microcontroller or it is part of the AOCS. Nevertheless, the data produced and stored for downlink to the ground station has to be handled additionally. Moreover, the on-board computer is responsible for the synchronization and timing accuracy of the subsystems (see

Section 2.1.3). If the time is provided by the GNSS receiver, together with the 1-PPS signal, synchronization can be handled precisely. Once the signal is gone, the clocks drift and an inconsistency between subsystem times has to be taken into account. The effects on the ADCS depend on the requirements on the GNSS receiver availability. In Section 3.3.3 a distinguished approach is taken to see the different consequences. The thermal control system is indirectly affected by the additional heat generation of the GNSS receiver. For BEESAT-4 and BEESAT-9 there was no impact, thus it is not addressed any further.

3.3.1 Electrical Power System

The EPS has several functions on a satellite. It is responsible for the generation of energy, which is usually done with solar panels. In a Low Earth Orbit, 1U CubeSats will most likely have some eclipse time, where the solar panels do not generate further energy. There are options without eclipse time, e.g. dawn/dusk orbit, but usually CubeSats use a ride share, which implies some limitations. Thus, the energy needs to be saved in rechargeable batteries. Furthermore, the batteries are also required to capture peaks of energy consumption, which cannot be covered by solar cells alone. The consumer loads typically work with a dedicated stable voltage, which is another task handled by the EPS. Additionally, the distribution of energy via switches to the subsystems and components is controlled by the PCU, which also monitors the consumers, to detect anomalies in the system.

On system level, the energy budget must remain positive for a cycle of recurring operations. Though, the duration of a cycle can be adaptable, at the start of a new cycle, the energy level of the batteries needs to be greater or equal, compared to the previous one. A negative energy budget would subsequently lead to a critical voltage of the batteries and a change to safe mode, where most consumers are switched off and no regular operations can be conducted.

The energy consumption of a GNSS receiver can be crucial for a 1U CubeSat (see Table 2.1). Typically the solar panels are attached to the structure and the satellite is tumbling in space, which leads to an average energy generation of about 2.3 W ([126]). Most of the receivers of Table 2.1 would require 30–70 % of that energy. Further requirements, e.g. a three-axis stabilized satellite, automatically lead to a negative energy budget (see consumers in [126]), if the GNSS receiver is operated continuously. Even during the sun phase additional energy would be required from the batteries. This can only be overcome by the use of deployable solar panels,

in order to generate more energy and additional batteries during eclipse. These adaptations automatically imply more complexity and require additional space inside the satellite which might not be available. A continuous operation of a low power GNSS receiver can be an option for a 1U CubeSat, if the limitations of the EPS have been overcome with the suggested modifications.

For BEESAT-4, a scenario was developed to support the AVANTI experiment. In this scenario, the Phoenix receiver would acquire navigation data for 15 min, seven to eight times a day (every second orbit). This is a usage rate of 7–9% daily, far away from continuous operation. In [126] it can be seen, that this rate is only achievable with limitations to the standard operations.

AeroCube-4 (see Section 2.2.3) only acquired navigation data once a day for a maximum of 27 fixes due to power reasons [87]. Since 2018, three GNSS receivers are available (GNSS200, Venus 828/838 and Warpspace), that have a much lower power consumption (see Table 2.1), which leads to a higher usage rate. Nevertheless, continuous operation still does not result in a positive energy budget for BEESAT-9, even without active attitude control (see [127]).

Generally, a determination of the position at discrete points in time is possible with a 1U CubeSat, referring to the EPS. On-board orbit determination might be possible, depending on the used GNSS receiver and the implemented algorithms (minimum required resolution and data points). The quality of orbit determination and propagation on the ground, depending on the amount of navigation data, was analyzed and is described in Section 7.4

3.3.2 Communication System

Most 1U CubeSats are equipped with a VHF or UHF transceiver. Having low power consumption, while being able to transmit omnidirectional, has a big benefit for picosatellites, since no dedicated attitude is required for communication. On the other hand the data rate is low and leads to a limited data downlink for both, housekeepings and payload data. Continuous operation of a GNSS receiver produces data, that is needed on the ground for further processing, regarding orbit determination or correcting the position data using carrier phase and pseudorange measurements. Some 1U CubeSats already demonstrated the technology of higher communication bands such as S-Band or X-Band. This requires further components from the attitude control system as well as higher energy consumption. Thus, a

concept which includes high data rates, a continuously operated GNSS receiver and an active attitude control will require further miniaturization as proposed in [124]. In [128] a link data budget for BEESAT-9 was calculated. The possibilities to downlink continuous stored data is limited, leading to a low sampling rate. A possible solution could be the implementation of a big network of ground stations. Nevertheless, operating the transceivers in transmission mode consumes more energy than in receiving mode (see [126]), which sets limits here as well.

Assuming the GNSS receiver would run continuously for one day and a basic navigation data set (see Appendix B) is stored every 10 s, a total amount of 8640 telemetry packets needs to be downloaded. After nine months of operations, 1930 source packets were downloaded on average via three ground stations daily from BEESAT-9. Although, the efficiency on the ground station could be increased, further data sets need to be downloaded, including extended navigation data. Being the primary mission objective, still the GNSS data amounts for only 29.8% of the downloaded data (see Table 6.8).

In conclusion, operating a GNSS receiver and transmitting the generated data to the ground is finite and continuously generated data requires huge efforts to be sent to the ground with a 1U CubeSat via VHF/UHF. The on-orbit determination and propagation does not involve the communication system, thus it does not have effects on it.

3.3.3 Attitude Determination and Control System

Section 3.2 describes the subsystems that are obligatory for a 1U CubeSat. The ADCS is not necessarily one of them, if the payload is independent of both, the attitude of the satellite as well as the knowledge of it. With the integration of a GNSS receiver, an ADCS is required. A tumbling satellite might not get a navigation fix at all, depending on the angular rate and the TTFF of the receiver. A single GNSS satellite has to remain inside the lobe of the antenna for a certain time to be acquired. Lowering the angular rate passively or with magnetic coils might enable a tumbling satellite to acquire a navigation solution, but there is no guarantee, that the satellite is pointing away from the Earth. While pointing to Earth, no GNSS signal will be received and consequently no navigation data can be obtained.

Hence, the impact on the ADCS varies significantly with the requirements regarding the acquisition of navigation data. In case the data is needed continuously and at any time, a three-axis stabilized satellite is necessary. The attitude determination on 1U CubeSats is often based on sun and magnetic field sensors. Recent developments have also seen star trackers, with dimension small enough to fit as well. Without a star tracker an angular rate sensor is required during eclipse to propagate the attitude or provide a virtual sun vector. The inaccuracies on MEMS gyroscopes have to be taken into account, even though the last years have seen a significant improvement. The combination of four angular rate sensors, in orbit calibration and filtering the values, made attitude control during eclipse on the S-Band Network for Cooperative Nanosatellites (S-NET) satellites possible. The accumulated error after an eclipse was 3° [129]. Furthermore, reaction wheels are required to ensure three-axis stabilization, which affects the available space and the energy consumption significantly.

The combination of a three-axis stabilized satellite, using reaction wheels for attitude control, magnetic coils for desaturation, several sensors for attitude determination and a GNSS receiver is a huge challenge to any 1U CubeSat and especially the EPS.

3.4 Conclusions of Challenges for 1U CubeSats Regarding On-Board Navigation

A highly theoretical approach of a 1U CubeSat, that includes all the mentioned developments from different companies or universities might be capable of a continuous operation of a GNSS receiver as well as the download of all the stored data. Nevertheless, up to date in 2020 no 1U CubeSat was built, which is close to overcome all the mentioned challenges and limits.

With the preconditions set for BEESAT-4 and BEESAT-9, most of the subsystems were not adaptable during the implementation of the PPOD package, making it complicated to operate the GNSS receivers for a long time. This applies especially to BEESAT-4, due to the high energy consumption of Phoenix compared to the GNSS200, as well as the necessity of a three-axis stabilization. For BEESAT-9, a continuous operation was possible under certain circumstances for several days, but it required several other sensor systems to be switched off. Furthermore, the

download of the data took around 10 times longer than its acquisition. Nevertheless, orbit determination and propagation of ephemerides with the navigation data from the GNSS200 showed that for certain applications it might not be required to operate a GNSS receiver continuously to achieve certain accuracies (see Section 7.4), which helps to overcome the challenges.

The development of low power GNSS receivers, the usage of deployable solar panels and a communication system in S-Band or X-Band could see a continuously operated GNSS receiver on a 1U CubeSat at one particular time, but the system concept of the BEESAT line does not yet fulfill all the requirements.

4 System Concept

The possibilities and challenges of the integration of a GNSS receiver have to be taken into account for the development of a 1U CubeSat. For BEESAT-4 and BEESAT-9 many subsystems were already defined, narrowing down the possible implementations as well as the operational concepts. Furthermore, the usage of the Phoenix receiver was obligatory, whereas the GNSS receiver for BEESAT-9 was chosen deliberately. Changes had to be applied both times, due to different power settings, no available space for the GNSS receivers and the integration of further new technology.

The next sections will describe the subsystems of the BEESAT satellite bus which were identified to be mostly affected by the integration of a GNSS receiver. Adaptations to the satellite were introduced with every flight model, affecting soft- and hardware. The implementation of a PPOD also requires tools on the ground, which will conclude the system concept.

4.1 BEESAT Satellite Bus

After the development of miniaturized reaction wheels in collaboration with Astro- und Feinwerktechnik GmbH, in March 2005 the project Microwheels II was launched [130]. The primary objective was the development of a 1U CubeSat to verify the reaction wheels on orbit. Most of the subsystems were built at the Chair of Space technology for several reasons. Developing satellite subsystems for a 1U CubeSat fit many research topics of the Chair, e.g. miniaturization, system engineering and space sensor technology [131]. Another reason was the lack of CubeSat components on the market. In 2020 many companies sell CubeSat components and subsystems, but in 2005 almost no space-qualified components fitting into a CubeSat were available [15]. Figure 4.1 shows the configuration of the four BEESATs based on the same satellite bus. The differences can be seen mainly on the payload data handling board.

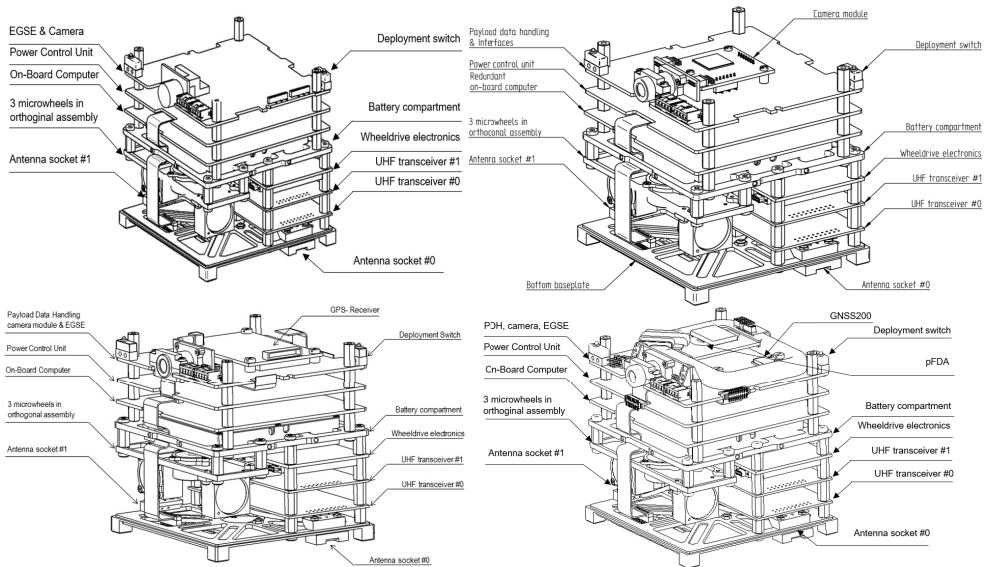


Figure 4.1: Evolution of the payloads on BEESAT. Top left: BEESAT-1 (CAD-model created by Sebastian Trowitzsch, image credit: Diego Garcia). Top right: BEESAT-2 (CAD-model adapted by Sebastian Trowitzsch, image credit: Sebastian Trowitzsch). Bottom left: BEESAT-4 (CAD-model adapted by the author). Bottom right: (CAD-model adapted by Sebastian Grau, image credit: Diego Garcia)

4.1.1 Development of BEESAT-1

In 2005 a 1U CubeSat was proposed to integrate the reaction wheels RW1 [120]. Besides the reaction wheels and its electronic board, the development started from scratch. First of all, a concept was introduced with the guideline to build a single fault tolerant satellite. Nevertheless, it was taken into account, that the complexity might surpass the benefits. Therefore, some subsystems were deliberately built without redundancy.

In Figure 4.2 a system overview is displayed. All the subsystems with microcontrollers can be seen. They exchange messages via a dual Controller Area Network (CAN) bus. Further interfaces are used within the subsystems to connect memories, sensors and Analog-to-Digital Converters (ADCs).

The following paragraphs will give an overview of the ADCS, the EPS and the COM, since they were identified to be mainly affected by the integration of a

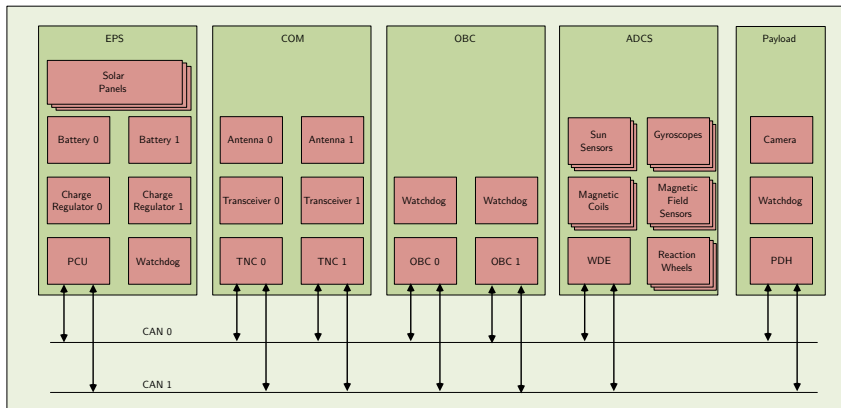


Figure 4.2: System overview of the subsystems of BEESAT-1 (adapted from [132])

GNSS receiver into a 1U CubeSat. Furthermore, the payload board is introduced, since it changed entirely throughout the missions. The other subsystems play a minor role in the context of the integration of a GNSS receiver into a 1U CubeSat (for details on the redundancy concept and the other subsystems see [132]).

Electrical Power System

The main tasks of the EPS are described in Section 3.3.1. Additionally the PCU supervises the redundant CAN bus and the connected subsystems. Currents, voltages and temperatures are also measured by the PCU [132, p. 65].

Energy Generation Triple Junction Gallium-Arsenid solar cells are the unique source to generate energy on the satellite. They are placed on all six side panels of the BEESATs, since it will tumble most of the time with no dedicated attitude. The cells have an efficiency of 30%. Five side panels integrate two solar cells with a dimension of 80 mm × 40 mm connected in series. On the interface panel four strings with two cells each are connected in series as well. The cells have dimensions of 20 mm × 20 mm. All panels are connected in parallel and Schottky diodes prevent the backflow of the solar current [132, p. 65].

Energy Storage Storing the generated energy is necessary for two reasons. On one hand the satellite requires energy during eclipse to be operated continuously and on the other hand a temporary high power consumption of the satellite cannot be covered by the solar cells [126]. Rechargeable Lithium Polymer batteries are integrated into BEESAT-1. They have a high energy density and a bigger temperature range than other battery technologies. On the downside a charge regulator is required, which makes the electronic board more complex [132, p. 68].

Power Control Unit The distribution of the energy is controlled and supervised by the PCU. It converts the unregulated voltage from the solar cells to regulated voltages of 9 V for the charge regulators and 3.3 V and 5 V for the subsystems. All switches of the system are operated by the PCU. Overcurrents can be detected and affected subsystems can be switched off automatically. A watchdog circuitry toggles the PCU in case of a software error, which equals a power down of the entire satellite [132, p. 69].

Communication System

Exchanging commands, telemetry and payload data on BEESAT-1 is realized with a transceiver using the UHF band of radio amateurs. The utilized modulation is Gaussian Minimum Shift Keying (GMSK) with a data rate of 4.8 kbit/s, with an option of increasing it to 9.6 kbit/s [132, p. 37].

The link budget is positive for both options with a SNR of 13.8 dB and 10.7 dB respectively [132, p. 42].

Hardware A microcontroller is connected to the redundant CAN bus to receive data from the on-board computer and to forward the commands from the ground station. Together with a modem a Terminal Node Controller (TNC) is formed to demodulate the incoming and modulate outgoing signals. The other two components are the antenna and a transceiver to receive and send the data. Figure 4.3 shows the schematics of the communication system [132, p. 37].

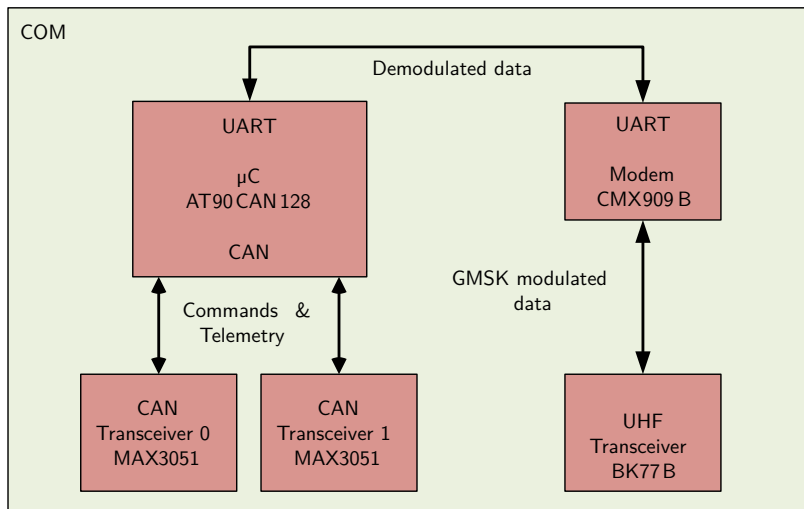


Figure 4.3: Schematic configuration of the communication system (adapted from [132])

Software The TNC Software is written in the programming language C. It is based on interrupts, while the microcontroller is basically kept in idle mode most of the time for power reasons. There are five interrupt sources: CAN transceiver, A/D-Converter, UART interface, the modem or a timer. Depending on the source, distinct routines are executed. All interrupt routines share the data buffer of the microcontroller. Furthermore, the telemetry and commands are buffered here [132, p. 38].

Attitude Determination and Control System

The ADCS consist of several sensors, actuators, control boards and algorithms to determine the attitude accurately, stabilize the satellite in three axis and align it to a desired orientation. In Figure 4.4 an overview of the ADCS is displayed.

Sensors BEESAT-1 uses three types of attitude sensors: sun sensors, magnetic field sensors and gyroscopes. The first two are used for attitude determination within the QUEST algorithm. The last one is used for control and general

knowledge of the angular rate of the satellite. All three sensors are displayed in Figure 4.5.

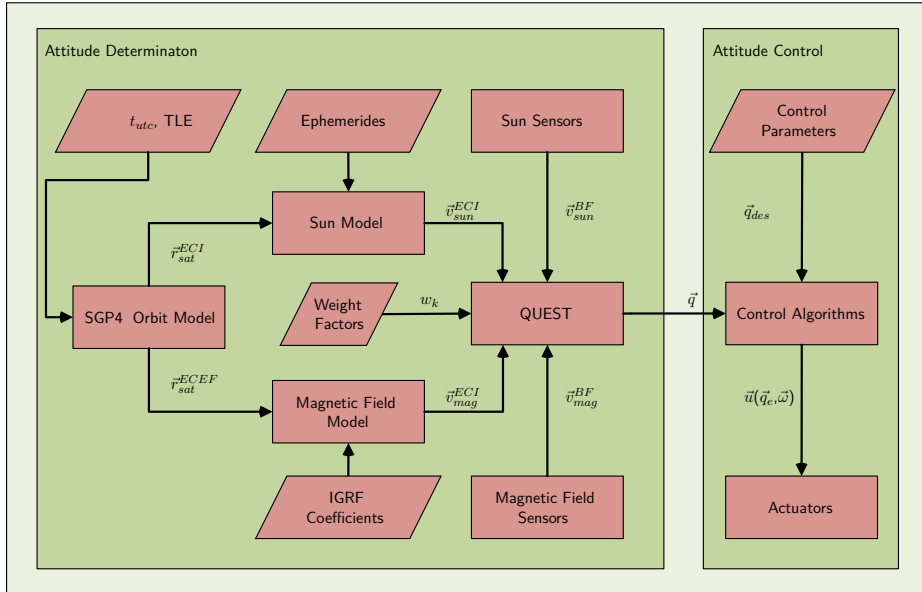


Figure 4.4: Overview of the ADCS (adapted from [132])

Sun Sensors Each panel of the satellite implements a sun sensor ensuring the availability of a sun vector during the sun phase full time. With a half cone angle of 60° the sensors overlap, which allows for a maximum of three sensors to contribute to the sun vector at once.



Figure 4.5: Attitude sensors of BEESAT-1: Magnetic field sensors on left side, gyroscopes in the center, sun sensor aperture plate and PSD on right side [132, 133]

Developed at the TU Berlin, the sensor is based on a Position Sensitive Device (PSD) [133], which reacts to emitted photons within the visible wavelength up to near infrared. On top of the PSD an aperture plate with a hole of $200\ \mu\text{m}$ is placed to let a small point-shaped sunbeam generate a current on the PSD. Each axis has two electrodes to determine the focus on the PSD in two dimensions. Through an operational amplifier the analog signals are directly routed to the ADC of the OBC which calculates the sun vector [132, p. 44 ff].

Magnetic Field Sensors Two magnetic field sensors are placed on the controller boards. The identical sensors measure the magnetic field in all three axes using the anisotropic magnetoresistive effect [134]. For each axis a wheatstone bridge is implemented, consisting of four resistors. An instrumentation amplifier preprocesses the data ahead of the ADC. Conducted tests show a high reproducibility, but distinct noise behavior [132, p. 50].

Gyroscope Three single axis gyroscopes were used on BEESAT-1. One was placed on the controller board, while the other two were soldered to the same board and fixed in small notches of the battery case (see Figure 4.5). With a power consumption of 30 mW for each sensor (90 mW for three axes) it is highly problematic for the energy budget (BMG250 used on BEESAT-9 consumes 3 mW). Furthermore, tests on a rotary table showed a high noise ratio of $0.6^\circ/\text{s}$ with low angular rates near zero. Angular rates above $20^\circ/\text{s}$ lowered the noise to $0.3^\circ/\text{s}$, but on satellites especially low angular rates are important. Different settings on the ADC did not lead to improvements [132, p. 52 ff].

Actuators Two different types of actuators are integrated into BEESAT-1, six magnetic coils and three reaction wheels. An implemented Blind Damping Mode reduces the angular momentum of the satellite with an interaction of the magnetic coils with the magnetic field. Furthermore, they can be used to desaturate the reaction wheels. The magnetic coils are integrated into all the solar panels, which inherently provides redundancy, although the performance decreases with a failure of one magnetic coil. For three-axis stabilization and accurate pointing the reaction wheels are used. They are orthogonally aligned to the satellite axes [132, p. 44].

Magnetic Coils Four layers of every solar panel are reserved for the magnetic coil. In Figure 4.6 the dark rectangular ring can be seen through the circuit board material. Dimensioning and design were done by Yoon [135] in 2008. The five big solar panels each produce a magnetic moment of $\vec{m}_{mag} = 0.030 \text{ A m}^2$. For the small panel the value was calculated to be $\vec{m}_{mag} = 0.018 \text{ A m}^2$. Each pair of magnetic coils can be controlled separately by the PCU with a voltage of 5 V. Temperatures and currents are measured for each magnetic coil [132, p. 55].

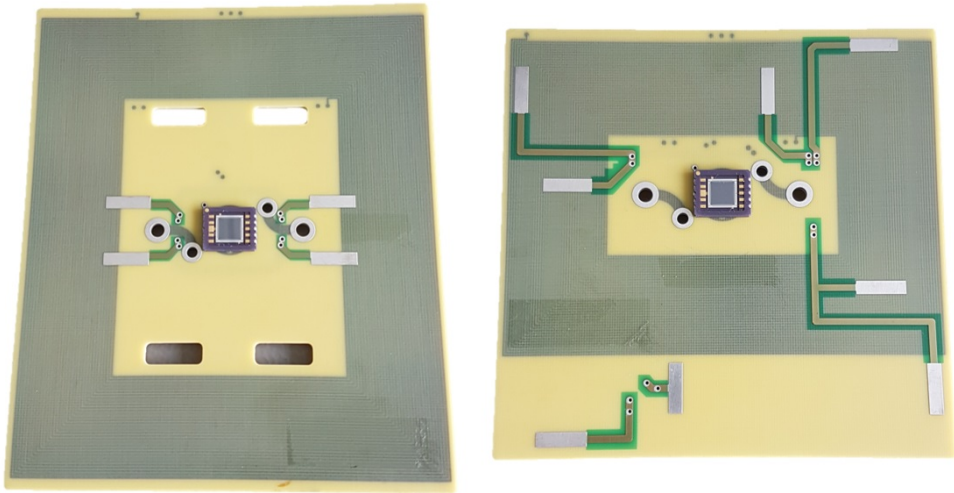


Figure 4.6: Solar panel with dark rectangular magnetic coil (panels of BEESAT-4)

Reaction Wheels The reaction wheels RW1 from Astro- und Feinwerktechnik GmbH are integrated orthogonally into BEESAT-1. In Figure 4.7 the reaction wheels and the WDE are displayed.

The rotating masses apply a maximum angular momentum of $L = 1 \times 10^{-4} \text{ N m s}$ at 8000 rpm. This corresponds to a maximum torque of $\tau = 4 \times 10^{-6} \text{ N m}$. With a limitation to 16000 rpm of angular velocity, the wheels allow for an angular rate of $\vec{\omega} = 5^\circ/\text{s}$ in each axes of BEESAT-1.

A test campaign was carried out by Herfort [136, p. 35 ff]. Due to an oversampling of the Hall sensors, the angular velocity of the wheels cannot be measured precisely around the zero crossing at low rates. For attitude control this has to be taken into account and zero crossings should be avoided.

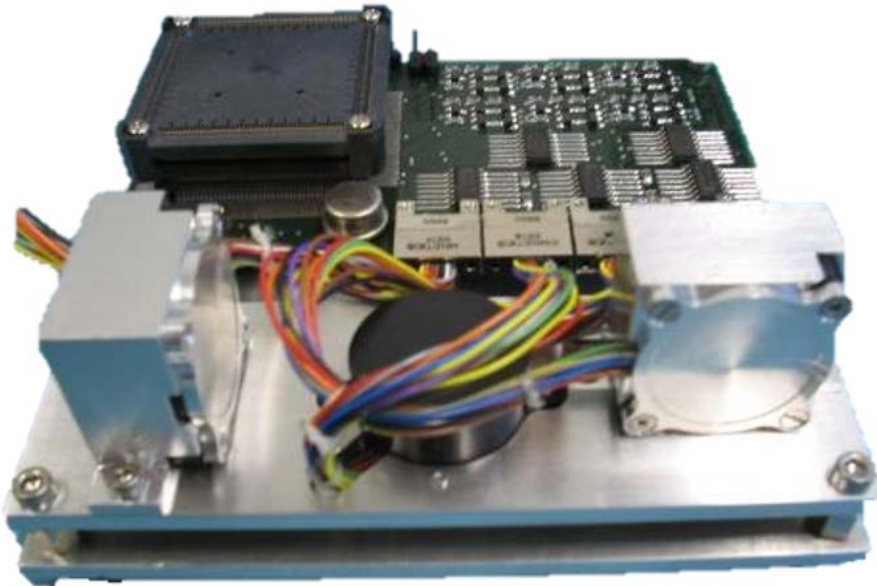


Figure 4.7: Reaction wheel system with WDE [132]

Algorithms Several models are used to obtain the current attitude as an input for the control algorithms. Additionally to those described in the next paragraphs, classes to process the sensor measurements are implemented as well. A detailed description of all classes and functions can be found in [136, p. 41]

Orbit Propagator SGP4 and Sun Model For the orbit model of BEESAT-1 several requirements were proposed by Geyer [137, p. 23]. Next to the provision of all necessary inputs for the attitude control system one main requirement was a maximum execution time of 200 ms. It derived from the necessity to obtain a propagation once in every duty cycle of the ADCS which lasts 500 ms. Initial tests by Herfort and Geyer with the original implementation by Kevin Born showed running times of 400 ms on the internal flash memory on the microcontroller of the OBC [136, p. 50]. Several minor adaptations were made to fit it better into the

operating system, avoiding unnecessary redefinitions and initializations of variables and defining the orbit model as a class member of the main ADCS routine. A runtime of 26 ms internally and 106 ms on the external flash was the final result, providing all necessary inputs well within the 500 ms duty cycle of the ADCS [136, p. 50–51].

The input parameters for the orbit model are TLEs and a time stamp in UTC. Velocity and position of the satellite are calculated in several coordinate systems for further use. Included in the orbit model, the sun vector is calculated in an Earth Centered Inertial (ECI) coordinate system from the same input parameters [137, p. 39].

Magnetic Field Model IGRF For the reference magnetic field vector in an ECI coordinate system, the IGRF model is used. It relies on input from the orbit model, using latitude, longitude, altitude and the time stamp in UTC and was adjusted by Berlin for BEESAT-1 [138, p. 71 ff]. The original code and coefficients were taken from [139].

The implementation was tested extensively and compared to the model set up by the British Geological Survey. The results showed no differences [136, p. 61].

Attitude Estimation Determining the attitude of the satellite is the task of finding the direction cosine matrix or quaternion to transform the body-fixed into an inertial frame. Both representations can be converted into each other [140, p. 80 ff]. The transformation of the inertial into the body-fixed vector is represented by:

$$\vec{v}_{BF} = T_{bf \leftarrow i} \cdot \vec{v}_I \quad (4.1)$$

For the ADCS of BEESAT several requirements were set (see [136, p. 66]). The computational time must not exceed 50 ms and should be reproducible within 10 ms. Furthermore, different numbers of input vectors should be handled, as well as a wide noise range from these inputs.

Four different approaches were discussed by Herfort [136, p. 66 ff] to be used as the attitude determination method on BEESAT-1. The triad algorithm which combines exactly two vectors from each coordinate frame and provides a direction

cosine matrix as a result [141, p. 410] Two approaches use the loss function J which was introduced by Wahba [142] and allows for least-square estimation of the attitude: The first one is Davenport's q-method which provides a quaternion from a variable number of input vectors by calculating eigenvectors. The other one is the QUEST algorithm, which was introduced by Shuster and Oh [143] in 1981. The last approach was a Kalman filter, a widely used method to reconstruct state vectors of a system.

Finally, the QUEST algorithm was chosen for several reasons: robustness, accuracy and small processing power requirements [136, p. 71]. Based on the measured and modeled sun and magnetic field vectors the current attitude is estimated by QUEST (see Figure 4.4). Singularities are handled as suggested by Markley and Mortari [144]. Tests with the algorithm showed that the mentioned requirements are fulfilled [136, p. 76–77]. Furthermore, small adaptations to the algorithm allow for any number of input vectors, making it easy to include new sensors. Adjustability is given by the use of weight factors, which also allows to remove broken sensors completely from the estimation by setting them to zero [136, p. 77].

It is taken into account, that the two input vectors have to be independent. In case of collinearity of sun and magnetic field vector a rotation around the vector axis is undetermined, which can lead to large errors. Without another reference, such as a star tracker, these uncertainties are inevitable [136, p. 73]. Another option could be sensor fusion, using a relative sensor, e.g. a gyroscope to calculate a virtual sun vector. This requires highly accurate angular rate sensors, which were not available for BEESAT-1.

Control Algorithms Different modes were implemented for three-axis stabilization and the reduction of the angular momentum of the satellite. The attitude modes and their paths are displayed in Figure 4.8

The baseline of the ADCS is the Suspend Mode, which determines the attitude with a rate of 2 Hz, without using the actuators. Given the mission objective, a Six Minutes Wheeltest was implemented to verify the functionality of the reaction wheels during the mission lifetime.

For three-axis stabilization and pointing nadir or to an inertial target, an Inertial and an Earth Pointing mode were developed [145]. The control parameters and algorithms are linear and work within a small window, thus non-linear controllers

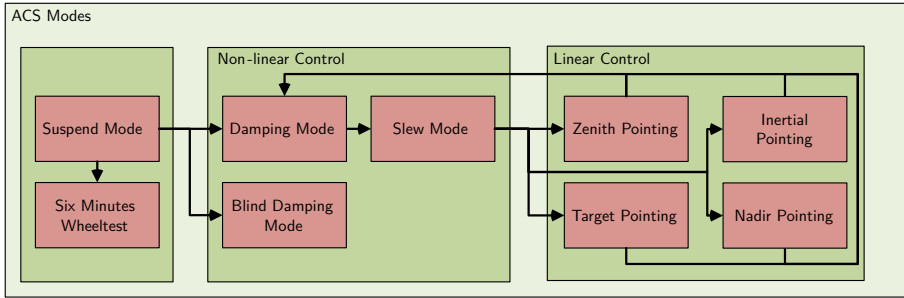


Figure 4.8: Modes of the ADCS (adapted from [132])

are used in advance. In a first step the angular rate is minimized using the Damping Mode, the parameters to enter and exit this mode are adaptable on orbit by telecommand [132, p. 63]. Afterwards the Slew Mode executes a large angle maneuver towards the desired attitude. As a control law the Slew Mode features a quaternion feedback controller as suggested by Bon Wie [146, p. 403]:

$$\vec{u} = -\mathbf{K}\vec{q}_e - \mathbf{C}\vec{\omega} \quad (4.2)$$

with \mathbf{K} and \mathbf{C} being gain matrices to be determined according to the given system. The error quaternion vector \vec{q}_e is calculated from the desired and the current attitude and the angular rate $\vec{\omega}$ is provided directly by the gyroscopes.

Linear Control Modes were developed and simulated by Geile [145], but during the verification campaign on orbit all the modes used the quaternion feedback controller (see Section 6.1.2).

Developed by Lucia [147], a Blind Damping Mode was implemented to reduce the angular rate of the satellite using the magnetic coils. Based on the B-Dot controller several strategies were introduced to either optimize for time or energy. A summary of the simulation results can be found in [147, p. 79].

Combined modes using the magnetic coils and reaction wheels simultaneously were not planned for BEESAT-1 for power budget reasons [132, p. 62].

EGSE and Camera Board

The top electronic board of BEESAT-1 featured a camera, directly connected to the OBC via Universal Asynchronous Receiver Transmitter (UART), connectors for the Remove Before Flight (RBF)-pin, the Electrical Ground Support Equipment (EGSE) and the deployment switches. In Figure 4.9, the board is displayed. The functionality of the camera could not be shown in BEESAT-1 on orbit, but the same camera model produced pictures on BEESAT-3 [30]. While the jumper on the RBF-pin is connected, the satellite is off. Pressing both deployment switches turns the satellite off as well. For the vibration and thermal-vacuum tests, it is necessary to communicate with the satellite. Switching on the satellite, even though both deployment switches are pressed, is possible with a “Force On” Jumper next to the RBF-Pin.

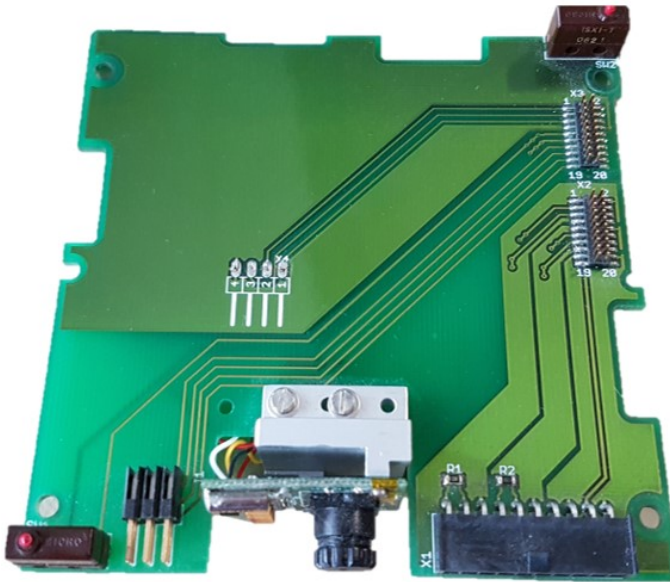


Figure 4.9: EGSE and camera board of BEESAT-1

4.1.2 Summary of the System Concept of BEESAT-1

At the time of its development BEESAT-1 was one of the first CubeSats worldwide with a single fault tolerant system concept and redundancies of many subsystems

and components. A decent base was set for further implementation of payloads and other technologies. Nevertheless, for the purpose of three-axis stabilization new developments in sensor technology were needed to fulfill the requirements set by Herfort [136]. Moreover, the software concept needed adaptations to ensure mission operations that allow for continuous execution of experiments and the download of the acquired data.

During the mission BEESAT-2 various required modifications were addressed and applied.

4.1.3 Adaptations to BEESAT-2

The orbit results of BEESAT-1 were used to improve the performance of the satellite bus and include the lessons learned into hard- and software as much as possible. Considering the hardware, the OBC, the PCU and the COM did not require any improvements, since they fully met the expectations during the mission time of one year. Only the performance of the ADCS was not satisfactory, regarding the actuators and sensors. The maximum angular momentum of the reaction wheels was reached quickly and the magnetic coils could only be operated in one direction. High noise and power consumption of the gyroscopes required a new component to be able to perform highly accurate attitude control. Furthermore, the temperatures of the satellite were lower than expected, which led to conclusions regarding the thermal properties of the structure [132, p. 79].

The software of BEESAT-1 was basic and only suitable for simple operations. Even though the objectives were fulfilled, a major software update for the OBC, COM and ADCS was required for the more ambitious mission objectives of BEESAT-2.

Hardware

Changes on the hardware were applied to the structure and its thermal properties, the PCU, the ADCS and the PDH including the camera. The OBC, the COM system and the WDE remained the same.

Attitude Control System In Section 4.1.1, it was stated that the gyroscopes on BEESAT-1 have a high noise of $0.6^\circ/\text{s}$. Even the low requirements set for BEESAT-2 by Herfort [136, p. 10–11] to a drift rate of $0.477^\circ/\text{s}$ and a pointing accuracy of 7.5° cannot be met with such a high noise.

The availability of new low-power three-axis angular rate sensors with a digital interface solved this problem. The chosen sensor lowered the noise by a magnitude of up to 20 [148].

With experience from tests, simulations and on-orbit results of BEESAT-1, it turned out, that the maximum angular momentum of the reaction wheels was inadequate for some applications, because of quick saturation of the wheels within a couple of minutes (see Section 6.2.2). This led to a reaction wheel remodeling with a higher rotating mass, which increased the maximum angular momentum by nearly the order of six to $L = 5.8 \times 10^{-4} \text{ N m}$ as well as the nominal torque for higher maneuverability [120]. For BEESAT-2 the remodeled wheels were chosen. The dimension of the platform, interface and connector remained the same.

Payload Data Handling and Camera For BEESAT-2, a payload data handling board was developed by Trowitzsch [149] for the processing, storage and management of Earth observation data from the camera. The design of the camera was done by Trowitzsch [150] as well. An additional controller module, working as an interface between the sensor module and the PDH was developed externally. It provided a parallel data and control interface to read out the camera sensor. In Figure 4.10 the flight model of the PDH with the integrated camera module is displayed. The PDH is connected to the OBC via CAN-bus to receive commands, send telemetry and payload data. A non-volatile external flash memory for software images and pictures is partitioned to handle one external software image and includes 14 picture slots. The camera module takes pictures with a resolution of $1\,600 \times 1\,200$ pixel in the visible spectrum [132, p. 28 ff].

Software

The software of BEESAT was continuously improved and expanded. Mentioning every single change would be rather confusing than helpful in the context of the system concept. Nevertheless, the software of the satellite has seen some major changes that will be addressed here.



Figure 4.10: Payload Data Handling of BEESAT-2 with camera module (image credit: Sebastian Trowitzsch)

OBC Software The basic concept remained the same, but for safer and easier changes of parameters, the parameter container was rewritten by Lieb [151]. Most of the parameters belong to the ADCS and allow for changes of calibration parameters for sensors, controller gains and weight factors for the QUEST algorithm.

Another significant change was the implementation of a software upload. It allows to replace any of the four images on board of each OBC.

PCU Software Due to the additional angular rate sensor connected to the PCU, a device driver had to be written. It configures the sensor and provides measured and preprocessed data to the ADCS. Furthermore, the magnetic coil control was rewritten. The main concept remained the same.

COM Software The TNC software was completely rewritten. It was still based on the MOBITEX protocol, but needed a major revision for the implementation of several new features. Software upload and an acknowledge mode were introduced

by Scharich [152, p. 46 ff]. Furthermore, an instance was included to enable an ISL with BEESAT-3. The implementation was done by Scharich [152] and Werner [153].

PDH Software A PDH was only introduced to BEESAT-2, thus a new software was implemented. It was based on the same operating system as the OBC. Requirements, development aspects and features were introduced by Trowitzsch [149, p. 30 ff]. Summarized, the software handles incoming commands from the OBC, stores data from the camera module and sends it via CAN-bus to the OBC. Furthermore, the PDH provided two slots for software images, that are both capable of uploads.

4.1.4 Summary of the Modifications of BEESAT-2

Several modifications were applied to fulfill the primary mission objective, a three-axis stabilized satellite. Mainly a new gyroscope and reaction wheels with increased performance were integrated. Furthermore, the software was revised to improve mission operations and to increase the variability for experiments with the ADCS. One major improvement was the availability of a software upload mechanism to enable further modifications on orbit.

Additionally, a complex PDH with a camera was developed and added to the BEESAT satellite bus. It was planned to be used as part of the verification strategy of the three-axis stabilization.

Basically, the preconditions were set to implement a GPS receiver, nevertheless several modifications on the satellite bus were applied on the next mission.

4.1.5 Adaptations to BEESAT-4

Integrating the GPS-receiver Phoenix into a highly integrated CubeSat was a challenge, which entailed changes to several subsystems. Besides this, all functionalities of BEESAT-2 were supposed to remain on BEESAT-4. Moreover, the satellite should be based on its predecessors to rely on as many space qualified subsystems as possible.

Hardware

During the development of BEESAT-4, changes were applied to the EPS, the ADCS and the PDH. Structure and mechanisms underwent very small changes, that do not need further description, the OBC, COM, WDE and reaction wheels remained the same as for BEESAT-2.

Electrical Power System A new PCU was required to supply the GPS receiver, according to its electrical specifications. Due to the ongoing developments in the sector of Micro-Electro-Mechanical System (MEMS) sensors, a new gyroscope and a magnetic field sensor were placed on the PCU and connected to its microcontroller additionally to the existing sensors.

One solar panel underwent a redesign as well, because further space was required to integrate the GPS antenna. This led to a second panel with small solar cells, thus a slightly lower average energy generation.

Attitude Control System The concept of the ADCS already met the requirements of the on-orbit navigation. Nevertheless, another gyroscope and magnetic field sensor were integrated for further technology demonstration and redundancy in case of the gyroscope. The single axis gyroscope was not integrated between the OBC and the battery case, since it was not used during the entire BEESAT-2 mission.

Further research regarding the sun sensors by Avsar [154] led to a redesign of the aperture plate to avoid reflections from the edges of the drilling hole. Additionally, the PSD had to be replaced, since the PSD of BEESAT-1/2 was not produced anymore. Having different dimensions and another package, small mechanical and electrical changes had to be applied [155].

Payload Data Handling, GPS receiver and Camera For the integration of the GPS receiver only one option was available, on top of the PDH. It can be seen in Figure 4.10, in the configuration of BEESAT-2, that there is no space left for an additional board due to the controller module of the camera. It was mainly used to provide an interface for the camera. A new microcontroller for the PDH of BEESAT-4 solved this issue, providing that interface directly. Around the microcontroller, a new PDH was developed, which still kept the capability to

operate the camera and added the GPS receiver. In Figure 4.11 the PDH with integrated camera and GPS receiver is displayed.

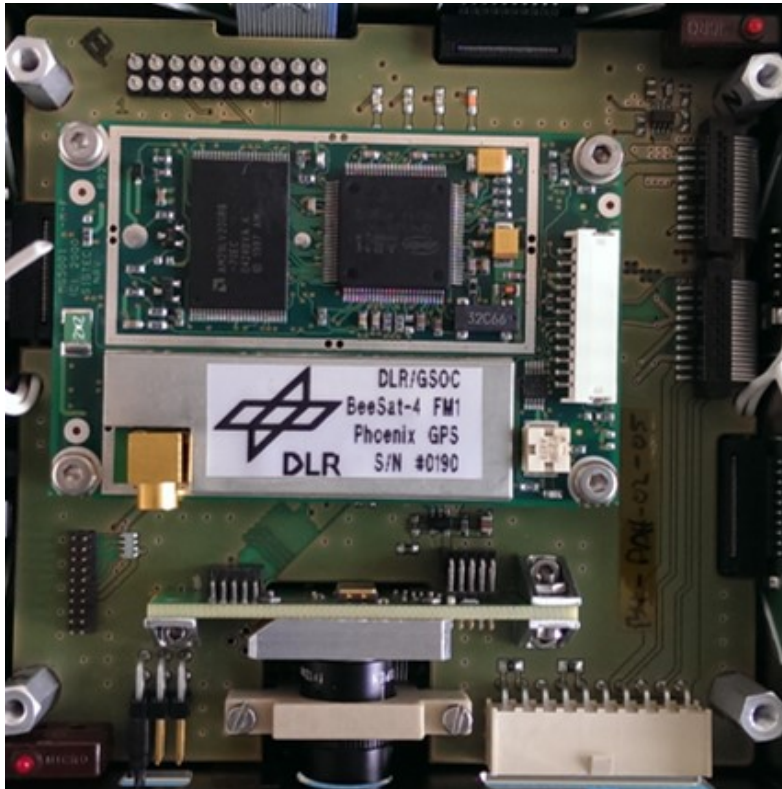


Figure 4.11: PDH with GPS receiver and camera

The selection of the Phoenix was mandatory, but the choice of the antenna needed some research. In a collaboration with the GSOC it was decided to use an active antenna, since the available space was limited and a passive antenna needs a big ground plane. Furthermore, the interface was preset to a MCX connector, which was not adaptable to all available antennas. One important parameter was the maximum gain of the attached LNA. Finally, an active antenna with a gain of 30 dB was chosen [156]. The ground plate had dimensions of 22.2 mm x 23.6 mm, which allowed for solar cells on the same panel.

Software

Continuous improvements of all software images were applied to BEESAT-4. Several major changes will be described here.

OBC Software Handling the data of the GPS receiver and the new sensors were some additional implementations. Furthermore, the ADCS implementations underwent a major revision, which was subsequently also uploaded to BEESAT-2 to improve the three-axis stabilization. Generally, the scalability and modularity of the software was increased.

PCU Software For the additional ADCS sensors, an I²C interface was included and respective drivers for the gyroscope and the magnetic field sensors were implemented to read out the measurements. The basic power control software remained untouched.

COM Software The implemented instance for the ISL between BEESAT-2 and BEESAT-3 was used to support the ISL of BEESAT-4 to BIROS. A new address was assigned to BIROS, with most of the additional work applied to N-Link, regarding the ISL. Another change was applied to the acknowledge protocol. For BEESAT-2, the scrambling was not working properly, resulting in transmission with no alternating signal. This led to a desynchronization and the reception of commands was not acknowledged.

PDH Software The usage of a new microcontroller entailed the implementation of the operating system RODOS by Montenegro [157]. The GPS receiver provides multiple options to be operated and several additional outputs next to the position and velocity of the satellite. Managing all these commands and data on the microcontroller and in the flash memory was implemented next to the necessary software for the additional camera interface.

4.1.6 Summary of the Modifications to BEESAT-4

The Phoenix receiver was integrated on the PDH without reducing any capabilities from the predecessor mission. Several required modifications to the EPS and ADCS were applied additionally to support the implementation of the PPOD package. Moreover, a new operating system on the new PDH microcontroller was used and is the standard implementation on all TU Berlin missions since. Several new attitude sensors were integrated as well, to improve the performance of the attitude determination compared to BEESAT-2. During the BEESAT-4 mission the algorithms of the ADCS were adapted, which resulted in a reliable three-axis stabilization (see Section 6.1.2).

4.1.7 Adaptations to BEESAT-9

The flight model of BEESAT-9 was the former EQM of BEESAT-4 and the transformation had to be done within a few months. Thus, the changes were minimized. Nevertheless, the opportunity was taken to integrate a new GNSS receiver which is significantly smaller than Phoenix. Additional space was used to further enhance the technologies used on the BEESAT satellite bus.

Hardware

Only one electronic board was adapted compared to BEESAT-4, namely the PDH. This also made changes in the ADCS possible. Additionally, the transceivers, the battery case, the OBC electronic board including the TNC and the PCU were replaced with flight spares of BEESAT-4, since the EQM boards were used for several years.

Attitude Control System Arrays of four magnetic field sensors and gyroscopes were added to put the accuracy to a new level (see Section 6.2.2). Furthermore, a newly developed actuator was integrated as well. The pFDA was developed by Grau [158] based on an idea of Noack [159]. A rotating liquid metal, accelerated by an electro-magnetic pump is the basic principle to induce a torque to the satellite. Due to its properties the maximum available angular momentum is reached nearly instantly, which opens new application possibilities, e.g. wide swaths with one camera. On-orbit experiments to analyze its properties were intended.

Payload Data Handling The only electronic board mostly renewed and designed was the PDH. Initially the intention was the technology demonstration of the GNSS receiver GNSS200. It replaced the bigger Phoenix receiver. The GNSS200 is directly connected via UART to the microcontroller of the PDH, which sends the time stamp and navigation data via CAN to the flash memory of the OBC at the requested data rate. Extended data is stored on the payload memory. Another technical difference was the replacement of the old GNSS antenna, which seemed fine by its technical specifications, but the unsatisfactory performance on BEESAT-4 made a replacement inevitable (see Section 6.1.3).

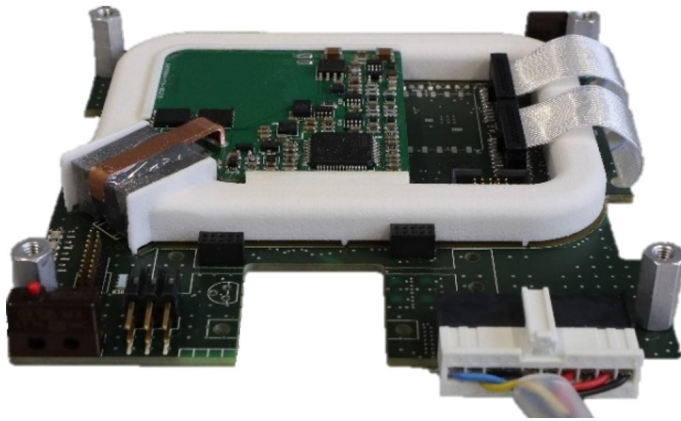


Figure 4.12: PDH of BEESAT-9 (image credit: Sebastian Grau)

The small dimensions of the GNSS200 offered further opportunities, having more space on top of the PDH. The space was used to integrate the tube for the metallic fluid used by the pFDA, the electrode and the electronic board to control the pump. In Figure 4.12 the top of the PDH is shown before the GNSS200 was soldered.

Software

Being the same system as BEESAT-4, the software of the satellite bus was mostly reusable. Nevertheless, the integration of new hardware always requires the implementation of further commands and telemetry routines.

OBC Software Gathering the telemetry and distributing commands to the other subsystems is part of the OBC software. The new attitude sensors, the GNSS receiver and the pFDA were added to the Telecommand (TC) and Telemetry (TM) system. Furthermore, the download of payload data, stored in the flash memory of the PDH was organized differently. A FIFO was created for this data, allowing for a maximum of 1000 telemetry packets to be stored on the OBC. This improved the handling significantly, since downloading this data does not require a running PDH. Downloading 1000 telemetry packets can be spread over several ground station passes and days [160].

PCU Software The PCU software remained the same. New systems are switched on by the PDH directly, since the PCU was taken from BEESAT-4 and could not be adapted.

COM Software The call sign of BEESAT-9 was changed to its registered code DP0BEM. Furthermore, the telemetry frame size is adaptable for BEESAT-9. Apart from that, the COM software remained untouched.

PDH Software The GNSS200 receiver works with two different protocols, the National Marine Electronics Association (NMEA) and a binary protocol. For BEESAT-4 the WinMon protocol was implemented, which was the extended version for Phoenix. Thus, both NMEA and binary had to be written from scratch to support acquiring all the available data from the GNSS200. Furthermore, the drivers of the attitude sensors were implemented as well as the control and command software for the pFDA. Additionally a software upload via UART to the pFDA was implemented.

4.2 Summary of the Modifications to BEESAT-9

For BEESAT-9 only one electronic board was modified. The rest of the satellite was assembled with flight spare parts from the predecessor mission. Nevertheless, it entailed the technology demonstration of a new GNSS receiver, the pFDA and newly developed attitude sensors. Additionally, a new lens was selected for the camera to increase the Field of View (FOV) and to include an infrared filter.

Several modifications were introduced to the software to improve and ease the missions operations, especially the download of payload data.

4.3 Ground Station

For the operation of a satellite a ground station is obligatory. The Chair of Space Technology has a dedicated system on top of their building on the campus of TU Berlin. Furthermore, all the required tools were developed in-house. Those tools can be separated into basic tools, which are used by every satellite and specific tools for different payloads, a GNSS receiver in case of BEESAT-4/9.

4.3.1 Ground Operations Software

Together with the BEESAT satellites the ground station was planned and developed simultaneously. Three tools were developed and used throughout the entire mission operation time of most of the launched satellites of TU Berlin since 2009. The development continued throughout the missions and always needed specific adaptations for dedicated satellites.

One tool, TC-Control, provides the interface to the database and the telecommand server. It is used in all ground stations in Berlin, Svalbard, Buenos Aires and San Martin Base in Antarctica for the upload of command lists or new software.

The other two tools are based on the same program code. One is used to display live telemetry received from the satellites (Telemetry-Viewer) to check the status of the subsystems and for confirmation of the successful transmission of command lists. On the other hand, the TM-Analyzer converts the received frames, including the payload data, for further analysis. Included in the TM-Viewer and -Analyzer, a 3D visualization tool was developed by Melan [161] under the supervision of the author. It is displayed in Figure 4.13. It was developed for the verification of the ADCS and for Earth observation, but it can also be used to see where the GNSS antenna is pointing to.

Comparison of SGP4 Ephemerides to GNSS Based Positions

A MATLAB script was developed to compare the GNSS position data to TLE based ephemerides calculated by the SGP4 orbit model. The main purpose of this analysis is the determination of the quality of the TLEs published by the JSpOC. Operations on the BEESATs, which include the ADCS, rely on these orbital elements. Updating them on the satellite is done via a ground station. A systematic analysis of the long-term accuracy of the TLEs helps to estimate the time in which they remain valid for the commanded experiments.

For a good representation of the deviations between the TLE based ephemerides and the navigation data of the GNSS receiver a LVLH reference frame is used. Its origin is in the center of the satellite, as given by the GNSS data. The positions and velocities calculated by the SGP4 orbit model propagator are transformed into that LVLH frame. This allows to calculate the distances in in-track, cross-track and radial direction. In Section 7.2 the analysis of the data, the functions behind this script and the evaluation is described.

Signal Strength over Time Depending on Attitude

A tool was developed, using a combination of MATLAB and STK to determine the signal strength of GNSS signals, dependent on elevation and distance from the GNSS receiver to the GNSS satellites. Furthermore, the evolution over time was analyzed to determine potential degradation of the antenna and its LNA.

The GNSS receiver of BEESAT-9 outputs the signal strength and the tracked satellite for each used channel. According to the data sheet of the GNSS antenna [163] a GNSS satellite located 16° from zenith for the yz-plane and at 19° from zenith for the xz-plane will produce the highest C/N_0 . In Figure 4.14 the radiation pattern of the antenna is displayed for both planes. Values above the center line, between 90 and 270 represent a positive elevation over the antenna. A decreasing elevation leads to a lower C/N_0 until GNSS signals cannot be acquired and satellites not tracked anymore.

At first, the scenario in STK is fed with attitude data of the satellite to determine the distance, azimuth and elevation to the GNSS satellites in relation to the GNSS antenna. This data was then compared inside the MATLAB script with

each channel in a given time frame. The method and the results are described in Section 7.3.

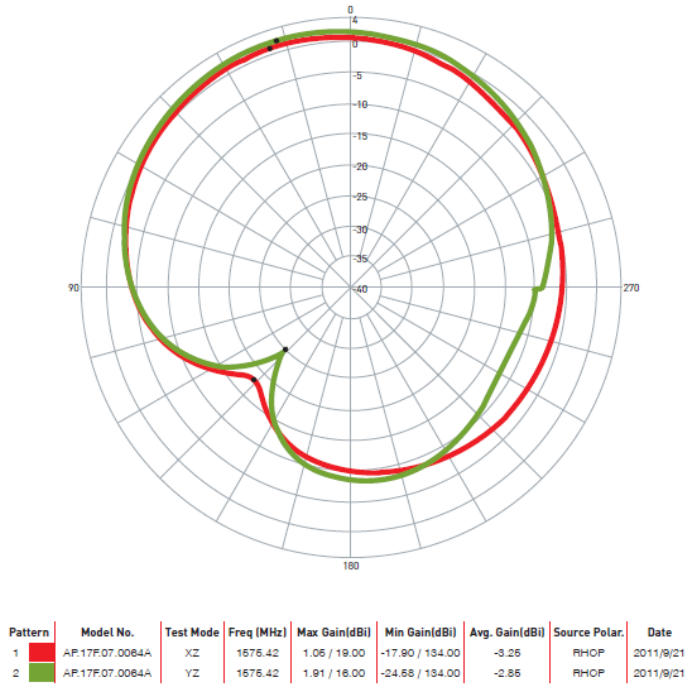


Figure 4.14: Radiation pattern of GNSS antenna of BEESAT-9 [163]

Orbit Determination and Propagation

Based on Orekit [164] a script was developed by Jonglez [162]. It was used for an initial orbit determination in the first weeks after launch in July 2019. It was adapted to enable orbit determination for any period of the entire GNSS data set available from navigation experiments with BEESAT-9. Furthermore, the time frame for the propagation was extended to estimated ephemerides up to two weeks into the future. It was then used to determine the orbit of BEESAT-9 and propagate the ephemerides based on the GNSS data set. The propagated ephemerides are compared to the prospective GNSS data sets of BEESAT-9 to develop the best strategy for the most accurate, but still energy efficient operation of the GNSS receiver. The different strategies and results are described in Section 7.4.

4.4 Conclusions of the System Concept of the BEESAT line

Starting with the development of a single-fault tolerant 1U CubeSat the system concept of BEESAT-1 set a basis which allowed for modifications and integration of further payloads. Within the three successor missions, the satellite bus was improved steadily. Regarding the hardware, most of the improvements were applied on the ADCS with the reaction wheels and the magnetic coils as well as all the attitude sensors. Furthermore, the payload was revised for every mission, always maintaining the capabilities of the former mission and adding new technologies. The first payload was a simple camera, which was directly connected to the OBC via UART. For BEESAT-9 it consists of a complex PDH, includes the camera introduced in BEESAT-2 with a more advanced lens, the GNSS200 as the main payload, a pFDA for technology demonstrations as well as two arrays of gyroscopes and magnetic field sensors.

In the ground segment continuous adaptations were applied as well. All the basic tools were modified during the missions to comply with the increasing number of satellite missions of TU Berlin and to include further capabilities. Additionally several tools were developed for the analysis of the navigation data.

In general, a highly integrated 1U CubeSat was developed which can be used for navigation experiments, research regarding attitude determination and for basic Earth observation. In Table 4.1 the highlights and specifications of BEESAT-1/2/4/9 are listed. Several parameters, in particular within the ADCS are given approximately within a $2\text{-}\sigma$ standard deviation, meaning about 95 % of the experiments deliver the given accuracies.

Table 4.1: Overview of modifications on the BEESAT satellites

	BEESAT-1	BEESAT-2	BEESAT-4	BEESAT-9
OBC				
Redundancy	✓	✓	✓	✓
SW/HW				
SW-Upload	-	✓	✓	✓
Param Container	static	dynamic	dynamic	dynamic
Continuation on next page				

Table 4.1: Overview of modifications on the BEESAT satellites

	BEESAT-1	BEESAT-2	BEESAT-4	BEESAT-9
TM/TC System	custom	CCSDS, VC	CCSDS, VC	CCSDS, VC
Data interfaces	CAN, SPI, UART	CAN, SPI, UART	CAN, SPI, UART, I ² C	CAN, SPI, UART, I ² C
Telemetry Storage	4 MB			
COM				
Redundancy	✓	✓	✓	✓
Digipeater	✓	✓	✓	✓
ISL capability	-	BEESAT-2 ↔ BEESAT-3	BEESAT-4 ↔ BIROS	✓
Acknowledge protocol	-	implemented, not reliable	✓	✓
Downlink	4.8 kbit/s or 9.6 kbit/s			
EPS				
Redundant battery system	✓	✓	✓	✓
Energy storage	5.2 A h			
Peak Power	18.7 W			
Independent solar cells	✓	✓	✓	✓
Solar array power	2.3 W			
ADCS				
Gyroscopes	3 analog single axis	3 analog single axis, 1 MEMS three axis	2 MEMS three axis	6 MEMS three axis
Noise	0.6 °/s	0.1 °/s	0.1 °/s	0.01 °/s

Continuation on next page

Table 4.1: Overview of modifications on the BEESAT satellites

	BEESAT-1	BEESAT-2	BEESAT-4	BEESAT-9
Resolution	0.6 °/s	0.1 °/s	0.004 °/s	0.004 °/s
Magnetic Field Sensors	2 analog	2 analog	2 analog, 1 MEMS	2 analog, 5 MEMS
Noise	300 nT	300 nT	500 nT	40 nT
Resolution	12 nT	12 nT	8 nT	25 nT
Sun Sensors	✓	✓	New PSDs, improved aperture plate	
Reaction Wheels	RW1 Typ B	RW1 Typ A	RW1 Typ A	RW1 Typ B
Magnetic Coils	✓	Improved control	✓	✓
Attitude Determination	no on-orbit verification	✓	3–5°	1–4°
Attitude Control	-	✓	3–7°	1–3°
TCS				
Temperature Sensors	20, 12-bit	22, 12-bit	24, 12-bit	32, up to 16-bit
Coating applied to increase mean temperature of the satellite	-	✓	✓	✓
Payload				
Volume available			0.1U	
PDH	-	✓	✓	✓
SW-Upload	-	✓	✓	✓
Camera	COTS	In-house design	Improved interface	New optics, IR-cut filter
Continuation on next page				

Table 4.1: Overview of modifications on the BEESAT satellites

	BEESAT-1	BEESAT-2	BEESAT-4	BEESAT-9
GNSS receiver	-	-	✓	✓
TTF	-	-	600 s/180 s	90 s/30 s
Power	-	-	850 mW	150 mW
PFDA	-	-	-	✓
Ground Segment				
Multi mission operation	-	✓	✓	✓
ADCS visualization tool	-	-	✓	✓
GNSS data processing tools	-	-	-	✓

5 Verification and Launch Campaign

One big part of a satellite mission is the manufacturing of the hardware, assembly of all the parts and verification of the chosen system concept with a wide variety of simulations, tests and calibration campaigns. For BEESAT-4 and BEESAT-9 the verification extent was reduced, since the predecessors were already in space, making many subsystems space qualified. Thus, the test campaigns described in this chapter focus on the verification of the ADCS and the GNSS, which were both considered essential for the implementation of the PPOD package. The following sections will distinguish between the two satellites, since some subsystems required different approaches.

5.1 Verification Campaign of BEESAT-4

Integrating the Phoenix receiver into the BEESAT satellite bus was the main challenge. It took around six months until the first development boards for its integration were manufactured. Followed by many tests and further iterations, a final concept was introduced. This was the initial point for procuring and manufacturing of all the subsystems of the FM, because the OBC was the only subsystems left from the predecessor missions with a FM status.

Dedicated pointing and three-axis stabilization was considered essential for the tracking of GPS satellites, thus many simulations and tests were executed to verify the ADCS. Additionally, starting in July 2015, experiments were uploaded to BEESAT-2 to test the ADCS on orbit and the results were used for the development of BEESAT-4 [165]. The implementation of navigation data handling from Phoenix on the PDH was accompanied with outdoor tests as well as tests with a GPS simulator.

For a proper attitude determination and control, all the involved sensors were calibrated and their performance was evaluated. An environmental test campaign, including radiation, vibration and thermal-vacuum tests was performed immediately

before the delivery to the launch provider. Just before the ascent to its dedicated orbit, the satellite was checked out at the launch site in Sriharikota, India.

In Table 5.1 the qualification status of the subsystems, components and several applications can be seen. A classification in four categories has been applied, where A stands for a fully qualified system, that does not require further verification to category D, representing new components or software applications. In category B all the subsystems and components are listed that were already space proven, but modifications were applied nonetheless, e.g. additional sensors of the same type. The three-axis stabilization was labeled C, since it was already implemented, but not yet fully reliable.

Table 5.1: Qualification matrix of subsystems, components and applications of BEESAT-4

System	Status	Remarks
Structure	A	Manufacturing required
Mechanisms	A	Manufacturing required
Electrical Power System	A	Manufacturing and assembly required
Communication System	A	Reordering of Transceivers
On-Board Computer	A	Available
Attitude Determination and Control System		
Sun Sensors	B	New Position Sensitive Device
Magnetic Field Sensor	B	One new sensor
Gyroscopes	B	One new sensor
Magnetic Coils	A	Manufacturing required
Reaction Wheels & WDE	A	Reorder of flight models
Attitude determination	B	Accuracy improvements were sought
Attitude control	C	Verify three-axis stabilization
Thermal Control System	A	Integration of temperature sensors
Payloads		
Payload Data Handling	D	New board, full verification process
Camera	B	Already in space, but new implementation
Phoenix	A	Space proven GPS receiver
GPS software algorithms	D	New on BEESAT-4

All the systems which were already space proven are not further disaggregated. It was described in Chapter 4, that all the software modules were adapted during the BEESAT-4 mission. Nevertheless, this does not apply to their basic functions and thus is not described here in further detail.

5.1.1 Manufacturing and Integration

Some of the space proven subsystems were ordered as ready for operation products. The UHF transceiver BK77 and the reactions wheels including the Wheel Drive Electronic (WDE) to be conform to the other BEESATs, the Phoenix receiver due to the collaboration with the DLR. Furthermore, electronic boards of the OBC were still available from the BEESAT-1 mission. These boards, considered flight models, also include the TNC.

Apart from that, the satellite had to be manufactured. All the other electronic boards, PCU, PDH and solar panels were in-house developments, but the manufacturing and the assembly was executed by specialized companies. The primary structure and the battery case were machined at the department's workshop. Changes of the aperture plate of the sensors required a new process to drill the 200 μm hole, which was realized at the Chair of Micro- and Precision Devices of TU Berlin. Moreover, the pasting of the solar cells was ordered externally, due to the lack of proper machines and facilities.

Several further steps are necessary before the satellite can finally be integrated. External temperature sensors are connected to the magnetic field sensors (see 4.5), the reactions wheels and transceivers. Moreover, the batteries have to be prepared for their integration, soldering two cells in parallel for the required voltage. Afterwards, they are covered in epoxy inside the battery case to be isolated from the rest of the satellite properly. Additional thermistors and temperature sensors next to the batteries allow for proper monitoring during the mission. Solar panels and the primary structure are irreversibly connected with space proven epoxy as well. After the assembly of all the subsystems, the final integration process can be started. In Figure 5.1 it is displayed.

The integration starts with the bottom plate, including the antennas of the UHF transceivers, which are stacked on top of it. Followed by the WDE and the battery case, which is also connected to the reaction wheel assembly, half the satellite is already integrated. The upper part consists of the three electronic boards,

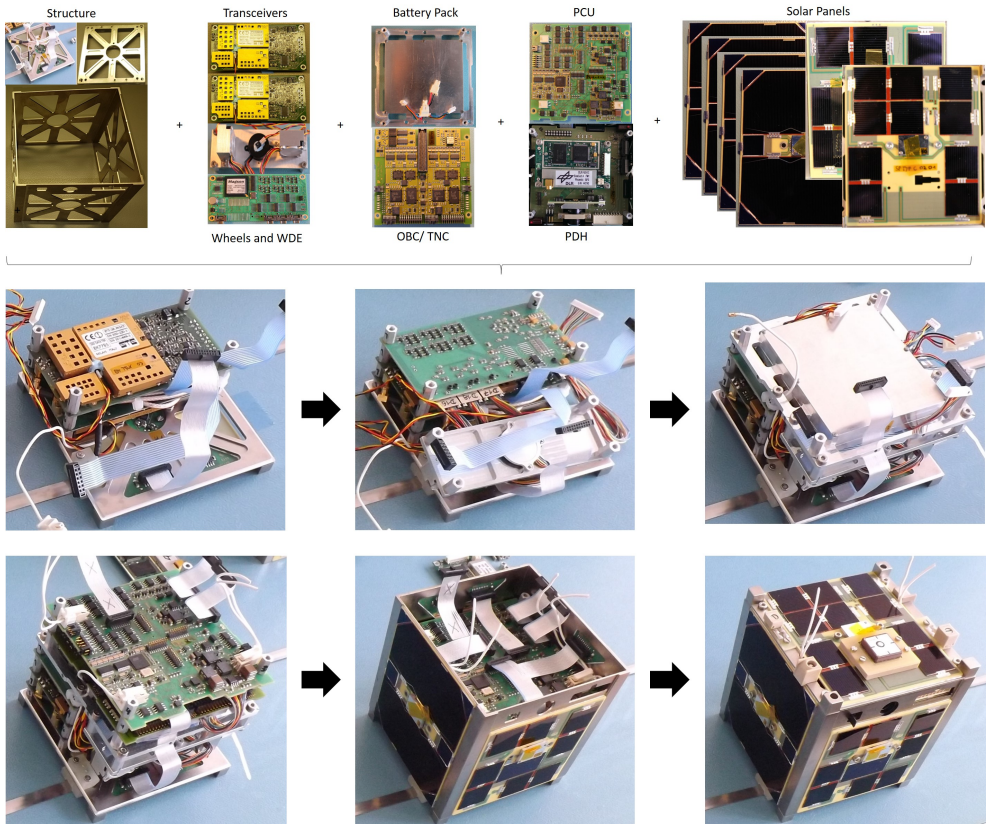


Figure 5.1: Integration process of BEESAT-4

OBC/TNC, PCU and PDH. The square tube with the integrated solar panels is slipped over the stack followed by the PDH. After the top plate, with the integrated GPS antenna, is connected to the rest of the stack, the UHF antenna release mechanism is loaded and the cables for its activation are soldered. This concludes the integration process and the satellite is ready for final functional and environmental tests and the calibration campaign.

5.1.2 Ground Testing of ADCS

During the development of BEESAT-1 the components, both hard- and software, were tested by Herfort, Berlin and Yoon [136, 138, 135] and the orbit, magnetic

field and sun models were verified with certified implementations by Herfort and Geyer [136, 137]. Further testing with the additional gyroscopes and magnetic field sensors was conducted by Korn [132, p. 52] during the BEESAT-2 mission and by the author for BEESAT-4 and it showed significant improvements regarding the noise. The tests, conducted by the predecessor missions remain valid for BEESAT-4.

After the final integration all the devices of the ADCS were tested end-to-end. Furthermore, the assignment of actuators and sensors to the satellite axes was verified for the entire chain, from commanding to displaying the values in the telemetry viewer.

Due to a lack of an ADCS testbed for picosatellites, three-axis stabilization was simulated using alternative implementations. A MATLAB based simulation developed by Geile [145] was the base for further improvements by the author [166]. According to the simulations, the reaction wheels were capable of damping angular rates of more than $15^\circ/\text{s}$, before the Slew Mode turned the satellite towards the desired attitude. At an adjustable attitude error the fine pointing modes took over and achieved accuracies at sub-degree level.

On-orbit experiments with BEESAT-2 were used for the implementation of the ADCS on BEESAT-4 and presented by the author in 2016 [167]. Due to deviations between the simulations and the on-orbit performance of BEESAT-2, another simulation was set up by Kapitola and the author [168], based on the implemented flight software. First comparable results were achieved by using a unit quaternion of $\vec{q}_{des} = (0,0,0,1)$ as the desired attitude. Simulation and on-orbit experiments showed similar successful executions and a three-axis stabilization of the satellite was achieved and presented by the author in 2016 [169]. A fully functional attitude control with a variable desired quaternion for target, nadir or zenith pointing required several modifications of the on-board software and was achieved after two software uploads and presented by the author in 2017 [170]. Results of on-orbit experiments are described in Section 6.1.2.

Blind damping of the satellite was already verified with the FM on the ground. All the different suggested modes by Lucia [147] were implemented and tested on an air bearing table in the laboratory at the TU Berlin. starting with a rotational speed of $30^\circ/\text{s}$. Reducing the angular rate from $30^\circ/\text{s}$ to an angular rate lower than $1^\circ/\text{s}$ takes around 30 min, which is significantly lower than in space (see Section 6.1.2), mostly to air resistance with a small addition from the remaining friction of the table.

All the ADCS modes were successfully tested or simulated and the integration and axes transformation of the sensors and actuators was verified.

5.1.3 Ground Tests of GPS

Initially, solely outdoor tests were planned with an engineering model of Phoenix, due to the lack of a GPS simulator. Successful tests preconditioned, another campaign with the flight model was meant to follow. Further into the mission, a GPS simulator was purchased within PiNaSys [38], another project of the Chair and was also available for tests of BEESAT-4. Tests with a simulator improved the verification possibilities significantly. In case of GNSS the simulated signals represent the real environment thoroughly.

For all the performed tests the same properties were analyzed. In Table 5.2 the criteria are summarized and the results from the GSOC are included. A verified command chain indicated, that all the commands were executed properly by the Phoenix receiver. For a validation of the command chain the acknowledgment messages of the receiver were stored as well.

Table 5.2: Test parameters for Phoenix

Test Case	Command Chain	Clock Fix	TTFF	Peak C/N_0	Tracked Satellites
EQM "cold start" outdoor	Verified?	< 1 min	< 10 min	~ 45 dB-Hz	~ 6
FM "cold start" GPS-Sim	Verified?	< 1 min	< 10 min	~ 45 dB-Hz	~ 8
FM "warm start" GPS-Sim	Verified?	-	< 10 min	~ 45 dB-Hz	~ 8
EQM GSOC "cold start"	Yes	30 s	5 min	49 dB-Hz	10
FM GSOC "cold start"	Yes	100 s	13 min	48 dB-Hz	10
FM GSOC "warm start"	Yes	-	~ 2 min	48 dB-Hz	10

Outdoor Tests of Phoenix

The two models were tested before delivery by the GSOC and the report stated “cold starts” with navigations fixes within 5 min for the EQM and 13 min for the FM [171]. “Warm starts” (detailed description in Section 6.1.3) with the FM provided a navigation fix within 2 min. These tests were performed with a Spirent STR4500 GPS simulator.

At that point, neither a GPS simulator was available nor did BEESAT-4 have the recommended antenna usually used for Phoenix [99]. Thus, outdoor tests with a small GPS antenna were planned to analyze the performance under different circumstances. Due to the changed test setup, the expectations regarding the peak value of C/N_0 as well as the number of tracked satellites were lowered. All the outdoor tests are based on the “cold start”, since “warm starts” are only available on orbit with the FM. The Phoenix receiver requires TLEs of the satellite which have to be provided to the Phoenix receiver and are not available at a static position.

In spring 2014 basic initial tests were executed, including only the Phoenix receiver, the antenna and a connection to a terminal program to display the output on the UART lines. Results were not deterministic, with every experiment resulting in a completely different time period for the Time-To-First-Fix (TTFF). The used Phoenix receivers had a hard coded starting time in GPS week 1073 (2000-07-30), which was overwritten with the current time, once a signal from any GPS satellite was acquired. With this basic setup, it took between 1–30 min to obtain the time from a GPS satellite. Additionally, after the time was set correctly, it took between 5–40 min to acquire a navigation fix with up to five GPS satellites. Having 12 channels available, this is not a good performance. Even worse, the receiver kept on running, but the fix was lost repeatedly, even in this static position.

For the number of tracked satellites it has to be mentioned that the channel status of Phoenix has several levels once a signal from a GPS satellite is received. At first it states “code locked” meaning the code search of the assigned GPS satellite was successful. Once it is locked to the carrier frequency (“Carrier locked”), synchronizes to the bits (“bit locked”) and finally synchronizes to the frame of the GPS data stream, the status changes to “frame locked” [31, p. 69]. Only a “frame locked” GPS satellite is included into the navigation solution.

An analysis of the C/N_0 values of the individual channels and the assignment of GPS satellites to those channels was made. Low values of less than 33 dB-Hz showed a “code locked” status additionally to the maximum amount of five tracked GPS satellites. To classify the undetermined performance the C/N_0 of every channel was recorded. Values for “frame locked” GPS satellites, which were included in the navigation solution varied from 35 dB-Hz to 44 dB-Hz, depending on the elevation of the GPS satellites over the antenna. According to Markgraf [172] these values should be between 40 dB-Hz and 50 dB-Hz, which derives from the spectral noise power density $N = -174$ dB/Hz [173] and the expected GPS signal strength including the gain from the LNA of the antenna. As mentioned before, lower peak levels were expected, due to the different antenna, thus the recorded values of up to 44 dB-Hz met the criteria. The problem occurred from the selection of GPS satellites, with some of them being on the other side of the Earth at the time of the experiment. Furthermore, satellites changed their “lock status”, even though the signal strength remained stable (Figure 5.2).

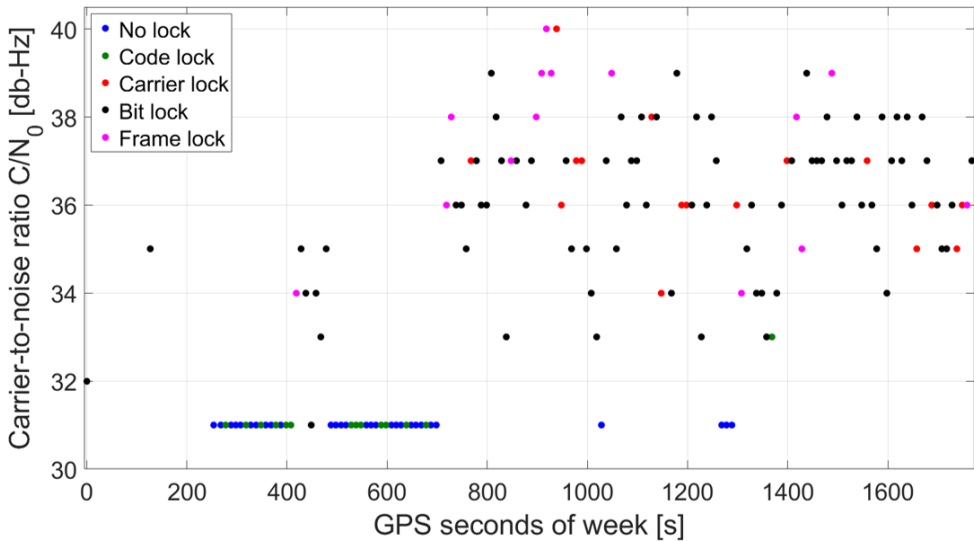


Figure 5.2: Lock status in relation to signal strengths of the Phoenix receiver

In the displayed case, a “frame lock” was achieved with $C/N_0 = 34$ dB-Hz, but values of up to 39 dB-Hz did not lead to a “frame lock”. The cause of this behavior remains unknown, also due to the lack of access to the algorithms running on the Phoenix receiver.

Thirty minutes after the first navigation fix the receiver was rebooted to start the next experiment. The experiments were conducted on three different days within a two week period. Even though the performance was not as expected, a navigation fix was acquired in every single experiment. In Table 5.3 the results are summarized. Analyzing the channel status helped to identify the problem, but a solution was not found at that point. The setup of the experiment was seen as a potential reason, thus a fully integrated satellite was required for the next test campaign.

Further tests were executed once the satellite was fully integrated in March 2015. The antenna was properly connected to the top plate of the satellite which enlarged the ground area. This setup led to highly deterministic results, with an acquisition time of around 60 s to set the current GPS time on the receiver. Furthermore, the TTFF was constantly between eight to ten minutes, which is close to the report of the GSOC[171]. Most of the other parameters improved accordingly. The number of tracked satellites included into the navigation solution increased to a maximum of eight and the navigation fix was not lost once it was acquired, but remained constant over the duration of the experiments. After the first navigation fix the experiment continued for 15 min, as suggested by the energy budget report ([126]). The C/N_0 of the individual channels was similar to the basic initial tests, which confirmed the observation, that the maximum signal strengths for the selected antenna is 44 dB-Hz. The results were satisfactory and demonstrated the “cold start” capabilities of the chosen concept. A summary of the results is displayed in Table 5.3

GPS simulator tests

Performing tests with a GPS simulator is one of the most realistic setups to evaluate a satellite system. It is basically a one-to-one representation of an on-orbit situation.

The NavX-NCS Professional GNSS Simulator was used for the tests with the Phoenix receiver on BEESAT-4. It is equipped with one Radio Frequency (RF)-Output, which transmits the GPS L1 frequency and is configured for 12 channels. Thus, a total of 12 GPS satellites can be simulated.

For the final system tests of BEESAT-4 in April 2016, the antenna input of the Phoenix receiver was connected to the GPS simulator. A Sun Synchronous Orbit

(SSO) with an altitude of 510 km was set for the satellite and the GPS signal strength was set to -130 dBm at 90° elevation for a peak C/N_0 of 44 dB-Hz. In space the signal was expected to be higher, because it does not have to cross the atmosphere, but this setup was comparable to the outdoor tests.

The experiment was performed as if the satellite was already in orbit. A “warm start” requires a set of commands, which were transmitted via UHF. The data generated by the Phoenix receiver was stored in the flash memory of the PDH, downloaded via UHF and stored in the database of the ground station for further processing. Both, “cold and warm start” of the Phoenix receiver were checked, while a pointing of the antenna towards zenith was assumed.

For the “cold start”, a command was sent to switch on the Phoenix receiver and its output from the UART interface was stored. The results of the outdoor test could be confirmed with similar outcomes for TTFF, signal strengths and the number of eight tracked satellites. Moreover, the navigation solution was not lost, after its first fix and for a duration of 15 min position, velocity, status and performance data was stored.

A “warm start” requires additional information. First of all the current Universal Time Coordinated (UTC) is set on the receiver, followed by the TLEs of the satellite. Another input are the almanacs and ephemerides of the entire GPS constellation. Further settings, like the Doppler search window, an elevations mask or different track modes are optional. A full description by Montenbruck can be found in [31, p. 21ff]. Once all the necessary inputs are sent, the “warm start” is commanded. Every command is confirmed by the receiver with an ASCII-message, which is stored in the flash memory as well.

As expected the TTFF was significantly lower compared to the “cold start” with the output of valid navigation data after three to four minutes in several tests. All the other parameters remained similar. Nevertheless, the report from the GSOC as well as the manual of the receiver state a TTFF of less than two minutes. With the setup described above and throughout all the performed tests during the mission, the best result for a first navigation solution remained above three minutes. Internal discussions, additional to consultations of the manufacturers did not improve the results. Since the results were promising and a “warm start” was executed successfully many times, no further actions were taken to lower the TTFF. It seemed that too many variables, e.g. a different GPS simulator, the construction of the satellite or the used Phoenix receiver could have an impact on the output. The result of the simulator tests are summarized in Table 5.3.

Table 5.3: Test results for Phoenix

Test Case	Command Chain	Clock Fix	TTFB	Peak C/N_0	Tracked Satellites
EQM Outdoor test basic	-	1–30 min	5–40 min	44 dB-Hz	5
EQM Outdoor test fully integrated	Yes	60 s	8–10 min	44 dB-Hz	8
FM “cold start” GPS-Sim	Yes	60 s	8–10 min	44 dB-Hz	8
FM “warm start” GPS-Sim	Yes	-	3–4 min	44 dB-Hz	8

Even though the performance was slightly worse than expected (see Table 5.2), all the tests were successfully completed. The entire setup and concept was confirmed to be functional and the implementation showed no errors. For successful operation of Phoenix on orbit, an accurate ADCS was a precondition. It requires properly calibrated sensors to ensure a correct attitude determination and orientation of the satellite.

5.1.4 Calibration Campaign

All the implemented attitude sensors need several calibration parameters to deliver the required accuracy for a three-axis stabilized satellite. For the three different types, individual setups were used to obtain polynomials, offsets, scale and orthogonality factors and temperature dependencies.

Table 5.4: Calibration parameters of attitude sensors on BEESAT-4

Sensor type	Polynomials	Offset	Scale factor	Orthogonality factor	Temperature dependency
Sun sensors	✓	-	-	-	-
Magnetic field sensors	-	✓	✓	✓	-
Gyroscopes	-	✓	-	-	✓(Offset)

The methods, developed by Jahnke for BEESAT-2 [174], were adapted to BEESAT-4 and presented by the author in July 2016 [175] along with the results. In Table 5.4 all the parameters, which were determined during the campaign are assorted. For the sun and the magnetic field sensors the temperature dependency was investigated, but no significant change was found. The performance of the gyroscopes could have been improved by taking the scale and orthogonality into account. Time constraints to further look into the calibration strategy as well as the sufficient performance stopped a more sophisticated calibration.

Sun Sensors

A powerful light source, roughly equaling the solar power at the satellite, was used to calibrate the sun sensors. Between the source and the satellite a collimator was placed to parallelize the rays to avoid any disturbances from transversal light. In Figure 5.3 the entire setup is displayed.

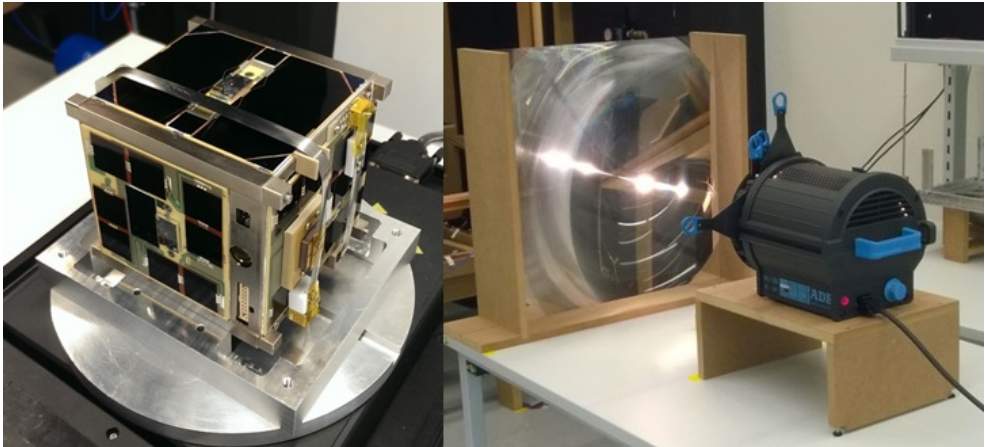


Figure 5.3: Setup for the calibration of sun sensors on BEESAT-4

The satellite was placed on a highly precise rotary table and was turned through the entire Field of View (FOV) of each sensor from both axes. Data was taken in steps of five degrees from -60° to 60° starting from a centered position. Each PSD outputs four currents, which are combined to calculate two angles. A third degree polynomial was considered sufficient to reproduce the calibration adequately.

Thus, a total of eight parameters is stored in the parameter container on board of the satellite to acquire a sun vector accuracy of less than one degree.

Gyroscopes

For BEESAT-4, only the offset of the gyroscopes and its temperature dependency were calibrated, disregarding the scale factors as well as the orthogonality and misalignment errors. During the calibration campaign of BEESAT-2, described by Jahnke [174, p. 46], all four parameters were determined. Including the scale and orthogonality factors decreased the accuracy partially and it was suggested to reconsider the used method. On orbit, the performance of the three-axis gyroscope was according to the calibration results, confirmed by a comparison of the angular rates, derived from the sun and magnetic field sensors. Due to time constraints, there was no research done to further improve the accuracy with the integration of additional calibration parameters.

Thus, the satellite was placed into a thermal chamber fully integrated and a temperature span from -10°C to 30°C was programmed. Angular rates, connected to the non-calibrated temperatures of each sensor, were stored and put into a diagram. It was found that a square correlation was sufficient to represent the gradient of the offset over the temperature, which can be seen in Figure 5.4.

Magnetic Field Sensors

The calibration of the magnetic field sensors was carried out several times due to uncertainties of the results. Since there is nearly no change over temperature (around $2\text{ nT}/\Delta^{\circ}\text{C}$, with noise figures of 300 nT), only offsets, scale and orthogonality factors were obtained during the calibration. At first it was executed in an iron free cabin on the countryside. A reference proton magnetometer measured the total magnetic field strength on the dedicated spot. Afterwards the satellite is turned downwards with each of its six sides consecutively and the measured values from the three sensors were averaged over 20 s. A fitting algorithm estimated the calibration parameters according to the total field strength. All the parameters were added to the flight software on site and a verification test was performed, which was successful.

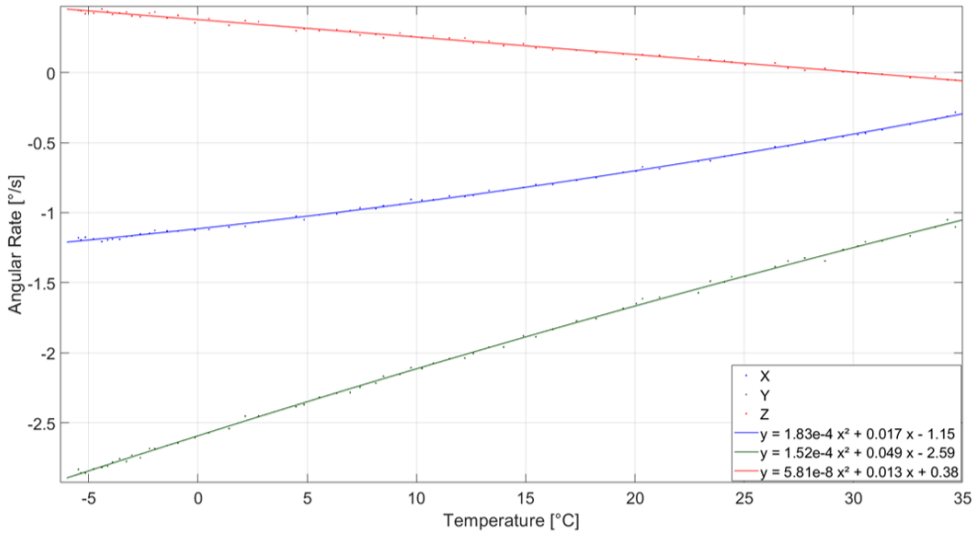


Figure 5.4: Temperature dependency of the offset of gyroscope MAX21000

During the check out at the launch site all the sensors were validated during a functional test. Using the same parameters, the offset was huge. A simple re-calibration was executed, changing only the offsets. A non-magnetic test setup was installed, the satellite was placed on top and turned by 180° . Values were measured in both positions and the average was used to re-calculate the offset. Validating the new calibration parameters with random measurements showed similar results for all three sensors.

Nevertheless, after the launch the values seemed off again, leading to a third calibration campaign for the magnetic field sensors. Calibrating on orbit is more complicated, because the total magnetic field strength around the satellite changes constantly. It requires a big dataset from the orbit for calibration using a least-square algorithm as suggested by Springmann [176]. Using the IGRF model to produce reference data, new offsets and scale factors were estimated. Table 5.5 shows the values from all three calibrations performed during the mission.

The huge differences between the calibration campaigns remain unknown. During the first calibration in the countryside, the satellite was covered in foil and the antennas were folded. Unfolding the antennas was further analyzed, but it changed the magnetic field measurement only up to 3000 nT, thus contributing just partially to the different calibration parameters. Furthermore, it was investigated if the

Table 5.5: Calibration parameters of magnetic field sensors on BEESAT-4

Offset parameter	Berlin [nT]	Launch Site [nT]	Orbit [nT]
MFS0 X	-76 029	-79 622	-80 622
MFS0 Y	65 156	33 776	15 776
MFS0 Z	10 146	7 351	2 351
MFS1 X	18 354	20 422	14 422
MFS1 Y	32 504	8 642	142
MFS1 Z	-11 930	-14 448	-22 948
MFS2 X	11 584	8 863	12 094
MFS2 Y	-7 968	963	-57
MFS2 Z	10 266	-13 596	-10 623

current flow in different subsystems could explain the differences, but that was not the case.

After the final on-orbit calibration the magnetic field sensors provided valid data to the ADCS. Regardless, all three campaigns showed a successful calibration at first. For further missions it could be considered to spare the campaign on the ground and directly calibrate on orbit.

5.1.5 Environmental Test Campaign

For the verification of the implemented system concept of the newly integrated components and the proper integration of the entire satellite, a test campaign was performed. During the development, the PDH and the GPS antenna were exposed to a radiation source, checking their capability to withstand the radiation in space. The fully integrated flight model was tested on acceptance level on a shaker, simulating the expected loads during launch. Furthermore, a thermal vacuum test and bake out was conducted. Finally, the satellite was checked out at the launch site in Sriharikota, India ahead of the integration into the SPL inside BIROS.

Radiation Tests

The newly developed electronic board for the Payload Data Handling (PDH) consists of several ICs, which were never flown in space by the TU Berlin before. Main concerns were given to the microcontroller, flash memory and the RAM. According to Bri , based on European Cooperation for Space Standardization (ECSS) norms, only Total Ionizing Dose (TID) tests are obligatory [177, p. 35]. Further radiation tests with electron, protons or ions are only performed exceptionally, since these tests are expensive and only limited facilities provide them. Thus, a gamma emitter is chosen to expose the subsystems with the expected total radiation during the minimum operation time. A Cobalt-60 source, located at the Helmholtz-Zentrum Berlin f r Materialien und Energie, was used for the experiments.

According to Spennis [178], the expected radiation in a 510 km SSO over one year can be estimated to 10 krad. Uncertainties in the model were compensated by a margin of 20 %, adding to a maximum expected radiation of 12 krad for the mission time of one year. A radiation dose of 3 krad/h was chosen as a trade-off between required test duration and ability to detect transient effects due to radiation. Success criteria was set to the following specifications.

- Current and voltage of PDH remains within 2 %
- Flash memory and RAM show no degradation
- Flawless program test run on microcontroller
- Post radiation outdoor test of GPS antenna provides similar signal strengths over elevation compared to pretest conditions

During the entire procedure, the board was switched on and communication via UART was performed continuously. A test program kept the microcontroller busy, while both memories were constantly used for three operations. Data was written to it, read again and deleted afterwards.

The board was placed at a distance to the source to be exposed at a rate of 3 krad/h. After four hours the test was completed and the PDH did not show any degradation or anomalies. It has been used as a development board since the TID test in January 2014.

Testing the GPS was a bit more challenging, due to the lack of navigation signals inside the test chamber. Thus, the performance of the antenna could not be

evaluated during the testing. The test was conducted by another project team and only one antenna was available for testing. It was suspected, that a radiation dose of 12krad could degrade the antenna to a level where no GPS signals would be received anymore. Thus, it was tested only to a dose of 6krad, to evaluate potential lower performances. A navigation experiment was then conducted on the roof of the Chair and there were no indications of a degradation. Due to the on-orbit performance of the GPS antenna on BEESAT-4, another radiation test was performed with a radiation dose of 12krad. It decreased the performance of the antenna significantly (see Section 5.3.5). The on-orbit experiments and the second radiation test led to a replacement of the antenna on BEESAT-9 .

All the selected and developed components passed the radiation tests conducted before the launch of BEESAT-4 and no device was replaced.

Vibration Tests

During a launch the spacecrafts are exposed to very high loads, which have to be absorbed by the primary structure. Making sure it will withstand these loads until the spacecraft is deployed into its orbit requires a certain set of vibration and shock tests.

During the BEESAT-1 mission a shock test was executed and since there were no modifications affecting the structural characteristics, this test was skipped for BEESAT-4. Nevertheless, several vibration tests are obligatory, requested by the launch provider. For a successful test, no visual damages, a pass of the Full Functional Test (FFT) after every cycle and no changes of the resonance frequency above 10 % were set as the criteria.

For BEESAT-4 a protoflight test strategy was chosen, thus only the FM was tested. The campaign took place at the facilities of Astro- und Feinwerktechnik GmbH. The satellite was integrated into an SPL, same as the flight model, and attached to the shaker (see Figure 5.5).

Afterwards the satellite was exposed to a sinusoidal vibration from 5 Hz to 100 Hz and a random vibration test from 20 Hz to 2 000 Hz with an overall load of $8 g_{rms}$. Every test was executed for all three axes individually and followed by a resonance survey test. A specification was published by Ritzmann and Rose from Astro- und Feinwerktechnik GmbH in 2007 [179, p. 18ff], including all the test loads for



Figure 5.5: BEESAT-4 on the shaker in an SPL

the launchers available for rideshare launches. For BEESAT-4 the maximum test specifications were taken on a protoflight level from each launch vehicle.

All the tests were followed by a functional test of the satellite, which was passed successfully. Furthermore, the resonance survey showed no significant changes after the tests. The values remained similar within a margin of 10%. Testing within a deployer adds some random factors, since the satellite is not exposed to the loads directly, but through the deployer. After every test, the satellite might change its position minimally inside the deployer, which causes changes in the resonance survey as well. Nevertheless, the vibration test campaign on a protoflight level was considered successful by the review board.

Thermal Vacuum Test

In its space environment the spacecraft encounters a broad bandwidth of temperatures, unless an active Thermal Control System (TCS) keeps it within a small range. The TCS of BEESAT-4 is passive and the expected temperatures inside the

spacecraft lie between -5°C and 35°C according to the simulations by Just [180]. The simulation was adjusted to the orbit temperatures of BEESAT-2, making it more accurate for BEESAT-4 as well.

Validating the system concept and the proper integration, a thermal vacuum test is conducted. In 2007 Astro- und Feinwerktechnik GmbH developed specifications especially for CubeSat verification including test parameters for thermal-vacuum tests [179, p. 22ff]. It was used for an acceptance campaign, with some temperatures tailored to the BEESAT satellite bus. Having the knowledge of two former missions, additionally to the simulation, the temperature range was narrowed down.

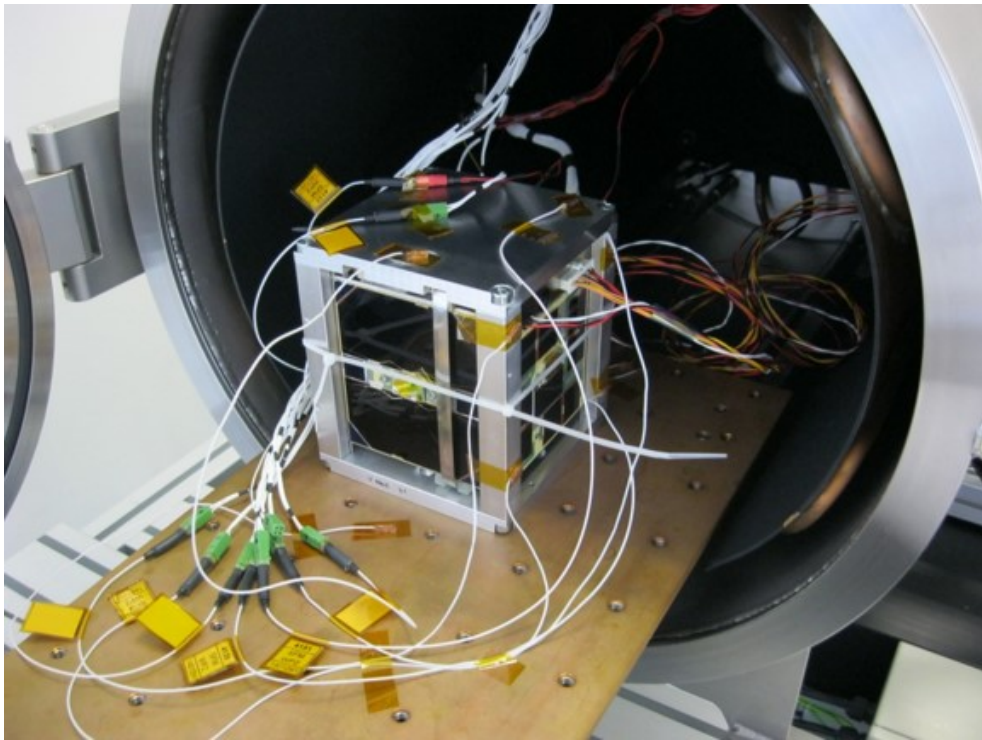


Figure 5.6: BEESAT-4 in a thermal vacuum chamber

According to [179, p. 22] the temperatures vary from -35°C to 65°C . For BEESAT-4 it was set from -25°C to 60°C for one non-operational cycle and three operational cycles with temperatures from -15°C to 45°C .

Ahead of the thermal-vacuum test, the satellite underwent a FFT, which was passed. A dwell time of two hours and a special adapter, which can be seen in Figure 5.6, made sure that the entire satellite reached each temperature level.

A FFT was executed after every dwell time. After four days, including a 24 h bake-out procedure, the thermal-vacuum test was finished and a final test was performed. The satellite did not show any anomalies and passed the test successfully.

This concluded all the tests and calibration of the sensors and the satellite was prepared for delivery to be sent to the launch site.

5.1.6 Check Out and Launch

BEESAT-4 was integrated into BIROS in Adlershof, Berlin, Germany in the clean room of the DLR in the beginning of May 2016. It was then shipped to Sriharikota, India and taken out inside the clean room facilities at the launch site at the end of May 2016 for the check out.

All the subsystems were tested with the predetermined FFT. Since there was no option to test outside, a navigation fix was not received from the GPS receiver. Regardless, all of the subsystems endured the transport in mint condition and the initial test was successful. Another purpose of the check out was uploading the newest software image to OBC and PDH, followed by another FFT. Further action was only taken to calibrate the magnetic field sensors, as described in Section 5.1.4.

Finally, the satellite was integrated into the SPL inside BIROS again, before BIROS was mounted to its deployment adapter on the fairing of the launch vehicle. On 2016-06-22 the launch and the separation of BIROS took place, bringing both satellites safely to their dedicated orbits. For the commissioning and the preparation of the AVANTI experiment the DLR took until 2016-09-09, the day BEESAT-4 was deployed.

5.2 Conclusions from Verification Campaign of BEESAT-4

The Phoenix receiver together with the space proven subsystems of the predecessor missions forms the flight model BEESAT-4.

After the final integration the modes of the ADCS were tested and simulated. Several modifications were applied according to flight results from BEESAT-2 to enable a reliable three-axis stabilization.

Outdoor and GPS simulator tests with the Phoenix receiver were executed accordingly to meet the criteria set by the test report from the GSOC [171]. The chain of command was verified and both, "cold and warm starts" were executed successfully and fulfilled the requirements (see Table 5.3).

For an accurate performance of the ADCS all the sensors were calibrated. The results for the sun sensors and the gyroscopes were satisfactory and the discrepancies from the ideal values became low, in contrary to the magnetic field sensors which had to be re-calibrated several times and were not useful until an on-orbit calibration.

An environmental test campaign, including radiation, vibration and thermal-vacuum tests, concluded the verification of the flight model BEESAT-4 and it was ready for the check-out at the launch site and operations in its SSO.

5.3 Verification Campaign of BEESAT-9

BEESAT-9 was mostly manufactured already, being the former EQM of BEESAT-4. Nevertheless, the integration of the GNSS200, the pFDA and additional gyroscopes and magnetic field sensors to the PDH was challenging, too. Furthermore, as far as possible, all the electronic boards were replaced with the unused flight spares from BEESAT-4.

After the final integration, the ADCS was validated mainly for correct integration and transformation of coordinate systems. The GNSS receiver underwent intensive testing, the receiver itself as well as the implemented software to process the data.

A further developed calibration campaign for the attitude sensors took place to ensure an accurate attitude determination and pointing of the satellite. Some weeks before the shipment to the launch site, an environmental test campaign was performed, including vibration and thermal vacuum tests. A final check out at the facilities in Vostochny, Russia took place just ahead of the launch into the dedicated orbit.

5.3.1 Manufacturing and Integration

For the integration of BEESAT-9 two subsystems were manufactured. An empty battery case was still available and was filled with new batteries. Furthermore, a new PDH was developed to include the GNSS200, the pFDA and new attitude sensors (see Figure 4.12). Due to a non-satisfactory performance of the GPS antenna (see Section 5.3.5 and Section 6.1.3), a new model was chosen [163], which was ordered from Taoglas (see Section 5.3.3).

The EQM of BEESAT-4 was completely disintegrated and all the parts remaining for the flight model of BEESAT-9 were cleaned and rated flight ready. The entire structure including the solar panels with its integrated magnetic coils and sun sensors was reused. Furthermore, the WDE, purchased during the BEESAT-4 mission, along with the flight spare reaction wheels of BEESAT-1 remained. Besides, flight spare modules of the transceivers BK77, the PCU and the OBC replaced the EQM parts.

The integration process remained the same as described in Section 5.1.1. All the new devices were integrated successfully and the satellite was ready for tests and calibration.

5.3.2 Ground Testing of ADCS

The basic concept of the ADCS remained the same and was already verified in space within the BEESAT-4 mission. Nevertheless, some modifications had to be applied to the control parameters of the pointing algorithms due to the lower angular momentum and torque of the used reaction wheels [120].

The simulations described in Section 5.1.2 were adapted to determine these parameters and analyze the maximum amount of time available for performing a three-axis stabilization. As expected, the reaction wheels are saturated after a shorter time period, with variations from 15 min to 5 h, depending on several variables, e.g. the angular rate of the satellite, the current and the desired quaternion and the position on orbit at the beginning of the experiment. According to the experiences with the GNSS200 (see Section 5.3.3) and the ADCS experiments performed with BEESAT-4 as described in Section 6.1.2 these values are sufficient for successful navigation experiments.

After the final integration all the components were tested. The correlation of the sensors to the satellite axes was validated for the entire chain of data flow on both paths, transmission and reception. Furthermore, the satellite was placed on an air bearing table. It was accelerated to $30^\circ/\text{s}$ on each axis individually and the ADCS was switched to Blind Damping Mode to verify the functionality of the mode and the magnetic coils. Moreover, each reaction wheel was commanded to its maximum rotation speed to estimate the dynamic capabilities of the ADCS for slew maneuvers and to validate the wiring.

All the tests were passed and the ADCS was ready for operations in space.

5.3.3 Ground Tests of GNSS

At first the EQM of the Phoenix was tested on the roof again, due to some new information from the experiments conducted in space with BEESAT-4 (see Section 6.1.3). The experiments revealed that only one or two satellites were tracked with Phoenix and the signal strengths were significantly lower than during the ground tests. Furthermore, one of the used GPS antennas was exposed to a total ionizing dose of 12 krad, during another radiation test. The outdoor tests were performed with the exposed antenna as well as a new one.

All the outdoor tests with the Phoenix receiver in May and September 2018 showed similar results. Using an antenna that was not exposed to radiation matched the results from the previous tests, prior to the launch of BEESAT-4, described in Section 5.1.3. The antenna exposed to a radiation dose of 12 krad did not deliver satisfactory results. In fact, not a single satellite was tracked, neither in May nor in September. During these experiments, the Phoenix receiver was reset at least 10 times. The setup was exactly the same, the only difference being the exchanged antenna.

All the tests performed with the Phoenix receiver, the orbit results of BEESAT-4 and the used antenna, together with the confirmed funding for BEESAT-9, led to the selection of a new GNSS antenna as well as the GNSS200 (see Section 1.2.2).

Prior to the first manufactured PDH (see Section 4.1.7) an adapter board was put together. To connect the GNSS200 properly, a socket with pogo pins was used. Figure 5.7 displays the adapter for the GNSS200.

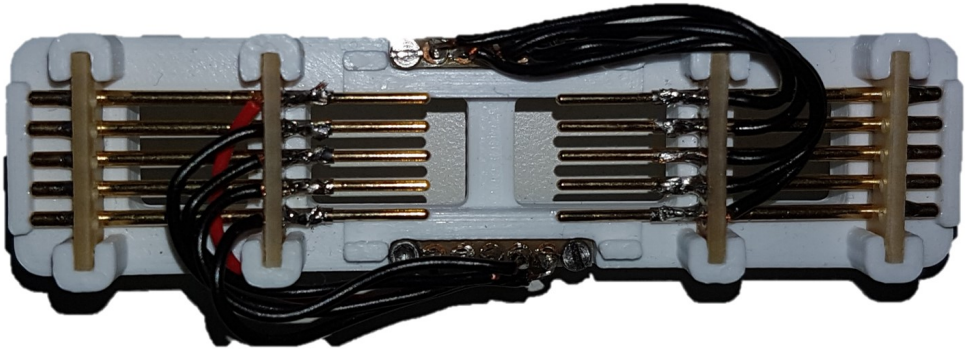


Figure 5.7: Adapter for the GNSS200 (built by Sebastian Grau)

In October 2018 the receiver finally arrived and the first test campaign was started. Basically, the experiments were performed to obtain results as summarized in Table 5.2 about the clock fix, the TTFF, the C/N_0 depending on elevation and the number of tracked satellites. Furthermore, the necessity of a “warm start” was evaluated. The signal strength is provided as described for the Phoenix receiver in Section 5.1.3, but it is not recommended to compare the values from different receivers, since various producers set the starting point differently [181].

The test campaign showed very promising results. A signal from a GPS satellite was received within less than five seconds on every test run. It could be validated with the updated current GPS time. Furthermore, a 3D-navigation fix was achieved within 20–40 s, being faster than described in the data sheet with up to 90 s [53]. This entailed the decision to not implement a “warm start”, which delivers a 3D-navigation solution within less than 30 s according to the data sheet [53].

The analysis of the individual channels and the C/N_0 revealed, that six satellites were tracked within 40 s, more than required to calculate a 3D-navigation solution. During all test campaigns 10 satellites were tracked maximally and included in the solution. The C/N_0 ranged from 30 dB-Hz to 51 dB-Hz depending on the elevation, indicating a GPS signal strength of up to -123 dBm at the receiver. Generally, higher elevations lead to a higher C/N_0 . Nevertheless, the radiation pattern of the antenna (see Figure 4.14) has to be taken into account as well, leading to comparable results, if the azimuth is considered accordingly.

Two more test campaigns were conducted, one with the first development board of the PDH in December 2018 and a second one after the final integration in

May 2019, just before the delivery of the flight model to EXOLAUNCH. Both campaigns showed similar results and moreover the entire telecommand and telemetry handling of GNSS data was validated, successfully concluding all ground tests of the GNSS200 (see Table 5.6).

Table 5.6: Test results for GNSS200

Test Case	Command Chain	Clock Fix	TTFF	Peak C/N_0	Tracked Satellites
FM test "cold start"	Yes	2–5 s	20–40 s	51 dB-Hz	> 10

5.3.4 Calibration Campaign

The implemented sensor types of BEESAT-9 for attitude determination and control were the same as BEESAT-4. Just the number of different sensors increased to expand the portfolio of space-qualified MEMS sensors. Moreover, a more sophisticated calibration concept was tailored to the needs of BEESAT-9 by students during a lecture [182, 183, 184], determining further parameters compared to BEESAT-4 (see Table 5.4). All the calculated parameters are displayed in Table 5.7. Results from the campaign were presented by the author in November 2019 [185].

Table 5.7: Calibration parameters of attitude sensors on BEESAT-9

Sensor type	Polynomials	Offset	Scale factor	Orthogonality factor	Temperature dependency
Sun sensors	✓	-	-	-	-
Magnetic field sensors	-	✓	✓	✓	-
Gyroscopes	-	✓	✓	✓	✓(Offset)

Sun Sensors

The calibration campaign for the sun sensors was not modified compared to BEESAT-4. Measurements were taken as described in Section 5.1.4 and in

[182]. Afterwards, the data was processed and the parameters for a third-degree polynomial were determined and added to the flight software. A comparison with polynomials of fourth and fifth degree showed no improvement, thus these options were discarded. Figure 5.8 show two full rotations on the rotary table before and after the calibration.

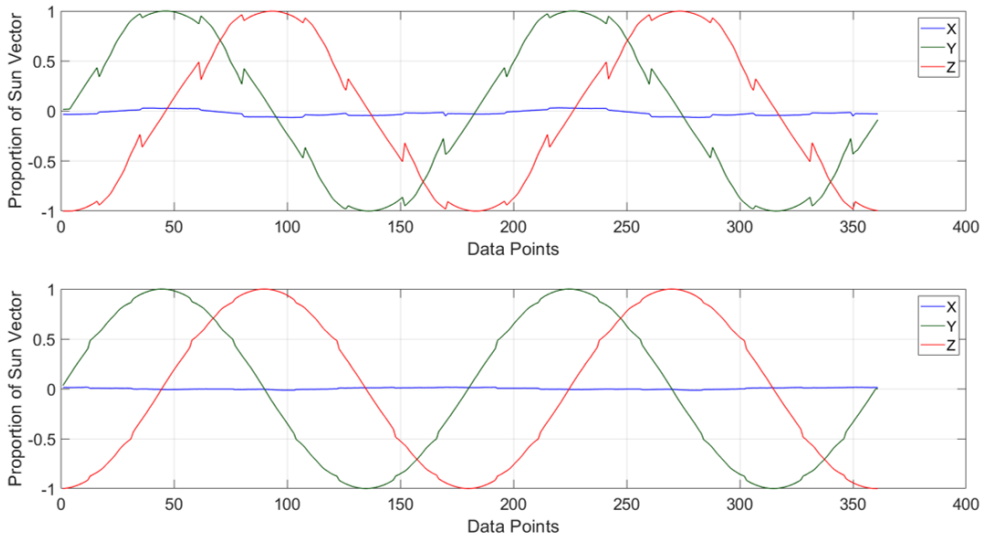


Figure 5.8: Sun sensors of BEESAT-9 before (top) and after (bottom) calibration (adapted from [182])

The transitions between the sensors are clearly seen in the jumps of the sun vector. Even after calibration, the transition is not ideal, but the error is less than one degree. Furthermore, the proportional part of the vector in the Y-axis is set closed to zero.

Gyroscopes

The baseline for the calibration of all six gyroscopes remained the same as for BEESAT-4 (see Section 5.1.4). Placing the satellite in a thermal chamber to determine the offset for each axis within a temperature range from -10°C to 30°C . For the offset, a square correlation seemed sufficiently to represent the results accurately.

Additionally, the satellite was placed on a rotary table, which was set to different angular rates between $-30^\circ/\text{s}$ to $30^\circ/\text{s}$ to determine the scale factors, orthogonality and alignment errors. An algorithm was developed by Bartels [184] to determine the transformation matrix.

The overhead produced by this calibration was not obligatory for the reception of GNSS signals, but necessary to use an array of four gyroscopes to provide a virtual sun vector during eclipse as described by Binder [129]. Using the QUEST algorithm for attitude determination, this vector is indispensable to perform three-axis stabilization of the satellite.

After the calibration, the results of the gyroscopes improved significantly, especially the fusion of the four new sensors (see Section 6.2.2).

Magnetic Field Sensors

For BEESAT-9, the strategy for the determination of all the calibration parameters was renewed (see [183]). On the one hand a setup was looked for to maintain the satellite in the laboratory rather than calibrating at an external facility. This included the second reason, having unfolded antennas during the calibration, since this was considered one of the reasons for insufficient results for BEESAT-4 (see Section 5.1.4). Nevertheless, all the desired calibration parameters remained the same compared to BEESAT-4.

The satellite was placed inside a Helmholtz Cage and a preprogrammed magnetic field was generated. All the measured values were put in an algorithm to determine the calibration parameters. Those were included in the flight software and a validation program was executed.

After the calibration the measured values for all seven sensors were within the error margin of 1 000 nT. For the new sensors, introduced for BEESAT-9 the results were even within 200 nT to the reference fluxgate magnetometer.

However, once the satellite was launched into its orbit the sensors had to be re-calibrated again with the algorithm proposed by Springmann [176] (see Section 5.1.4). The results of both calibrations can be found on Table 5.8.

Table 5.8: Calibration parameters of magnetic field sensors on BEESAT-9

Offset parameter	Berlin [nT]	Orbit [nT]
MFS0 X	−3 512	−62 426
MFS0 Y	−5 054	22 851
MFS0 Z	35 280	6 047
MFS1 X	−27 364	11 057
MFS1 Y	−10 003	−29 090
MFS1 Z	30 493	−1 447
MFS2 X	9 606	28 731
MFS2 Y	−47 520	−62 110
MFS2 Z	−10 062	−30 753

5.3.5 Environmental Test Campaign

To fulfill the requirements of the launch provider and ensuring the correct integration of the satellite, several test were conducted. The test levels were partially adapted to the loads expected from the dedicated launcher, a Soyuz rocket. Furthermore, the satellite went through thermal cycles under vacuum conditions on acceptance level. Just ahead of the launch, the check out of the satellite took place in Vostochny, Russia.

Radiation Tests

After the launch of BEESAT-4, the selected GPS antenna was exposed to a radiation dose of 12krad, the expected amount within a year including a 20% margin. In Section 5.3.3 it was mentioned, that the antenna failed to receive the signals in a sufficient strength. It seems that the LNA mounted to the antenna is not reliable for space applications.

The antenna was replaced, but due to the short time between kick off and launch and limited financial resources, no radiation test was conducted during the verification campaign of BEESAT-9. Besides the GNSS antenna, only the new magnetic field sensors were never exposed to radiation by the TU Berlin. The

other subsystems and components were tested by the developers, e.g. GNSS200 or other projects, e.g. pFDA.

Vibration tests

According to the specifications by EXOLAUNCH [186], a vibration test was conducted. The criteria to pass the test was the same as for BEESAT-4 (see Section 5.1.5), but the setup slightly changed. The sinusoidal vibration test was not executed, due to very low loads on the Soyuz rocket compared to other launchers. Instead a sine burst test was performed to simulate quasi-static loads. Moreover, the test loads during the random vibration test were separated into two different profiles, matching the expected profiles during the launch.

All the tests were passed successfully, with a FFT following after each tested axis. The resonance survey showed that the eigenfrequency remained within a margin of less than 10 %.

Thermal Vacuum Test

A thermal vacuum test was conducted for BEESAT-9 according to the specifications from Astro- und Feinwerktechnik GmbH. Some modifications, as described in Section 5.1.5 were applied.

A FFT was followed by one cycle within the non-operating temperature range. Afterwards, three cycles were programmed, while the satellite was operational. Each dwell time of two hours was followed by a functional test.

No anomalies occurred during the entire test procedure and the thermal vacuum test was passed successfully.

5.3.6 Check Out and Launch

At the end of May 2019 the satellite BEESAT-9 was integrated into its deployer at the clean room facilities of EXOLAUNCH in Berlin. It was shipped to Vostochny, Russia afterwards and taken out at the launch site three weeks later for the check out campaign. All the subsystems were tested and the telemetry was checked for plausibility. Similar to BEESAT-4, there was no option to test the GNSS

receiver. Nevertheless, all the tests were passed successfully. A software upload to all the slots of OBC and PDH, followed by another FFT, concluded the check out. In a final step, the satellite was integrated into the deployer again, which was then attached to the fairing of the launch vehicle. On 2019-07-05 the satellite was launched into its dedicated orbit and was deployed around four hours later, concluding a successful launch campaign.

5.4 Conclusions from Verification Campaign of BEESAT-9

For BEESAT-9 the PDH was re-developed, integrating a new GNSS receiver, several attitude sensors and a pFDA. Together with parts of the EQM and flight spare subsystems of BEESAT-4, a new flight model evolved.

Several simulations were performed to adapt the control algorithms of the ADCS due to the different reaction wheels. Further tests showed the proper implementation of all actuators and sensors.

Initially the EQM of Phoenix underwent another test campaign, but a decision towards the GNSS200 was taken early in the mission, because of its low power consumption and fast TTFF. The performance was tested in outdoor setups and the results concluded that it is well suited for a 1U CubeSat.

All the attitude sensors were calibrated following newly developed methods tailored to BEESAT-9. The magnetic field sensors showed similar problems and required a re-calibration on orbit. Sun sensors and gyroscopes showed high accuracies after calibration.

According to the specifications of the launch provider, vibration and thermal-vacuum tests were conducted before the satellite was sent to Vostochny, Russia for the check out ahead of the launch. Afterwards the satellite was ready for mission operations and it was concluded that the objectives of BEESAT-9 could be fulfilled on orbit.

6 Mission Operations of BEESAT-4 and BEESAT-9

On the day of their deployment the satellites were operated via a ground station for the first time. Immediate responses followed, indicating a successful execution of the first part of the LEOP procedure (see Section 6.1.1 and Section 6.2.1). The second part was quickly finished, starting the commissioning of the satellites. Once all subsystems were considered operational, the first experiments were conducted.

Both satellites focused on attitude control and navigation experiments. For BEESAT-4 a three-axis stabilization was the precondition for navigation experiments, which was confirmed during the operational period (see Section 6.1.3). Operating the GNSS200 on BEESAT-9 turned out to be easier than expected. Early in the mission it was determined, that a three-axis stabilized satellite was not required to obtain navigation fixes (see Section 6.2.3). Next to the common experiments, an inter satellite link between BEESAT-4 and BIROS was tested.

Mission operations of the satellites will be presented individually, starting with BEESAT-4 [187].

6.1 On-Orbit Experiments of BEESAT-4

Obtaining a navigation fix with the Phoenix receiver to acquire accurate position and velocity data of the satellite was the first part of the Precise Position and Orbit Determination (PPOD) package, followed by orbit determination on the ground, using the navigation data. Several requirements had to be met beforehand, starting with a successful commissioning of the satellite.

Afterwards, many experiments were executed to obtain a three-axis stabilized satellite for any desired attitude. Several navigation experiments were already conducted during this process and intensified once the ADCS was fully operational. Nevertheless, a navigation fix was not acquired with the Phoenix receiver, due to several reasons (see Section 6.1.3).

Initially the Inter Satellite Link (ISL) was planned to be used during the AVANTI experiment. It was meant for the exchange of GPS data from BEESAT-4 to BIROS via N-Link. Due to several setbacks in the operation of the N-Link module, the ISL was first tested in May 2017, long after the AVANTI experiments were finished in October 2016. Since then several flybys were used to operate the ISL, as listed in Table 6.3.

A general overview of the operations with BEESAT-4 summarizes the results and concludes this section.

6.1.1 LEOP and Commissioning

LEOP and commissioning were described by Kapitola and the author at the IAA symposium in Berlin [188]. During the LEOP, a hard coded list of time tagged commands is executed on the OBC, which has been kept very simple and starts with commanding the satellite to store standard telemetry from all subsystems with a sample rate of 10 s. It also includes the unfolding of the UHF antennas, with the execution time depending on the orbit. This procedure requires around 6 W for each antenna, thus the batteries need to be charged on orbit beforehand. In case of BEESAT-4 an extended period within the deployer was caused by the additional time to commission BIROS, thus it stayed inside the SPL longer than originally planned. Even though the satellite was turned off, the batteries were expected to be discharged steadily. This is due to the charge regulator which consumes a current of several μA . Finally, an analysis showed that a period of one entire sun phase of 65 minutes is sufficient before the command is executed in the worst case of a three-month period inside the deployer. Once the antennas are deployed, the beacon is switched on. Afterwards the satellite transmits its call sign every 40 s. Before the first ground station pass over Berlin, several recordings of the beacon were made over the Netherlands, Brazil, Australia, USA and Japan. In Table 6.1 the events of the LEOP are chronologically summarized.

Within the first ground station contact the general status of the satellite is checked. Afterwards, the commissioning phase started. A FFT was performed within the first days, including all the redundant systems. Generally, all the components worked as expected. Nevertheless, re-calibration of the magnetic field sensors and the unreliable attitude control needed to be taken care of for a three-axis stabilized satellite. Regardless, the commissioning phase was completed within a few days, since these issues were considered part of the mission objectives.

Table 6.1: Events during LEOP of BEESAT-4

Time [UTC]	Event	Outcome
2016-06-22 03:30:00	Launch	BEESAT-4 in dedicated orbit
2016-09-09 11:00:15	Deployment by BIROS	BEESAT-4 switched on
2016-09-09 12:40:25	Antenna Deployment	Antenna unfolded
2016-09-09 12:40:25	Switch to Beacon Mode	Beacon transmitted every 40 s
2016-09-09 12:41:37	BEACON received	BEACON recording sent from the Netherlands
2016-09-09 14:06:07	First pass over Svalbard	Telemetry received

6.1.2 Orbit Experiments with the Attitude Determination and Control System on BEESAT-4

On-orbit verification of the ADCS was split into two sections, the determination and the control of the satellite. Based on the QUEST algorithm, which requires four vectors (namely the inertial and body-fixed sun and magnetic field vectors, see Figure 4.4), the attitude determination was addressed first.

Attitude Determination

The sun and the magnetic field model were already verified on the ground and did not need further testing. Thus, the focus was put on the sensor measurements.

For a coarse validation of the sun vector, it was compared to the “sun vector”, estimated from solar currents of the solar cells. It showed that the sun vector algorithm was generally working properly and the threshold, to exclude sensors exposed to Earth albedo or reflections, was set to a reasonable level. Furthermore, the modifications particularly on the aperture plate of the sun sensors, showed improvements and removed the discontinuous drops which were seen on BEESAT-2 [27, p. 33]. These drops were induced by reflections from the aperture plate at high entrance angles of more than 50°.

The magnitude of the magnetic field vector of each sensor was compared to the magnitude of the IGRF model. As described in Section 5.1.4 a re-calibration was necessary. A dataset of magnetic field measurements over the period of one orbit

with a sample rate of five seconds was stored and downloaded via a ground station. A least-square algorithm applied from [176] was used to calculate the offsets and scale factors. The results (see Table 5.5) were uploaded to the parameter section of the software to be used on board.

For further verification, the angle between the sun and the magnetic field vector was analyzed, as suggested by Binder [189]. A data set for an entire sun phase was taken, including the two inertial and the two body-fixed vectors. This is the input data of the QUEST algorithm, thus accurate measurements lead to an accurate attitude determination. The calculated quaternion, representing the attitude of the satellite, is a transformation between the inertial and body-fixed coordinate systems [190]. Unit vectors were formed from the inertial and body-fixed sun and magnetic field vectors and the angles between each pair were calculated with the equations:

$$\Theta_i = \arccos(\vec{v}_{sun}^{ECI} \cdot \vec{v}_{mag}^{ECI}) \cdot 180/\pi \quad (6.1)$$

$$\Theta_{bf} = \arccos(\vec{v}_{sun}^{BF} \cdot \vec{v}_{mag}^{BF}) \cdot 180/\pi \quad (6.2)$$

Ideally, the angles should be the same, but due to noise in the measurements, calibration errors and inaccuracies in the models, there will always be a discrepancy. In Figure 6.1, the difference between the two angles is displayed.

The error remains below five degrees within the measured period of 35 min. From these calculations it can be assumed that the attitude determination is functional, but flawed with some errors. The main contribution to inaccuracies come from the magnetic field sensors. On one hand the values include noise of at least 300 nT and on the other hand the on-orbit calibration was not ideal. The difference of the magnitude between the IGRF and the sensor measurements remained between -3000 and 3000 nT. A small error was induced by the sun sensors as well. It can be seen in Figure 5.8 that the transition between different sensors is not flawless. These inaccuracies derived from the calibration method, which handles each sensor separately.

Compared to the sensor measurements the errors from the sun and the magnetic field model can be neglected. For the sun model it is assumed that updated TLEs are used once an accurate attitude determination is required. The position error of the satellite remains within 1 km in that case (see Section 7.2), tiny compared

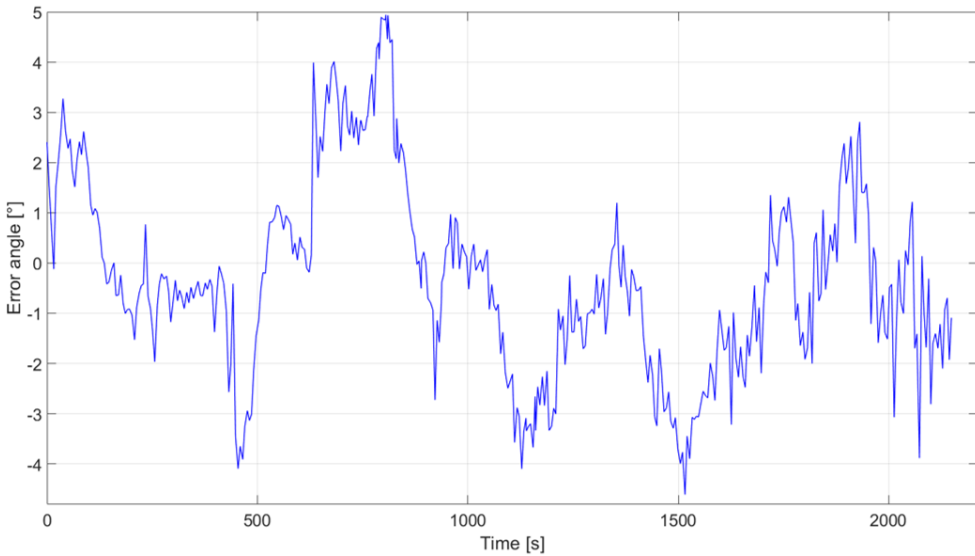


Figure 6.1: Difference of angles between inertial and body fixed frames

to the distance to the sun. Several satellites analyzed the IGRF model from an altitude of 280–850 km and Matteo and Morton summarized the results [191]. For an orbit of 510 km more than 99.5 % of the values are within 200 nT. Furthermore, no jitter is induced by the two models.

In the last verification step the attitude data was compared to an image taken by the camera. Figure 6.2 shows the field of view of the camera with attitude telemetry of BEESAT-4.

The yellow frame shows the frame of the actual picture. Compared to the green frame, which displays the estimated quaternion, representing the attitude, an error of 4.8° occurs. Another frame, displayed in red, represents the desired attitude. The difference to the yellow frame is 2.8° and represents the error of the control algorithm. Analysis of several pictures showed similar errors, with a range between one and four degrees.

All the verification steps confirmed that the attitude determination is working properly on BEESAT-4, although inaccuracies from known sources were included. Filtering the magnetic field data to remove the noise and a more advanced calibration algorithm to lower the offsets could improve the accuracy. All the

analyzed experiments of the attitude determination showed a maximum offset of 5° . Once it was verified the focus was put on the three-axis stabilization and the Phoenix receiver.



Figure 6.2: Comparison of field of view of the camera

Attitude Control

There are several control modes implemented on BEESAT-4, as displayed in Figure 4.8. Except the Blind Damping Mode, all of them use the reaction wheels as actuators. During the commissioning phase the general functionality was tested. The Six Minutes Wheeltest was executed, following a hard coded profile for all three wheels with different accelerations and rotation speeds. All three wheels followed the preset profile and the power consumption was nominal. Furthermore, the magnetic coils were switched on in both directions, comparing their measured currents to those taken during the verification campaign on the ground.

Afterwards, the modes were tested. First of all, the Damping Mode decreased the angular rate to $\vec{\omega} = 0.3^\circ/s$. Theoretically, it is meant to damp the satellite to zero, but due to the noisy gyroscopes, the remaining angular rate can be explained. External disturbances, mainly the magnetic field, cause the reaction wheels to saturate slowly. Once the maximum rotation speed was reached, the ADCS was

switched to Suspend Mode, stopping the wheels to rotate and transferring the angular momentum to the satellite. At that point the ADCS is switched to the Blind Damping Mode to reduce the angular rate of the satellite, using the magnetic coils. A time modulated B-Dot controller was used, which activates the magnetic coils in all three axis simultaneously. The dipole momentum of the coils cannot be adjusted, the coils are either on or off. To form the required vector, each axis is switched on for different durations within one duty cycle. It is the fastest option of the three modes, but has a high peak power consumption (see [147, 188]).

For BEESAT-4 the Blind Damping Mode was used to damp a maximum angular rate of $\vec{\omega} = 25^\circ/\text{s}$.

The highest measured angular rate of $\vec{\omega} = 45^\circ/\text{s}$ for BEESATs was damped on BEESAT-2. The result was presented by Kapitola and the author [188] and is displayed in Figure 6.3.

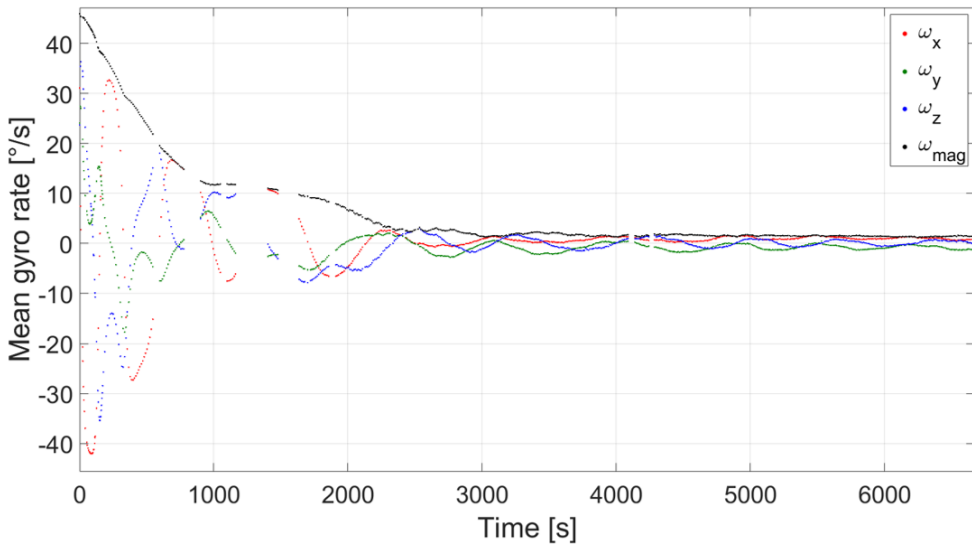


Figure 6.3: Angular rates during Blind Damping Mode (adapted from [188])

After roughly 3000s the angular rate stays below $\vec{\omega} = 2^\circ/\text{s}$. The experiment continued, decreasing the angular rate to less than $\vec{\omega} = 1^\circ/\text{s}$.

Theoretically, the physical possibilities would allow for angular rates to a minimum average of $\vec{\omega} \approx 0.12^\circ/\text{s}$, due to the rate of change of the magnetic field. At the poles it changes quicker than at the equator, thus the minimum is variable.

Getting near the minimum would require a filter of the noisy inputs from the gyroscopes and the magnetic field sensors. Additionally, the magnetic field sensor measurements should be integrated and averaged over time, dependent on the present change rate of the external magnetic field, as suggested by Binder [129]. This avoids generating control values that are more driven by the sensor than the change of the field. Nevertheless, the performance is sufficient to fit the needs of BEESAT-4, reducing the angular momentum of the satellite, thus neither the filter nor the integration algorithm were implemented.

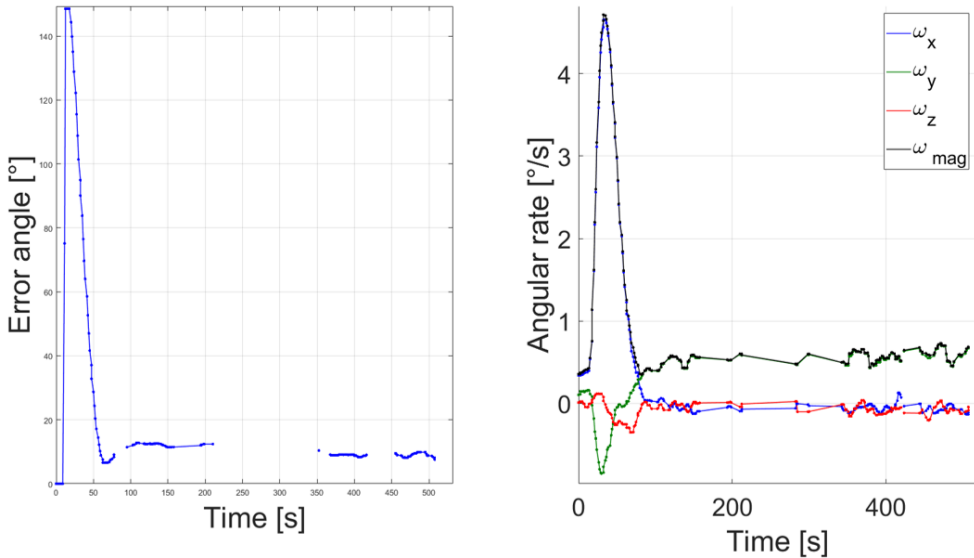


Figure 6.4: Control error angle and angular rates of BEESAT-4 during zenith pointing [170]

Modes with three-axis stabilization were tested accordingly. First of all the Slew Mode was verified. As described in Section 5.1.2, at first it only worked for a unit quaternion $\vec{q}_{des} = (0,0,0,1)$. These experiments were presented by the author in 2016 [169], showing the basic functionality of three-axis stabilization at an accuracy of 3° . Several experiments also showed successful three-axis stabilization for random desired quaternions, calculated by the Zenith and Nadir Pointing Mode. Nevertheless, it was not reliable, due to problems induced by the QUEST algorithm, whenever the scalar part of the quaternion switched to a negative value. It was switched back by the algorithm, but the allocation to the attitude control caused an error. Furthermore, the calculations of the error quaternion were not reliable,

until further software was uploaded to fix the ADCS. After the third upload, that contained changes of the ADCS, in August 2017 the reliability of the three-axis stabilization was brought to 100 %. Analysis of all conducted ADCS experiments show an error angle $\alpha_{err} = 3^\circ$ to 7° . In Figure 6.4 the performance of an attitude experiment is shown.

In this experiment, the attitude error was more than $\alpha_{err} > 150^\circ$ in the beginning. After 90 s the satellite finished its slew maneuver with a maximum angular rate of $\vec{\omega} = 4.5^\circ/\text{s}$ and settled at an error angle $\alpha_{err} = 5^\circ$. Results from the ADCS were presented by the author in 2017 [170].

During the operations of BEESAT-4, the experiments were evaluated and several aspects were addressed to increase the performance of the ADCS. The control parameters of the attitude modes were modified and the quaternion feedback controller was extended with an integral part to lower the final error angle. It was used for all three-axis stabilized maneuvers and the control law, introduced in Section 4.1.1 was adapted to:

$$\vec{u}_{slm} = I_{sat} \cdot (-k_{slm} \cdot \vec{q}_e - c_{slm} \cdot \vec{\omega} - i_{slm} \cdot \vec{q}_e) \quad (6.3)$$

$$\text{with } k_{slm} = 0.007 \text{ and } c_{slm} = 0.12 \text{ and } i_{slm} = 0.000012$$

Using these parameters the attitude control was stable and reliable to the mentioned accuracy. Furthermore, the calibration parameters of the gyroscopes and the magnetic field sensors were adapted several times. Averagely, this resulted in improved results.

Conclusions from ADCS experiments of BEESAT-4

After several iterations, the ADCS was fully functional. The attitude determination worked constantly during the sun phase at a sufficient accuracy. Reducing the angular momentum of the satellite with the Blind Damping Mode was always successful and the three-axis stabilization was brought to a performance that allowed for GPS experiments and the usage of the camera in a dedicated manner.

Nonetheless, several conclusions were made regarding the accuracy and further improvements of the ADCS. Especially MEMS sensors were not as accurate as their

bigger counterparts, e.g. fiber-optical gyroscope or fluxgate magnetometer, during the development of BEESAT-4. Even with more advanced sensors a lot of effort has to be invested into calibration, filtering and sensor fusion to achieve similar results (see [129] and Section 6.2.2). For the attitude control, more advanced and complex algorithms were suggested for three-axis stabilization and together with less noise, better calibration of the sensors, the hardware of BEESAT-4 could theoretically achieve an accuracy of 1° , given the performances of other ADCSs from TU Berlin with similar sensor types, e.g. S-Net [129].

6.1.3 GPS Operations

Before the execution of GPS experiments, the command chain was verified. For the “cold start”, the receiver is switched on and then it starts to output the data messages F40 and F48 in WinMon Format (see Appendix A [31, p. 66 and p. 73]). These messages were stored to the telemetry flash memory and successfully transmitted to the ground.

For the warm start the procedure follows the instructions as described in detail in [31, p. 21].

- Activate power line
- Send current GPS time
- Send TLEs of the satellite
- Send and load almanac of GPS satellites
- Activate orbital aiding
- Set elevation mode
- Set Doppler window

Every command is acknowledged with an output message which is stored on the flash memory of the PDH. Procedures for the “cold and warm start” were verified on orbit and the satellite was ready for navigation experiments.

Nominal experiments with the receiver were based on a three-axis stabilized satellite, pointing its GPS antenna towards zenith. As described in Section 6.1.2, a reliable Zenith Pointing Mode was only available after nearly one year of on-orbit operations. Thus, the strategy was adapted beforehand.

GPS without Zenith Pointing

Before commanding a “warm start” of the Phoenix receiver, the angular rate of the satellite was minimized with the Blind Damping Mode. During the experiment, the Damping Mode, using the reaction wheels, was used to keep the satellite in a stable position.

Two problems occurred from this strategy. For the Damping Mode, one noisy MEMS gyroscope was used as a direct input to the following control algorithm.

$$\vec{u}_{dpm} = I_{sat} \cdot c_{dpm} \cdot \vec{\omega} \text{ with } c_{dpm} = 0.114 \quad (6.4)$$

Although it reduced the angular rate to $\vec{\omega} < 0.5^\circ/\text{s}$, it was never zero. Given the fact, that the “warm start” requires more than three minutes, according to the experiments performed with BEESAT-4 on the GPS simulator (see Section 5.1.3), the angular rate needs to be at approximately $\vec{\omega} < 0.1^\circ/\text{s}$.

At the mentioned rate of $\vec{\omega} = 0.5^\circ/\text{s}$ the satellite turns up to 90° in three minutes, hence having a different field of view with other GPS satellites in sight. An angular rate of $\vec{\omega} = 0.1^\circ/\text{s}$ would reduce the change of the FOV to 18° . Still, it was just an assumption, that a lower angular rate would lead to a successful “warm start” and was not tested, due to the limitations of the accuracy of the gyroscope.

A second issue with the Blind Damping and the Damping Mode entails from their properties. Both modes simply lower the angular rate, without any dedicated attitude, thus the satellite could end up pointing the GPS antenna towards Earth.

The planning, execution and retrieval of the experimental data took between two and three weeks. Afterwards, the data was evaluated to improve the performance of the next try. Due to these long periods, only eight experiments were performed, which executed the “warm start” correctly.

Phoenix received signals from GPS satellites, which was confirmed by an updated GPS time and the dump of a received GPS almanac into the storage of the PDH. The Phoenix receiver did not include any GPS satellite into the navigation algorithm during any experiment. During these experiments the C/N_0 was not recorded, thus no further analysis can be done regarding the “lock status” and the assignment of GPS satellites to the individual channels. In Table 6.2 the results of the experiments with Phoenix are summarized.

Once the ADCS was fully functional the strategy was changed and the Zenith Pointing Mode was used for further experiments.

GPS with Zenith Pointing

Over a time period of three months, from September to December 2017, another campaign of navigation experiments was executed. The satellite was pointing zenith with the GPS antenna, while the Phoenix receiver performed a “warm start”. During these experiments a maximum of two satellites were tracked by the receiver and included into the navigation algorithm. Analysis of the extended data, particularly the individual channels, confirmed, that the receiver partially included GPS satellites within its field of view. Nevertheless, the C/N_0 values were low, compared to the ground tests. It also showed, that further satellites were “code locked”, but their status never changed to “frame lock” (see Section 5.1.3).

Since there was no possibility to change the setting of the selected satellites, analysis was carried further and the “locked” satellites were investigated. Including the attitude data of BEESAT-4, the elevation of the GPS satellites above the GPS antenna was analyzed. In Figure 6.5 the elevation is displayed over a time period of 35 min.

The two satellites above 60° elevation are tracked by Phoenix for around eight minutes. Afterwards, the signals are lost, at an elevation of $35\text{--}40^\circ$. During this time the C/N_0 varies from $36\text{--}38$ dB-Hz for these two channels. All the other channels remain at the standard setting of 30 dB-Hz, even though one of the GPS satellites with an elevation higher than 40° is chosen by Phoenix as well. Some of the satellites randomly had a “code lock”, even though the C/N_0 did not exceed the default level. Including the “code locked” channels, the total number of acquired satellites passed the minimum of four to generate a navigation solution, but as mentioned before, these channels are not included for accuracy reasons.

The overall selection of satellites seems unreasonable, since some of them are at an elevation below 0° while others with higher elevations are not included. It did not improve further during the experiment, which continued another 25 min. Three more satellites reached an elevation of up to 80° , but none is selected by Phoenix. A manual assignment of satellites to dedicated channels is meant to be used for factory testing and not on orbit ([31, p. 21]), thus was not implemented.

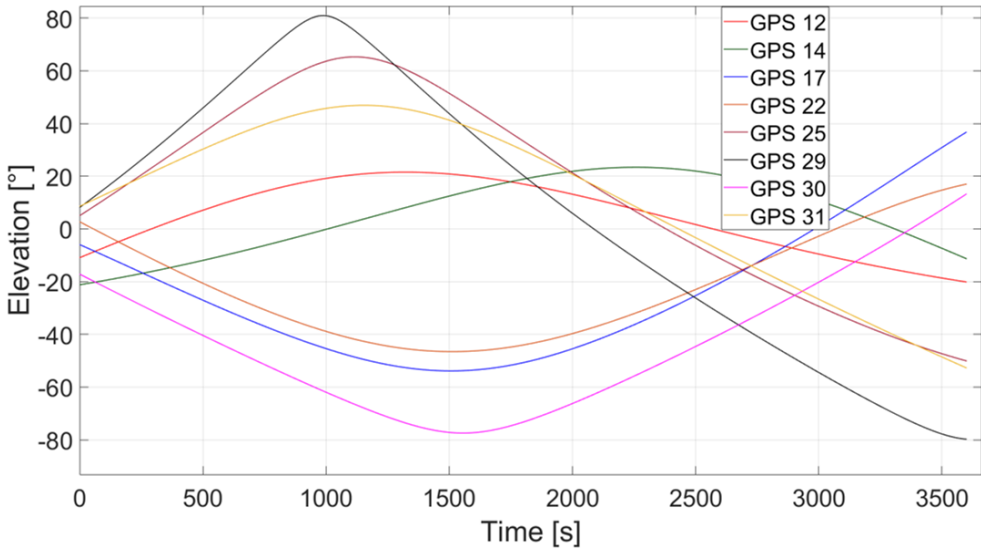


Figure 6.5: Elevation of GPS satellites over the antenna of BEESAT-4

For all the executed experiments time slots were chosen with many GPS satellites at a high elevation towards the GPS antenna. Simulations were run on STK to find the best availabilities. The outcome remained the same for all the experiments within the mentioned three-month period. Phoenix was able to track one or two GPS satellites for several minutes, but never “frame locked” four satellites for a navigation solution.

On-orbit experiments came to a hold, due to a “GPS End-of-week Rollover” in the beginning of January 2018. It occurs due to the representation of the GPS time in GPS weeks and GPS seconds of week. For the weeks 10 bit are assigned which last for nearly 20 years. Afterwards the counter is set to zero. It was based to the 1980-01-06 00:00 UTC and the Rollovers occurred in August 1999 and April 2019. Usually the GPS receiver take care of this issue themselves [192].

For Phoenix, a time frame had to be defined for operations. It was set from 1998 to 2018. An option to reset the receiver to a time frame from 2013 to 2033 was not available for BEESAT-4, since Phoenix could not be updated [193]. The only way to solve the problem was a software update on the OBC and the PDH of BEESAT-4 itself, which was carried out in July 2018.

Afterwards, another navigation campaign was performed with more than ten GPS experiments. The results remained the same, with the average C/N_0 remaining low, the peak value at 38 dB-Hz and one or two tracked satellites during each experiment.

The biggest issues seemed to be the poor GPS satellite selection by Phoenix, additionally to the low C/N_0 of the individual channels. Compared to the values from the outdoor ground tests (see Section 5.1.3), the C/N_0 were significantly lower.

With the announcement of the launch of BEESAT-9 in June 2018, the focus was switched and no further actions were taken, regarding the GPS experiments on BEESAT-4.

Conclusions of GPS Experiments on BEESAT-4

Many iterations in the PDH software and adaptations to the acquisition strategy including further analysis of the received data did not lead to a successful operation of the Phoenix receiver on BEESAT-4. During experiments without a three-axis stabilized satellite, Phoenix was not able to “frame lock” a single GPS satellite. According to the analysis, the cause was the rotating satellite, although it was at a very low angular rate, which apparently was still too high to acquire GPS signals. Once the three-axis stabilization was reliable, during all the GPS operations, signals were acquired and GPS satellites were tracked. Nevertheless, the individual channels showed low C/N_0 . During the preparation of the BEESAT-9 mission, further tests were executed with the GPS antenna used for BEESAT-4 (see Section 5.3.3). It seems, that the low C/N_0 are caused by degradation of the LNA due to radiation. It is attached to the GPS antenna, thus exposed to radiation directly and not protected by any structural parts. Table 6.2 summarizes the results with the Phoenix receiver on orbit.

Table 6.2: Results of on-orbit experiments with Phoenix

Test Case	Command Chain	Clock Fix	TTFF	Peak C/N_0	Tracked Satellites
No Zenith Pointing	Yes	1–2 min	-	-	-
Zenith Pointing	Yes	1–2 min	-	38 dB-Hz	2

Generally, the Phoenix receiver is not recommendable for 1U CubeSats, due to its high energy consumption and long TTFF. It made operations complicated and did not allow for a huge amount of experiments in a short time period.

6.1.4 Inter Satellite Link

Initially planned to support the AVANTI experiment, the UHF ISL module N-Link was developed and integrated into BIROS. Its functionality was validated via the ground station of TU Berlin. BIROS followed BEESAT-4 until September 2017. Maintaining this formation required several propulsion maneuvers to align the orbits of both satellites. In Figure 6.6 the average distance of BIROS and BEESAT-4 is displayed.

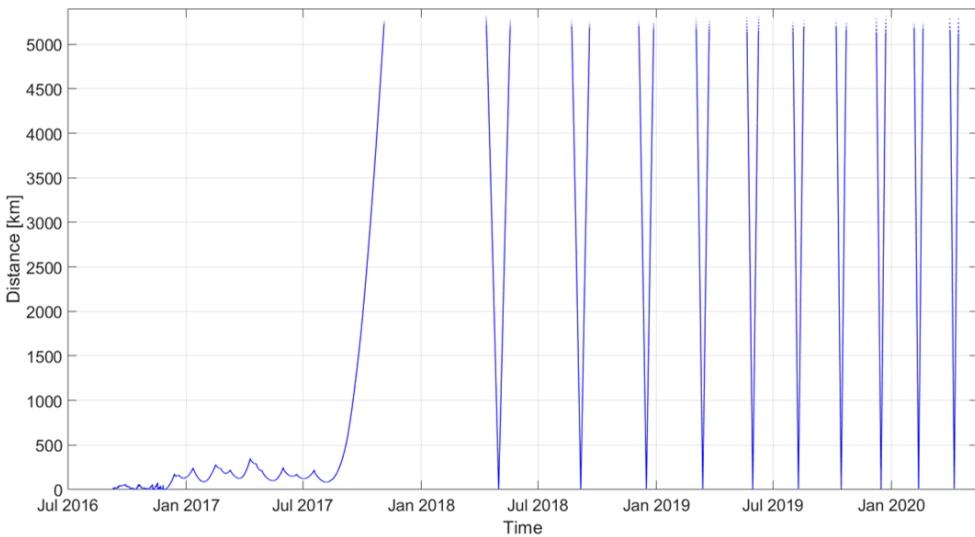


Figure 6.6: Distance between BEESAT-4 and BIROS for the entire mission time

Starting at a very low distance of a few kilometers after the deployment and during the AVANTI experiment, the distance was kept between 100–250 km for nine months. Once the maneuvers were stopped, the altitude of BEESAT-4 decreased faster compared to BIROS, which lowered the orbital period. This caused the satellites to drift away from each other, but flybys still occur on a regular basis. The first flyby occurred in May 2018 at a distance of 2 km, followed by nine

flybys until May 2020. The frequency of approaches of the two satellites increases constantly, together with a drift of the orbits, which results in larger distances for every experiment.

Several flybys of BEESAT-4, passing BIROS at low distances, were used to verify the ISL. In Table 6.3 all the events of N-Link or ISL are listed.

In [194] the author and Kapitola listed several milestones of the ISL. Starting with the commanding of N-Link from TU Berlin to the transmission of commands from BIROS to BEESAT-4. Commanding BEESAT-4 via BIROS, to execute a dedicated task and receiving the data afterwards via ISL on BIROS was the final milestone set in [194].

Using the “Flyby0819” experiment, the procedure of the ISL between BIROS and BEESAT-4 is disaggregated. One day before the flyby, telecommands are sent by the GSOC to switch on N-Link and enable data recording from its interface. Once the module is running, a time-tagged command list is uploaded via the TU Berlin ground station. This list includes only commands, that are meant to be executed on BEESAT-4. At the tagged time, the N-Link module transmits the command and it is immediately conducted on BEESAT-4.

The command sequence starts with a No Operation Command (NOP), i.e. the satellite is pinged, followed by a procedure for the attitude control. Using the reaction wheels, BEESAT-4 pointed its camera towards the Earth, as commanded by BIROS. Three pictures were taken of Bolivia (see Appendix D), stored on the PDH and partially transmitted to the PPU of BIROS. The experiment was successful and parts of one picture were downloaded from BIROS.

In Figure 6.7 the approach of BEESAT-4 can be seen for Flyby0819.

Due to the slightly different orbits, the closest approaches occur over the poles and the largest distances over the equator. According to Frese [195], an ISL from N-Link to BEESAT-4 has a positive link budget up to a distance of 100 km. Vice versa, the distance decreases to 40 km, due to the degradation of the UHF transceivers on BEESAT-4. The calculated distances are based on a transmission success of 95 %, thus commands and telemetry could be transmitted on larger distances occasionally.

All experiments confirmed the calculated budgets, even though, the transmission rate can be increased by a dedicated pointing of BIROS towards BEESAT-4. A detailed analysis of the ISL experiments has been done by Kapitola [160]. It

Table 6.3: Overview of all operations of N-Link and ISL

Name	Start Time	End Time	Minimal Distance [km]	Operations	Outcome
GS0517	-	-	-	Tests with Berlin ground station to BIROS	Commands received and telemetry sent
ISL0517	2017-05-09 09:21	2017-05-09 09:29	~ 115 km	Commands from BIROS to BEESAT-4	Successfully received and responded
GS0717	-	-	-	Software upload to N-Link	Successfully applied features for ISL experiments
Flyby0918	-	-	~ 2.3 km	N-Link off, BEESAT-4 camera experiment applied	Two pictures were taken of BIROS by BEESAT-4
Flyby1218	-	-	~ 3.5 km	N-Link off, BEESAT-4 camera experiment applied	14 pictures were taken of BIROS by BEESAT-4
Flyby0319	2019-03-13 22:00	2019-03-14 06:00	~ 6 km	BIROS sent NOPs	Inter Satellite Link successful
Flyby0519	2019-05-30 12:55	2019-05-30 21:55	~ 9.5 km	BIROS sent command list	ISL successful, Command List error
Flyby0819	2019-08-09 10:55	2019-08-09 16:50	~ 11 km	BIROS sent command list	BEESAT-4 captured images (see description)
Flyby1219	2019-12-15 18:35	2019-12-15 02:45	~ 12 km	BIROS sent command list	ISL successful, Command List error

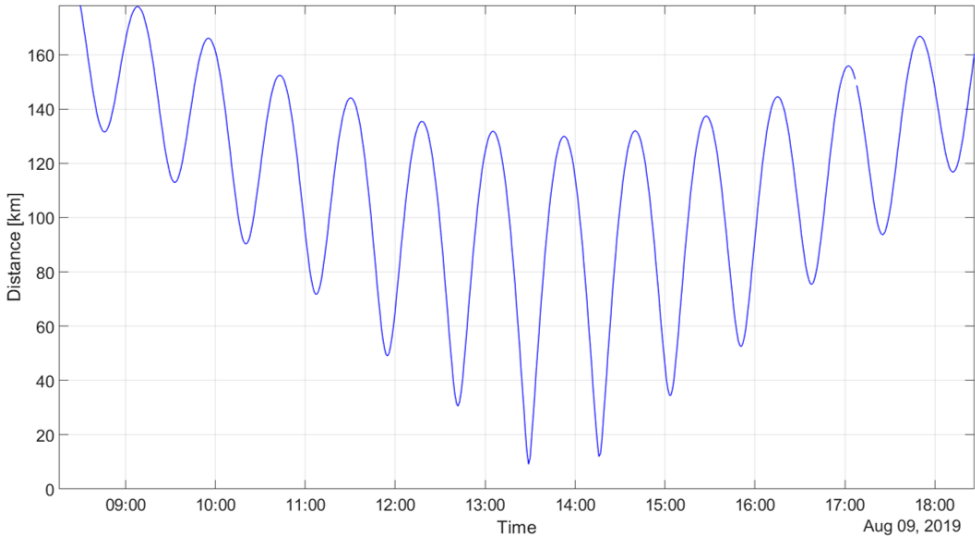


Figure 6.7: Approximation of BEESAT-4 to BIROS

included the attitude of both satellites, the antenna pattern and the data rate at certain distances.

Even though the ISL was not used to support the AVANTI experiment, all the milestones from [194] were successfully passed on “Flyby0819”. BEESAT-4 was completely commanded by BIROS, changed its attitude accordingly, took three pictures of Bolivia and sent them back to BIROS.

6.1.5 Conclusions from On-Orbit Experiments of BEESAT-4

Operations with BEESAT-4 started from the day of its deployment and were conducted daily via ground stations in Berlin, Germany, Svalbard, Norway, Buenos Aires, Argentina and San Martin, Antarctica. During the ADCS experiments 155 pictures (status of 2020-07-15) were downloaded (some shown in Appendix D). In Table 6.4 the statistics of the downloaded data is displayed, adding to a total data of 100.05 MB (status of 2020-07-15).

During the operations, a reliable three-axis stabilized ADCS was verified and constantly improved for determination and control. The ISL with BIROS was fully functional and further experiments are planned. Verifying the PPOD package was

Table 6.4: Operational statistics of BEESAT-4 including software uploads (SW-UL)

Ground Station	Passes	Frames	Data [MB]	SW-UL OBC/ADCS	SW-UL PDH
Berlin	3 667	199 351	95.8		
Svalbard	230	3 392	1.6		
Buenos Aires	308	4 972	2.4	8	1
San Martin	41	577	0.2		
DLR "BIROS"	4	105	0.05		
Total Data [MB]			100.05		
Housekeepings			47.4		
Debug			1.0		
ADCS			17.7		
GPS			1.8		
Pictures			32.1		

not fully successful, due to the lack of navigation data from the Phoenix receiver. Nevertheless, several conclusions, regarding the usage of Phoenix on a 1U CubeSat can be made.

Obtaining navigation data is theoretically possible and a duty cycle of 7 % can be realized on BEESAT-4 (see [126]). Most likely a navigation fix was not acquired due to the degraded LNA of the GPS antenna. Furthermore, the Phoenix receiver did not always choose the satellites with the highest elevation over the GPS antenna. A "select satellite" command to assign GPS satellites to individual channels could help to track them better, but it would not be feasible for nominal operation. Once a channel is manually overwritten with the select satellite command, Phoenix would not overwrite that channel automatically until further commanding. Thus, an implementation of the "select satellite" could only provide a short term solution for a navigation fix. Furthermore, the navigation algorithm of Phoenix should be changed for 1U CubeSats to include "code locked" satellites to the navigation solution to acquire a position faster.

The degradation of the LNA of the GPS antenna caused low values for C/N_0 , which resulted in only a few tracked GPS satellites. In recent years, new small antenna

modules were developed, some of them qualified for the space environment, which could solve this issue. Further problems resulted from the high TTFF compared to newer GNSS receivers. Regardless of the TTFF, most of the new receivers have a high energy consumption compared to the energy generation on 1U CubeSats (see Table 2.1).

Operations with BEESAT-4 are still ongoing and it is mostly used as an educational platform for student lectures. The satellite bus and the camera are still fully functional and operations are planned until it will burn up in the atmosphere in approximately five years. Since the project BEESAT-4 ended in March 2020, operations will be conducted mainly by the teaching assistants and the students.

6.2 On-Orbit Experiments of BEESAT-9

BEESAT-9 was developed within the same DLR funded project, thus the primary mission objective for BEESAT-9 remained the Precise Position and Orbit Determination (PPOD). Contrary to BEESAT-4 all the preconditions for PPOD were already fulfilled before the launch. This relates mostly to the fully functional ADCS, including the three-axis stabilization, which was verified in the predecessor mission.

Once the satellite was launched, the LEOP and commissioning phase were conducted to verify the correct function of all components. During the regular operations, navigation experiments were executed on a daily basis, being the focus of the on-orbit verification. Additionally, experiments with the ADCS were performed, including the new attitude sensors. Most of the attitude experiments were accompanied by the camera system to test the new optics.

An operational statistic of BEESAT-9 summarizes the results of the mission and concludes this chapter.

6.2.1 LEOP and Commissioning

In February 2020 the author and Kapitola [196] presented results from the first six months of operations of BEESAT-9, including the LEOP and commissioning of the satellite. For the LEOP the same hard coded list, implemented on the two predecessor missions, was used (see Section 6.1.1). One small modification was

made, regarding the latency of the antenna deployment. For BEESAT-9 the period inside the deployer was significantly smaller, which resulted in nearly no discharge of the batteries. Thus, the time was adapted to the dedicated deployment schedule, unfolding the antennas just one minute before the first pass over the ground station of TU Berlin. The entire procedure was executed flawlessly and the beacon was received from both transceivers during a low elevation pass with only 1° over the ground station at TU Berlin only 32 minutes after deployment. Telemetry was received within the follow-up passes. The events of the LEOP are summarized in Table 6.5

Table 6.5: Events during LEOP of BEESAT-9

Time [UTC]	Event	Outcome
2019-07-05 05:41:46	Launch	BEESAT-9 in dedicated orbit
2019-07-05 10:06:40	Deployment	BEESAT-9 switched on
2019-07-05 10:36:50	Antenna deployment	Antenna unfolded
2019-07-05 10:37:00	Beacon switched On	Beacon transmitted every 40 s
2019-07-05 10:39:20	First pass over Berlin	Beacon received twice at 1° elevation
2019-07-05 12:10:48	Second pass over Berlin	Telemetry received

Within two days, all the components of the satellite bus were successfully switched on and commissioned. The magnetic field sensors provided wrong data, due to calibration issues (see Section 5.3.4). A raw data set of all magnetic field sensors was recorded and transmitted to the ground station for recalibration. Afterwards, the new parameters were uploaded to the satellite and the ADCS was commissioned.

Together with the satellite bus, the payloads were tested from the first day. A picture was taken to ensure the functionality of the camera and the pFDA was switched on to check its telemetry. Furthermore, the GNSS receiver was operated just 12 h after the deployment of the satellite for a health check. Surprisingly, after only 30 s, a valid navigation solution was provided, while the satellite was tumbling at an angular rate of roughly $2^\circ/\text{s}$.

After two weeks, the satellite was fully commissioned and regular operations were started.

6.2.2 Orbit Experiments with the Attitude Determination and Control System on BEESAT-9

The ADCS of BEESAT-9 was fully functional after the recalibration of the magnetic field sensors (see Section 5.3.4). All sensors used for attitude determination and control were exactly the same models compared to BEESAT-4 in the beginning of the operations. The data of every magnetic field sensor, the gyroscopes and the sun sensors were verified during commissioning. Nevertheless, as described in Section 5.3.1, the reaction wheels had a lower torque and angular momentum than the ones of BEESAT-4. Adaptations to the control algorithm were applied according to the simulations (see Section 5.3.2) and showed promising results. After the first experiments, the parameters of the Slew Mode were modified to enhance higher dynamics, thus increasing the angular rate during slew maneuvers.

Table 6.6: Error angle of the control algorithm with old and new gyroscopes

Experiment	Error Angle	Gyroscope	Date
Nadir Pointing Picture of the Alps	6–7°	MAX21000 avg. Angular Rate	2019-07-22
Nadir Pointing Picture of Berlin	4–5°	MAX21000 avg. Angular Rate	2019-08-13
Nadir Pointing Picture of Malta	6–7°	MAX21000 avg. Angular Rate	2019-09-08
Nadir Pointing Picture of Malaga	3°	4 × BMG250 100 Hz avg.	2020-02-12
Nadir Pointing Picture of Dubai	2°	4 × BMG250 100 Hz avg.	2020-02-15

One objective was the technology demonstration of new gyroscopes and magnetic field sensors. Both sensor arrays showed accurate results during the calibration campaign, which could be confirmed on orbit. After a software update an array of four gyroscopes is used for the control algorithm. The angular rate is measured at a sample rate of 100 Hz. All the measurements from the four sensors are averaged within the duty cycle of 500 ms. It improved the average control error significantly. In Table 6.6 several experiments before and after the sensor change are displayed.

Using the array of the new gyroscopes BMG250 also reduced the noise, thus the acceleration of the reaction wheels was smoother. The difference between dedicated and estimated attitude decreased by a few degrees for every experiment conducted. In Figure 6.8 the Error Angle α_{err} is displayed during a Nadir Pointing on 2020-02-15.

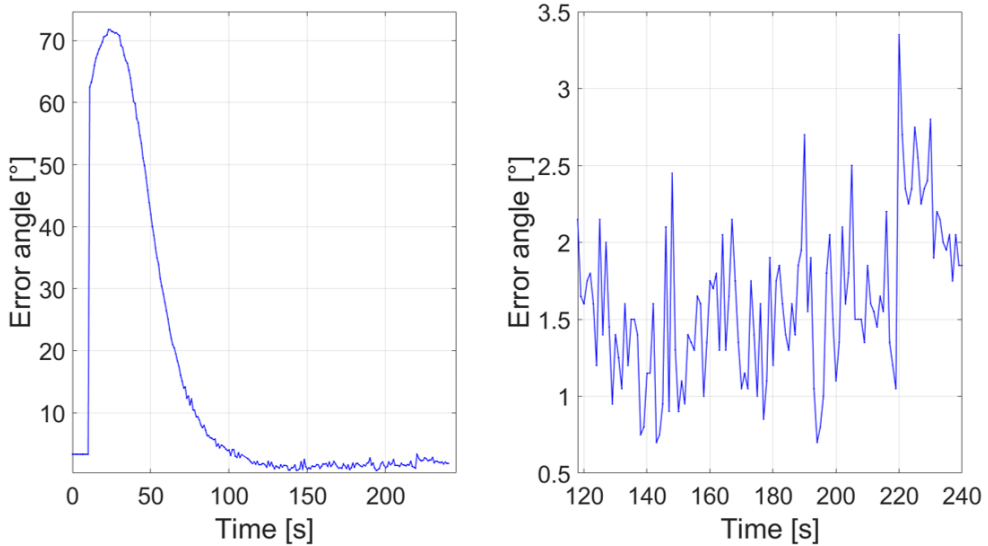


Figure 6.8: Error angle during experiment

In the diagram on the left side the entire development of the error angle during the experiment is shown. After 90 s the error angle is below $\alpha_{err} < 5^\circ$ and reaches $\alpha_{err} < 2^\circ$ around 30 s later. For the rest of the experiment, it jitters around 1.5° , mostly due to noisy magnetic field sensors, thus an unsteady attitude determination. This is clearly seen on the right hand side diagram. It was observed within the TechnoSat mission as well. For better results, the ADCS on TechnoSat used fiber-optic gyroscopes for the attitude estimation for short periods to cut out the jitter from the magnetic field sensors. It was discussed and implemented by Gordon [197].

For BEESAT-9, one solution to reduce the jitter and improve the accuracy, could be the integration of the new magnetic field sensor array from the electronics board of the PDH into the ADCS loop. In the laboratory, the results already showed an improvement of the accuracy and less jitter. Noise on a single sensor was reduced from 300 nT to 40 nT. On orbit, similar result are observed and using

an entire array of the four new sensors further reduces the noise, which reduces the jitter of the attitude determination. Simulations show an overall performance of the ADCS to values between $\alpha_{err} = 0-0.5^\circ$ as a final control error. Nevertheless, the new magnetic field sensors are not used as the default option for attitude determination, due to their sensitivity to changes in the current flow. A time varying bias correction would be required, but was not implemented yet.

Another part that was analyzed in detail was the angular rate during the experiment on 2020-02-15. For nadir pointing one axis of the satellite requires an angular rate of $\vec{\omega} = 0.06^\circ/s$ at the altitude of BEESAT-9 at 530 km, while the other two axes should remain stable. In Figure 6.9 the angular rate of the satellite from two different sensors is displayed, the MAX21000 on the right side, used in all ADCS experiments before the software upload and the array of four BMG250 gyroscopes on the left side.

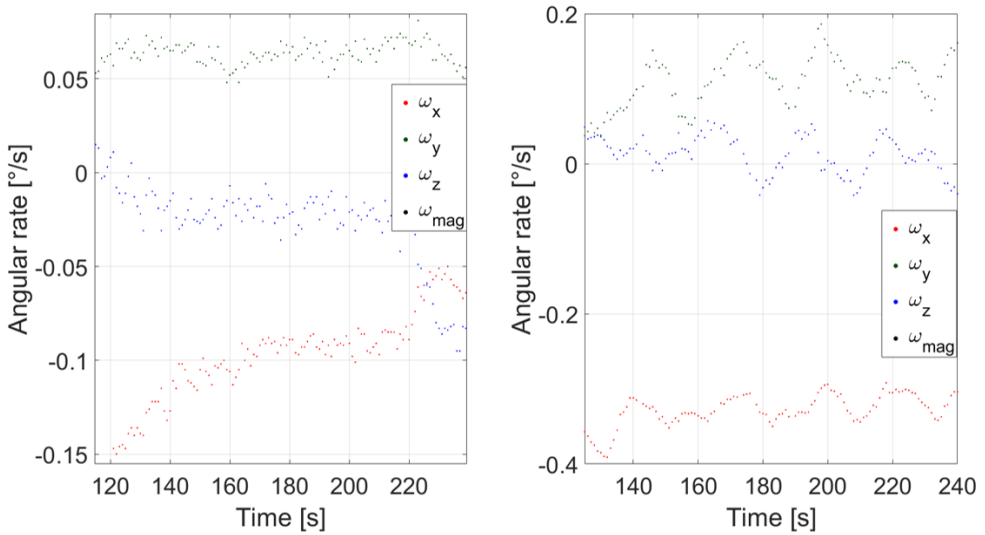


Figure 6.9: Comparison of angular rate between the sensors, left side: BMG250, right side: MAX21000

For the array of four sensors the noise is reduced and the y- and z-axis are close to their dedicated angular rate. The x-axis still has an average offset of $\vec{\omega} = 0.1^\circ/s$, which requires further investigation. Nevertheless, all axis show a significant improvement regarding accuracy and jitter.

Using the reaction wheels with a smaller rotating mass showed significant changes for the maximum duration of ADCS experiments. At least one wheel is usually saturated within 10 min, which leads to an immediate increase of the error angle α_{err} . For BEESAT-4 a saturation within one sun phase was never observed. The main reason for the high rotational speeds is the compensation of the disturbance from the magnetic field and random control torques due to sensor noise. It interacts with the residual dipole momentum of the satellite. A desaturation of the reaction wheels with the magnetic coils would be required to extend precise pointing periods.

Next to the integration of the desaturation, another interesting aspect to realize would be the usage of the gyroscope array during eclipse as a virtual sun vector. This would enable the possibility of three-axis stabilization during eclipse.

Conclusions from ADCS experiments of BEESAT-9

The ADCS was fully functional for its dedicated purpose and was mainly used to enhance the accuracies and the usage of the camera. One payload, the pFDA was initially dedicated to be included into the ADCS. As a first step a software upload is required to operate it in its dedicated manner. Afterwards the ADCS could benefit from the pFDA and increase its dynamics for slew maneuvers. The work on the pFDA was not part of the author's research, thus no further results are presented here (see [158] for more information).

Initially, a three-axis stabilized satellite was a precondition for the acquisition of navigation data, but it turned out, that a dedicated pointing was not required. Besides further research, all the GNSS experiments were conducted with a tumbling satellite, without a dedicated ADCS mode.

6.2.3 GNSS Operations

A navigation fix was generated on the first power on of the GNSS200 (see Section 6.2.1), taking the navigation achievements a step further than BEESAT-4 just hours after the launch. All the navigation data taken early in the mission was used to identify BEESAT-9 among all the other objects from the same launch (see Section 7.1).

Afterwards, the different command chains were validated, starting with the basic navigation data (see Appendix B). The output format of this data is binary and it is processed on board for immediate download and display in the TM-Viewer or storage in the flash memory of the OBC. Downloading archived navigation data was successful, allowing for verified time-tagged experiments.

For extended experiments, e.g. analyzing the signal strengths, the NMEA protocol was used. Switching the receiver to NMEA outputs the messages GPS Satellites in View (GPGSV) and Beidou Satellites in View (BDGSV), which include satellite information about elevation, azimuth and C/N_0 of GPS and Beidou. For the time, position and velocity data the Global Navigation Recommended Minimum Specific GNSS Data (GNRMC) message is used, to combine it with the elevation and C/N_0 information. The detailed description of the messages can be found in Appendix C. The NMEA data is an ASCII-based set, which is simply stored in the flash memory of the PDH, as outputted by the GNSS200. An end-to-end test was successful and the GNSS200 was fully commissioned.

For regular operations the strategy was adapted, because a three-axis stabilized satellite was no longer a precondition for the acquisition of navigation data. Thus, the frequency of experiments was increased from one data take per day to three data takes. During these experiments, the GNSS200 was switched on for 100 min and the data was stored every 60 s. This still led to a positive energy and downlink budget, including the possibility of additional experiments with the other payloads.

On a regular basis the experiments were modified to include the NMEA data for the analysis of the signal strengths over the mission time. In the beginning it was stored monthly in dedicated slots. It was increased to a weekly time interval after a software upload on the PDH which led to an improvement in operations. All the NMEA experiments were evaluated and discussed in Section 7.3.

Another interesting question that applies to CubeSat missions is the reliability of TLEs. The entire data set produced by the GNSS200 was compared to position data generated by an SGP4 model with current TLEs. Methods, statistics and results are explained and discussed in Section 7.2.

One important part of the PPOD package is the propagation of orbits. To compare different results, additional experiments were performed, e.g. 24 h data takes or higher sampling rates. For an operation of consecutive 24 h, all the ADCS sensors were switched off to maintain a positive energy budget. Moreover, it took six days

to download all the data from that experiment. In Section 7.4 the methods and results of the orbit determination and propagation are described.

From the operations of the GNSS200 it can be stated that the performance is reliable and the receiver is well suited for a 1U CubeSat. In Table 6.7 the statistics from operations with the receiver are summarized, focusing on TTFF.

Table 6.7: All GNSS experiments of BEESAT-9 and the TTFF statistics

	Quantity	Percentage
Executed experiments	782	100 %
GNSS200 off	43	5.5 %
GNSS200 on	739	94.5 %
TTFF within 60 s	708	95.8 %
TTFF within 2 min	14	1.9 %
TTFF within 3 min	4	0.5 %
TTFF within 4 min	3	0.4 %
TTFF within 5 min	6	0.8 %
TTFF within 6 min	2	0.3 %
TTFF within 7 min	2	0.3 %

A total number of 786 GNSS experiments were commanded and executed, but due to a communication issue on the CAN bus between the OBC and the PDH the command to switch on the GNSS200 was not received 43 times. Furthermore, all the experiments were time-tagged, thus stored in the RAM of the OBC until the execution time. Whenever a reset occurs, the commands are deleted to protect the satellite bus. Besides that, experiments were conducted three times a day on a regular basis.

All the properly executed experiments led to a navigation fix while the satellite was tumbling at absolute angular rates of $\vec{\omega} = 1-4 \text{ }^\circ/\text{s}$. In 95.8% of the cases the TTFF was less than 60 s. Some of the experiments with a higher TTFF were evaluated and showed a pointing of the GNSS antenna towards Earth. However, the attitude data was not stored for every experiment, thus this evaluation could not be done systematically for all the experiments.

Conclusions of GNSS Experiments on BEESAT-9

The performance of the GNSS200 on board of BEESAT-9 exceeded the expectations that emerged from the data sheet. Acquiring navigation fixes without a three-axis stabilization allowed for more experiments daily, hence more navigation data to analyze in detail. On a regular basis 300 data points were taken each day, with several exceptions, where higher data rates and longer experiments were conducted to evaluate the best strategy for orbit determination and propagation of ephemerides (see Section 7.4).

Generally, the GNSS200 is a good fit for a 1U CubeSat and continuous operation could be realized under certain circumstances. For BEESAT-9 several sensors had to be switched off to maintain a positive energy budget, but further improvements on other subsystems could decrease the power consumption. Due to the integration of the GNSS200 on the PDH, both boards needed to be powered for navigation experiments. The energy consumption of the PDH, excluding the GNSS200, roughly equals all switched off sensors, thus an integration on the OBC could already solve the energy issue.

All the gathered data from the GNSS200 was analyzed regarding several research questions, which are discussed in Chapter 7.

6.2.4 Conclusions from On-Orbit Experiments of BEESAT-9

BEESAT-9 was operated since the day it was deployed from the launch vehicle. It has been contacted daily via ground stations in Berlin, Germany, Buenos Aires, Argentina and San Martin, Antarctica. During the ADCS experiments, 73 pictures (status of 2020-07-15) were taken and downloaded (see Appendix E). In Table 6.8 the statistics of the downloaded data are displayed, adding to a total data of 59.8 MB (status of 2020-07-15).

During operations, the ADCS was tested and the control part was improved with the integration of a new gyroscope array. Furthermore, the GNSS receiver GNSS200 was successfully operated and delivered navigation data on a daily basis. Thus, the position determination of the PPOD package is completed, with the orbit determination explained in Section 7.4.

The satellite BEESAT-9 is still operated daily and partially used for student lectures, planning and executing experiments with the camera. Until the satellite will burn

Table 6.8: Operational statistics of BEESAT-9 including software uploads (SW-UL)

Ground Station	Passes	Frames	Data [MB]	SW-UL OBC/ADCS	SW-UL PDH
Berlin	1 526	117 681	56.6		
Buenos Aires	22	552	0.3	2	2
San Martin	375	6 081	2.9		
Total Data [MB]			59.8		
Housekeepings			20.7		
Debug			0.9		
ADCS			8.7		
GPS			17.8		
Pictures			11.7		

in the atmosphere in approximately eight years, the operations will continue. The end of the project BEESAT-4 also ended the financial support of BEESAT-9. Nevertheless, it will be used for educational purposes within the lectures and will continue to produce scientific data.

7 Analysis of Navigation Experiments

During the mission operations of BEESAT-9, navigation experiments with the GNSS receiver GNSS200 were performed successfully on a daily basis (see Section 6.2.3). The data gained from these experiments is used for various research questions.

During the LEOP and commissioning the acquired GNSS positions and velocities helped to identify BEESAT-9 amongst the 25 other satellites, that were launched simultaneously into the same orbit.

A script was written to compare the positions gained from the GNSS200 to the positions calculated with the SGP4 model with current TLEs. Differences were analyzed using the Hill reference frame to quantify the distances in radial, cross- and in-track direction.

The performance of the GNSS antenna during experiments and for the entire mission time was in the focus of another dedicated analysis. Generally, big ground planes are recommended to have a high gain on the GNSS signals. For 1U CubeSats the space is limited, thus most of the space proven antennas do not physically fit. Furthermore, the analysis of the navigation experiments of BEESAT-4 showed that the used GNSS antenna and its LNA were affected by radiation which led to low values of C/N_0 and a maximum of two tracked satellites (see Section 6.1.3). Therefore the performance of the new antenna of BEESAT-9 was investigated throughout the mission.

One part of the PPOD package is the propagation of ephemerides of the satellite. Based on Orekit, distinct navigation data sets were used to determine the orbit of BEESAT-9 and propagate ephemerides.

7.1 Object Identification during LEOP

On the launch day the TLE set of the launch provider was used to track the satellite with the ground station and telemetry was received. One day later, the inaccuracies were already too high to see signals on the transceiver of the ground

station, thus no telemetry was received. It was suspected, due to the generation of those TLEs. For the propagation, only one set of position and velocity data was available. Furthermore, no estimation of the atmospheric drag, expressed in the B^* value, was made. Thus, the received navigation data from the GNSS200 was used to identify BEESAT-9 using the TLEs published by the JSPOC.

7.1.1 Method for Orbit Identification of BEESAT-9

For the object identification the navigation data of the GNSS200 is compared to all the available TLEs from the same launch. In Figure 7.1 a block diagram of the method is displayed.

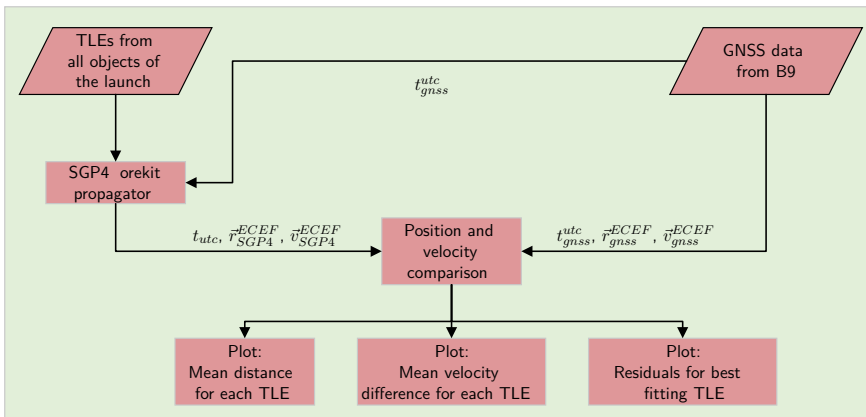


Figure 7.1: Flowchart of object identification of BEESAT-9

A set of all TLEs is used as an input for the SGP4 model from Orekit. The orbit model is preset to the required input reference frame and provides the position and velocity data in an Earth Centered Earth Fixed (ECEF) coordinate system for the comparison to the GNSS data from BEESAT-9. All the measured position and velocity data sets from the GNSS200 are compared to the SGP4 output. For comparison, the mean value of all the calculated distance residuals is taken and plotted for each available object. This analysis was executed for 12 days, until a doubtless identification of BEESAT-9 was ensured.

7.1.2 Results of Orbit Identification of BEESAT-9

Initially, JSpOC identified 13 objects two days after the launch. These were the baseline for the first analysis. BEESAT-9 was not identified at that point, instead “Object Q” had the smallest mean distances compared to the GNSS data (see Figure 7.2). From that point, the ground station used the set of TLEs, that showed the lowest distances ensuring flawless operations.

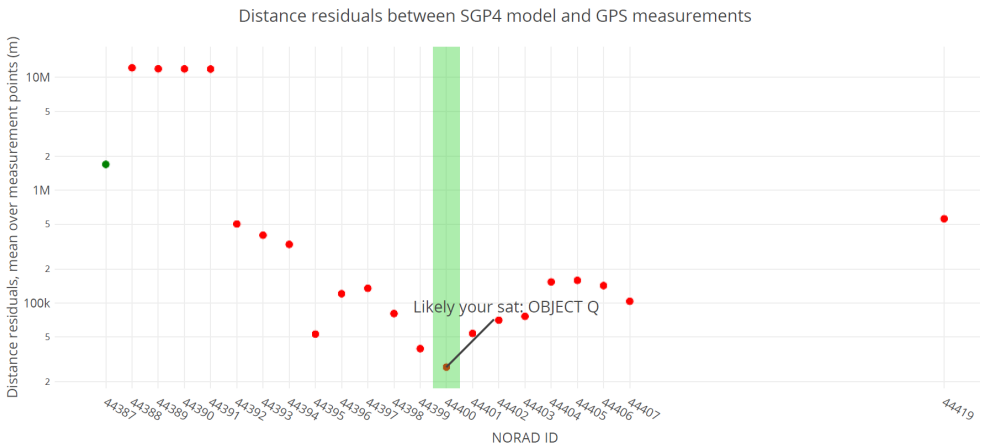


Figure 7.2: Object identification on 2019-07-07, GNSS data compared to TLEs (image credit: Clément Jonglez)

At the time of this analysis 17 of 25 objects were already assigned to TLEs. Another five objects on the upper left side of Figure 7.2 were launched together with BEESAT-9 but deployed at another orbit with a higher altitude. Green dots indicate, that the object was already identified. The single green dot was the primary payload of the launch, METEOR-M2-2.

The satellite ID 44412 for Object 2019-038AC, was only published four days after the launch. It was identified as BEESAT-9 on 2019-07-14 and was assigned on 2019-07-17 without a doubt. In Figure 7.3 the analysis from that day can be seen. The mean residuals showed distances of around 1 000 m, the next best approach showed difference of more than 50 000 m already. All the analysis was carried out by Clément Jonglez of TU Berlin in July 2019 and the results were provided to the BEESAT-9 team. For this thesis, the script was evaluated and re-run by the author in June 2020 with the data from 2019-07-17. It can be seen, that after nearly

one year in orbit, there are still several objects that were not officially assigned to satellites, indicated by the red dots.

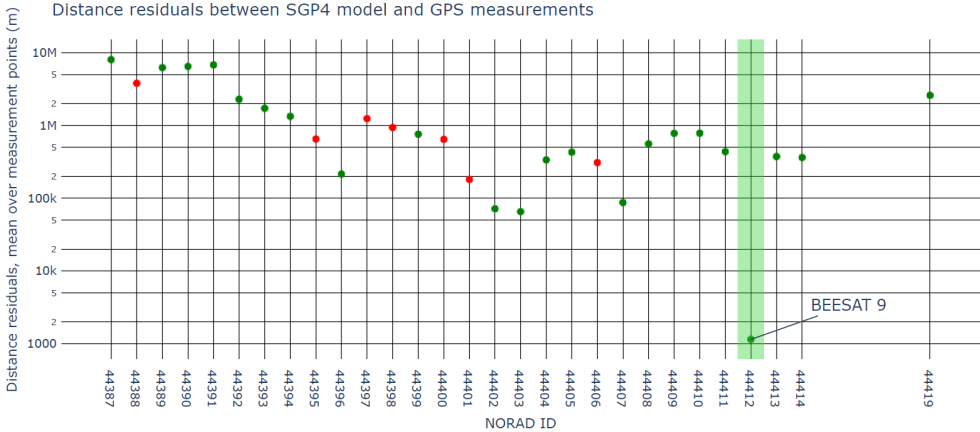


Figure 7.3: Object identification on 2019-07-17, GNSS data compared to TLEs (image credit: Clément Jonglez, rerun by the author)

Having the data of the GNSS receiver, clearly helped to improve the communication with BEESAT-9. Without the navigation data, the TLEs would have to be checked individually and an analysis of signal strengths on the ground station would be required. This is a common problem, since many ride share launches integrate a big amount of satellites. A GNSS receiver solves this issue satisfactory.

7.2 Comparison of SGP4 Ephemerides to GNSS Based Positions

The analysis, which is presented next, was carried out to estimate the accuracy of TLEs which are used by ground stations to track a satellite, as well as on orbit for the estimation of the position, which is a required input for the ADCS.

An orbit model like SGP4 is often used to determine the position and velocity of satellites. The input of the model is the current time in UTC and the TLEs. These orbital elements are usually updated daily by the JSpOC, based on observations of the objects orbiting Earth. The final output of their calculations are the estimated mean orbital elements, thus they inherently cannot represent the position accurately for the entire orbit. Errors of up to 1 km can be seen for propagated positions

from new TLEs. These errors are mainly in the in-track direction and vary during an orbit (see Figure 7.7).

It has to be stated that the quality of TLEs relies on numerous factors. The orbit of the satellite, e.g. its altitude, eccentricity and inclination have an influence on the prediction. Furthermore, the shape of the satellite highly influences the estimation of the aerodynamic drag on the satellite, which is modeled into the B^* parameter. Another aspect is the amount of observations of the satellite by the network of radar stations, which depends on the size of the tracked object. More interpolation points lead to a higher accuracy of the mean orbital elements.

For BEESAT-9, the orbit is nearly circular (small eccentricity) and sun-synchronous at an altitude of 530 km. Being a 1U CubeSat with similar properties in all three axes, a good estimation of the aerodynamic drag is expected. An analysis for a few selected TLEs was presented in 2020 by the author [196].

For a thorough understanding and an overview of the estimated TLEs the script was adapted by Morando under the supervision of the author [198] to include every TLE since the launch. The method and the results are presented in the following sections.

7.2.1 Method for Processing TLE Sets for Comparison

For the analysis of the quality of the TLEs, the data sets have to be converted into compatible formats. The final step is the comparison of positions from the GNSS200 and from the TLE based positions in the Hill reference frame. A conversion function by Vallado [199] programmed for MATLAB by Koblick [200] requires inputs from both systems in an ECEF coordinate system. The GNSS based positions are directly outputted by the receiver in that format (\vec{r}_{gnss}^{ECEF}), thus the conversion mainly concerns the TLE based data. In Figure 7.4 an overview of functions and data flow is displayed.

First of all, the GNSS data from BEESAT-9 and the TLEs from the online database of SpaceTrack [201] are loaded. Afterwards a loop is implemented to run the script for every single TLE.

At the start of this loop several inputs are required. The duration of the simulation is set to a period of two months for this analysis. It is considered adequate to investigate the development of the distances (see Section 7.2.2). Furthermore, the

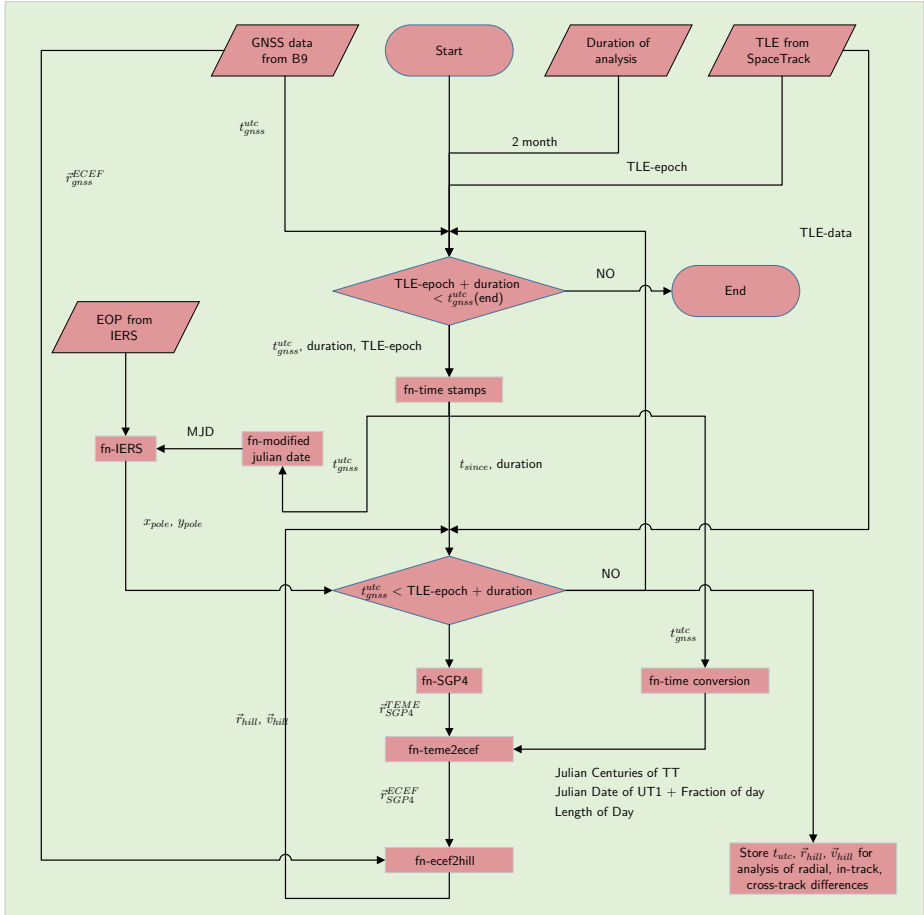


Figure 7.4: Flowchart of calculation of distances between GNSS and TLE ephemerides

epoch of the used TLE and the time from the GNSS data set is used. A conversion of the GNSS time to UTC is applied to the data set beforehand. Since January 2017 the GPS time is 18 s ahead of the UTC [202].

These inputs are used in the “Time Stamp”-function to extract the year, month, day, hour, minute and second from the GNSS time, which is given in seconds since 2000-01-01 00:00:00 on BEESAT-9. Additionally, the GNSS time stamps are

rebased to the epoch of the current TLE. To fit the requirements of the SGP4 model the time since the start of the epoch is given in minutes.

The extracted GNSS times are used to calculate the Modified Julian Date, which is an input for the “IERS”-function. Together with the Earth orientation parameters, acquired from the International Earth Rotation and Reference Systems Service, the polar motion coefficients x_{pole} and y_{pole} are calculated as well as the current time differences UT1-UTC and TAI-UTC.

An internal loop calculates the \vec{r}_{SGP4}^{ECEF} for the applied duration of two months. At first the positions are calculated in the TEME reference frame using the current TLE, and the time stamps from the GNSS input data, ensuring the data to be compared has the exact time stamp with a precision of 10 ms.

Within the same loop, another time conversion function “convtime” from Vallado [199, p. 195] is used to calculate Julian Centuries of TT, Julian Date of UT1 and Length of Day. These time stamps are converted using the extracted data from the GNSS time and the time differences UT1-UTC and TAI-UTC.

For the calculation of the data set of \vec{r}_{SGP4}^{ECEF} , the polar motion coefficients, the times Julian Centuries of TT, Julian Date of UT1 and Length of Day and \vec{r}_{SGP4}^{TEME} are put into the “teme2ecef”-function by Vallado [199, p. 231] and finally both data sets are available in the same coordinate systems.

To compare the data sets it is favorable to convert both into a LVLH Hill frame, with its point of origin being the satellite. Another function from Vallado, “ecef2hill” [199, 200] returns the differences for the radial, cross- and in-track positions. The described functions are repeatedly called for every TLE data set of BEESAT-9. The position discrepancies and its time stamp are stored for further analysis.

7.2.2 Results of Comparison between TLE and GNSS Data Sets

In total, 528 TLEs were compared to the GNSS based positions. The ephemerides based on the SGP4 orbit model were calculated for a duration of two months.

For all the comparisons it can be seen, that the in-track difference is always the most significant, while radial difference is the smallest. There is also a correlation between high discrepancies of all three directions, a big in-track difference comes along with big radial and cross-track differences. The radial and cross-track differences oscillate around zero, with an increasing amplitude over time. For the

in-track difference it can be stated, that it is highly dependent on the B^* value. If it is overestimated, leading to a higher drag from the atmosphere model, the altitude of the satellite decreases faster, which increases the mean motion and pulls the satellite ahead of the GNSS positions. For an underestimation the opposite can be seen.

For the duration of the comparison, some preconditions were set. The required pointing accuracy of the ADCS was set to $\alpha_{err} \approx 7^\circ$ by Herfort [136, p. 11]. The total error added by the attitude sensors and the control algorithms adds up to a maximum of $\alpha_{err} \leq 5^\circ$, based on Section 6.2.2. Thus, for a nadir pointing of the camera the maximum allowable error due to a wrong position is $\alpha_{err} = 2^\circ$.

In Figure 7.5, the relation between the error angle α_{err} and the in-track distance is shown.

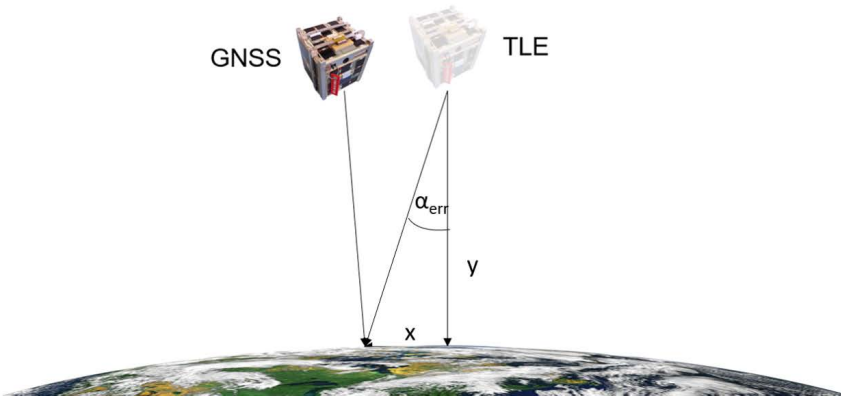


Figure 7.5: Calculation of limit for a TLE update

Radial difference is negligible for this use case, since the differences to the GNSS is within a few kilometers and furthermore, the axis remains the same for nadir pointing. The cross-track difference would contribute slightly to the error, but is left out to avoid unnecessary complexity. Analyzing the TLEs showed, that the cross-axis error was around 10 % of the in-track difference, thus can be left out for this precondition.

Assuming an angle of 90° between x and y on the surface of Earth, the following formula is used to find a limit.

$$x = y \cdot \tan \alpha_{err} \tag{7.1}$$

The perigee P and the apogee A of BEESAT-9 are 512 km and 546 km respectively (on 2020-06-20). Thus the tolerable in-track difference is calculated to:

$$x_P \approx 18 \text{ km} \tag{7.2}$$

$$x_A \approx 19 \text{ km}$$

Based on a maximal in-track difference of 18 km until a TLE update is required the duration was set to a maximum of two months. At that point the discrepancies are higher than the limit for most of the TLE. In Table 7.1 it can be seen on which day the in-track difference surpasses the limit. The percentage was calculated twice, once starting from the launch and once the satellite was identified doubtless 12 days afterwards (see Section 7.1). Within the first days the uncertainties are big, due to the low references and the huge amount of objects launched together with BEESAT-9 (see Figure 7.9).

Table 7.1: Statistics of the limit crossing by day

	Day 1–7	Day 8–10	Day 11–15	Day 16–30	Day 30–60	Limit not exceeded
Percentage [%] starting 2019-07-05	2.3	2.3	21.3	50.8	12.7	10.6
Percentage [%] starting 2019-07-17	0.8	2.0	21.8	51.6	12.9	10.9

Taking out the first 12 days in 10.9%, the limit is not crossed within two months, but for the majority of the TLEs it happens within the first 30 days. For the described use case, it is recommended to update the TLEs after a maximum of 10 days. Within the considered period it would cover more than 97 % of the cases. A modification of the B^* value of the TLEs could increase the percentage further (see Figure 7.13). The TLEs are used as an input of the ADCS, but for higher accuracies it is necessary to use the GNSS based positions directly. This derives from the fact, that the in-track difference calculated just after its release is up

to 1 km for BEESAT-9. In Figure 7.6, the in-track difference is displayed for a duration of two months including 148 navigation experiments.

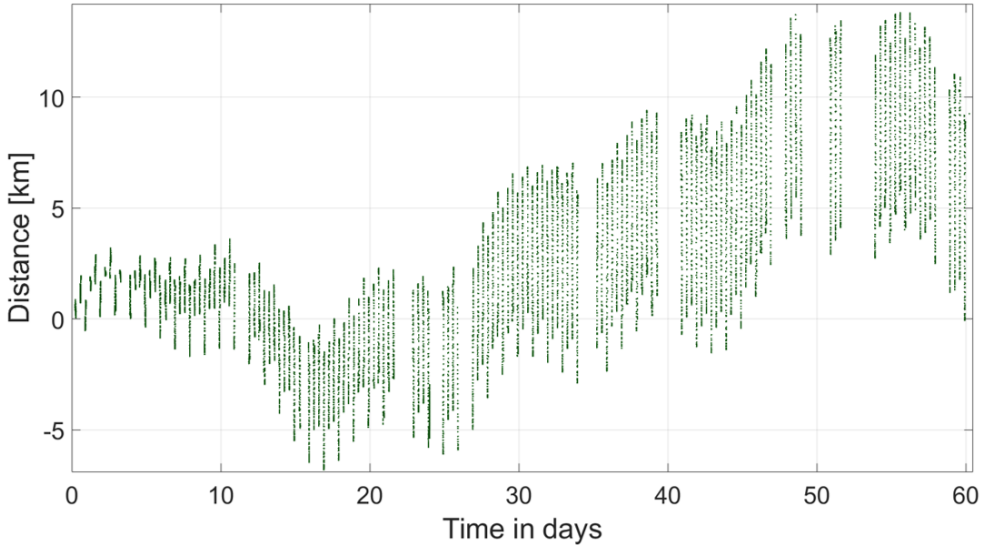


Figure 7.6: In-track difference development of the “best” TLE over two months

In this case, the TLE with the best outcome is used, with a maximum difference of 13.8 km after two months. The data was usually stored every 60 s for a total duration of each experiment of 100 min. Figure 7.7 shows the first experiment after the release of the TLEs and the last one within the two months.

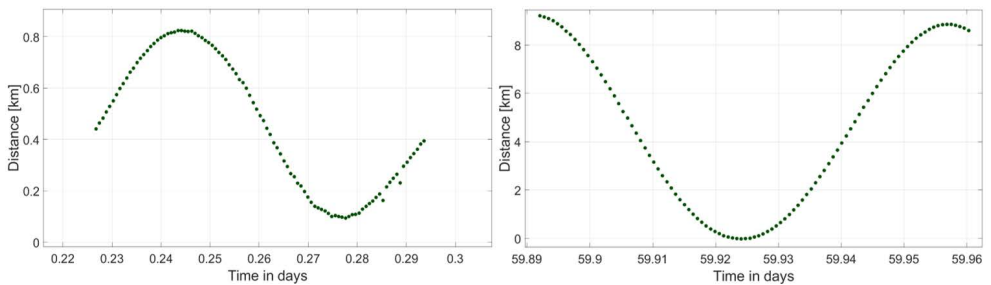


Figure 7.7: In-track amplitude change over two months of the “best” TLE

Even though the maximum is low compared to most of the other TLEs, the amplitude increases from 0.8 km to 8 km. The oscillations occur for every TLE and

apply to in-track, cross-track and radial difference. In Figure 7.8, the corresponding radial and cross-track differences are displayed for a duration of two months.

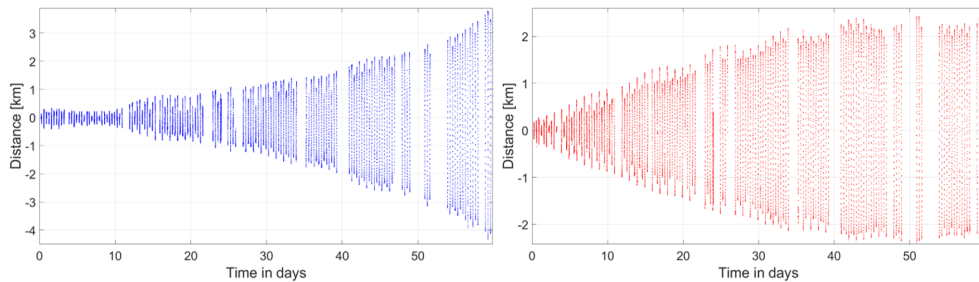


Figure 7.8: Cross-track (left) and radial (right) difference development over two months

The radial difference oscillates around zero with an amplitude of 320 m. For the entire time of two months, the radial difference above or below the GNSS positions remain nearly the same, only the amplitude increases. Nevertheless, the discrepancies remain at around 2 km, which would still be fine for the preset scenario.

Similar observations were made for the cross-track difference. Oscillations around zero occur for the entire duration of the analysis, with the amplitude increasing from 350 m to 8 km.

Table 7.1 shows that 4.6 % of TLEs cross the limit within a few days. Throughout the analysis these TLEs also showed the highest discrepancies after two months. In Figure 7.9, the maximum in-track difference is displayed for all 417 TLEs which could be compared for a duration of two months. It represents the period from 2019-07-08 until 2020-04-01 (GNSS data until 2020-06-01 was analyzed for this thesis).

Most of the outliers with discrepancies of up to 2200 km occur in the first days after the launch, but some also appear after more than a month of observability on orbit. A total of 25 satellites were launched into the same orbit simultaneously, which probably lead to misinterpretations during the observation of the objects, thus inaccurate TLEs in the first weeks after the launch. Nevertheless, for the extreme discrepancies after more than one month (three TLEs from 2019-08-10 to 2019-08-11), another reason was analyzed. First of all, the sun activity during that time was investigated, but no anomalies, which could have affected the orbit differently, were found. Furthermore, the experiments conducted with the satellite

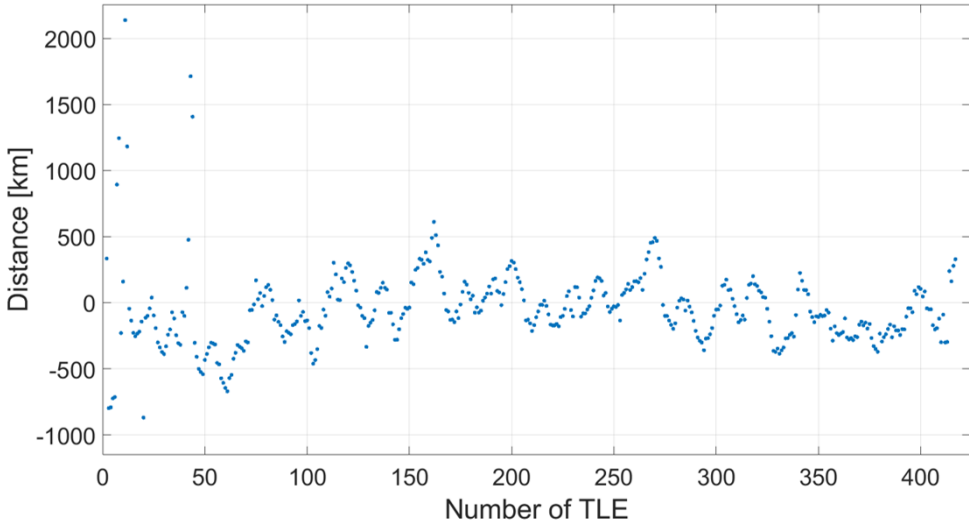


Figure 7.9: Maximum in-track difference after two months for all TLEs

and its commanded attitude were looked at. During the mentioned days, the satellite was tumbling all the time at a low angular rate, which is its nominal status throughout the entire mission. Discarding these two possibilities, one remaining cause could be the lack of observations to estimate the TLEs. Only assumptions can be drawn about the observations, since the information is not publicly available. Nevertheless, an analysis of the published TLEs showed a gap of two and a half days, before 2019-08-10. On 2019-08-13 the TLEs included a B^* value, which is not an outlier. The evolution of the B^* value can be seen in Figure 7.10. The three outliers are marked with red circles.

With the exception of 6 TLEs, the value varies from $B^* = 1 \times 10^{-5}$ to 1×10^{-4} . All these outliers of B^* directly cause huge errors of the SGP4 model. It can be seen in Figure 7.11, that the maximum in-track distance and the B^* value follow the same pattern.

It leads to the conclusion that the quality of the TLEs depends on the B^* value. Nevertheless, other orbital elements could contribute to errors as well, but the significance of B^* is outstanding.

This raised the question, if a TLE set could be improved by just replacing the B^* value. For this purpose, the TLEs from 2019-08-10 with $B^* = 1.05 \times 10^{-4}$ was

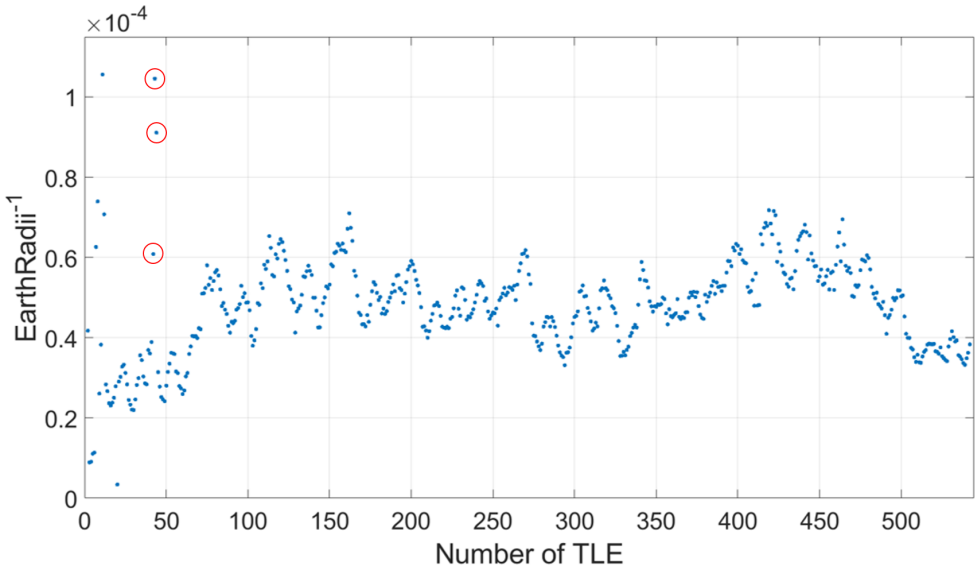


Figure 7.10: Development of the B^* value during the mission

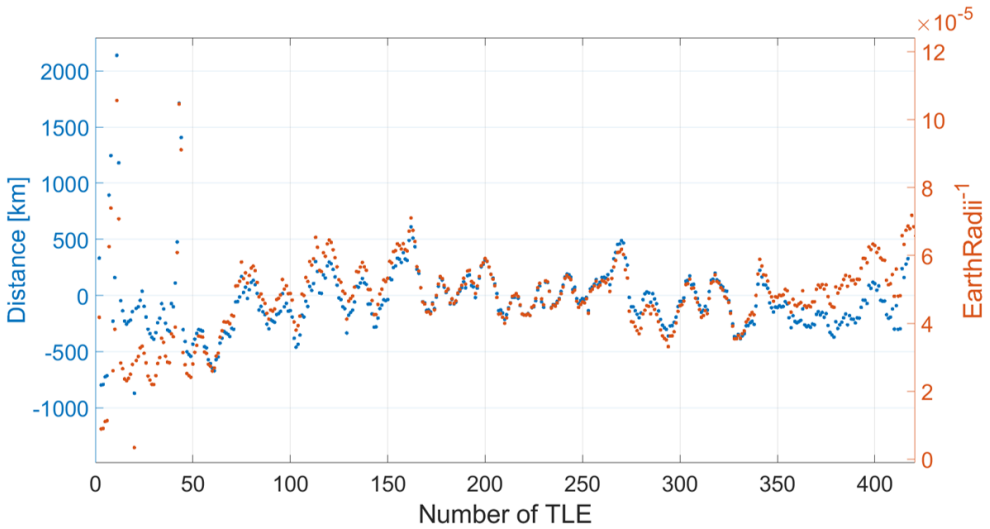


Figure 7.11: Correlation between in-track difference and B^*

taken (see top red circle in Figure 7.10). Figure 7.12 displays the development of the errors for all three directions.

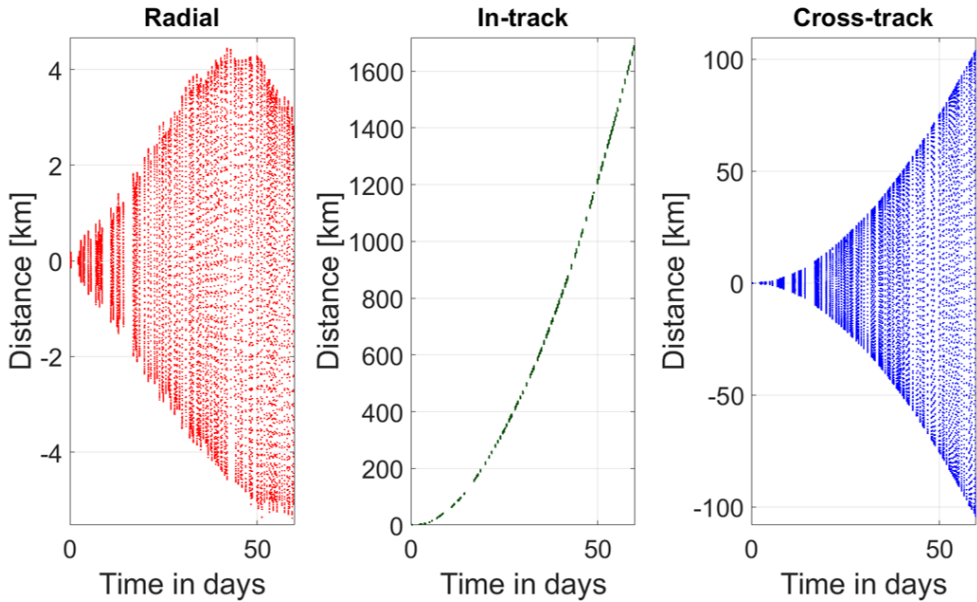


Figure 7.12: Differences from GNSS to SGP4 for all three directions for the “worst” TLE

For a quick improvement of the results and to decrease the discrepancies all the TLEs with extreme differences were modified. B^* was replaced with a value from another TLE. In this case a TLE was used, that showed low discrepancies and was released within a few days before the modified one. The B^* value from the TLEs on 2019-08-08 was 3.89×10^{-5} . Figure 7.13 shows the improvements in all three directions.

The in-track difference decreases from about 1700 km to -60 km, radial difference from 6 km to 4 km and cross-track difference from 100 km to 10 km after a period of two months. Similar results were observed for all the other modified TLEs. With some experience and a regular development of the B^* value over time, this is a reasonable way to improve the output of the orbit model on the satellite.

Next to the “best” and “worst” TLEs, the average and median differences were calculated. After two months the absolute average in-track difference was around 225 km and the median was at 155 km. In Figure 7.14, the development of the in-track difference over two months is plotted for all four examples.

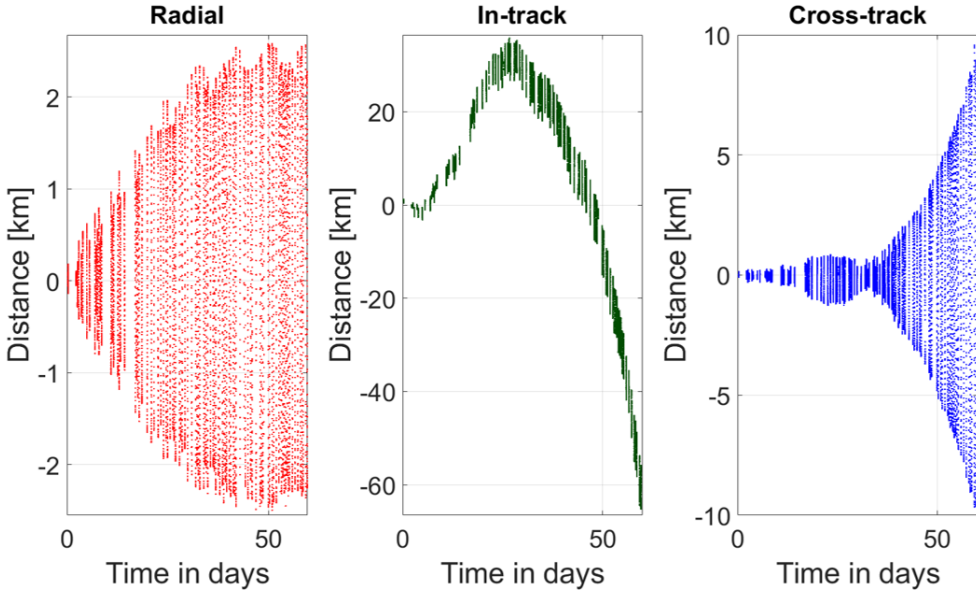


Figure 7.13: Differences from GNSS to SGP4 for all three directions for the “worst” TLE with a modified B^* value

It can be seen, that the outliers are rare and the average and median discrepancies are significantly closer to the “best” TLEs than to the “worst”.

In Table 7.2, the differences are summarized for the comparison of TLEs to GNSS based positions for several TLEs.

Table 7.2: Results of the comparison after two months for selected TLE

	Radial [km]	In-Track [km]	Cross-track [km]	B^* $EarthRadii^{-1}$
Best TLE	2.3	13.8	4.2	4.89×10^{-4}
Worst TLE	5.4	1712.6	104.2	1.05×10^{-4}
Worst TLE with modified B^*	2.4	65.1	9.6	3.89×10^{-5}
Median TLE	2.6	155.6	12.4	4.88×10^{-5}
Mean TLE	2.7	226.4	16.3	4.85×10^{-5}

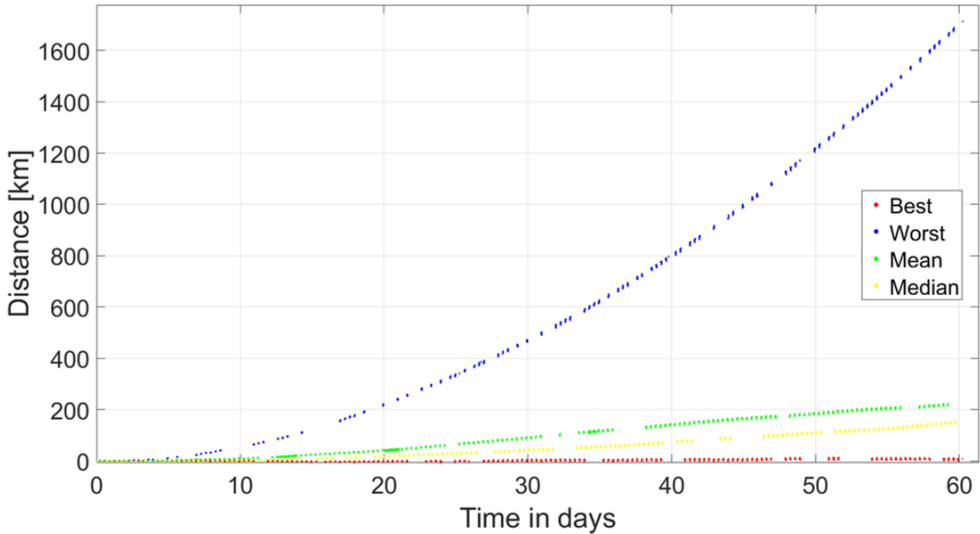


Figure 7.14: Differences from GNSS to SGP4 for all three directions for the “worst” TLE with a modified B^* value

7.2.3 Summary of the Comparison of TLE and GNSS Based Ephemerides

In case of BEESAT-9, an update of the TLE on orbit every 10 days is sufficient. Due to many variables, e.g. use case, accuracy of TLEs, requirements, a generalization cannot be made, but for 1U CubeSats without deployable solar panels the accuracy of the TLEs should be similar. It was shown, that inaccuracies, developed over time, derive mainly from the B^* value. A comparison to BEESAT-4 showed similar B^* values, which was expected, since the orbit is just slightly lower, with the satellite having the same shape.

The discrepancies can be estimated depending on the B^* value before the upload and a replacement can be considered. Nevertheless, it requires experience with the TLEs and results from previous TLEs to modify a new TLE before uploading it.

Furthermore, a comparison to the results from AeroCube-4 shows higher accuracies for BEESAT-9. In Figure 2.3 it can be seen, that the in-track differences are up to 200 km after only 10 days. For BEESAT-9, such a difference occurs after two months averagely. Three reasons were identified for the different results.

1. The sun activity was significantly higher in 2012/13 when the experiments were conducted on AeroCube-4 [203]
2. Deployable solar panels on a tumbling satellite highly affect the estimation of the drag coefficient B^* [87]
3. Models for the estimation of the TLEs were improved in the beginning of 2013, experiments of AeroCube-4 started before [87]

Generally, it can be stated, that TLEs are already inaccurate at their release. All of the orbit elements are mean values, which implies oscillations during each orbit. For high accuracies in position and velocity, it is inevitable to use a GNSS receiver.

7.3 GNSS Signal Strength at the GNSS200

Analyzing the strength of the GNSS signals at the receiver has been part of the PPOD package implementation since the first tests with the Phoenix receiver (see Section 5.1.3). One of the reasons was the smaller ground plane of the antenna which leads to lower C/N_0 on BEESAT-4 and BEESAT-9. It had to be verified, that a sufficient performance was still the expected outcome. Furthermore, the LNA of the antenna is exposed to radiation nearly unprotected, due to its location on the edge of the satellite. The antenna on BEESAT-4 was affected by radiation, which could be seen by the low C/N_0 on orbit compared to the tests. Moreover, an antenna was exposed in a TID test to 12 krad and afterwards no satellite was tracked. For the analysis of the effects of radiation on the LNA the signal strengths were recorded throughout the mission time.

All the recorded data had to be preprocessed for the analysis and merged with data from the ADCS as well as data generated with STK.

7.3.1 Method for the Analysis of the Signal Strength

Several data sets from different sources have to be put together to get a comparable output for all the experiments.

- Attitude data from BEESAT-9
- NMEA data sets including the elevation, azimuth and C/N_0 of all tracked satellites

- STK based data sets of the actual elevation, azimuth and distance of the GNSS satellites towards BEESAT-9

Section 6.2.3 describes that the satellite BEESAT-9 was tumbling at absolute angular rates of $\vec{\omega} = 1\text{--}4^\circ/\text{s}$. Since the signal strength depends on the elevation of the GNSS satellites over the antenna, the attitude of BEESAT-9 has to be taken into account. Furthermore, the ASCII-based data set of NMEA messages GNRMC, GPGSV and BDGSV (see Appendix C) included the information of the amount of tracked satellites and their signal strength at the GNSS200. To put the signal strengths into perspective, the position of the GNSS satellites were included as well. In Figure 7.15 the data processing is displayed.

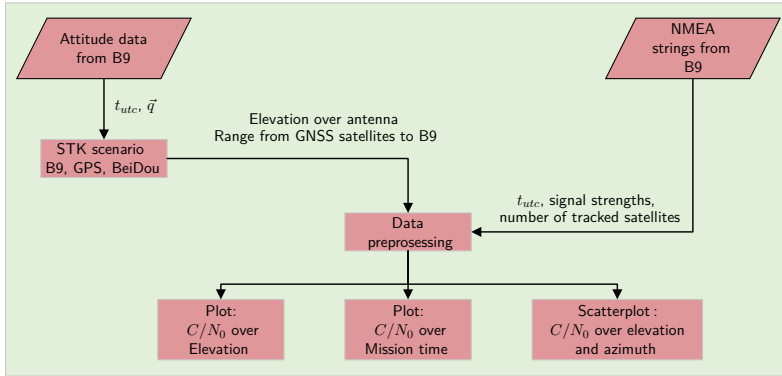


Figure 7.15: Flowchart of calculation of signal strengths over elevation

At first, the attitude of BEESAT-9 during the navigation experiments is implemented in the STK scenario. It includes all GPS and BeiDou satellites as well as BEESAT-9. A report is generated that assigns elevations and distances of GNSS satellites towards BEESAT-9. The elevation is reported in reference to the GNSS antenna of BEESAT-9, while an angle of 90° represents a satellite in zenith over the antenna.

The STK report as well as the NMEA messages require further processing before an analysis can be conducted. A script to write an array which sorts all the inputs according to their time stamps was implemented by Nicole Gress under the supervision of the author.

Additionally to the signal strength recorded by the GNSS200, an adapted value is added, which includes the free space path loss according to the distance of the GNSS satellites to BEESAT-9. It is calculated starting with the following formula to calculate the power density at the receiving antenna P_r [204]:

$$P_r = P_t \left(\frac{c}{4\pi Df} \right)^2 \quad (7.3)$$

Furthermore, the ratio between transmitting power density to received power density represents the free space path loss, which is represented in dB.

$$FSPL = \frac{P_t}{P_r} = \left(\left(\frac{4\pi Df}{c} \right)^2 \right) \quad (7.4)$$

$$FSPL(\text{dB}) = 20 \log_{10}(D) + 20 \log_{10}(f) + 20 \log_{10} \left(\frac{4\pi}{c} \right) \quad (7.5)$$

The frequency is given in MHz and the distance in km, thus the last term of the equation is calculated to the following:

$$20 \log_{10} \left(\frac{4\pi}{c} \right) = 20 \log_{10} \left(\frac{4\pi}{0.299792} \right) = 32.44 \text{ dB} \quad (7.6)$$

The adaptation of the signal strengths according to the distance is based on the minimal distance of 19479 km reported by STK for all the executed experiments. At this given distance the free space path loss is calculated to a value of $FSPL(\text{dB}) = 182.2 \text{ dB}$, which is subtracted from all the calculated free space path losses of the respective distance. The result is added to the measured signal strength and is referred to as "adapted signal strength". In Table 7.3 the final array for analysis is displayed with two example data sets.

For each experiment the signal strengths were adapted according to the distance and the data was ready for analysis.

Table 7.3: Assorted array of NMEA data in reference to elevation and range of GNSS satellites

Time stamp	Sat. ID	Signal Strength [dB]	Adapted Signal Strength [dB]	Elevation [°]	Range [km]
2020-05-13 18:05:10	24	42	42	8	19 479
2020-05-13 18:05:10	13	44	45.7	77	23 744

7.3.2 Results from the Analysis of GNSS Signal Strength

After all the received values of signal strengths are adapted, it was analyzed, if there is any degradation throughout the mission time. The criteria is generalized for all the values from each experiment and a distribution of GNSS satellites over the antenna is assumed to have a similar pattern for every commanded experiment. Small variations of the distribution of the elevation over the antenna are expected, but there will be always satellites with high elevation, based on the orbits of the GPS and BeiDou satellites.

As mentioned in Section 6.2.3 the strategy of obtaining the signal strengths values was adapted after a software upload in January 2020. Before the upload three experiments were executed with a data acquisition for 10 minutes. Afterwards, the experiments were commanded on a weekly basis with data acquisition for one minute three times during the basic GNSS experiment of one orbit. The data was stored every 10 s, which accumulated to 360 data sets for 10 tracked satellites of up to 720 data sets for 20 tracked satellites each week. The amount of tracked satellites is variable, depending on their position compared to BEESAT-9. In Figure 7.16, the accumulated signal strengths during the mission are displayed.

Values from 10 dB to 50 dB can be seen, with the majority being between 30 dB and 50 dB. Small fluctuations between experiments are observed, but a general degradation is not seen throughout almost one year on orbit. Furthermore, the values are similar to those acquired on the ground during the verification campaign (see Section 5.3.3).

Understanding the distribution of the signal strengths was the next step. It was expected, that the C/N_0 decreases with a lower elevation with a plateau around

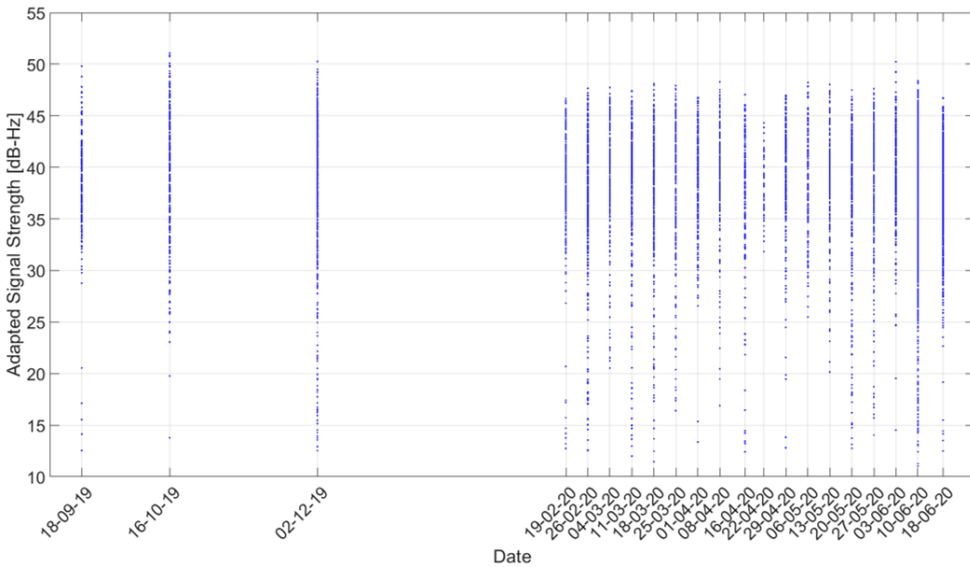


Figure 7.16: Accumulated signal strengths of GNSS satellites during the mission

73° (see radiation pattern in Figure 4.14). Nevertheless, high values should be seen for elevations from 30–90°. From the radiation pattern the difference for these elevations varies up to 4 dB, also depending on the azimuth. Figure 7.17 shows the distribution of the C/N_0 plotted to the elevation of GNSS satellites relative to the GNSS antenna of BEESAT-9.

The C/N_0 increases with higher elevation and settles at around 70°. It includes the attitude data of BEESAT-9, thus an error of the elevation of up to 5° applies to these values. Another focus was put on the huge amount of tracked satellites at a negative elevation. GNSS signals would have to pass the satellite to be received by the antenna from that side. These signals were analyzed regarding a potential reflection from the Earth, which could be excluded. The elevations match the analysis done with STK, which means the GNSS signals transit BEESAT-9, before being received by the antenna. The fitting line, a polynomial of 6th degree does not represent the distribution well at elevations near -90°, due to the lack of data points, but was included to the plot to see the plateau at 70° properly. Another representation of the C/N_0 over elevation is displayed in Figure 7.18, split into two plots, one for positive and one for negative elevation.

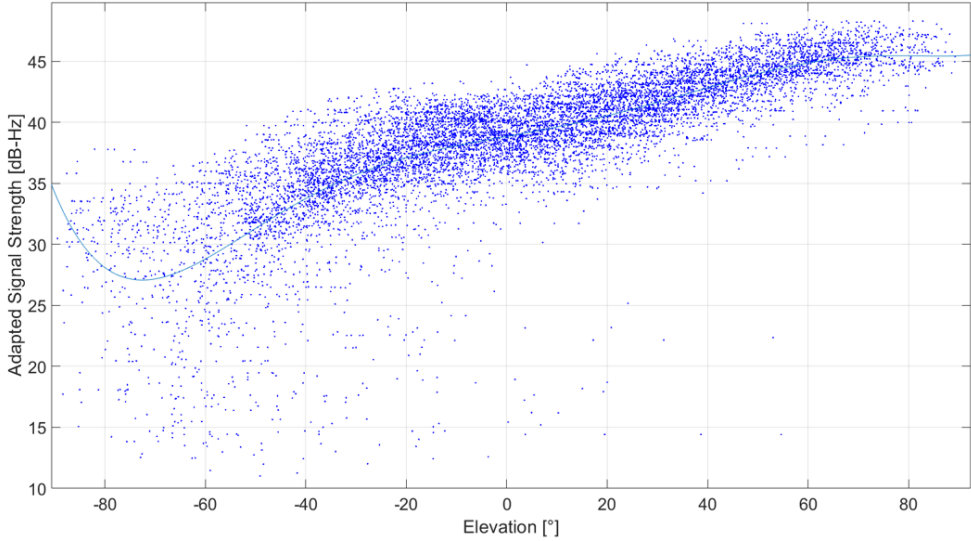


Figure 7.17: Carrier Signal-to-Noise Ratio of tracked GNSS satellites depending on elevation

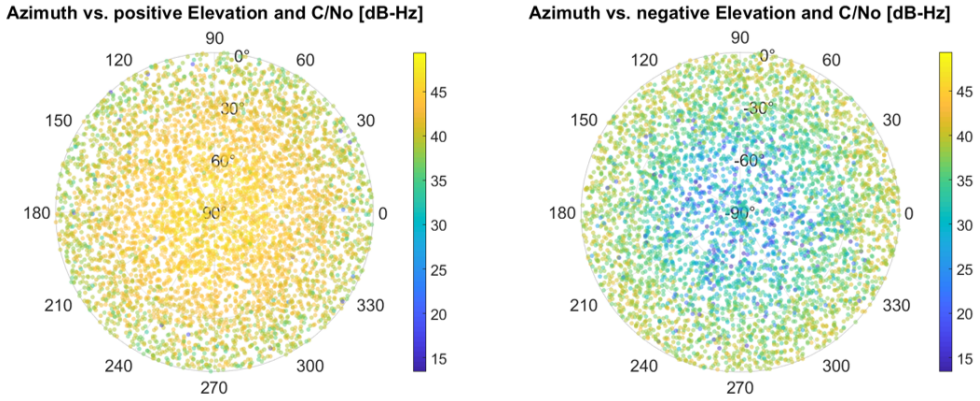


Figure 7.18: Carrier Signal-to-Noise Ratio over elevation and azimuth

It is plotted according to the azimuth of the antenna coordinate system. On the left side all the values with a positive elevation are displayed. The C/N_0 decreases from the center to the outer parts of the plot. The radiation pattern of the antenna is not seen here, thus it was not further looked into the entrance

area of the antenna. The plot on the right side shows decreasing values from the outside to center, which represents an elevation of -90° .

7.3.3 Summary of Signal Strength Analysis of GNSS Satellites

After one year in orbit no degradation of the LNA of the GNSS antenna is seen and experiments are still ongoing for further investigations. The values of the C/N_0 are comparable to those that were acquired during the tests on ground. Furthermore, it can be seen that the values decrease with lower elevation over the antenna, which was expected. Another interesting outcome was the high number of tracked satellites at low elevations below zero degree. The GNSS signals from these satellites transit the satellite before they reach the antenna. This can be explained by the small form factor of BEESAT-9. For bigger sized satellites signals will not be received at negative elevations. Furthermore, the radiation pattern of the selected antenna influences the reception of signals.

The GNSS antenna used on BEESAT-9 lasted for the minimum mission time of one year and can be recommended for further use in space.

7.4 Orbit Determination and Propagation of Ephemerides

One part of the mission objective of BEESAT-4 and BEESAT-9 is the orbit determination and propagation of the satellites ephemerides, based on GNSS data. The analysis was carried out on the ground, using a Python script for the determination and propagation. The script was written by Jonglez [162], based on Orekit [164] and was adapted for this analysis. For the comparison of the propagated ephemerides to the prospective navigation data from the GNSS200, the “`ecef2hill`” function of MATLAB, introduced in Section 7.2, is used.

In Chapter 2 several approaches were discussed, based on the required accuracy which is usually set by the application. The used GNSS module acquires basic navigation data (see Appendix B) with the output either in binary or NMEA format. Thus, the approaches which require dual-frequency receivers, carrier phase and pseudo range data had to be excluded from this analysis.

Based on the available data format and the challenges for 1U CubeSats to integrate a GNSS receiver, the focus of the orbit determination was set in the following

way. Data sets of different durations and sample rates were used to determine the accuracy of the orbit determination and the propagation of the ephemerides for a certain time period. The ephemerides are compared to future GNSS data to analyze their accuracy. For the orbit determination most outliers were filtered. Moreover, the navigation data sets include an indicator for the quality of the navigation solution, the Dilution of Precision (DOP) values (time, position, geometrical, vertical, horizontal, see Appendix B). Generally, lower values indicate a higher accuracy of the navigation solution as described by Langley [205]. Nevertheless, the values cannot be converted into an absolute deviation in meters. The geometrical DOP (GDOP) includes the time (TDOP) and the 3D position (PDOP) and is used as a reference for this analysis. These values mainly derive from the constellations of the tracked satellites, as it is seen by the receiver. A wide spread constellation leads to low values, down to a minimum of 1 [205]. Four satellites in view can produce GDOPs of six or lower, which is an acceptable value for orbit determination (used by Gangestad et al. for AeroCube-4 [87]). For the navigation solutions of the GNSS200 on BEESAT-9, eight or more satellites were tracked most of the time, leading to low DOP values. For the orbit determination navigation solutions with a GDOP bigger than three were filtered to obtain good results.

In Chapter 3 the EPS and the COM were considered two of the most affected subsystems regarding the integration of a PPOD package, with the duty cycle and the produced data of a GNSS receiver as the main drivers. The applied analysis helps to understand the required duty cycle of the receiver to obtain a certain accuracy. Furthermore, a statement can be made regarding the sample rate and the amount of data which is needed. This could also apply for on-board orbit determination and is part of future investigations within the NanoFF project (see Section 8.3).

7.4.1 Method of Orbit Determination for Ephemerides

The orbit determination requires data sets of position and velocities which were obtained from the GNSS200. For the initialization, TLEs are used for a first prediction of the orbit. Additionally, several parameters are set, e.g. physical properties of the satellite, estimated position and velocity noise of the GNSS data and parameters for the orbit propagator. In Figure 7.19, an overview of the main blocks and data flow is shown.

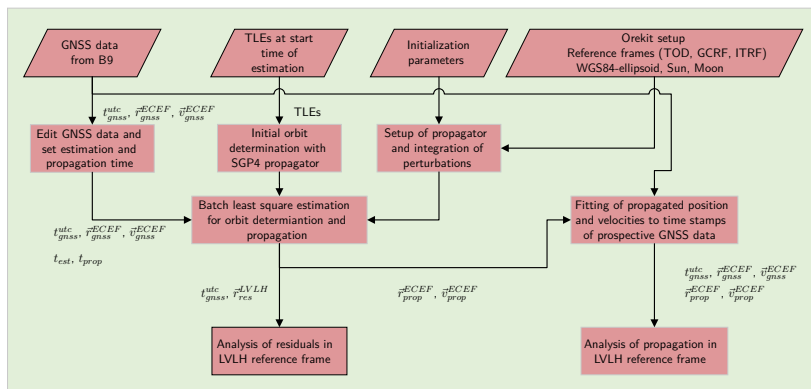


Figure 7.19: Flowchart of orbit determination and propagation

In the next step, the required functions of Orekit are imported to the script, including the definitions of coordinate systems. In this case the inertial reference frames TOD and GCRF are used as well as the Earth fixed ITRF. Furthermore, the World Geodetic System 1984 (WGS84) Earth ellipsoid is loaded along with models of the Sun and the Moon. Using the initialization parameters and the Orekit library, the propagator is set up. It includes an Earth gravity model of degree and order of 64. The perturbations induced by the Sun and the Moon are taken into account as well as the solar radiation pressure. An estimated drag coefficient of BEESAT-9 together with its dimensions feeds the atmospheric model. The initial orbit is determined with TLEs with the epoch being within the used GNSS data set.

For the orbit determination and propagation, the batch least square estimator of Orekit is used. All the navigation data is included and transformed into an inertial frame. For the estimation, a time scope is set, that defines the used GNSS data from the GNSS200. Furthermore, a propagation time scope is set to calculate prospective ephemerides for up to two weeks. Within these two weeks no new navigation data is included in the propagation.

One result of the determination are the residuals, which describe the differences in radial, in-track and cross-track direction between the estimated orbit and the observed GNSS data sets. For the analysis of the propagation, an array is fitted to the time stamp of the prospective navigation data. This array contains a unique

time stamp, converted to UTC and the position and velocity data in the WGS84 frame from the GNSS200. Furthermore, the ephemerides are propagated, using the same time stamp, and stored within the array for further analysis.

For the comparison of the accuracy, eight GNSS data sets were chosen to be discussed here (see Table 7.4). All of them are within a time scope of two weeks to ensure similar conditions regarding the perturbations. The availability of data sets was taken into account for the choice of the time scope, e.g. a sample rate of 10 s produces a huge amount of data and was only collected once during the mission.

The first four data sets estimate the orbit until 2020-03-01, each including a different amount of navigation data. A similar approach is taken for the other four data sets, which are separated into two experiments. Over time the perturbations change, thus a maximum amount of three days of input data was used for the analysis. Furthermore, for a potential on-board implementation the data needs to be stored which is limited as well.

Table 7.4: Used data sets for orbit determination and propagation

Exp.	Start time	Estimation time	Data set	Sample Rate
1	2020-02-28 02:00:00	66 h	9 × 100 min every 8 h	60 s
2	2020-02-29 02:00:00	42 h	6 × 100 min every 8 h	60 s
3	2020-03-01 02:00:00	18 h	3 × 100 min every 8 h	60 s
4	2020-03-01 02:00:00	100 min	continuous	60 s
5	2020-03-03 02:00:00	20 h	continuous	60 s
6	2020-03-03 02:00:00	100 min	continuous	60 s
7	2020-03-10 15:00:00	10 h	continuous	10 s
8	2020-03-10 15:00:00	100 min	continuous	10 s

7.4.2 Results from Orbit Determination

One of the outputs of the orbit determination script are the residuals of the observed and estimated data. The initial settings of the estimator led to residuals of up to 60 m for the in-track direction. For the cross-track direction the minimal values are around 20 m and for the radial direction 10 m. These values remain quite constant for estimation times of less than one day. Once the estimation is extended to two or nearly three days, the residuals increase to more than 300 m. The residuals are an indicator for the uncertainties of the measurement, which is specified by Hyperion to be less than 8 m [53]. Tuning the propagator (maximum propagation step, GPS position noise, convergence threshold) led to results of 15–30 m. A longer estimation time, increased the residuals, which is the expected outcome, due to the changing perturbations. Figure 7.20 shows residuals for one day compared to residuals for three days estimation time.

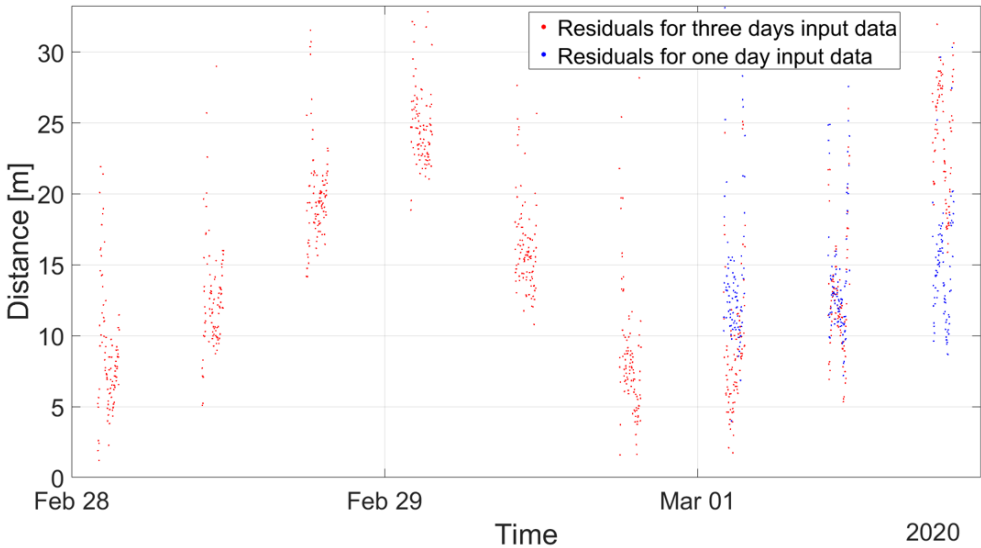


Figure 7.20: Comparison of residuals for different estimation times

In particular for the data set on 2020-03-01 the residuals can be compared for the different estimation times. For the longer estimation time the variation becomes higher. In general for the used propagator, a longer estimation time, as well as a high sample rate or a long continuous data set do not necessarily lead to better

residuals. In Table 7.5, the results of the residual analysis are summarized. All the plots for the three directions and the eight data sets are displayed in Appendix F.

Several observations can be made from the orbit propagation. Similar to the analysis carried out in Section 7.2 the in-track difference is the highest. It is caused by the atmospheric model, which is the most unpredictable and mainly affects the evolution of the in-track component and small contributions to the radial component. Out-of-plane perturbations causing cross-track errors do not include contributions from the atmosphere. Furthermore, for all the data sets, the in-track difference accumulates to at least 2 900 m and up to 6 900 m after 14 days. It is lower than the average difference calculated with the TLEs using the SGP4 model. Especially, the propagation within the first three days is more accurate and the error is significantly better than the one of a TLE set just after publication. Moreover, the amplitude of the in-track difference of TLEs is around 1 km in the beginning (see Figure 7.7). Even for the worst propagation (experiment no.8), the amplitude still remains at 500 m after 14 days. For the first three days, the maximum amplitude of in-track difference is around 60 m. In Figure 7.21, the first propagated error after one day is displayed for all three directions for experiment no.7.

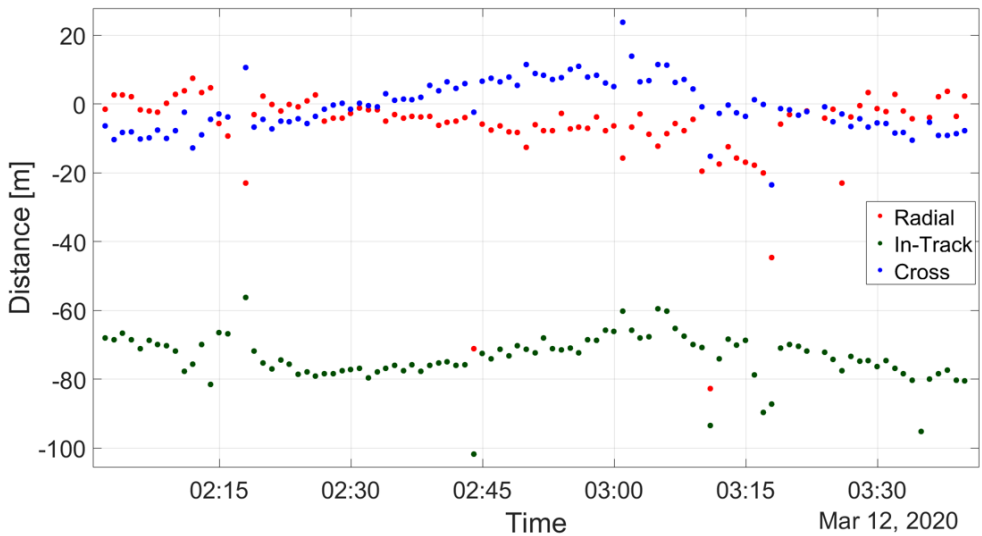


Figure 7.21: In-track, cross-track and radial difference 24h after last GNSS data input

Table 7.5: Residuals and orbit propagation results for the eight data sets after 1/3/7/14 days

Exp.	In-track diff. / Amplitude [m]	Cross-track diff. / [m]	Radial Diff. / [m]	Residuals [m]
1	50 / 10	10	5	30
	190 / 40	25	10	
	990 / 80	80	20	
	3 650 / 60	300	40	
2	15 / 10	10	5	20
	175 / 30	15	10	
	520 / 60	25	10	
	2 900 / 100	130	30	
3	70 / 15	10	5	15
	310 / 40	30	10	
	1 680 / 80	120	20	
	6 800 / 190	500	50	
4	90 / 10	10	10	15
	360 / 30	30	10	
	1 680 / 90	120	20	
	6 300 / 170	470	40	
5	10 / 10	5	5	15
	190 / 40	20	10	
	1 300 / 80	120	20	
	4 370 / 150	380	35	
6	130 / 20	15	10	15
	510 / 60	40	10	
	2 120 / 100	160	20	
	6 600 / 160	500	40	
7	70 / 10	10	10	15
	160 / 40	20	10	
	480 / 70	60	20	
	3 800 / 150	300	40	
8	270 / 40	20	10	15
	720 / 60	100	20	
	2 080 / 100	160	20	
	6 900 / 180	500	80	

The entire set of plots for the three directions and the eight data sets is displayed in Appendix F. The cross-track and radial errors are small for the GNSS-based orbit propagation, even after 14 days. Similar to the analysis of the TLE quality, higher in-track differences come along with larger errors in cross and radial direction. The errors summarized in Table 7.5 are the maximum values within one orbit for the cross and radial direction. All the values are nearly symmetrically distributed around zero (see Appendix F). Therefore, an additional amplitude value was not included to Table 7.5 for the radial and cross direction.

For the first four experiments the residuals increase with additional navigation data, even though the same data set from 2020-03-01 is included in all of them. Nevertheless, the higher residuals do not lead to worse results for the orbit propagation. In this case a combination of average residuals and a data set over two days leads to the best results (experiment no.3).

Furthermore, the comparison of experiment three and four, five and six, seven and eight shows that the inclusion of a larger data set, having the same values for the residuals, will mostly also increase the accuracy in all the directions. Nevertheless, the differences are small compared to the much bigger amount of data, e.g. seven times for experiment no.7 and no.8. The only available data set with a sample rate of 10s shows similar errors after two weeks. The expected output was an improvement compared to a lower sample rate. Further data sets are required to investigate the influence of the sample rate on the residuals as well as the accuracy of orbit determination and propagation in all three directions.

7.4.3 Summary of Orbit Determination and Propagation

Several modified navigation data sets were used to determine the orbit of BEESAT-9. A Python script was tuned to obtain residuals similar to the GNSS200 position error. Longer estimation times led to slightly higher residuals, due to the changing perturbations. Propagated orbits have significantly lower amplitudes for in-track errors and low errors for cross-track and radial in general for the first days compared to TLE based propagations. Furthermore, the results vary only slightly with the amount of included navigation data. Variations derive from other sources, which are included in the used perturbation models of Orekit.

7.5 Conclusion of Navigation Experiments

In the first days after the deployment of BEESAT-9, navigation data was used during the commissioning to identify the satellite amongst the other 25 in the same orbit. Before the first objects were observed on 2019-07-07 and TLEs were published, the initial TLE from the launch provider was used by the ground station to track the satellite. That TLE did not include a B^* value, which explains a drift of several thousand kilometers within the first day. As a consequence no signals were received by BEESAT-9 on 2019-07-06. With the release of the first TLEs flawless mission operations were realized with the help of the GNSS receiver from 2019-07-07, although BEESAT-9 was identified without a doubt only on 2019-07-17 (see Section 7.1). It emphasizes the importance of navigation data during the Launch and Early Orbit Phase to generate a TLE set independently of the JSpOC.

The entire data set of basic navigation data (see Appendix B) from July 2019 until June 2020 was used to analyze the quality of the TLEs and its dependency on certain parameters. A strong correlation was found between the in-track difference and the B^* value, which could help improving TLEs before the upload to the satellite.

Additional data, acquired using the NMEA protocol, was used to analyze the development of the signal strengths throughout the mission time. Furthermore, the C/N_0 development depending on the elevation of GNSS satellites over the GNSS antenna of BEESAT-9 was evaluated. Over the first year on orbit, no degradation of the LNA was found and the C/N_0 plotted against the elevation showed a decrease with lower elevations, which is according to the radiation pattern of the antenna.

The navigation data was used to improve the propagation of the orbit significantly. For the next 24 hours after the last GNSS data set is available the error can be estimated to 50–270 m including the amplitudes throughout the orbit. Furthermore, the usage of the GNSS receiver for one orbit per day with a sample rate of 60 s is sufficient for the mentioned accuracy. Getting to lower discrepancies, e.g. sub-meter, carrier phase and pseudo range data is required (see Chapter 2). Depending on the requirements, a duty cycle of one orbit per day could be implemented on a 1U CubeSat. For BEESAT-9, the energy and data downlink budget remains positive for that configuration, including a three-axis stabilization.

8 Summary, Conclusion and Outlook

The research about the integration of a GNSS receiver on a 1U CubeSat and the implementation of a Precise Position and Orbit Determination package was the main purpose of this thesis. Further investigations were put into the three-axis stabilization, which was considered a precondition for navigation experiments. These two main topics were accompanied by the modification of the existing system concept of the predecessor mission BEESAT-2 and the verification of all the implemented systems on the ground and on orbit. Recommendations for the implementation of a GNSS receiver into a 1U CubeSat can be derived from the work described in this thesis.

8.1 Summary

This thesis starts with a brief introduction about the development of satellites, starting with the nanosatellite Sputnik-1 to ever increasing sizes of satellites back to nanosatellites in the 1990s. With the publication of the CubeSat Design Specification in 1999 a new era began, the rise of the CubeSats. It was mainly used by universities for educational purposes and technology demonstration in the beginning with many launches of 1U CubeSats. Latest from 2010 the focus switched to 3U CubeSats and the foundation of many companies, providing satellites, subsystems, components and ride share launches. It was pointed out that many application fields could be complemented by pico- and nanosatellites with several constellations already fully implemented in orbit (Planet, Spire Global), successful technology demonstrator missions or announced concepts. Furthermore, it was stated, that within all these commercially driven projects, niches for universities are always found and the TU Berlin, categorized as a flagship university is playing a major role. A GNSS receiver and alongside the implementation of a PPOD package is essential for future missions. To put the integration of the GNSS receivers into a context, the mission objectives of all BEESAT projects are summarized. Using the example of BEESAT-4 and BEESAT-9 the idea of the PPOD package is introduced.

The history of Global Navigation Satellite Systems starting with the US-American Global Positioning System is described, followed by the investigation into all the benefits of GNSS receivers on board of satellites. Next to the inherent basic navigation data (position, velocity, DOPs, status) and a precise timing for the synchronization of all the subsystems, additional data can be provided to further increase the accuracy of the position and velocity for several applications, such as altimetry, gravimetry and SAR interferometry. Until now, these missions require processing of navigation data on the ground for the necessary precision and accuracy. Recently, simulations with Swarm-C showed possible implementations on board of the satellites in the near future. Outlining the importance of GNSS receivers for constellations, formations and swarms is another part of Chapter 2. Partially these missions will be performed with CubeSats, e.g. the formation flight mission NanoFF. To put the research of this thesis into a context of the state of the art, an overview of 1U CubeSats with integrated GNSS receivers is given and results of the AeroCube-4 mission are summarized. Moreover, all the GNSS receivers on the market, which physically fit into a 1U CubeSat are categorized and a short estimation for their potential use is given.

In Chapter 3 it was analyzed, that a physically fitting receiver does not immediately ensure its continuous operation or the downlink of the acquired data to the ground. There are many challenges that arise from the implementation of the PPOD package. For each subsystem, the potential consequences were outlined and it can be seen, that the Electrical Power System, the Communications System and the Attitude Determination and Control System are affected most. Nevertheless, for each subsystem a distinctive analysis is necessary, which is driven by the selected receiver. The selection mainly depends on the mission objective and the requirements of the navigation subsystem. Looking at the introduced modules in Table 2.1 the power consumption varies from 150 mW to 2 W, which is a huge range for 1U CubeSats. For the COM, it depends on the required data on the ground, but recent developments on S-Band and X-band transmitters could solve this issue soon and increase the downlink capacity by a margin of up to 500 compared to the commonly used VHF/UHF. Similar thoughts have to be put into the ADCS. To ensure a navigation fix all the time, a dedicated pointing of the GNSS antenna is required, which challenges the EPS additionally. Moreover, some of the receivers have TTFFs of up to 15 minutes, which also calls for a stabilized satellite. A summary of the recent developments of these three subsystems showed, that a hypothetical 1U CubeSat could fulfill the previously discussed requirements in the near future, once these developments are merged.

For this thesis, the preconditions were already set and the GNSS receivers had to be integrated in the mature picosatellite bus of BEESAT-2, which is based on the development of the single-fault tolerant BEESAT-1. Its evolution is described for selected subsystems and the redundancy concepts are summarized. All the used sensors and actuators as well as the implemented algorithms of the ADCS are introduced, with most of them still being in use on BEESAT-9. Nevertheless, modifications were applied to all successor missions according to their primary objective. For BEESAT-2, the focus was set on the three-axis stabilization and the integration of a PDH together with a new camera. Furthermore, the ground segment was prepared for multi-mission operations. The integration of the GPS receiver Phoenix on BEESAT-4 entailed several modifications to other subsystems and came along with the implementation of new attitude sensors to make use of the latest development in the MEMS sensor segment. The density of payloads and the amount of MEMS sensors was further increased on BEESAT-9, where also the development of new GNSS receivers was taken advantage of. The smaller dimensions of the GNSS200 compared to the Phoenix allowed for further integration of ADCS components, the pFDA and arrays of magnetic field sensors and gyroscopes. Next to the ground operations software tools, special scripts were implemented for the analysis of the navigation data.

The implemented modifications and additional features of BEESAT-4 and BEESAT-9 were verified with tests and simulations. Chapter 5 starts with a table of all the subsystems and components and their status. It is discussed afterwards which steps of the manufacturing and assembly are done in-house or externally. The integration process is displayed and the preliminary work is described. For a successful on-orbit performance, the focus of the tests and simulations in this thesis was put on the ADCS and the GNSS. Available facilities and testbeds were utilized to set up conditions as close as possible to the space environment. Afterwards, an environmental test campaign was conducted to space prove the two satellites and to fit the requirements of the launch providers. For an accurate ADCS all the attitude sensors were calibrated. For BEESAT-9 the strategy was adapted to further enhance the accuracy. After the verification campaign, both satellites were well prepared to fulfill their mission objectives.

With the deployment of the satellites the mission operations started, which were initiated with the LEOP and commissioning. For BEESAT-4 the focus was set on the ADCS. After the re-calibration of the magnetic field sensors, the attitude determination was verified and its accuracy quantified. A reliable three-axis stabilization could be confirmed after several software updates and is used for

dedicated pointing since August 2017 with an overall accuracy of $\alpha_{err} = 3-7^\circ$. All the implemented ADCS modes were tested and reliably point the satellite towards its desired target. The operations with the GPS receiver Phoenix used two strategies, one without zenith pointing and one with zenith pointing of the antenna. For the latter, two GPS satellites were tracked, but a navigation fix was never achieved. Being launched inside BIROS and equipped with the same UHF transceiver, Inter Satellite Link experiments were executed. All the initially established verification steps were fulfilled on orbit. During an approach in August 2018, BIROS commanded BEESAT-4 to point its camera nadir, take three pictures and transmit them to BIROS. Afterwards the pictures were downloaded from BIROS to the ground. Statistics from operations with BEESAT-4 showed a download of 100.05 MB via four ground stations, at around 95 % being received in Berlin. BEESAT-9 went through the LEOP and commissioning as well and the magnetic field sensors required a re-calibration, too. Further enhancements of the ADCS were tested and showed an improvement of the accuracy of the control algorithm with the usage of the new gyroscope array. Experiments with the GNSS200 were the main focus and were executed daily for the acquisition of navigation data. Position and velocity data, as well as status parameters of the navigation fix was stored and downloaded together with extended telemetry to evaluate the signal strength of the GNSS satellites at the receiver. For BEESAT-9 the amount of accumulated downloaded data is 59.8 MB from three ground stations.

All the acquired navigation data was used for detailed analysis in Chapter 7. After the deployment it helped to identify BEESAT-9 among the 25 objects launched into the same orbit simultaneously. It ensured a flawless communication, once the first TLEs were published. Navigation data sets from July 2019 until June 2020 were compared to the TLE based ephemerides, calculated with the SGP4 orbit model. It was shown, that the quality of a TLE for a 1U CubeSat significantly depends on the atmospheric drag coefficient B^* . Radial, in-track and cross-track discrepancies between the GNSS and the TLE based positions were plotted for the “best” and the “worst” TLE. A modification of the B^* value in the “worst” TLE improved the results significantly. For all the TLEs, it can be seen, that the in-track difference is affected the most and the discrepancies are always higher than for radial and cross-track directions. Another research question addressed the signal strength of the GNSS satellites at the receiver. The degradation of the LNA of the GNSS antenna was investigated over the mission time. After one year the distribution of signal strengths remains similar to the start of the mission. Furthermore, the elevation of the GNSS satellites was taken into account, since BEESAT-9 was tumbling during

the data acquisition. High elevations accordingly lead to higher C/N_0 , but also satellites with elevations of less than zero degree are tracked by the GNSS200. The navigation data was also used for orbit determination and the propagation of the ephemerides up to 14 days to the future. It was analyzed how various amounts of navigation data affect the accuracy of the propagation. Furthermore, different sample rates were used for the same analysis. The propagated orbits were also compared to the ephemerides obtained from the analysis in Section 7.2 using a TLE based SGP4 orbit model.

8.2 Conclusion

CubeSats have an increasing role in the development of future applications by complementing bigger satellites. Moreover, technical developments and miniaturization of their components are of relevant importance for the near future. Despite the significant and predominant growth in the market of commercial constellations, missions executed by flagship universities are seemingly relevant, given their particular focus on miniaturization, which in consequence leads to the reduction of costs and increase of scientific and technological outcomes.

Given, that most of the applications require an accurate position determination and timing, a GNSS receiver should be part of the satellite bus. In particular for missions that require formation flight capabilities, a reliable solution is absolutely crucial. Recent developments of compact GNSS receivers led to multiple solutions which are suitable for different applications and can be integrated and operated on a 1U CubeSat.

Individual challenges need to be addressed for every CubeSat mission, mainly regarding the EPS, the COM and the ADCS. Recent component development for each subsystem could solve the determined problems and support a continuous, reliable operation of a GNSS receiver, while allowing the download of the acquired data for further data processing which would guarantee an increase in accuracy for ground based data processing. The system of BEESAT-1 was ahead of its time in 2006, being a 1U CubeSat with a single-fault tolerant design and enhanced redundancy concepts. The achievements of all successor missions are related to the integration density of the payloads and the inclusion of the latest technologies. However, it must be acknowledged that the requirements by 2020 demand the development of new concepts that allow further miniaturization with maximal

performance, i.e. including latest integrated circuits such as microcontrollers or sensors to optimize the performance of the subsystems. Nevertheless, the integration of two different GNSS receivers into BEESAT-4 and BEESAT-9 was realized. Additionally, ground station tools for the analysis of the acquired data were adapted and could be implemented on orbit for future missions.

During the verification of the integrated subsystems, several test procedures were applied to ensure a reliable system on orbit. Enhanced strategies are required to verify both, the software and hardware concepts, particularly when dedicated testbeds are lacking, as for the ADCS of BEESAT-4. Finally, on-orbit experiments were used to solve the problems with the ADCS, but a combination of hardware-in-the loop simulations and the usage of external test facilities could have solved these issues on the ground before the launch.

Problems related to the calibration of the magnetic field sensors were taken into account when preparing a new script to enable a re-calibration of the sensors right after the launch. Although, BEESAT-4 and BEESAT-9 successfully finished the calibration campaign, on-orbit adaptations were necessary to accomplish their mission objectives.

Both satellites withstood the loads during the launch without any damage and were commissioned successfully. On BEESAT-4, a reliable three-axis stabilization was implemented and the accuracy was increased compared to BEESAT-2. A new generation of MEMS attitude sensors was integrated on BEESAT-9 and the control of the satellite was enhanced even further. Regardless, several issues were identified, that could increase the ADCS accuracy further. The fusion of all the attitude sensors and filtering of the measurements could lead to better results and is highly recommended for future missions.

Operating the Phoenix receiver did not produce the expected outcome, since it is not quite feasible for a 1U CubeSat, although acquiring navigation data should still be possible. It can be concluded, that the selection of the antenna and its LNA probably required more testing on the ground and a different selection might have led to a successful implementation of the receiver. Still, the analysis of the energy budget showed, that a duty cycle of no more than 7–9% is possible, including a power off of the attitude sensors during standby. Clearly this does not support many applications, e.g. formation flights, which require continuous recording of navigation data. Another feature of a formation flight mission, the ISL was verified with BEESAT-4 and commanding another satellite from a distance of up to 100 km is possible with the implemented hardware.

During the mission of BEESAT-9 a smaller and more power efficient GNSS receiver fulfilled its purpose perfectly and acquired navigation fixes on a daily basis without the satellite being stabilized. For several experiments, a continuous operation of the GNSS200 was commanded. Downloading the acquired data exceeded the acquisition time by a factor of up to ten. Furthermore, the magnetic field and sun sensors were switched off to maintain a positive energy budget. Still, it can be concluded, that small modifications in the system concept could enable a continuous operation. On BEESAT-9, the PDH has to be switched on for navigation experiments, this could be avoided by putting the receiver on a satellite bus electronic board. Downloading the data, especially extended telemetry, like pseudorange and carrier phase data definitely requires a different frequency band than UHF, e.g. S-Band or X-Band. Another issue is the reliability, which can only be near 100 % with a dedicated attitude of the satellite to avoid the GNSS antenna to point towards Earth. For BEESAT-9, the TTFF was low and the navigation fix was usually not lost, but on several occasions no position data was provided for a few minutes within an experiment. Since the data is available at a sample rate of 60s, the navigation fix losses were not systematically analyzed. It would require a data set every second to ensure the identification of the losses.

Most of the ride share launches include big numbers of CubeSats, which are usually deployed into the same orbit. Identifying the satellites with the help of navigation data is essential to support the ground station personnel, particularly during the LEOP and commissioning. Once the first TLEs were released, a small amount of navigation data helped to assign BEESAT-9 to some of those objects. Assigning the correct TLEs to BEESAT-9 took two weeks, since some time was required to include the GNSS200 into daily mission operations. For future missions, the GNSS receiver will be part of the satellite bus and the required amount of navigation data will be produced and downloaded to propagate the orbit and estimate TLEs on the ground after the first pass over a ground station.

Furthermore, the TLEs could be directly estimated on orbit to further improve the operations. A systematic analysis of the TLEs for nine months showed a high dependency of the quality on the B^* value. Experience with the development of the B^* value and the quality of the TLEs is essential before a modification of B^* for its usage on orbit can be considered. For BEESAT-9, an update rate of 10 days was concluded to be sufficient to fulfill the accuracy requirements constantly.

The analysis of the signal strength confirmed most of the expectations. The C/N_0 decreases with lower elevations of GNSS satellites over the antenna. One

unforeseen outcome of the experiments was the high amount of received signals from an elevation of less than zero degree. These signals enter the back of the antenna and additionally have to cross the satellite. Nevertheless, the C/N_0 was high enough for the receiver to include these satellites into the navigation solution. In contrast to BEESAT-4, a decreasing C/N_0 cannot be seen for the first year of operations.

An orbit propagation was carried out for several navigation data sets. It could be shown, that the results lead to significantly better accuracies compared to the SGP4 orbit model based on TLEs. Furthermore, duty cycles of one orbit per day were analyzed as well and only showed slightly less accurate results compared to higher sample rates or longer duty cycles. These findings can be used to adapt the operations of the AOCS according to the energy budget of the satellite. Especially if a receiver with a higher power consumption than the GNSS200 is used, most likely it can not operate continuously. Nevertheless, the adapted strategy will always depend on the required accuracy of the orbit determination and it was demonstrated, that decent accuracies are already achieved with the strategy applied on BEESAT-9

This thesis remarks the feasibility of three-axis stabilization, ISL and operations with a GNSS receiver on a 1U CubeSat, which can be adapted to satellites of larger dimensions. Furthermore, it can be concluded that the BEESAT satellite bus is feasible and reliable for the utilization in space and the implementation of a PPOD package.

8.3 Outlook for Future Missions

The experiences gained throughout the BEESAT projects were already included into other missions of the Chair of Space Technology at TU Berlin. In particular, one future mission will mainly benefit from the results and conclusions drawn from this work. Within NanoFF, the operational scenario includes flying several formations with two satellites down to a minimum distance of 50 m. This requires an accurate AOCS with on-board navigation and the exchange of data between the two satellites. The attitude control will feature star trackers to increase the accuracy of the attitude determination and also the mentioned improvements, e.g. filtering of sensor measurements and sensor fusion will be applied. Baseline of the ADCS are the implementations from the BEESAT line and the work of Gordon

[140]. The analysis of the navigation data will be used to implement an on-board navigation system, extended with relative navigation features. Furthermore, the knowledge gained from the ISL experiments of BIROS and BEESAT-4 will help to setup a reliable connection between the two satellites of the NanoFF during their autonomous flight maneuvers.

The author's future work will focus on further technology demonstration of components, subsystems and applications on CubeSats within the NanoFF project. With the experience and knowledge from the conducted and successfully completed missions, the performance of the next missions will be taken to the next level, regarding the miniaturization as well as the scientific output in formation flight technology and Earth observation with a hyperspectral camera.

Bibliography

- [1] J. Bouwmeester and J. Guo. "Survey of worldwide pico- and nanosatellite missions, distributions and subsystem technology". In: *Acta Astronautica* 67 (Oct. 2010), pp. 854–862.
- [2] K. Brieß. "Small Satellite Programmatics of the Technische Universität Berlin". In: *11th IAA Symposium on Small Satellites for Earth Observation*. Berlin, Germany, Apr. 2017.
- [3] R. Schulte. "TUBSAT-N, A Global Communication Ssatellite System, based on Nanosatellites". In: (1998). presented at the Small Satellites Systems and Services Symposium, Antibes, France.
- [4] *CubeSat Design Specification, Rev 13*. The CubeSat Program, Cal Poly SLO. 2014.
- [5] C. Williams, B. Doncaster, and J. Shulman. *Nano/Microsatellite Market Forecast 8th Edition*. Tech. rep. SpaceWorks Enterprises, 2018.
- [6] C. Williams and S. DelPozzo. *Nano/Microsatellite Market Forecast 10th Edition*. Tech. rep. SpaceWorks Enterprises, 2020.
- [7] E. Kulu. *Nanosats Database*. visited on 2020-07-15. URL: <https://www.nanosats.eu/>.
- [8] Planet. *Planet*. visited on 2020-07-15. URL: <https://www.planet.com/>.
- [9] Spire. *Spire*. visited on 2020-07-15. URL: <https://www.spire.com/en>.
- [10] Astrocast. *Astrocast – Global M2M connectivity for global businesses at the lowest cost*. visited on 2020-07-15. URL: <https://www.astrocast.com/products-astronode-s/>.
- [11] Spacewatch Asia Pacific. *Fleet Space Selects Tyvak To Mass-Produce Satellites For Its Low Earth Orbit constellation*. visited on 2020-07-15. URL: <https://spacewatch.global/2020/02/fleet-space-selects-tyvak-to-mass-produce-satellites-for-its-low-earth-orbit-constellation/>.
- [12] E. Kulu. *NewSpace Constellations*. visited on 2020-07-15. URL: <https://www.newspace.im/>.

- [13] NASA. *NASA Space Science Data Coordinated Archive*. visited on 2020-07-15. URL: <https://nssdc.gsfc.nasa.gov/nmc/spacecraft/query>.
- [14] J. Chin et al. *CubeSat 101 Basic Concepts and Processes for First-Time CubeSat Developers*. Technical Report. NASA, 2017.
- [15] H. Kayal and K. Brieß. "Pico- and Nanosatellite Technologies at the TU Berlin". In: *56th International Astronautical Congress (IAC)*. Fukuoka, Japan, Oct. 2019.
- [16] E. Kulu. *Nanosatellites and CubeSat Companies*. visited on 2020-07-15. URL: <https://www.nanosats.eu/companies>.
- [17] S. Weiß et al. "NanoFF: A 2U-CubeSat formation flight mission". In: *70th International Astronautical Congress (IAC)*. Washington D.C., USA, Oct. 2019.
- [18] S. Doshi, D. Lam, and H. Panag. "Cubesat Constellation for Monitoring and Detection of Bushfires in Australia". In: *Fourth Annual Mission Idea Contest*. Bulgaria, 2016.
- [19] B. Lal et al. *Global Trends in Small Satellites*. Tech. rep. 2017.
- [20] M. Swartwout and C. Jayne. "University-Class Spacecraft by the Numbers: Success, Failure, Debris. (But Mostly Success.)" In: *Proc. of 30th Annual AIAA/USU Conference on Small Satellites (SmallSat 2016)*. Logan, UT, USA, 2016.
- [21] M. Barschke et al. "The TUBIN mission - Wildfire Detection Dsing Nanosatellites". In: *presented at the 64th German Aerospace Congress*. Rostock, Germany, Sept. 2015.
- [22] J. Großhans. *SALSAT - Spectrum AnaLysis SATellite*. visited on 2020-07-15. URL: https://www.raumfahrttechnik.tu-berlin.de/menue/forschung/aktuelle_projekte/salsat/parameter/en/.
- [23] V. McGregor. *Mars Cube One Demo*. visited on 2020-07-15. URL: https://www.jpl.nasa.gov/news/press_kits/insight/launch/appendix/mars-cube-one/.
- [24] F. Baumann. *Verification of miniaturized Reaction Wheels for Picosatellites (Microwheels II) – BEESAT-1*. visited on 2020-07-15. URL: https://www.raumfahrttechnik.tu-berlin.de/menue/forschung/abgeschlossene_projekte/beesat/parameter/en/.

- [25] H. Kayal, F. Baumann, and K. Brieß. "Beesat – A Pico Satellite for the In-Orbit Verification of Miniaturised Wheels". In: *6th IAA Symposium on Small Satellites for Earth Observation*. Berlin, Germany, 2007.
- [26] S. Trowitzsch. *BEESAT-2*. visited on 2020-07-15. URL: https://www.raumfahrttechnik.tu-berlin.de/menue/research/current_projects/beesat_2/parameter/en/.
- [27] S. Trowitzsch, F. Baumann, and K. Brieß. "BEESAT-2 – A Picosatellite Demonstrating Three-Axis Attitude Control with Reaction Wheels". In: *62. Deutscher Luft- und Raumfahrtkongress*. Stuttgart, Germany, 2013.
- [28] T. Funke et al. "Development of a distributed ground segment for multi-mission satellite operations". In: *2nd IAA Conference on University Satellites Missions*. Rome, Italy, Feb. 2013.
- [29] M. Barschke. *BEESAT-3*. visited on 2020-07-15. URL: https://www.raumfahrttechnik.tu-berlin.de/menue/research/current_projects/beesat_3/parameter/en/.
- [30] M. F. Barschke, P. Werner, and S. Kapitola. "BEESAT-3 commissioning - better late than never". In: *Proceedings of the 69th International Astronautical Congress*. 2018.
- [31] O. Montenbruck and M. Markgraf. *User's Manual for the Phoenix GPS Receiver*. Manual. July 2008.
- [32] S. Weiß. *Die Picosatellitenmission BEESAT-4*. presented at internal Colloquium on 2013-12-16, unpublished.
- [33] T. Terzibaschian. *Zwei ungleiche Brüder - Warum 'kann' BIROS "AVANTI" und TET-1 nicht?* visited on 2020-07-15. URL: https://www.dlr.de/blogs/desktopdefault.aspx/tabid-7023/11643_read-938/searchtagid-61665/.
- [34] G. Gaias, J.-S. Ardaens, and C. Schultz. "The AVANTI experiment flight results". In: *Proceedings of GNC 2017*. 2017.
- [35] S. Weiß. *BEESAT-4*. visited on 2020-07-15. URL: https://www.raumfahrttechnik.tu-berlin.de/menue/forschung/aktuelle_projekte/beesat_4/parameter/en/.
- [36] S. Weiß, F. Kempe, and K. Brieß. "GPS-Tracking on the Three-Axes-Stabilized Satellite BEESAT-4". In: *7th Pico and Nano Satellite Workshop 2013*. Würzburg, Deutschland, Sept. 2013.

- [37] S. Weiß, F. Kempe, and K. Brieß. "Mission objectives of the picosatellite BEESAT-4". In: *8th Pico and Nano Satellite Workshop 2015*. Würzburg, Deutschland, Sept. 2015.
- [38] F. Baumann. *BEESAT-5-8*. visited on 2020-07-15.
- [39] S. Weiß and S. Kapitola. *Die Picosatellitenmission BEESAT-9*. presented at internal Colloquium on 2020-07-15, unpublished.
- [40] S. Weiß. *BEESAT-4 Abschlussbericht Phase B*. Technical Report. unpublished. TU Berlin, 2013.
- [41] ESA. *Landsat-4 and Landsat-5*. visited on 2020-07-15. URL: <https://earth.esa.int/web/eoportal/satellite-missions/l/landsat-4-5>.
- [42] DLR. *Real-Time Onboard Navigation*. visited on 2020-07-15. URL: https://www.dlr.de/rb/en/desktopdefault.aspx/tabid-10749/10533_read-23359/.
- [43] O. Montenbruck and M. Markgraf. *User's Manual for the GPS Orion-S/-HD Receiver*. June 2003.
- [44] DLR. *Phoenix Spaceborne GPS Receiver Datasheet*. visited on 2020-07-15. URL: https://www.dlr.de/rb/en/Portaldata/38/Resources/dokumente/GSOC_dokumente/RB-RFT/Phoenix_DataSheet_v11.pdf.
- [45] SSTL. *Space GPS Receiver SGR-05P Datasheet*. visited on 2020-07-15. URL: <https://www.sstl.co.uk/getattachment/Media-Hub/Featured/Navigation/SGR-05P-Datasheet-2018-V2-Read-Only.pdf?lang=en-GB>.
- [46] SSTL. *Space GNSS Receiver SGR-Ligo Datasheet*. visited on 2020-07-15. URL: <https://www.sstl.co.uk/getattachment/Media-Hub/Featured/Navigation/SGR-Ligo-Datasheet-2018-V2-Read-Only.pdf?lang=en-GB>.
- [47] New Space Systems. *NGPS-03-422 Datasheet*. visited on 2020-07-15. URL: http://www.newspacesystems.com/wp-content/uploads/2018/10/NewSpace-GPS-Receiver_8b.pdf.
- [48] Space Quest. *GNSS-701 Satellite GNSS Receiver Datasheet*. visited on 2020-07-15. URL: <http://www.spacequest.com/attitude-determination-control/gps12-v1>.
- [49] Novatel. *Space GPS Receiver OEM4-G2L Datasheet*. visited on 2020-07-15. URL: <https://www.novatel.com/assets/Documents/Papers/oem4g2l.pdf>.

- [50] Gomspace. *Nanosense GPS Kits Datasheet*. visited on 2020-07-15. URL: [https://gomspace.com/UserFiles/Subsystems/datasheet/gs-ds-nanosense-gpskit-\(1\).pdf](https://gomspace.com/UserFiles/Subsystems/datasheet/gs-ds-nanosense-gpskit-(1).pdf).
- [51] Pumpkin Space. *GNSS Receiver Module (GPSRM 1) Kit Datasheet*. visited on 2020-07-15. URL: https://www.pumpkinspace.com/store/p58/GNSS_Receiver_Module_%28GPSRM_1%29_Kit.html#.
- [52] u-blox. *NEO-M8 series*. visited on 2020-07-15. URL: <https://www.u-blox.com/en/product/neo-m8-series?lang=de>.
- [53] Hyperion Technologies. *GNSS200 Datasheet*. visited on 2020-07-15.
- [54] WARPSPACE. *Space GNSS Receiver Warpspace Datasheet*.
- [55] SkyTraQ Technologies. *Space GPS Module Venus838 Datasheet*. visited on 2020-07-15. URL: <http://navspark.mybigcommerce.com/gps-for-small-micro-satellite-cubesat/>.
- [56] W. Ley, K. Wittmann, and W. Hallmann. *Handbook of Space Technology*. John Wiley and Sons, Ltd., 2009.
- [57] Saika Aida et al. "Accuracy Assessment of SGP4 Orbit Information Conversion into Osculating Elements". In: *6th European Conference on Space Debris*. Darmstadt, Germany, 2013.
- [58] G. Bonin et al. "CanX-4 and CanX-5 Precision Formation Flight: Mission Accomplished!" In: *29th AIAA/USU Conference on Small Satellites*. SSC15-I-4. Utah, 2015.
- [59] O. Montenbruck and E. Gill. *Satellite Orbits*. Springer, 2005.
- [60] E. Gill and O. Montenbruck. "Comparison of GPS-based Orbit Determination Strategies". In: *European Space Agency, (Special Publication) ESA SP 548* (Jan. 2004), p. 169.
- [61] O. Montenbruck, E. Gill, and R. Kroes. "Rapid Orbit Determination of LEO Satellites Using IGS Clock and Ephemeris Products". In: *GPS Solutions* 9 (Sept. 2005), pp. 226–235.
- [62] M. Wermuth et al. "TerraSAR-X precise orbit determination with real-timeGPS ephemerides". In: *Advances in Space Research* (Mar. 2012).
- [63] A. Hauschild et al. "Precise Onboard Orbit Determination for LEO Satellites with Real-Time Orbit and Clock Corrections". In: *29th International Technical Meeting of the Satellite Division of The Institute of Navigation*. Portland, Oregon, Sept. 2016, pp. 3715–3723.

- [64] A. Hauschild et al. *Innovation: Orbit determination of LEO satellites with real-time corrections*. visited on 2020-07-15. Apr. 2017. URL: <https://www.gpsworld.com/innovation-orbit-determination-of-leo-satellites-with-real-time-corrections/>.
- [65] Smithsonian. *Synchronized Accurate Time*. visited on 2020-07-15. URL: <https://timeandnavigation.si.edu/satellite-navigation/gps/synchronized-accurate-time>.
- [66] NASA. *What is an Atomic Clock*. visited on 2020-07-15. URL: <https://www.nasa.gov/feature/jpl/what-is-an-atomic-clock>.
- [67] NASA. *Deep Space Atomic Clock*. visited on 2020-07-15. URL: https://www.nasa.gov/sites/default/files/atoms/files/dsac-factsheet_2019.pdf.
- [68] ESA. *Precise Time Reference*. visited on 2020-07-15. URL: https://gssc.esa.int/navipedia/index.php/Precise_Time_Reference.
- [69] National Oceanic and Atmospheric Administration. *Other Global Navigation Satellite Systems (GNSS)*. visited on 2020-07-15. URL: <https://www.gps.gov/systems/gnss/>.
- [70] OneWeb. *OneWeb*. visited on 2020-07-15. URL: <https://www.oneworld.com/>.
- [71] SpaceX. *Starlink Mission*. visited on 2020-07-15. URL: <https://www.spacex.com/webcast?>.
- [72] A. Farrag, T. Mahmoud, and A. Y. ElRaffiei. "Satellite swarm survey and new conceptual design for Earth observation applications". In: *The Egyptian Journal of Remote Sensing and Space Sciences* (Dec. 2019).
- [73] GP Advanced Project Srl. *Flexible Experimental Embedded Satellite Mission*. visited on 2020-07-15. URL: <http://www.gpadvancedprojects.com/fees>.
- [74] ESA. *JC2Sat-FF (Japan Canada Joint Collaboration Satellites – Formation Flying)*. visited on 2020-07-15. URL: <https://directory.eoportal.org/web/eoportal/satellite-missions/j/jc2sat-ff>.
- [75] ESA. *FAST (Formation for Atmospheric Science and Technology Demonstration)*. visited on 2020-07-15. URL: <https://earth.esa.int/web/eoportal/satellite-missions/f/fast>.
- [76] NASA. *The Afternoon Constellation*. visited on 2020-07-15. URL: <https://atrain.nasa.gov/>.

- [77] NASA. *Landsat-7*. visited on 2020-07-15. URL: <https://landsat.gsfc.nasa.gov/landsat-7/>.
- [78] DLR. *TanDEM-X*. visited on 2020-07-15. URL: https://www.dlr.de/rd/desktopdefault.aspx/tabid-2440/3586_read-16692/.
- [79] ESA. *Swarm*. visited on 2020-07-15. URL: https://www.esa.int/Applications/Observing_the_Earth/Swarm.
- [80] Space Flight Laboratory. *CanX-1: Canada's First Nanosatellite*. visited on 2020-07-15. URL: <http://www.utias-sfl.net/nanosatellites/CanX1/CanX1Index.html>.
- [81] eoPortal Directory. *CubeSat - Launch 1*. visited on 23.01.2020. URL: <https://earth.esa.int/web/eoportal/satellite-missions/c-missions/cubesat-launch-1>.
- [82] E. Kulu. *Database Nanosats Airtable*. visited on 2020-07-15. URL: <https://airtable.com/shrafcwXODMMKeRgU/tbldJoOBP5wINOJQY?blocks=hide>.
- [83] Sky Fox Labs. *Lucky-7 Mission*. visited on 2020-07-15. URL: <https://www.lucky7satellite.org/mission>.
- [84] B. Welsh. *Andesite*. visited on 2020-07-15. URL: <https://www.bu.edu/busat/missions/andesite/>.
- [85] J. B. Parham et al. "Networked Small Satellite Magnetometers for Auroral Plasma Science". In: *Journal of Small Satellites* (2019).
- [86] NavSPark Store. *GPS for Small Satellite, Micro Satellite, CubeSat*. visited on 26.01.2020. URL: <http://navspark.mybigcommerce.com/gps-for-small-micro-satellite-cubesat/>.
- [87] J. W. Gangestad, B. S. Hardy, and D. A. Hinkley. "Operations, Orbit Determination, and Formation Control of the AeroCube-4 CubeSats". In: *27th AIAA/USU Conference on Small Satellites*. SSC13-X-4. Utah, 2013.
- [88] J. Gangestad et al. *Flight Results from AeroCube-6 :A Radiation Dosimeter Mission in the 0.5U Form Factor*. Presentation. The Aerospace Corporation, Apr. 2015.
- [89] L. Stras et al. *The Design and Operation of the Canadian Advanced Nanospace eXperiment (CanX-1)*. 2003.
- [90] Space Flight Laboratory. *CANX-1: Canada's first nanosatellite*. visited on 2020-07-15. URL: https://www.utias-sfl.net/?page_id=393.

- [91] K. Sarda et al. "Canadian Advanced Nanospace Experiment 2: On-Orbit Experiences with a Three-Kilogram Satellite". In: *22nd AIAA/USU Conference on Small Satellites*. SSC08-II-5. Utah, 2008.
- [92] A. Scholz. *COMPASS-1 Concept Study Report*. Technical Report. FH Aachen, Sept. 2003.
- [93] J. Giebelmann, M. Plischke, and A. Scholz. *Compass-1 Qualification Review*. Presentation. FH Aachen, June 2006.
- [94] A. Scholz et al. *Flight results of the COMPASS-1 Mission*. Technical Report. FH Aachen, Mar. 2009.
- [95] EO-Portal. *COMPASS-1*. visited on 2020-17-15. URL: <https://directory.eoportal.org/web/eoportal/satellite-missions/c-missions/compass-1>.
- [96] DLR. *Phoenix Miniature GPS Receiver*. visited on 2020-17-15. URL: https://www.dlr.de/rb/en/desktopdefault.aspx/tabid-10749/10533_read-23353/.
- [97] J. Giesselamnn and A. Aydinlioglu. *COMPASS-1: Phase B Documentation*. Technical Report. FH Aachen, June 2004.
- [98] DLR. *PRISMA Formation Flying Misson*. visited on 2020-17-15. URL: https://www.dlr.de/rb/desktopdefault.aspx/tabid-10749/10535_read-23364/.
- [99] Sensor Systems Inc. *GPS L1 Antenna*. visited on 2020-17-15. URL: <http://www.sensorantennas.com/product/gps-l1-antenna-2/>.
- [100] C. Hall. *Spacecraft Attitude Dynamics and Control*. 2003.
- [101] M. D. Shuster and S. Oh. "Three-Axis Attitude Determination from Vector Observations". In: *Journal for Guidance and Control* (1981).
- [102] D. Hinkley and B. Hardy. *Picosatellites and Nanosatellites at The Aerospace Corporation*. Presentation. The Aerospace Corporation, Feb. 2012.
- [103] SpaceRefInteractive. *AeroCube-4 Captures Images of the Moon's Shadow*. visited on 2020-07-15. Sept. 2013. URL: <http://spaceref.com/nasa-hack-space/aerocube-4-captures-images-of-the-moons-shadow.html>.
- [104] EO-Portal. *AeroCube-4*. visited on 2020-17-15. URL: <https://directory.eoportal.org/web/eoportal/satellite-missions/a/aerocube-4#foot8%29>.
- [105] Swarm. *Swam Technologies*. visited on 2020-17-15. URL: <https://www.swarm.space/>.

- [106] G. D. Krebs. *SpaceBEE 1,2,3,4*. visited on 2020-17-15. URL: https://space.skyrocket.de/doc_sdat/spacebee.htm.
- [107] NASA. *Global Positioning System History*. visited on 2020-17-15. Aug. 2017. URL: https://www.nasa.gov/directorates/heo/scan/communications/policy/GPS_History.html.
- [108] National Oceanic and Atmospheric Administration. *Selective Availability*. visited on 2020-07-15. URL: <https://www.gps.gov/systems/gps/modernization/sa/>.
- [109] Ravtrack. *COCOM GPS Tracking Limits*. visited on 2020-17-15. 2020. URL: <http://ravtrack.com/GPStracking/cocom-gps-tracking-limits/469/>.
- [110] DLR. *GPS Orion Receiver*. visited on 2020-17-15. URL: https://www.dlr.de/rb/desktopdefault.aspx/tabid-10749/11127_read-25360/.
- [111] O. Montenbruck, B. Nortier, and S. Mostert. "A Miniature GPS Receiver for Precise Orbit Determination of the Sunsat 2004 Micro-Satellite". In: *ION NTM* (2004).
- [112] ESA. *BIROS (Bi-spectral InfraRed Optical System)*. visited on 2020-07-15. URL: <https://directory.eoportal.org/web/eoportal/satellite-missions/b/biros>.
- [113] TUI. *The MAST experiment Blog*. visited on 2020-17-15. URL: http://www.tethers.com/MAST_Blog.html.
- [114] M. Rupprecht. *DK3WN Satblog*. visited on 2020-17-15. URL: <http://www.dk3wn.info/p/?s=uwe-2>.
- [115] SSTL. *Space GNSS receiver, parametric comparison*. visited on 2020-17-15. URL: <https://www.sstl.co.uk/getattachment/Media-Hub/Featured/Navigation/GNSS-Selector-Datasheet-2018-V2-Read-Only.pdf?lang=en-GB>.
- [116] NovAtel. *OEM719 Performance Specifications*. visited on 2020-17-15. URL: https://docs.novatel.com/OEM7/Content/Technical_Specs_Receiver/OEM719_Performance_Specs.htm.
- [117] Warpspace. *CubeSat modules*. visited on 2020-17-15. URL: <https://warpspace.jp/en/#products>.
- [118] Move Project Team. *Solar Panel Deployment*. visited on 2020-17-15. Sept. 2016. URL: <https://www.move2space.de/MOVE-II/weekly-update-24-solar-panel-deployment-and-pdr-feedback-str/>.

- [119] N. Korn. *pinasys STAR*. visited on 2020-17-15. URL: http://pinasys.de/?attachment_id=201.
- [120] Astro- und Feinwerktechnik Adlershof GmbH. *Reaction Wheel RW 1 for Pico- and Nano Satellites*. 2015.
- [121] Hyperion Technologies. *RW210, data sheet*. 2019.
- [122] Cube Space. *Cube Wheel, data sheet*. 2019.
- [123] J. M. Diez et al. "TUPEX-7: Expanding CubeSat Capability". In: *8th European Conference for Aeronautics and Space Sciences*. Madrid, Spain, July 2019.
- [124] S. Grau. *Contributions to the Advance of the Integration Density of Cube-Sats*. Universitätsverlag der TU Berlin, 2018.
- [125] ESA. *UWE-4 (University Würzburg Experimental Satellite-4)*. visited on 2020-07-15. URL: <https://directory.eoportal.org/web/eoportal/satellite-missions/u/uwe-4#foot1%29>.
- [126] F. Baumann and S. Weiß. *Energiebilanz BEESAT-4*. Technical Note. unpublished. TU Berlin, 2013.
- [127] S. Weiß. *Energiebilanz BEESAT-9*. Technical Note. unpublished. TU Berlin, 2019.
- [128] S. Weiß. *Datenbudget BEESAT-9*. Technical Note. unpublished. TU Berlin, 2019.
- [129] M. Binder. *Lageregelung mit S-Net*. E-Mail conversation. Apr. 2018.
- [130] Bundesministerium für Bildung und Forschung. *Förderkatalog*. visited on 2020-07-15. URL: <https://foerderportal.bund.de/foekat/jsp/SucheAction.do?actionMode=searchlist>.
- [131] M. Buscher. *Chair of Space Technology: Research*. visited on 2020-07-15. URL: <https://www.raumfahrttechnik.tu-berlin.de/menue/research/parameter/en/>.
- [132] S. Trowitzsch et al. *BEESAT-2 Abschlussbericht Phase C*. Technical Report. unpublished. TU Berlin, Apr. 2011.
- [133] Hamamatsu. *Two-dimensional PSD S7848 series data sheet*. Apr. 2001.

- [134] S. Kokado and M. Tsunoda. "Intuitive explanation of Anisotropic Magnetoresistance (AMR) effect and necessary condition for half-metallic ferromagnet "negative AMR" (Conference Presentation)". In: *Spintronics XI*. Ed. by H.-J. Drouhin et al. Vol. 10732. International Society for Optics and Photonics. 2018.
- [135] Z. Yoon. "Drei-Achsen-Stabilisierung eines Pico-Satelliten mit Magnetspulen". Diplomarbeit. Technische Universität Berlin, Fakultät V – Verkehrs- und Maschinensysteme, Institut für Luft- und Raumfahrt, Fachgebiet Raumfahrttechnik, 2009.
- [136] M. Herfort. "Design, implementation and test of attitude determination and control system software of the pico satellite BeeSat". Studienarbeit. Technische Universität Berlin, Fakultät V – Verkehrs- und Maschinensysteme, Institut für Luft- und Raumfahrt, Fachgebiet Raumfahrttechnik, July 2008.
- [137] E. Geyer. "Entwurf, Implementierung und Test eines Programms zur Bahnberechnung an Bord des Picosatelliten BeeSat". Diplomarbeit. Technische Universität Berlin, Fakultät V – Verkehrs- und Maschinensysteme, Institut für Luft- und Raumfahrt, Fachgebiet Raumfahrttechnik, Mar. 2008.
- [138] M. Berlin. "Implementierung und Test von Algorithmen zur Lagebestimmung des Picosatelliten". Studienarbeit. Technische Universität Berlin, Fakultät V – Verkehrs- und Maschinensysteme, Institut für Luft- und Raumfahrt, Fachgebiet Raumfahrttechnik, May 2007.
- [139] National Centers For Environmental Information. *Geomagnetic Calculators, Maps, Models and Software*. visited on 2020-07-15. URL: <https://www.ngdc.noaa.gov/geomag/models.shtml>.
- [140] K. Gordon. *A flexible attitude control system for three-axis stabilized nanosatellites*. Universitätsverlag der TU Berlin, 2018.
- [141] J. Wertz. *Spacecraft Attitude Determination and Control*. Astrophysics and Space Science Library. Springer Netherlands, 1978.
- [142] G. Wahba. "A Least Squares Estimate of Satellite Attitude". In: *SIAM Review* 7.3 (1965), pp. 409–409.
- [143] M. D. SHUSTER and S. D. OH. "Three-axis attitude determination from vector observations". In: *Journal of Guidance and Control* 4.1 (1981), pp. 70–77. DOI: 10.2514/3.19717.

- [144] L. Markley and D. Mortari. "Quaternion Attitude Estimation Using Vector Observations". In: *Journal of the Astronautical Sciences* 48 (Apr. 2000).
- [145] H.-P. Geile. "Entwurf der Regler und Algorithmen sowie deren Implementierung zur Lageregelung des Picosatelliten BeeSat mit Hilfe von Reaktionsrädern". Studienarbeit. Technische Universität Berlin, Fakultät V – Verkehrs- und Maschinensysteme, Institut für Luft- und Raumfahrt, Fachgebiet Raumfahrttechnik, July 2008.
- [146] B. Wie. *Space Vehicle Dynamics and Control*. education series. American Institute of Aeronautics and Astronautics, 1998. ISBN: 9781563472619.
- [147] S. Lucia. "Damping of Picosatellites using Magneto Torquers: Design and Real Time Test". Masterarbeit. Technische Universität Berlin, Fakultät V – Verkehrs- und Maschinensysteme, Institut für Luft- und Raumfahrt, Fachgebiet Raumfahrttechnik, Sept. 2010.
- [148] *L3G4200D MEMS motion sensor, data Sheet*. STMicroelectronics. 2010.
- [149] S. Trowitzsch. "Payload Data handling of BEESAT-2". Diplomarbeit. Technische Universität Berlin, Fakultät V – Verkehrs- und Maschinensysteme, Institut für Luft- und Raumfahrt, Fachgebiet Raumfahrttechnik, July 2010.
- [150] S. Trowitzsch. "Auslegung, Implementierung und Test einer Kamera zur Erdbeobachtung für Picosatelliten". Studienarbeit. Technische Universität Berlin, Fakultät V – Verkehrs- und Maschinensysteme, Institut für Luft- und Raumfahrt, Fachgebiet Raumfahrttechnik, July 2009.
- [151] J. Lieb. *BeeSat-2 OBC Betriebsparameter*. Technical Report. TU Berlin, Nov. 2010.
- [152] S. Scharich. "Entwicklung und Implementierung der Software für den Terminal Node Controller (TNC) für BEESAT-2". Diplomarbeit. Technische Universität Berlin, Fakultät V – Verkehrs- und Maschinensysteme, Institut für Luft- und Raumfahrt, Fachgebiet Raumfahrttechnik, 2010.
- [153] P. Werner. "Entwicklung und Verifikation eines Terminal-Node-Controllers (TNC) zur Kommunikation zwischen CubeSats". Studienarbeit. Technische Universität Berlin, Fakultät V – Verkehrs- und Maschinensysteme, Institut für Luft- und Raumfahrt, Fachgebiet Raumfahrttechnik, 2012.
- [154] C. Avsar. "Entwurf und Aufbau eines Sonnensensors für Picosatelliten". Diplomarbeit. Technische Universität Berlin, Fakultät V – Verkehrs- und Maschinensysteme, Institut für Luft- und Raumfahrt, Fachgebiet Raumfahrttechnik, 2010.

- [155] Hamamatsu. *Two-dimensional PSD S5990-01 series data sheet*. June 2020.
- [156] *GPS Antennas - AP-AP17-30*. 1st ed. Sectron.
- [157] S. Montenegro. *Rodos*. visited on 2020-07-15. URL: <http://www8.informatik.uni-wuerzburg.de/en/wissenschaftsforschung/rodos/>.
- [158] S. Grau et al. "Control of an Over-Actuated Spacecraft using a Combination of a Fluid Actuator and Reaction Wheels". In: *70th International Astronautical Congress (IAC)*. Washington D.C., USA, Oct. 2019.
- [159] D. Noack, J. Ludwig, and K. Brieß. "Untersuchungen zu einem fluidynamischen Aktuator für den Einsatz auf dem Nanosatelliten TechnoSat". In: *62. German Aerospace Congress*. Stuttgart, Germany, Sept. 2013.
- [160] S. Kapitola. "Mission Operation of Academic Small Satellites". unpublished, PhD-thesis not submitted on 2020-07-15. 2020.
- [161] E. Melan. "Ergänzung des Bodensegments der TU Berlin zur Vorbereitung des Missionsbetriebs des Satelliten BEESAT-4". Bachelorarbeit. Technische Universität Berlin, Fakultät V – Verkehrs- und Maschinensysteme, Institut für Luft- und Raumfahrt, Fachgebiet Raumfahrttechnik, Mar. 2015.
- [162] C. Jonglez. *Orbit Determination of BEESAT-9*. unpublished python script, adapted by the author.
- [163] Taoglas. *Specification AP.17F.07.0064A*. 2020.
- [164] CS Group. *Orekit*. visited on 2020-07-15. URL: <https://www.orekit.org/>.
- [165] S. Kapitola, S. W. N. Korn, and K. Brieß. "Von BEESAT-2 zu BEESAT-4: Weiterführende Nutzung als In-Orbit Testplattform". In: *DLRK*. Braunschweig, Germany, Sept. 2016.
- [166] S. Weiß. "Synthese und Verifikation eines Regelkerns zur lageunabhängigen Stabilisierung und Ausrichtung des Picosatelliten BEESAT-2". Diplomarbeit. Technische Universität Berlin, Fakultät V – Verkehrs- und Maschinensysteme, Institut für Luft- und Raumfahrt, Fachgebiet Raumfahrttechnik, July 2012.
- [167] S. Weiß et al. "BEESAT-2 to BEESAT-4: In flight demonstration of attitude control to GPS based positioning and orbit determination". In: *4S Symposium Malta*. Valleta, Malta, May 2016.
- [168] S. Kapitola and S. Weiß. *Simulation des ADCS mit Flugsoftware*. Technical Note. unpublished. TU Berlin, 2016.

- [169] S. Weiß, K. Brieß, and S. Kapitola. "BEESAT-4: 3-Axis attitude control and GPS based positioning and orbit determination". In: *67th International Astronautical Congress (IAC)*. Guadalajara, Mexico, Sept. 2016.
- [170] S. Weiß and S. Kapitola. "One Year of BEESAT-4 Operation: Long-Term Analysis of Housekeeping, GPS and Attitude Control Data". In: *68th International Astronautical Congress (IAC)*. Adelaide, Australia, Oct. 2017.
- [171] M. Markgraf. *Functional Test Report of Phoenix-S GPS Receiver for BEESAT-4*. Technical Report. TU Berlin, Dec. 2010.
- [172] M. Markgraf. *Signalstärken des Phoenix-Empfängers*. E-Mail conversation. Mar. 2014.
- [173] R. Küng. *Rauschen*. 2010.
- [174] S. Jahnke. "Planung, Vorbereitung und Durchführung einer Testkampagne zur Kalibrierung der Lagebestimmungssensoren des Picosatelliten BEESAT-2". Bachelorarbeit. Technische Universität Berlin, Fakultät V – Verkehrs- und Maschinensysteme, Institut für Luft- und Raumfahrt, Fachgebiet Raumfahrttechnik, Apr. 2012.
- [175] S. Weiß. *AIV des Flugmodell BEESAT-4*. presented at internal Colloquium on 2016-07-18, unpublished.
- [176] J. C. Springmann and J. W. Cutler. "Attitude-Independent Magnetometer Calibration with Time-Varying Bias". In: 2012, pp. 1080–1088.
- [177] K. Brieß. *Verifikation durch Tests*. Presentation for the lecture "Raumfahrtsystementwurf", unpublished. 2014.
- [178] Spenvis. *Space Environment Information System*. visited on 2020-07-15. URL: <https://www.spenvis.oma.be/>.
- [179] S. Ritzmann and M. Rose. *Environmental Testing Specification PICOSAT and PICOSAT Equipment*. Technical Report. Astro- und Feinwerktechnik GmbH, June 2007.
- [180] D. Just. "Thermal-Mathematisches Modell für den Satelliten BEESAT". Studienarbeit. Technische Universität Berlin, Fakultät V – Verkehrs- und Maschinensysteme, Institut für Luft- und Raumfahrt, Fachgebiet Raumfahrttechnik, Oct. 2010.
- [181] D. DePriest. *NMEA data*. visited on 2020-07-15. URL: <https://www.gpsinformation.org/dale/nmea.htm>.

- [182] D. Maurer and Y. Denizler. *BEESAT-9: Sun Sensor Calibration Procedure*. Technical Report. unpublished. TU Berlin, Jan. 2019.
- [183] E. Klioner and J. Stamm. *BEESAT-9: Calibration Report of Magnetic Field Sensors*. Technical Report. unpublished. TU Berlin, Mar. 2019.
- [184] F. Bartels. *BEESAT-9: Calibration Procedure of Gyroscope Sensors*. Technical Report. unpublished. TU Berlin, Jan. 2019.
- [185] S. Weiß, S. Kapitola, and S. Grau. "BEESAT-9: A CubeSat's qualification model was launched". In: *2nd IAA Latin American Symposium on Small Satellites*. Buenos Aires, Argentina, Nov. 2019.
- [186] EXOLAUNCH. *Environmental Conditions for Small Satellites*. Technical Report. unpublished. Nov. 2018.
- [187] S. Weiß and S. Kapitola. *BEESAT-4 Missionsbetrieb*. presented at internal Colloquium on 2018-02-12, unpublished.
- [188] S. Kapitola, S. Weiß, and K. Brieß. "Flight Experience and Operations with the CubeSat BEESAT-4". In: *11th IAA Symposium on Small Satellites for Earth Observation*. Berlin, Germany, Apr. 2017.
- [189] M. Binder. *Angle between sun and magnetic field vector*. Oral Conversation. Mar. 2018.
- [190] K. Großekathöfer and Z. Yoon. *Introduction into Quaternions for Spacecraft Attitude Representation*. Tech. rep. TU Berlin, 2012.
- [191] N. Matteo and Y. Morton. "Ionosphere geomagnetic field: Comparison of IGRF model prediction and satellite measurements 1991-2010". In: *Radio Science - RADIO SCI* 46 (Aug. 2011).
- [192] R. B. Langley. *The GPS End-of-Week Rollover*. Tech. rep. University of New Brunswick, 1998.
- [193] M. Markgraf. *Phoenix GPS Firmware Bug*. E-Mail conversation. Mar. 2018.
- [194] S. Weiß and S. Kapitola. *Experiment Szenarien für den Inter Satellite Link zwischen BIROS und BEESAT-4*. Technical Report. unpublished. TU Berlin, May 2017.
- [195] W. Frese. *N-Link Inter-Satellite Link Radio Module Link Budget*. Technical Note. unpublished. TU Berlin, May 2017.
- [196] S. Weiß, S. Kapitola, and D. Roychowdhury. *BEESAT-9: Flugergebnisse*. presented at internal Colloquium on 2020-02-24, unpublished.

- [197] K. Gordon. *A flexible attitude control system for three-axis stabilized nanosatellites*. presented during defense of PhD-Thesis. 2017.
- [198] E. Morando. "Precise position and orbit determination using GNSS". (not submitted on 2020-07-15). Bachelorarbeit. Technische Universität Berlin, Fakultät V – Verkehrs- und Maschinensysteme, Institut für Luft- und Raumfahrt, Fachgebiet Raumfahrttechnik, Aug. 2020.
- [199] D. A. Vallado and W. D. McClain. *Fundamentals of Astrodynamics and Applications*. 4th ed. Springer Netherlands, 2013.
- [200] D. C. Koblick. *ECEF2Hill-Vectorized*. Matlab code for conversion of ecef to hill reference frame. Nov. 2012.
- [201] JSpOC. *TLE database*. visited on 2020-07-15. URL: <https://www.space-track.org>.
- [202] Quality Positioning Services B.V. *UTC to GPS Time Correction*. visited on 2020-07-15. URL: <https://confluence.qps.nl/qinsy/latest/en/utc-to-gps-time-correction-32245263.html>.
- [203] Space Weather Live. *Solar Cycle progression*. visited on 2020-07-15. URL: <https://www.spaceweatherlive.com/en/solar-activity/solar-cycle>.
- [204] J. C. Whitaker. *The Electronics Handbook*. Taylor & Francis, 1996.
- [205] R. B. Langley. *Dilution of Precision*. Tech. rep. University of New Brunswick, 1999.
- [206] NavSpark. *NMEA Output Description*. visited on 2020-07-15. URL: http://navspark.mybigcommerce.com/content/NMEA_Format_v0.1.pdf.

A Basic Navigation Data of BEESAT-4 from [31]

The Phoenix receivers uses the WinMon protocol additionally to NMEA. For BEESAT-4 WinMon was used to be conform with BIROS. All the messages provided by Phoenix could be stored on-board, but mainly F40 (Cartesian Navigation Data) and F48 (Configuration and Status Parameters) were used. Both are outputted automatically, once the receiver is switched on.

Table A.1: F40 - Cartesian navigation data from WinMon protocol

MsgID	Chars.	Format	Description
F40	104		Cartesian navigation data
1	x		<STX>
3	xxx		Message Id (=F40)
4	xxxx		GPS week
12	xxxxxx.xxxxxx		GPS seconds of week [s] (of navigation solution)
2	xx		GPS-UTC [s]
12	sxxxxxxxx.xx		x (WGS84) [m]
12	sxxxxxxxx.xx		y (WGS84) [m]
12	sxxxxxxxx.xx		z (WGS84) [m]
12	sxxxxx.xxxxxx		vx (WGS84) [m/s]
12	sxxxxx.xxxxxx		vy (WGS84) [m/s]
12	sxxxxx.xxxxxx		vz (WGS84) [m/s]
			Navigation status
1	x		(0=no-Nav, 1=First Fix, 2=continuous 3D-Nav)
2	xx		Number of tracked satellites
4	xx.x		PDOP
2	xx		Checksum
1	x		<ETX>

Table A.2: F48 - Cartesian navigation data from WinMon protocol

MsgID	Chars.	Format	Description
F40	104		Cartesian navigation data
	1	x	<STX>
	3	xxx	Message Id (=F48)
	4	xxxx	GPS week
	8	xxxxxx.x	GPS seconds of week [s] (at output)
	2	xx	GPS-UTC [s]
	4	xxxx	Almanac week
	5	sxxxx	Doppler offset [Hz]
	1	x	Mode (0=default,1=rocket,2=orbit)
	1	x	Output format (0=default,1=extended)
	1	x	Update rate of navigation and display task [Hz] (1Hz, 2Hz, 5Hz)
	2	xx	Spare CPU capacity [%]
	3	sxx	Elevation mask [deg]
	2	xx	PDOP mask
	8	xxxxxx.x	Launch time (GPS seconds of week [s])
	2	xx	Checksum
	1	x	<ETX>

B Basic Navigation Data of BEESAT-9 (Binary Protocol)

On BEESAT-9 a binary protocol is used and the parameters are gathered customary in an Application Identifier (APID) and stored directly in the telemetry flash of the OBC. The following parameters are stored as the basic navigation data set.

Table B.1: Basic navigation data from GNSS200 on BEESAT-9

Name	Description	Unit	BitLength
PDHCTSTUTC	PDH Time UTC	s	32
GPSUTCS	GPS sensor time seconds	s	32
GPSUTCf	GPS sensor time fraction of second	s	16
GPSFIXM	GPS Fix-Mode		8
GPSSV	GPS Number of tracked satellites		8
GPSGDOP	Geometric dilution of precision		16
GPSPDOP	Position dilution of precision		16
GPSHDOP	Horizontal dilution of precision		16
GPSVDOP	Vertical dilution of precision		16
GPSTDOP	Time dilution of precision		16
GPSPOSX	ECEF-System X coordinate	m	32
GPSPOSY	ECEF-System Y coordinate	m	32
GPSPOSZ	ECEF-System Z coordinate	m	32
GPSVELX	ECEF-System X velocity	m/s	32
GPSVELY	ECEF-System Y velocity	m/s	32
GPSVELZ	ECEF-System Z velocity	m/s	32
GPSBMOR	Measurement Output Rate	Hz	16
GPSPUR	Position Update Rate	Hz	16

C NMEA Messages of BEESAT-9 from [206]

The NMEA protocol outputted by the GNSS200 supports the NMEA-0183 standard. For the analysis of the signal strength three messages are used.

- GPGSV: GPS satellites in view
- BDGSV: Beidou satellites in view
- GNRMC: Time, date, position, course and speed data

C.1 GPGSV and BDGSV

Both messages are built in the following format:

$\$-GSV,x,u,xx,uu,vv,zzz,ss,uu,vv,zzz,ss,\dots,uu,vv,zzz,ss*hh$

Table C.1: NMEA message for GNSS satellites in view

Field	Name	Description
x	Number of messages	Total number of GSV messages to be transmitted
u	Sequence number	Sequence number of current GSV message
xx	Satellites in view	Total number of satellites in view (00 - 12)
uu	Satellite ID	01–32 are for GPS; 201– 237 are for Beidou Max. 4 satellites are included in each GSV set.
Vv	Elevation	Satellite elevation in degrees, (00 - 90)
zzz	Azimuth	Satellite azimuth angle in degrees, (000 - 359)
ss	SNR	C/N_0 in dB-Hz (00–99) Null when not tracking
hh	Checksum	

C.2 GNRMC

The third message is built on the following format:

\$-RMC,hhmmss.sss,x,IIII.III,a,yyyyy.yyy,a,x.x,u.u,xxxxxx,,v*hh

Table C.2: NMEA message for time, date, position, course and speed data

Field	Name	Description
hhmmss.sss	UTC time	UTC time in hhmmss.sss format (000000.000–235959.999)
x	Status	Status 'V' = Navigation receiver warning 'A' = Data Valid
IIII.III	Latitude	Latitude in dddmm.mmmm format Leading zeros are inserted
A	N/S indicator	'N' = North; 'S' = South
yyyyy.yyy	Longitude	Longitude in dddmm.mmmm format Leading zeros are inserted
A	E/W Indicator	'E' = East; 'W' = West
x.x	Speed over ground	Speed over ground in knots (000.0–999.9)
u.u	Course over ground	Course over ground in degrees (000.0–359.9)
xxxxxx	UTC Date	UTC date of position fix, ddmmyy format
v	Mode indicator	Mode indicator 'N' = Data not valid 'A' = Autonomous mode 'D' = Differential mode 'E' = Estimated (dead reckoning) mode
hh	Checksum	

D Pictures of BEESAT-4

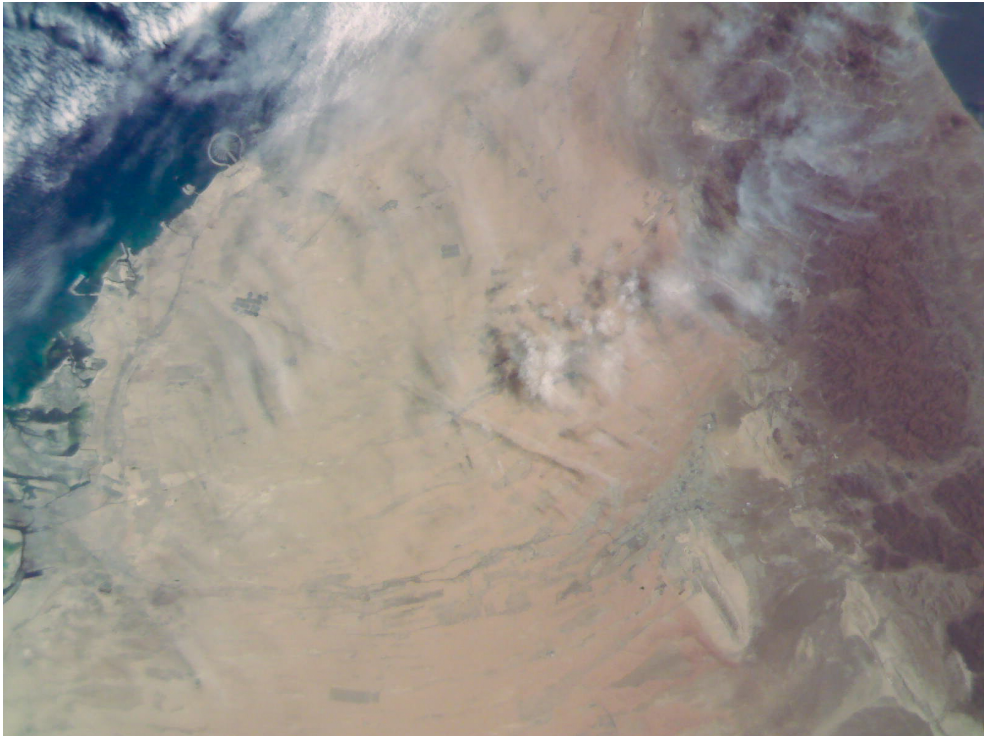


Figure D.1: Dubai palm tree, used for ADCS experiment in Section 6.1.2 (colorized)
(Scenario by Sascha Weiß)

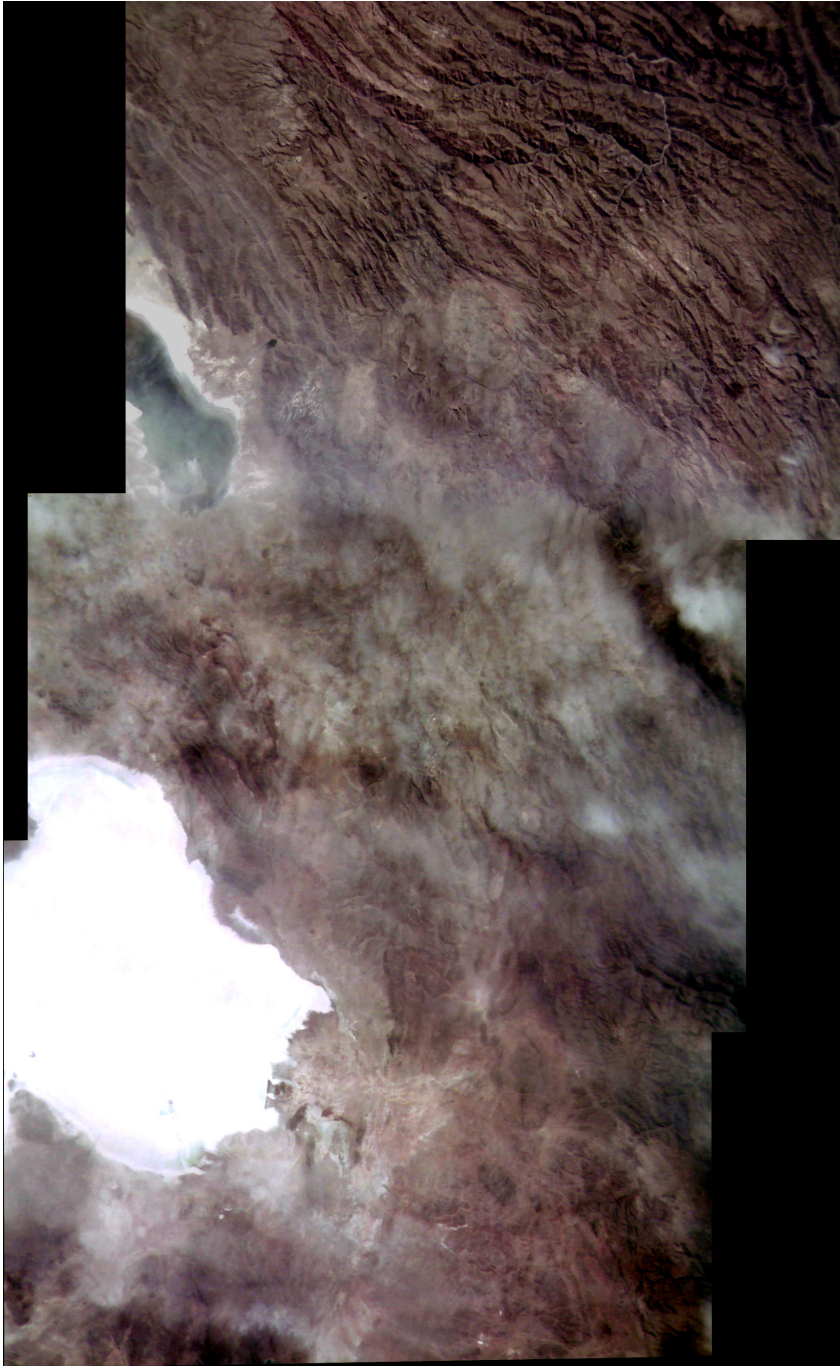


Figure D.2: Salt desert Salar de Uyuni in Bolivia, commanded via BIROS (colorized)
(Scenario by Sascha Kapitola)

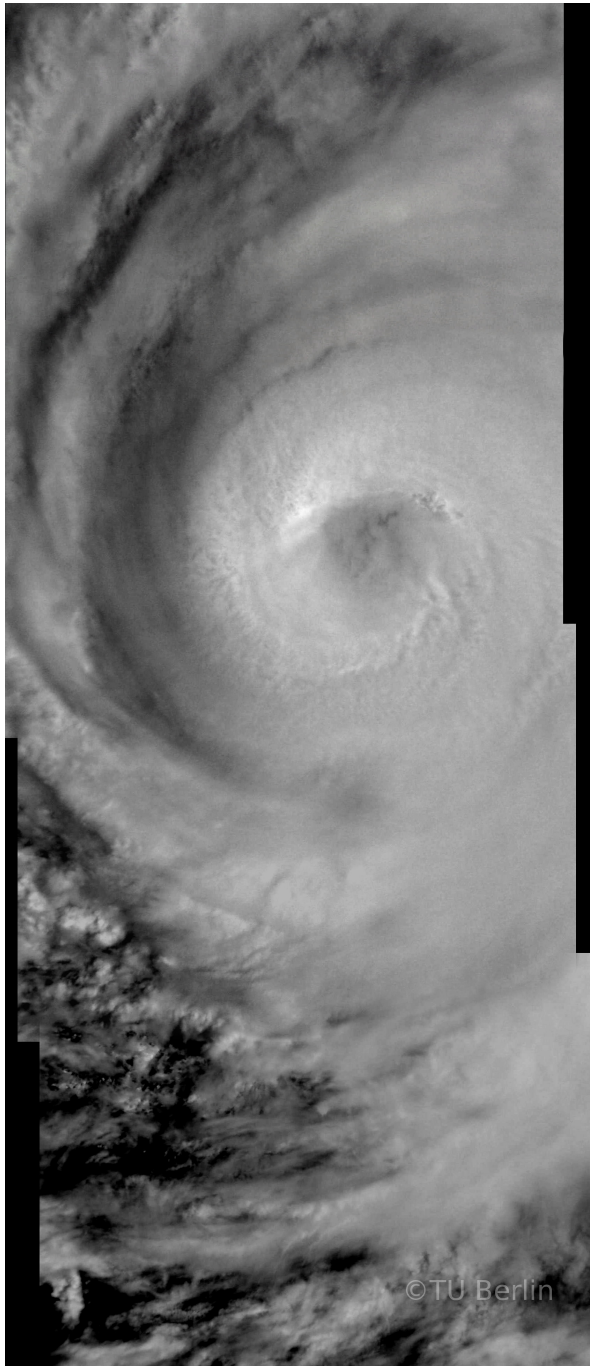


Figure D.3: Hurrigan Irma on top of the Caribbean Sea, September 2017 (Scenario by Sascha Kapitola)

E Pictures of BEESAT-9



Figure E.1: Palm tree in Dubai, used for ADCS experiment in Section 6.2.2 (Scenario by Sascha Weiß)



Figure E.2: Bahamas on 2020-03-26 (Scenario by Nicole Gress)

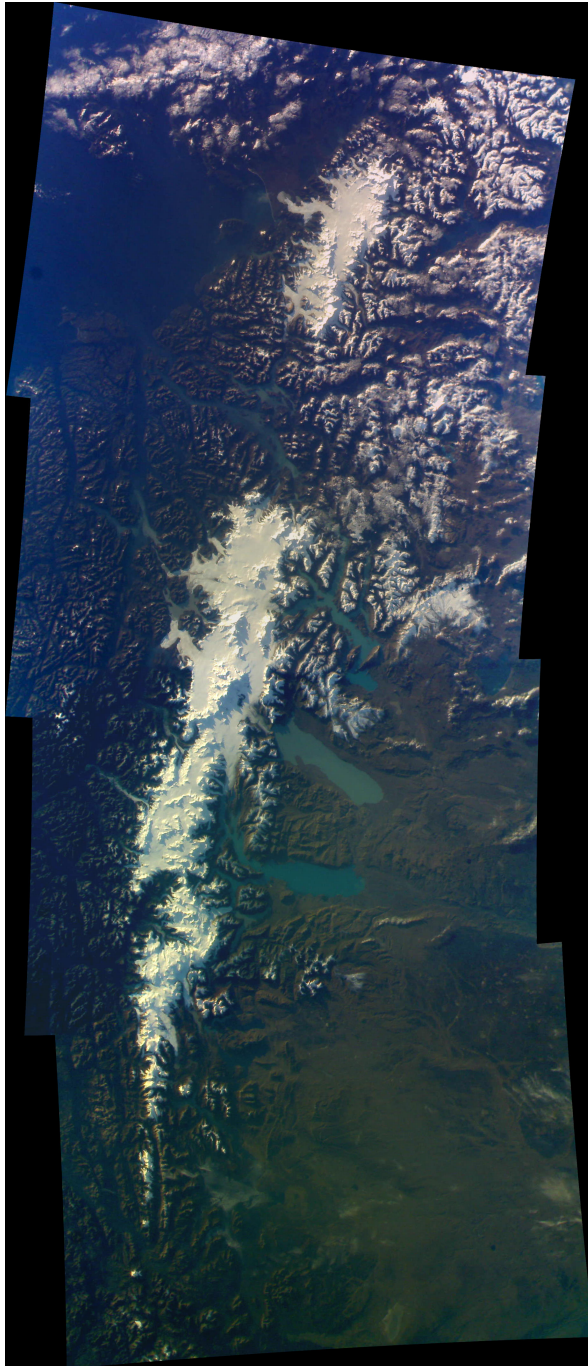


Figure E.3: Chile on 2020-05-04 (Scenario by Nicole Gress)



Figure E.4: Moon over South America on 2020-04-01 (Scenario by students from project Mission Operations)

F Plots from Orbit Determination and Propagation

The next eight plots represent the residuals from orbit determination from Section 7.4 in the order of Table 7.4. Afterwards the plots for a two week orbit propagation are displayed for the same data sets, each with a zoomed in version of three days and the full two week version.

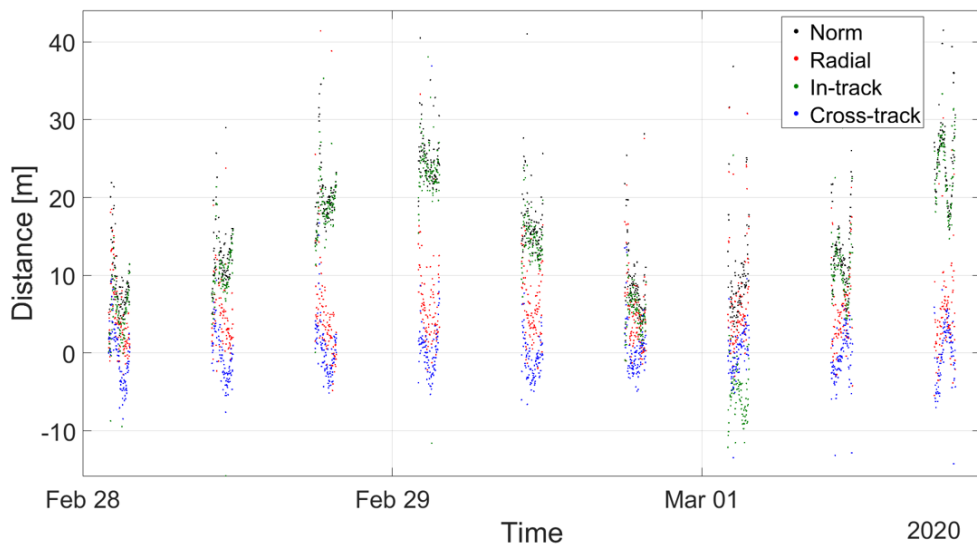


Figure F.1: Residuals for a three day GNSS data set from 2020-02-28

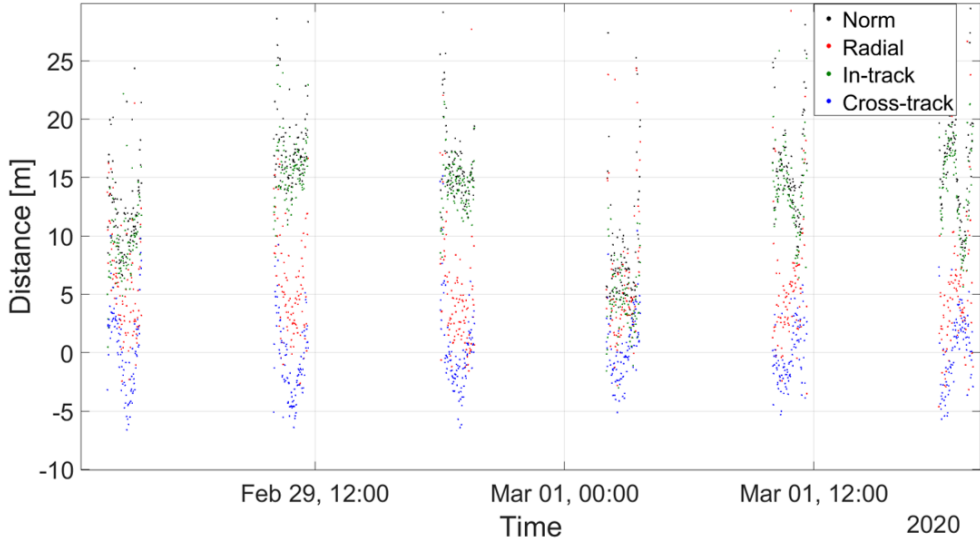


Figure F.2: Residuals for a two day GNSS data set from 2020-02-29

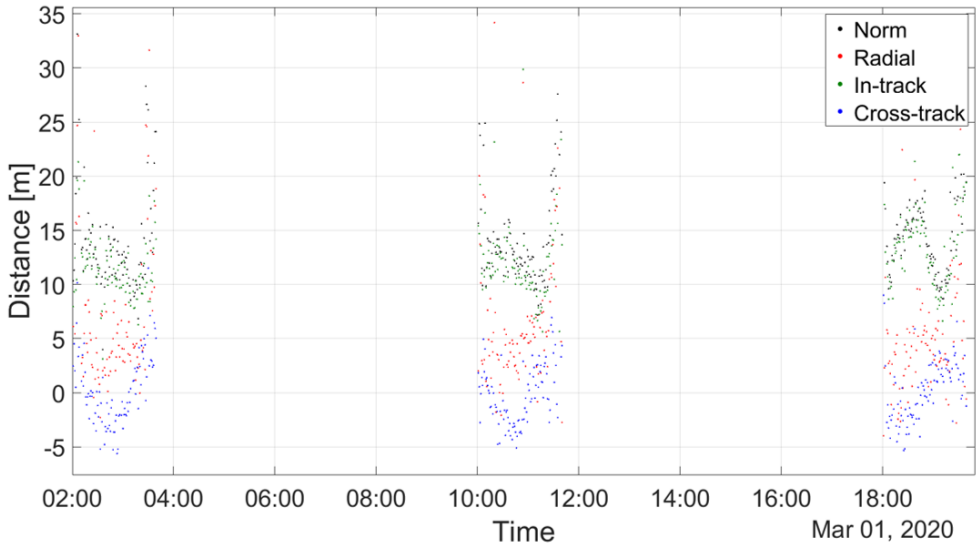


Figure F.3: Residuals for a one day GNSS data set from 2020-03-01

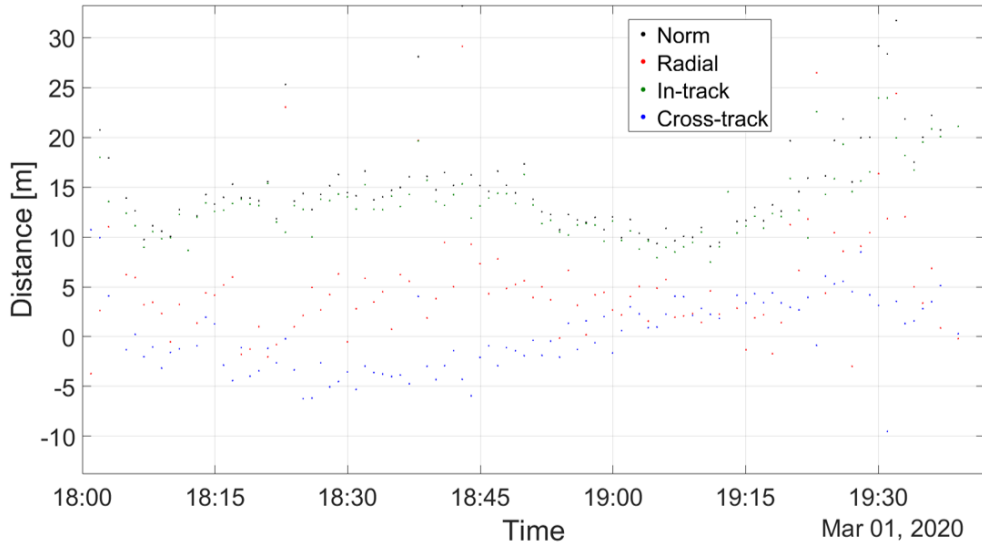


Figure F.4: Residuals for a one orbit GNSS data set from 2020-03-01

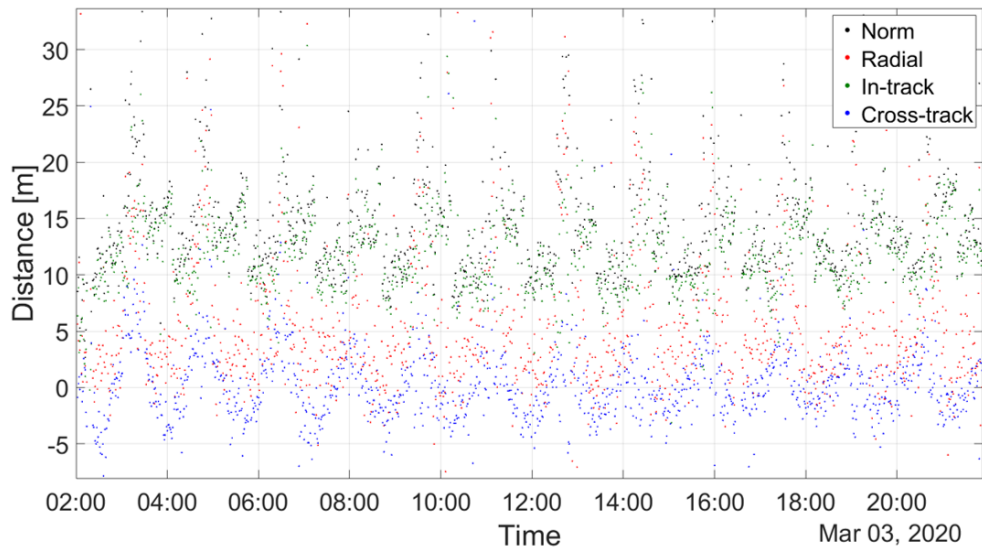


Figure F.5: Residuals for a one day GNSS data set from 2020-03-03

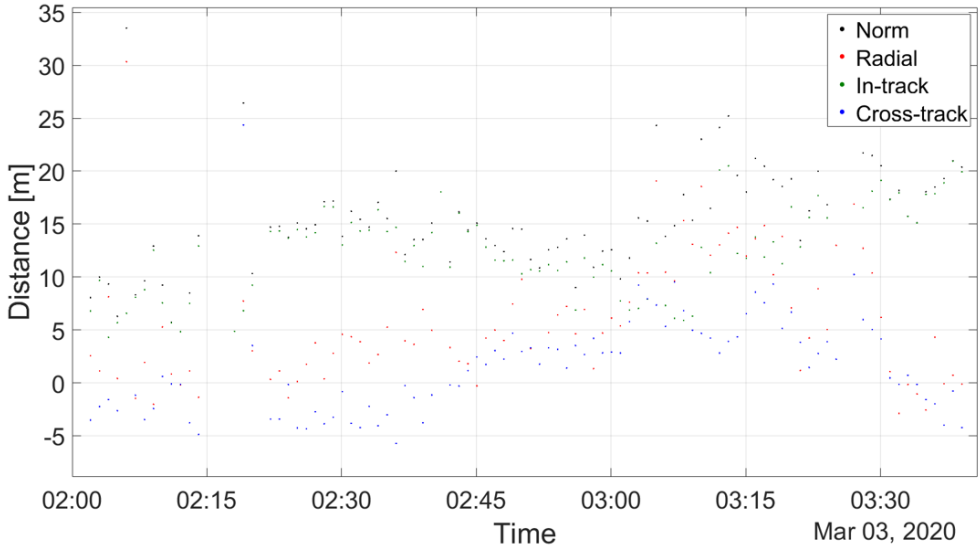


Figure F.6: Residuals for a one orbit GNSS data set from 2020-03-03

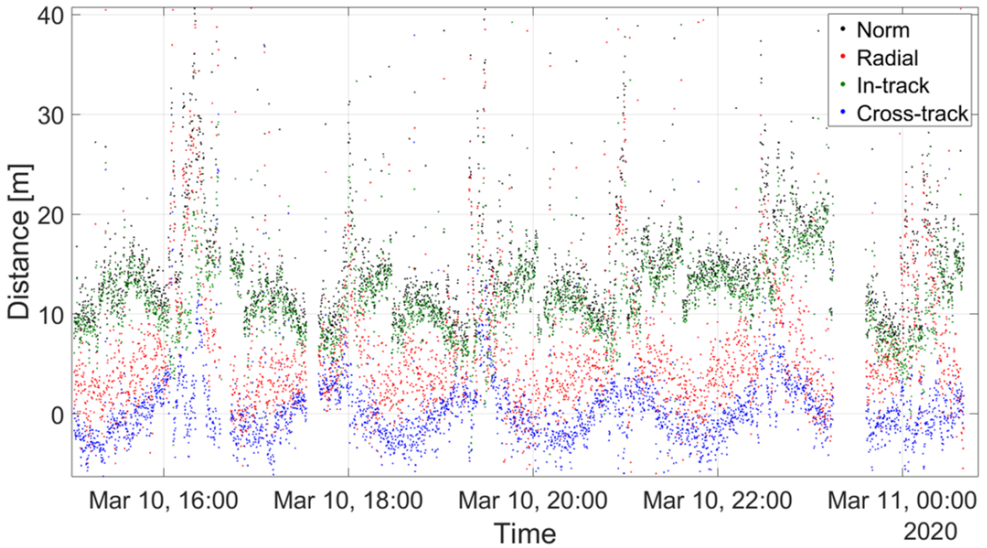


Figure F.7: Residuals for a one day GNSS data set from 2020-03-10

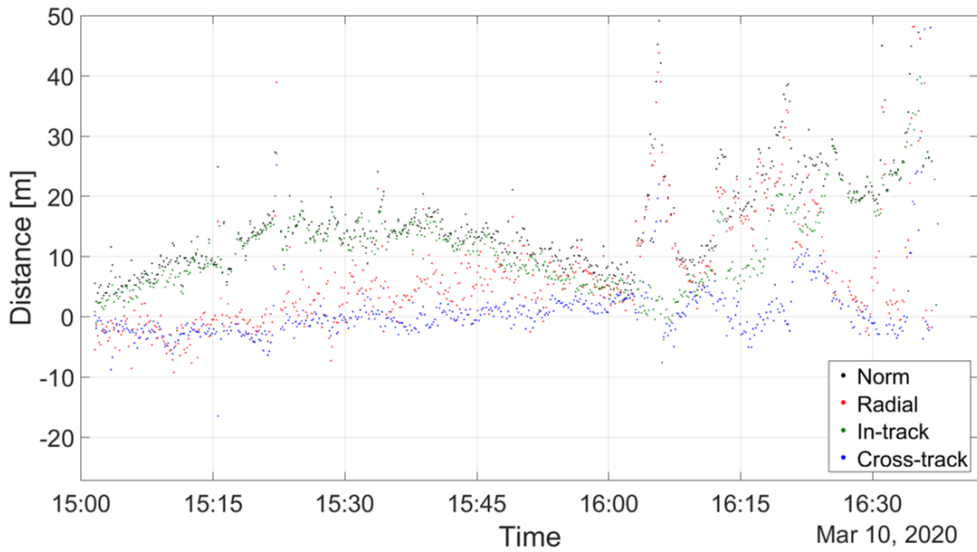


Figure F.8: Residuals for a one orbit GNSS data set from 2020-03-10

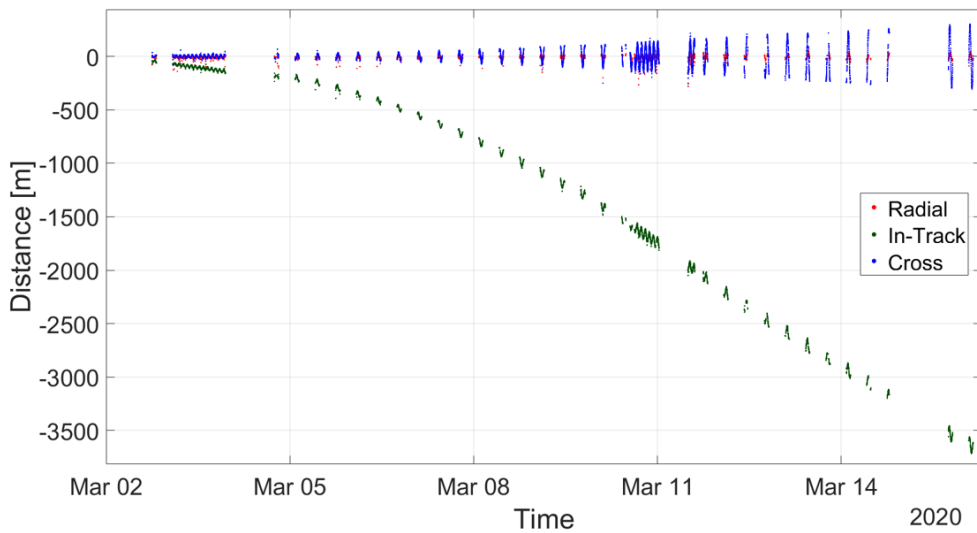


Figure F.9: Orbit propagation of two weeks from 2020-02-28, based on three days of GNSS data

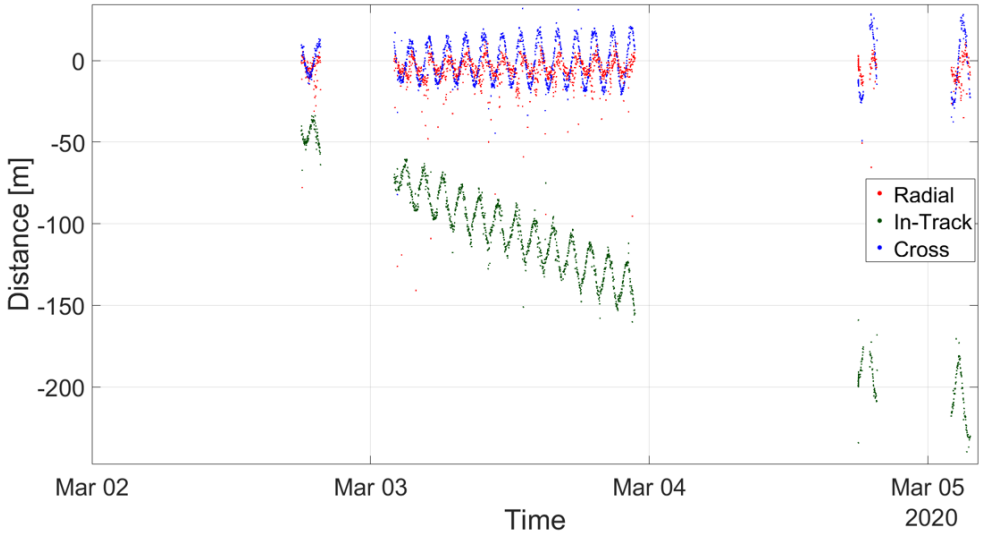


Figure F.10: Orbit propagation of two weeks from 2020-02-28, zoomed in

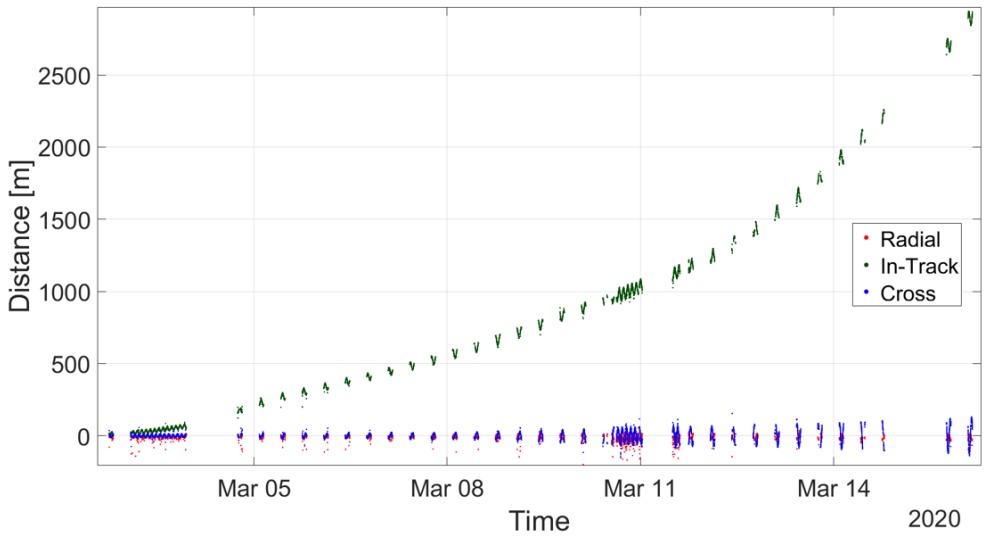


Figure F.11: Orbit propagation of two weeks from 2020-02-29, based on two days of GNSS data

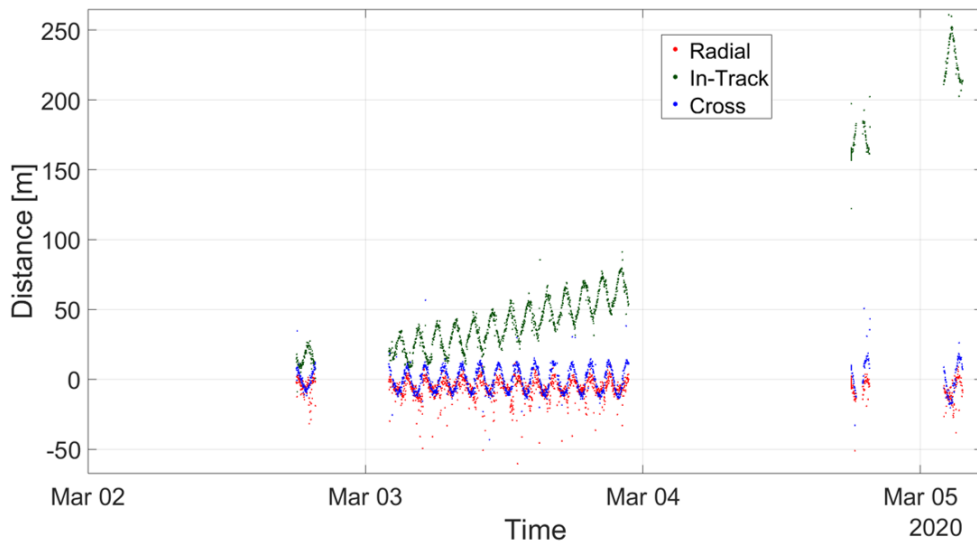


Figure F.12: Orbit propagation of two weeks from 2020-02-29, zoomed in

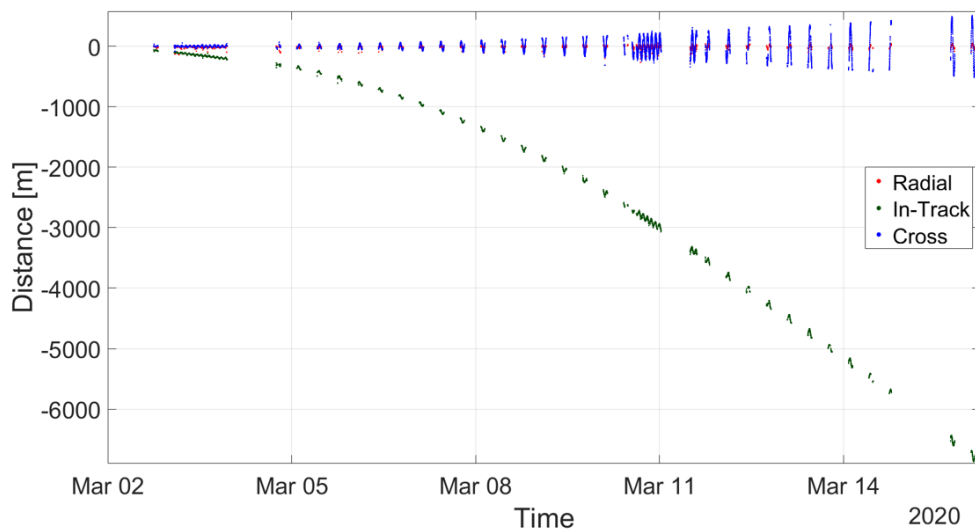


Figure F.13: Orbit propagation of two weeks from 2020-03-01, based on three orbits of GNSS data

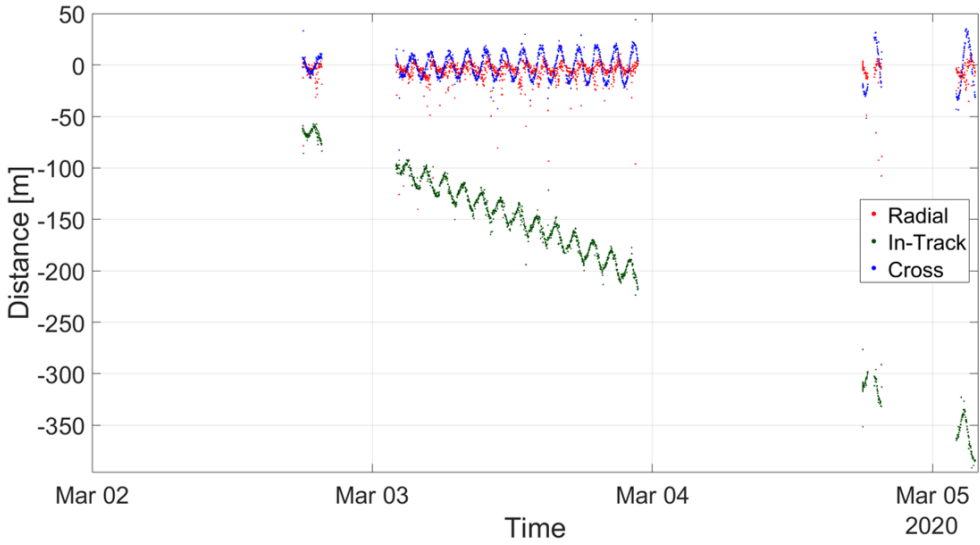


Figure F.14: Orbit propagation of two weeks from 2020-03-01, zoomed in

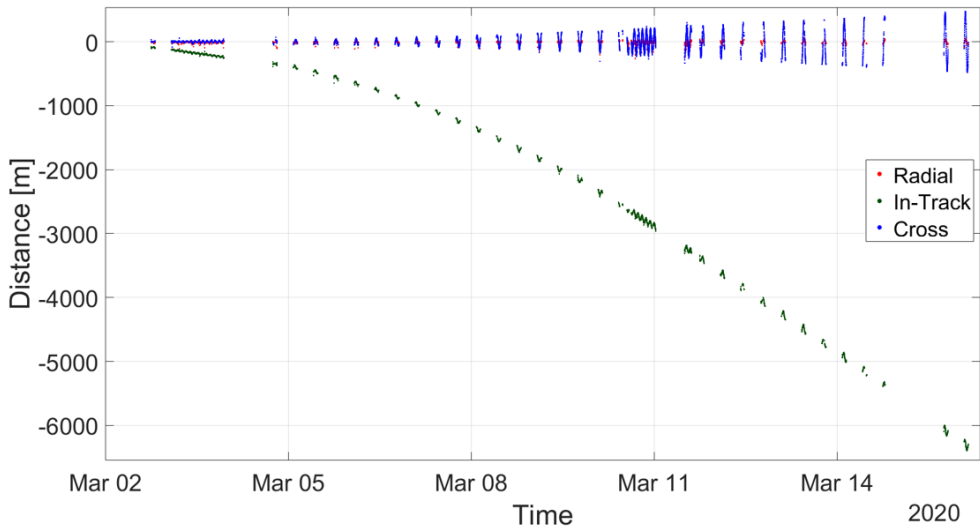


Figure F.15: Orbit propagation of two weeks from 2020-03-01, based on one orbit of GNSS data

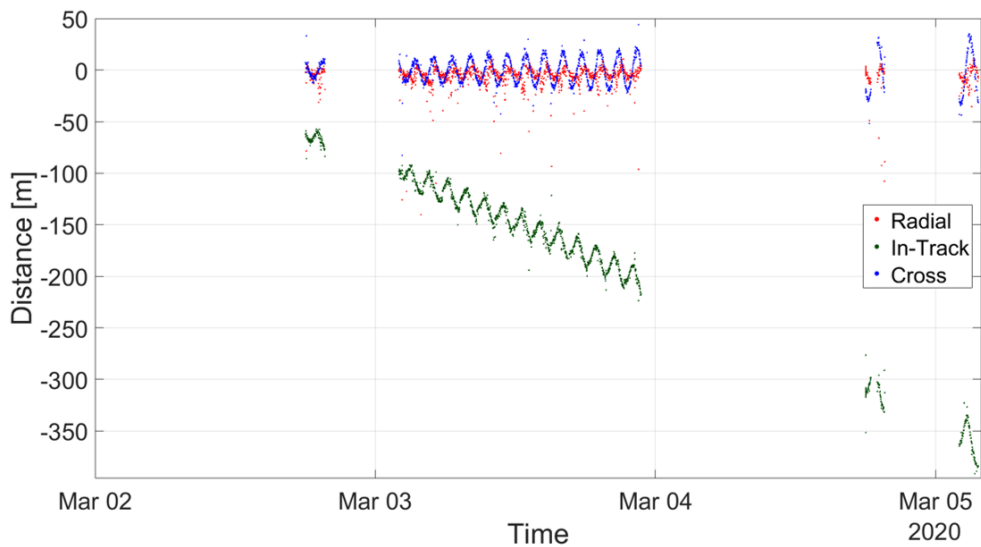


Figure F.16: Orbit propagation of two weeks from 2020-03-01, zoomed in

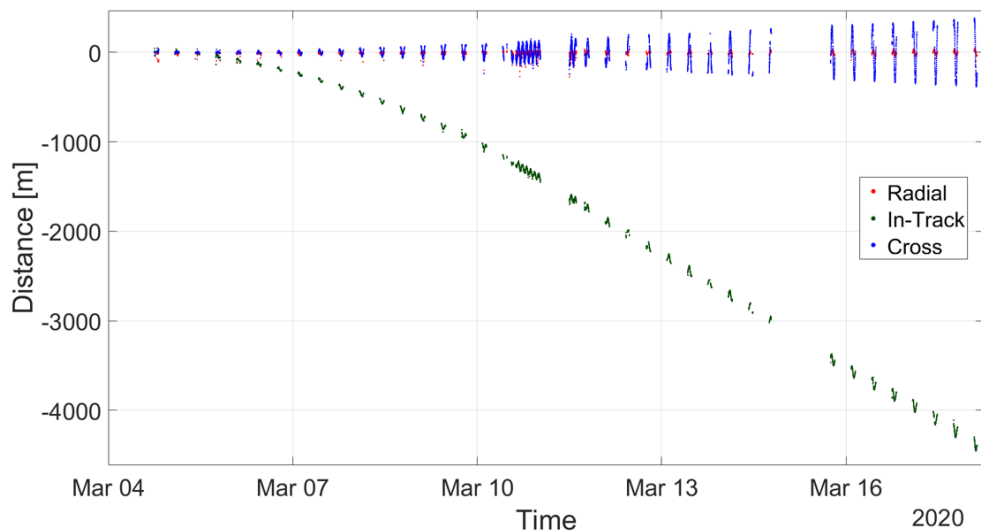


Figure F.17: Orbit propagation of two weeks from 2020-03-01, based on 20h of GNSS data

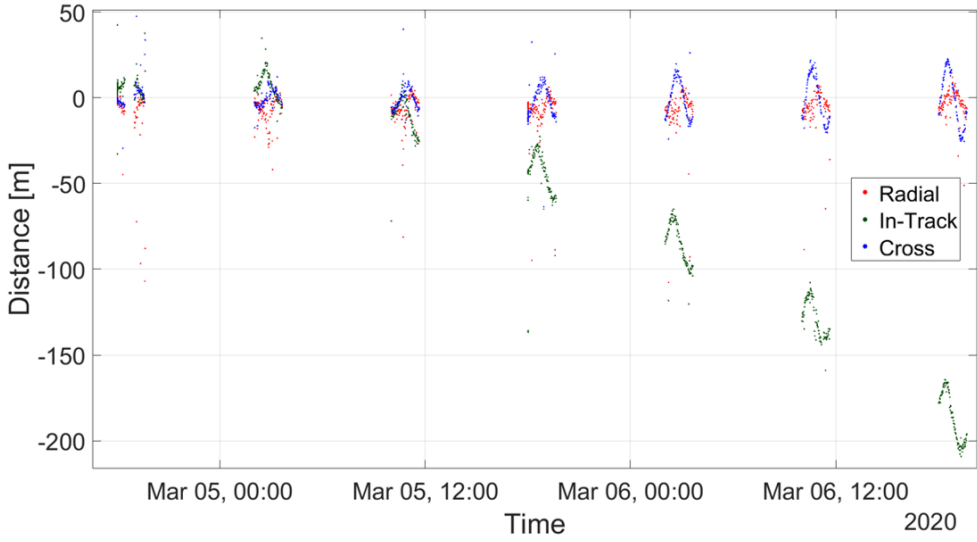


Figure F.18: Orbit propagation of two weeks from 2020-03-03, zoomed in

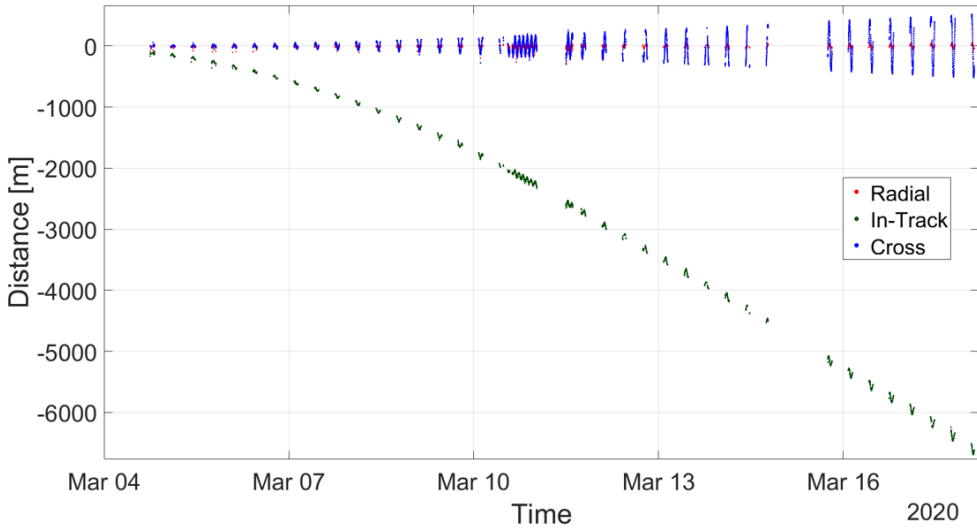


Figure F.19: Orbit propagation of two weeks from 2020-03-03, based on one orbit of GNSS data

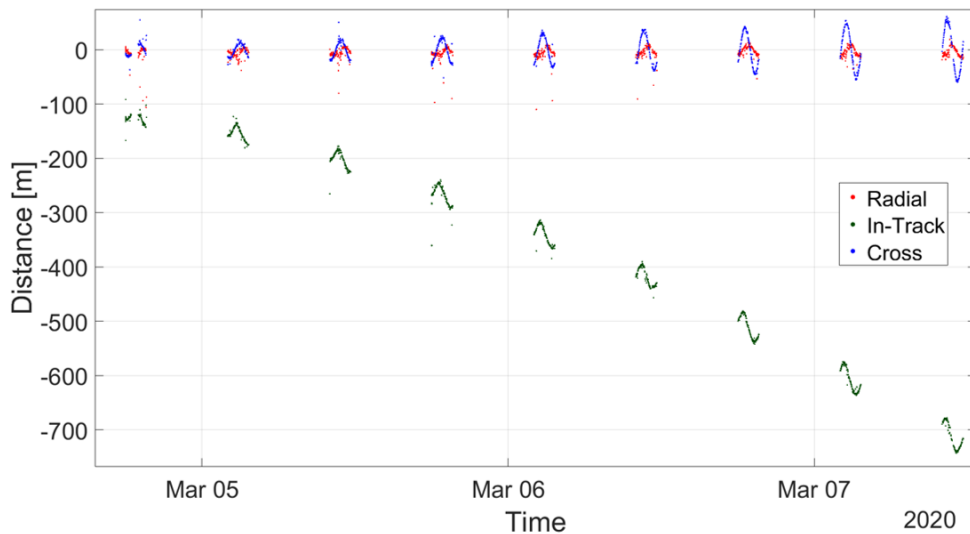


Figure F.20: Orbit propagation of two weeks from 2020-03-03, zoomed in

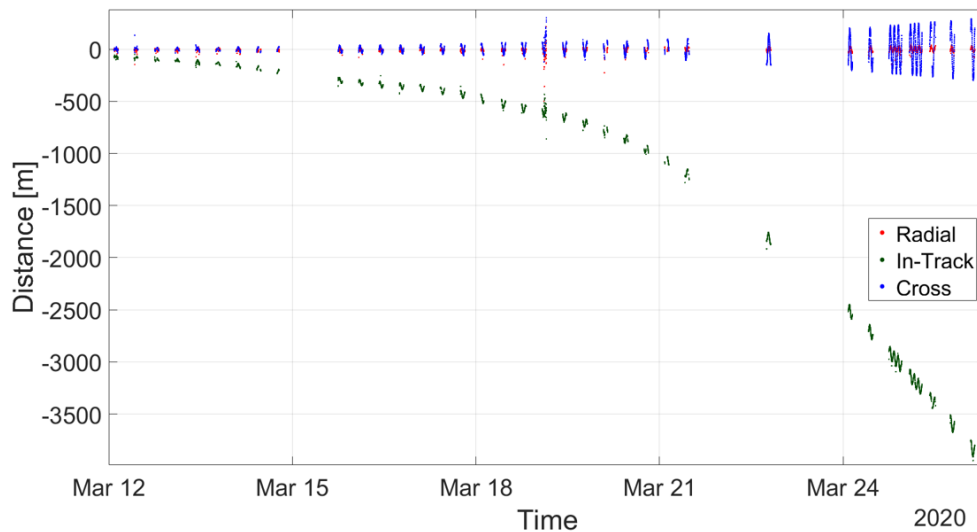


Figure F.21: Orbit propagation of two weeks from 2020-03-10, based on 10h of GNSS data

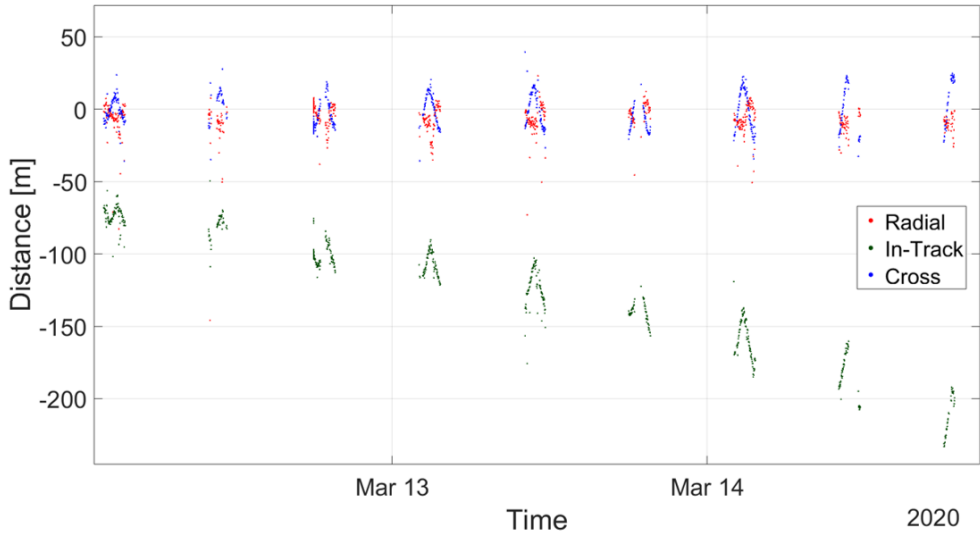


Figure F.22: Orbit propagation of two weeks from 2020-03-10, zoomed in

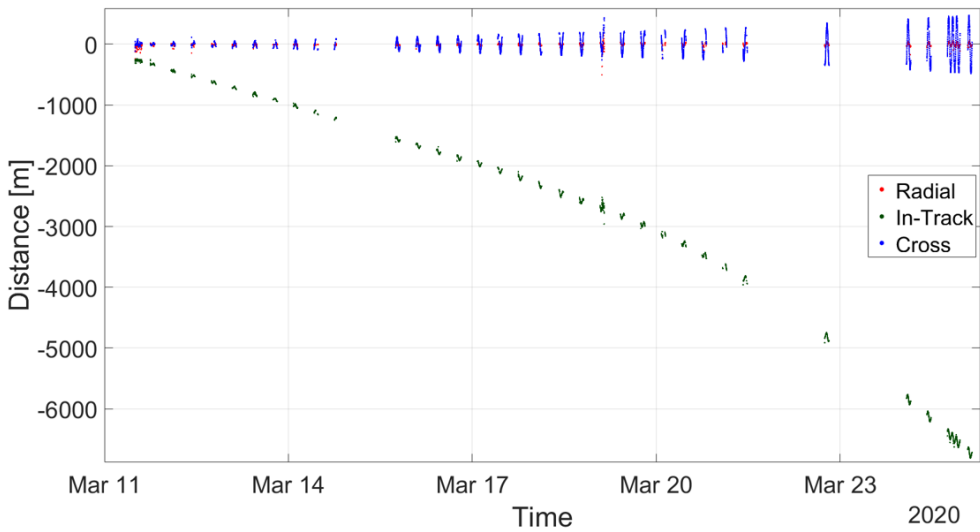


Figure F.23: Orbit propagation of two weeks from 2020-03-10, based on one orbit of GNSS data

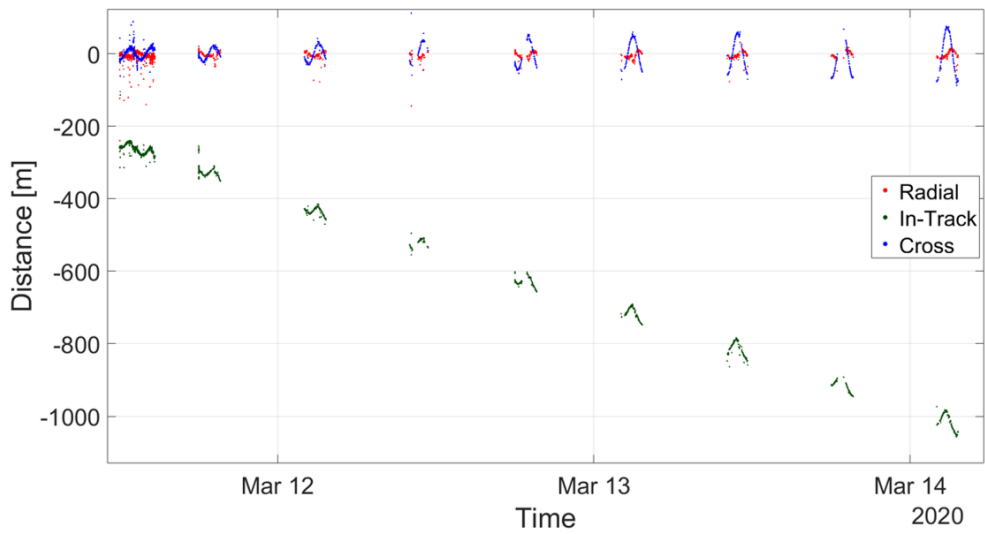


Figure F.24: Orbit propagation of two weeks from 2020-03-10, zoomed in

Schriftenreihe **Institute of Aeronautics and Astronautics: Scientific Series**

Hrsg.: Prof. Dr.-Ing. Dieter Peitsch, Prof. Dr.-Ing. Andreas Bardenhagen,

Prof. Dr.-Ing. Klaus Brieß, Prof. Dr.-Ing. Robert Luckner,

Prof. Dr.-Ing. Julien Weiss

ISSN 2512-5141 (print)

ISSN 2512-515X (online)

- 1: Behrend, Ferdinand: Advanced Approach Light System.** Der Einfluss eines zusätzlichen visuellen Assistenzsystems zur Steigerung des Situationsbewusstseins bei kritischen Wetterbedingungen hinsichtlich vertikaler Fehler im Endanflug – 2017. – XXIV, 206 S.
ISBN 978-3-7983-2904-1 (print) EUR 16.50
ISBN 978-3-7983-2905-8 (online)
DOI 10.14279/depositonce-5819
- 2: Gordon, Karsten: A flexible attitude control system for three-axis stabilized nanosatellites.** – 2018. – XXVI, 173 S.
ISBN 978-3-7983-2968-3 (print) EUR 14.00
ISBN 978-3-7983-2969-0 (online)
DOI 10.14279/depositonce-6415
- 3: Grau, Sebastian: Contributions to the Advance of the Integration Density of CubeSats.** – 2019. – XXVIII, 139 S.
ISBN 978-3-7983-3026-9 (print) EUR 13.00
ISBN 978-3-7983-3027-6 (online)
DOI 10.14279/depositonce-7293
- 4: Köthe, Alexander: Flight mechanics and flight control for a multibody aircraft.** Long-endurance operation at high altitudes. – 2019. – XX, 258 S.
ISBN 978-3-7983-3036-8 (print) EUR 14.00
ISBN 978-3-7983-3037-5 (online)
DOI 10.14279/depositonce-7555
- 5: Schönfeld, Andrej: Untersuchung von PIO-Tendenzen bei plötzlichen Umschaltungen in der Flugdynamik.** – 2019. – XIII, 264 S.
ISBN 978-3-7983-3056-6 (print) EUR 17.00
ISBN 978-3-7983-3057-3 (online)
DOI 10.14279/depositonce-7922
- 6: Meyer-Brügel, Wolfram: Präzisere Echtzeit-Flugsimulation kleiner Nutzflugzeuge durch Integration feingranularer Teilmodelle.** – 2019. – XXV, 355 S.
ISBN 978-3-7983-3058-0 (print) EUR 19.00
ISBN 978-3-7983-3059-7 (online)
DOI 10.14279/depositonce-7797
- 7: Buscher, Martin: Investigations on the current and future use of radio frequency allocations for small satellite operations.** – 2019. – XX, 150 S.
ISBN 978-3-7983-3072-6 (print) EUR 19.00
ISBN 978-3-7983-3073-3 (online)
DOI 10.14279/depositonce-8247
- 8: Grimm, Martin: Untersuchungen zur Anwendung von Entfernungssensoren für Kleinsatelliten.** – 2019. – XXIV, 164 S.
ISBN 978-3-7983-3084-9 (print) EUR 19.00
ISBN 978-3-7983-3085-6 (online)
DOI 10.14279/depositonce-8407
- 9: Schreiter, Karolin: Ein Beitrag zum reglergestützten manuellen Fliegen.** – 2020. – VII, 166 S.
ISBN 978-3-7983-3111-2 (print) EUR 19.00
ISBN 978-3-7983-3112-9 (online)
DOI 10.14279/depositonce-9071
- 10: John, Sebastian: Beitrag zur Analyse des Eigenspannungsverhaltens von Composite-Hochdruckspeichern mit metallischem Liner.** – 2020. – XXI, 162 S.
ISBN 978-3-7983-3179-2 (print) EUR 19.00
ISBN 978-3-7983-3180-8 (online)
DOI 10.14279/depositonce-10442

Contributions to On Board Navigation on 1U CubeSats

This thesis investigates the use of GNSS receivers on 1U CubeSats. Therefore, the state of the art of GNSS receivers, that could be integrated into 1U CubeSats, is described. It is shown how the verification of the satellite's subsystems was performed on the ground, with the focus on attitude control and GNSS receivers. It is shown how a three-axis stabilized attitude control was first verified on BEESAT-4 followed by a successfully operated GNSS receiver on BEESAT-9. In addition, the inter-satellite link between BEESAT-4 and BIROS is analyzed, since it is essential for the relative navigation of satellites. Several research questions using the navigation data are addressed, including object identification, a qualitative analysis of the orbital elements (TLE) of BEESAT-9 vs. GNSS solutions, signal strengths of the used antenna over time and the quality of orbit determination with limited navigation data. The analyzed questions allow a statement about the continuous use of GNSS receivers on 1U CubeSats and if it is necessary to achieve the mission objectives.

ISBN 978-3-7983-3232-4 (print)
ISBN 978-3-7983-3233-1 (online)



ISBN 978-3-7983-3232-4



<https://verlag.tu-berlin.de>